1-1-1979

Scattering studies from polymer blends.

Thomas P. Russell
University of Massachusetts Amherst

SCATTERING STUDIES FROM POLYMER BLENDS

A Dissertation Presented

By

THOMAS P. RUSSELL

Submitted to the Graduate School of the
University of Massachusetts in partial fulfillment
of the requirements for the degree of

DOCTOR OF PHILOSOPHY

February 1979

Polymer Science and Engineering

SCATTERING STUDIES OF POLYMER BLENDS

A Dissertation Presented

By

THOMAS P. RUSSELL

Approved as to style and content by:

Richard S. Stein
Chairperson of Committee

William J. MacKnight, Member

Robert W. Lenz, Member

Isaac C. Sanchez, Member

Robert W. Hendricks
Adjunct Member

William J. MacKnight, Head
Polymer Science and Engineering

Dedicated to my wife

Cathy

for her patience, understanding, and

love throughout the course of this work.

ACKNOWLEDGMENTS

My sincerest appreciation is extended to Dr. Richard S. Stein, thesis director, for his patience, guidance, and advice in both my scientific and personal life.

I am also deeply indebted to the members of my thesis committee, Drs. W.J. MacKnight, R.W. Lenz, and I.C. Sanchez, for the invaluable advice and continued support they have given to me throughout the course of this work. I am particularly grateful to the late Dr. F.P. Price for suggesting the application of small angle x-ray scattering in dilute polymer blends.

A special note of thanks is extended to Dr. R.W. Hendricks for the use of his facilities at the Oak Ridge National Laboratories, for his encouragement and support, scientifically and financially and, also, the use of his cot during those extended days.

I am also grateful to Manfred Kopp, Drs. J.S. Lin, H. Yakel, W. Koehler, and H.R. Child for their assistance, cooperation, and encouragement during my stay at the Oak Ridge National Laboratories. I would also like to thank A. Wohlpart who assisted in obtaining support for this work from the Oak Ridge Associated Universities.

I am deeply indebted to Drs. A. Wasiak, F.P. Warner, D. James, and Y. Shindo for the invaluable discussions on the experimental and theoretical aspects of polymer research. I am particularly indebted to R. Cembrola, E. Roche, J. Koberstein, G. Senich, P. Gilmore, and D.

Anderson for their stimulating discussions on polymer research aspects and, more importantly, for their friendship and support throughout my graduate career.

The assistance of Mrs. D. Keedy, E. Nuttleman, J. DeCaro, and C. Napikoski of the technical shops was greatly appreciated.

I would also like to thank Dr. C. Picot for supplying the deuterated polystyrene and to Dr. J.S. Higgins for her assistance with the neutron scattering experiment interpretations.

To all of these individuals and to the entire Polymer Department for creating an atmosphere conducive to conducting research I am extremely grateful.

This work was supported in parts by grants from the National Science Foundation, the Army Research Office (Durham), the Oak Ridge Associated Universities, and the Materials Research Laboratory of the University of Massachusetts.

ABSTRACT

Scattering Studies from Polymer Blends

(February 1979)

Thomas P. Russell

B.S., Boston State College
M.S., University of Massachusetts
Ph.D., University of Massachusetts

Directed by: Professor Richard S. Stein

Small angle x-ray (SAXS) and neutron (SANS) scattering studies have been performed on a series of polymer blends in both the dilute and concentrated composition ranges.

SAXS studies utilizing a step scanning Kratky apparatus were performed on polyvinylchloride (PVC)/poly(ε-caprolactone) (PCL) blends over the entire composition range above the melting point of the PCL, as well as on the blends crystallized at 30°C. Results on the semicrystalline blend indicate that the lamellae separate to accommodate the PVC forming a true compatible mixture in the interlamellar regions. Studies on the amorphous blends indicated that the two polymers are segmentally mixed and, consequently, form a true solution.

SAXS studies using a Kratky apparatus with a one dimensional position sensitive detector were conducted on several blend systems where one of the components was dilute. Using Guinier analyses as a function of composition the radius of gyration, R_g, and molecular weight, M_W, at zero composition were found. These analyses, also, were

used to obtain the second virial coefficient, A_2.

In a dilute blend of PCL in PVC it was found that the PCL R_g was expanded in the PVC matrix and that PCL was molecularly dispersed in the PVC. A_2 was found to be zero within experimental errors. In the poly (para-iodostyrene) (PpIS)/polystyrene (PS) mixture the PpIS was found to cluster with both the R_g and M_w increasing as a function of composition.

The system of PS/PoClS (poly(ortho-chlorostyrene) did not possess enough contrast to be examined by SAXS. Deuterating the PS allowed the use of SANS which indicated that PS was expanded in the PoClS matrix. Again A_2 was found to be zero within experimental errors.

The results of A_2 and R_g are discussed with the conclusion that even in very compatible systems a value of $A_2 = 0$ is expected.

TABLE OF CONTENTS

LIST OF TABLES

LIST OF FIGURES

CHAPTER I

1. Introduction

The subject of polymer mixtures has received a considerable amount of attention from both academic (1-7) and industrial (8) scientists. The reason for such interest is that the properties of a material can be modified to produce a material with tailored properties simply by adding another polymer. This basically allows the use of already existing materials to produce a new and better product without resorting to chemical modification of the chain or synthesis of an entirely new product. Quite clearly, this has extreme economic value.

The final properties of the polymer mixture or blend will depend upon the degree of mixing between the two homopolymeric species. In a blend where the homopolymers are miscible in each other and form a homogeneous, molecularly dispersed mixture the homopolymers are called compatible. If the materials do not mix and form a phase separated system where the phases are the pure homopolymeric components then the two are called incompatible. In between these two extremes are the partially compatible materials where the mixtures are phase separated but the phases are not pure homopolymer. In such cases, boundaries between phases are diffuse indicating partial mixing.

Numerous methods have been developed to determine the extent of mixing in a blend. Probably the most frequently employed and most accepted criterion for compatibility is a single glass transition

temperature, Tg. For a phase separated system there will be two distinct Tg's characteristic of the individual phases present, whereas in a compatible mixture only one Tg will be seen located between the Tg's of the pure components (1,2,9,10). Experimentally, Tg can be easily measured by differential scanning calorimetry, dynamic mechanical testing (11,12,13,14,15), nuclear magnetic resonance (16) and changes in the specific volume on thermal expansion (17). These techniques require a significant difference in the Tg's of the homopolymers and can not be used in cases where the Tg's of the homopolymers are similar. An alternate criterion for compatible systems is optical clarity. This method relies on the refractive index between the two homopolymers. If the refractive indices are dissimilar then phase separated system will scatter light and the material will be opaque (3). However, if the phases are small or the refractive indices are similar, then this test will be insensitive (18,19). A classic example of this insensitivity is seen in the case of styrene-butadiene-styrene block copolymer where phase separation is known to occur (20,21,22). Here the phases are quite small and small angle X-ray scattering (SAXS) can be used to detect the phases (23). Consequently, SAXS can be used to examine phase separation where the differences in the electron density of the phases produces the contrast necessary to observe the phases. Along these same lines, fracture surface studies can be performed on the electron microscope (22,24,25) to determine the presence of phase separation. These latter two techniques are rather elaborate and should only be used when the simple techniques are not adequate. Recently, Coleman et al. (26,27) have demonstrated that infrared spectroscopy can be used to

determine compatibility by subtracting the properly weighed spectra of the two homopolymers from that of the blend. If the system is incompatible then there is no difference between the spectra of the weighted sum of the homopolymers and the blend. In a compatible blend a difference is seen and the groups involved in specific interactions in the mixture can be determined.

In addition to the morphological behavior of a mixture, thermodynamic parameters can be used to determine compatibility. For example, if one of the components crystallizes, as is the case in polyvinylidenefluoride (PVF_2) and polymethylmethacrylate (PMMA) or polyethylmethacrylate (PEMA) blends the melting point depression of the crystals can be used to indicate a mixing in the amorphous phase (28). Similar observations have been made in blends of poly(ε-caproacetone) (PCL) and polyvinylchloride (PVC) (29). Thermodynamic parameters can also be obtained by mutual solvent techniques (30). Using binary solution theory (31,32,33,34,35,36) coupled with ternary solution theory (32,33,37) to describe the appropriate solution, the Flory-Huggins interaction parameter can be determined for the two polymers and, consequently, determine their compatibility. Olabisi (38), using a gas-liquid chromatography technique developed by Guillet (39,40) employed these ideas in the investigation of PCL-PVC blends.

However, as pointed out by Krause (1,2), compatible mixtures are more the exception than the rule. This can easily be understood by examining the free energy of mixing ΔG_m, given by

$$\Delta G_m = \Delta H_m - T\Delta S_m \qquad (1)$$

where ΔH_m is the heat of mixing reflecting the type of polymer-polymer interactions occurring and can be defined in terms of the Hildebrand-Scott interaction energies (41). ΔS_m is the entropy of mixing and is a measure of the degree of randomness in a system. ΔH_m depends upon the total number of segment-segment interactions whereas ΔS_m depends upon the total number of molecules in a system. Just from this consideration ΔS_m would be expected to be small due to the size of the polymer chain and, consequently, the small number of molecules present. Gee (42) pointed to this fact by demonstrating that ΔS_m is approximately one thousand times smaller for a polymer mixture than for a small molecule mixing. Therefore only a slightly positive ΔH_m will lead to a phase separated system (37).

Using equation (1), it would be predicted that raising the temperature in a polymer-polymer mixture would tend to compatibilize the polymers. Also, if a mixture were compatible at lower temperatures then it should remain mixed at elevated temperatures. Experimental observations on several systems indicated the opposite. In polyvinylmethylether (PVME) blends with polystyrene (PS) Bank et al. (43), Nishi et al. (16,44) and Bernstein et al. (45) have shown that the system phase separates at elevated temperatures. Alexandrovich (46) has demonstrated the same phenomenon in blends of PS with polyorthochlorostyrene (POClS). Bernstein et al. (45) established the same conditions for several more systems, including systems where one of the components crystallizes. Therefore, this phase separation at elevated temperatures appears to be a general phenomenon.

These observations cannot be predicted by the simple Flory-

Huggins treatment and have led to extensions and modifications of this theory. McMaster (47), Flory (48), Prigogine (49), Tager (50), Patterson (51,52), and LaCombe and Sanchez (53) have recently developed theories that encompass mixtures for any sized molecules. All of these treatments predict phase separation at both reduced and elevated temperatures. These theories incorporate temperature, pressure and concentration dependences of polymer-polymer interaction parameters leading to fairly accurate predictions of upper and lower critical solution temperatures (UCST and LCST, respectively). However, the theory of LaCombe and Sanchez (53) is more general and can be applied to polymer-polymer mixtures as well as liquid-gas equilibrium.

There are several interesting outgrowths of both the observations and the theoretical treatments. UCST is a general phenomenon and is readily observable in low molecular weight mixtures (49,54), as well as polymer solvent mixtures (31,32,35). In polymer-polymer mixtures this is not the case because the mixture exists either as a glass (below Tg) or is extremely viscous. Therefore, the motion of the molecules past one another is quite slow and phase separation can be prohibited on this account. Recently Ryan (55), using binary and ternary techniques, has examined mixtures of PS and POCLS at 35°C. A positive heat of mixing was found in apparent contradiction to the fact that the bulk blend at room temperature (<100°C below Tg of the bulk blend) is known to be compatible (56). However, the use of solutions has circumvented the barrier of diffusion allowing the molecules to interact and, consequently, lead to the result that the two polymers are incompatible at 35°C. These results can be explained thermodynamic-

ally but they also point to the cautions that must be used in making conclusions on bulk blends from solution results.

Another consequence of the critical solution phenomenon is the mode or mechanism in which the phase separation occurs. If the phase diagram of a mixture is considered, as shown in Figure 1, it is seen that then a homogeneous solution exists anywhere outside of the binodal, which from an equilibrium viewpoint defines where phase separation will occur with the chemical potential of the components being equal in the two phases. The absolute limit of stability is defined by the spinodal given by

$$\left(\frac{\partial^2 \Delta G_m}{\partial \phi_i} \right) = 0 \qquad (2)$$

Within the envelope defined by the spinodal phase separation must occur. Between the spinodal and binodal is a region called the miscibility gap where a solution can exist in a metastable state. In terms of fluctuations or perturbations in the system, phase separation can occur in the miscibility gap provided there is a fluctuation of significant magnitude to nucleate phase separation. Within the spinodal small perturbations will spontaneously lead to a phase separation process. These different modes of phase separation are distinguishable from one another in that the nucleation and growth process occurs by the nucleation of a phase with a given composition. This phase grows in size but retains its equilibrium composition defined by the binodal. Spinodal phase separation or spinodal decomposition occurs by a periodic fluctuation throughout the mixture. The magnitude of the

fluctuations will continually change until the composition of the two "phases" characterized by the amplitude of the periodic is that defined by the binodal. This essentially saturates periodic function and the mixture continues to separate to produce only two phases of the binodal composition. These are schematically illustrated in Figure 2. Theoretical characterization of the different types of phase separation processes have been described by Cahn et al. (57,58,59), Langer (60,61), and others (62,63). The results of Nishi and Kwei on PVME/PS blends (44) using optical microscopy indicate that spinodal decomposition is the preferred process. Unpublished results of Goldstein (64) and Gilmer (65) using light scattering to characterize the phase separation in PS/POClS blends are inconclusive since the long wavelength of light only revealed the latter stages of the separation. This indicates that X-ray scattering must be used to reveal the initial steps of the phase separation process and consequently distinguish between the two mechanisms.

In most compatible polymer systems, however, the LCST occurs above the decomposition point (66). The LCST can be lowered by the application of pressure so that the decomposition problem can be overcome. This fact could become important in some extrusion processes where molten polymer mixtures are subjected to large pressures. To date, this has not been observed, though.

From the above discussions it is apparent that a single polymer blend can exist in a wide range of mixed states. Consequently, in a given polymer blend system the interactions occurring between the two polymers as well as the conformations of the individual molecules will

depend upon the temperature, composition, and pressure in the system. The only technique that can be used to obtain this information is scattering.

Scattering techniques have proved to be a valuable tool in the investigation of the conformations and configurations of isolated polymer molecules in dilute solutions. It was Zimm (67) who first combined the concentration and angular dependence of scattering to obtain these parameters. From the limits of the scattering at zero angle and zero concentration the molecular weight, second virial coefficient, and the radius of gyration can be obtained. These parameters characterize the interactions occurring in the system and the effect of these interactions on the molecule. Others (68,69) have extended this work to include the effects of polydispersity of the molecules. Kratky (70,71,72) applied essentially the same type of analysis to X-ray scattering from solutions emphasizing the generality of the Zimm approach.

Recently, and more importantly for polymer blends, these techniques have been applied to solid mixtures where one polymer is blended with another without the presence of a solvent. Krigbaum and Godwin (73) and Hayashi et al. (74) have used X-ray scattering on bulk polystyrene samples where a dilute amount of the chains were iodinated to supply the contrast. Benoit et al. (75,76,77), Scheten et al. (78,79, 80,81,82), Kirste et al. (83,84,85,86,87) and Sadler and coworkers (88) have recently exploited neutron scattering for the same purpose. This technique avoids the use of heavy atoms to provide contrast and sufficient contrast can be provided by deuterating a dilute concentration of the chains. Works in this area have included the bulk conformations of

polyethylene, polymethylmethacrylate, polystyrene and polypropylene in both the amorphous and semicrystalline states. Very recently, this technique has been extended to polymer blends by Kirste (89), who investigated the conformation of polystyrene in a matrix of polyacrylonitrile-polystyrene copolymer and Higgins (90) on the conformation of a polystyrene chain in polyorthochlorostyrene-polystyrene blend matrix.

Consequently, this investigation was undertaken to utilize both X-ray and neutron scattering technique to examine the conformation of isolated polymer molecules in a matrix of different chemical composition. Using the values of the second virial coefficient and the radius of gyration the interactions occurring can be characterized and can furnish information concerning the compatibility or incompatibility of the mixture.

2. Amorphous Polymers

Since a major section of this work deals with a small amount of scattering in excess of the scattering from a blank where the blank sample is a glassy polymer, then a discussion of glassy or amorphous polymers is necessary, indicating the current views of such material and the possible ramifications of structure in the glassy state. Polymers of particular interest are PVC, PMMA, polycarbonate (PC), polystyrene (PS), and polyethyleneterepthalate (PET). These materials have been investigated rather extensively but there is still uncertainty about the order in these materials.

There are essentially two schools of thought concerning order

in amorphous polymers. The first simply denies the possibility of any long range order and that the polymer molecule assumes its unperturbed configuration in the bulk material. Proponents (91-100) cite numerous results from birefringence, small and wide angle X-ray scattering, light depolarization, and deformation studies to support their ideas. On the other hand, others feel that there must exist some sort of long range structure or even superstructure, particularly in crystallizable materials like PET. There is no one idea on what this order should be. From electron microscopy measurements and from small angle X-ray measurements on plasticized materials, Yeh et al. (101-105) state that there are nodular types of structures of approximately 20 nm in size composed of random chains. Pechold (106), Kargin (107), and Aharoni (108), however, propose an alternate form of a bundle like structure where a bundle of random chains (although this is not necessarily the case) meander through the amorphous material. Interestingly enough, proponents of these models cite the same works as the "no order school" to support their arguments. Indeed, these models become more feasible when one considers the recent neutron data of Schelten et al. (109), where in a sample of crystalline polypropylene the chain was found to retain its unperturbed dimensions.

Consequently, the question of order still remains unanswered. As to the effect of this possible order on this investigation is unknown. It is hard to imagine that a polymer molecule in an environment of another polymer would not be affected by the state of the alternate component. If the interactions occurring in the material are favorable then the segmental interactions should be maximized. Consequently, if

there is an overall superstructure then the dilute component should be able to penetrate the bundle in order to maximize the interactions. Consequently, this may lead to a decrease in the scattering due to disruption of this superstructure or there would at least be an over-subtraction of the background due to the intensity lost that originated from the bundle. It is also possible to envisage the molecule being retained with a bundle as are the chains of the host material. If the lack of order concept is correct, then there is no problem accommodating the dilute component in order to maximize the interactions and yield results that are characteristic of the dilute component. As will be seen, the results from this investigation support the idea that whatever order (or lack thereof) there is in the amorphous phase, it did not interfere with the analysis to within experimental errors. It is not felt that the results from the X-ray and neutron scattering experiments can shed any light in this area. It very well could indicate that radius of gyration measurements are not sensitive enough to distinguish between the two models, as Shelten's work indicates (109) also.

CHAPTER II

THEORY

1. Introduction to Scattering

Scattering in general can be used to elucidate the structure of a material. The size of the structure being examined will depend upon the wavelength of the incident radiation and the contrast present in the system. Light, typically having wavelengths of 450 nm or higher, examines polarizability fluctuations and is useful in a size range of 100 nm or higher. X-rays with wavelengths up to 0.3 mn examine fluctuations in the electron density in the size range from 500 nm and less. Neutrons, having a range of wavelengths up to 1 nm, rely on neutron scattering cross sections to provide the scattering and cover a similar range as x-rays.

Since the various type of radiation supply information at different levels, they are complementary in revealing the structure of a material from the macroscopic to sub-microscopic level. Recently, Higgins and Stein (181) have reviewed these three areas, emphasizing this complementarity.

The structure of a system is revealed by the interference observed in the scattered radiation. These interferences can be divided into two categories: where only intraparticle interference effects are important, as in dilute solutions, and where interparticle interference effects become important, as in concentrated solutions. Consequently,

these two effects will be treated separately in the presentation of the scattering theory.

2. Dilute Solution Scattering Theory

In general, the amplitude of scattering, Es, from a system composed of collections of Z_K electrons with an incident field amplitude, E_o, and frequency, ω, is given by (182)

$$E_s = \sum_K Z_K \left(\frac{-e^2\omega^2 E_o e^{i\omega t}}{M_o(\omega_o^2-\omega^2)}\right) \frac{\sin\psi}{rc^2} e^{-\frac{2\pi}{\lambda} \underset{\sim}{R}_K \cdot \underset{\sim}{S}} \qquad (3)$$

where e is the charge of an electron of mass, M_o, ω_o is the resonance frequency of the electron, r is the distance from the dipole to the observer at an angle ψ measured from the direction of the dipole, c is the speed of light, $\underset{\sim}{R}_K$ is a vector from the origin to the K^{th} scatterer, $\underset{\sim}{S} = \underset{\sim}{S}_1 - \underset{\sim}{S}_o$ where $\underset{\sim}{S}_o$ and $\underset{\sim}{S}_1$ are unit vectors in the direction of the incident field and scattering, respectively, $|\underset{\sim}{S}| = 2\sin(\theta/2)$ and $\underset{\sim}{h} = \frac{2\pi}{\lambda} \underset{\sim}{S}$.

Two cases can be considered in equation (3). If $\omega_o >> \omega$, then the electron can easily follow the applied field. This is the case for Rayleigh or light scattering and the scattering will depend upon the frequency of E_o. If $\omega_o << \omega$, then the electrons cannot respond rapidly enough to the applied field. This is the case for Thompson or x-ray scattering and equation (3) reduces to

$$E_S = \sum_K Z_K \frac{\sin\psi}{rc^2} \left(\frac{-e^2 E_o e^{i\omega t}}{M_o}\right) e^{-i\underset{\sim}{R}_K \underset{\sim}{h}} \qquad (4)$$

The Z_K electron can be considered as an average value Z plus a deviation from this average, $(\Delta Z)_K$. It is these deviations or fluctuations that give rise to the scattering. Consequently, Z_K can be replaced by $(\Delta Z)_K$. Therefore, the intensity of scattering can be given by

$$I_S = \frac{i_e I_o}{r^2} \sum\sum (\Delta Z_K)(\Delta Z_j) \cos \underset{\sim}{r}_{Kj} \cdot \underset{\sim}{h} \qquad (5)$$

where i_e, the Thompson scattering factor, is given by $e^2/M_o^2 c^2 = 7.9 \times 10^{-26}$ cm^2, $I_o = 1/4\Pi\ E_o^2$ and $\underset{\sim}{r}_{Kj}$ is a vector defined by $\underset{\sim}{r}_{Kj} = \underset{\sim}{r}_K - \underset{\sim}{r}_j$.

In the absence of intraparticle and interparticle interference the average scattering arising from this system is given by

$$I_S = \frac{i_e I_o}{r^2} N_v \overline{(\Delta Z)^2} = \frac{i_e I_o}{r^2} N_v V_o^2 \overline{(\Delta \rho)^2} \qquad (6)$$

where N_v is the number of scatterers per unit volume, $\Delta\rho$ is the fluctuation in the electron density and V_o is the scattering volume.

Employing the fluctuation theory of Einstein (110) and Debye (111), $(\Delta\rho)^2$ can be related to fluctuation in temperature, pressure and concentration in a dilute solution. If the fluctuations are independent of each other then fluctuations due to temperature and pressure can be subtracted out leaving the excess scattering, $\overline{(I_S)}_{ex}$, due to the dissolved material. Therefore,

$$\overline{(I_S)}_{ex} = \frac{i_e I_o N_v V_o^2}{r^2} \left(\frac{\partial \rho}{\partial c}\right)^2_{T,\rho} \overline{(\Delta C)^2} \qquad (7)$$

The fluctuation in concentration is related to the change in the

chemical potential with respect to concentration, $\overline{(\Delta C)^2}$, by (32)

$$\overline{(\Delta C)^2} = \frac{c}{\frac{N_A V}{RT}\left(\frac{-1}{\bar{V}_1}\left(\frac{\partial \mu_1}{\partial c}\right)\right)} \tag{8}$$

where N_A is Avogadro's number, R is the gas constant, V is the scattering volume, $\bar{V}_1$ is the molar volume of the solvent and T is the temperature.

The chemical potential is related to the osmotic pressure, π, which can be written in terms of a virial expansion by

$$\left(\frac{\partial \pi}{\partial c}\right) = \frac{-1}{\bar{V}_1}\left(\frac{\partial \mu_1}{\partial c}\right) = RT\left[\frac{1}{M_w} + 2A_2 c + \ldots\right] \tag{9}$$

where A_2 is the second virial coefficient.

Substitution of equation (8) and (9) into equation (7) results in

$$(\overline{I_S})_{ex} = \frac{N_A i_e I_o V_S \left(\frac{\partial \rho_M}{\partial c}\right)^2_{T,P} c}{r^2\left(\frac{1}{M} + 2A_2 c\right)} \tag{10}$$

where ρ_M is the molar electron density.

A convenient method of rewriting $(\overline{I_S})_{ex}$ is in terms of the Rayleigh factor, $R = I_S r^2 / I_o V_S$. This is independent of the scattering geometry and depends only on the system. Therefore equation (10) can be written as

$$\frac{Kc}{R} = \frac{1}{M_w} + 2A_2 c = \left(\frac{P(h)}{M_w}\right)_{h=0} + 2A_2 c \tag{11}$$

where $K = i_e N_A (\partial \rho m / \partial c)^2_{T,P}$. (12)

For the case of Rayleigh scattering the same equation would be obtained but the constant K would be

$$K_{LS} = 2\pi \bar{n}_o^2 \left(\frac{\partial n}{\partial c}\right)^2 / N_A \lambda \tag{13}$$

where n_o is the average refractive index of the medium, λ is the wavelength of the incident field, and $(\partial n/\partial c)$ is the change in the refractive index as a function of concentration.

Equation (11) defines the scattering from a system as a function of concentration in the absence of either interparticle or intraparticle interferences. If the solution is dilute where the particles are randomly distributed throughout the medium, the former assumption is valid. However, the latter assumption is not, since this arises from the structure of the particle.

When the particle that is scattering is larger than the wavelength of the incident radiation, the intraparticle interference function, $P(\theta)$, must be considered. From classical scattering theory (112) the amplitude of scattering, E(h), is given by:

$$E_S(h) = \sum_K E_K = E_e(h) \sum_K f_K e^{-i\underset{\sim}{h}\underset{\sim}{r}_K} \tag{14}$$

where f_K is the structure factor, $\underset{\sim}{r}_K$ is a vector from the origin to the scatterer and $E_e(h)$ is the scattering amplitude from one electron. The intensity of scattering averaged over all time is therefore given by (112):

$$\overline{I_S(h)} = I_e(h) \sum_{Kj}\sum f_K f_j \overline{\cos(\underset{\sim}{h}\cdot\underset{\sim}{r}_{Kj})} \tag{15}$$

$$= I_e(h) \sum_{Kj}\sum f_K f_j \frac{\sin h\,|\underset{\sim}{r}_{Kj}|}{h\underset{\sim}{r}_{Kj}} \tag{16}$$

where $\underset{\sim}{r}_{Kj} = \underset{\sim}{r}_K - \underset{\sim}{r}_j$.

The sine term can be expanded in a power series and noting that

$$|\underset{\sim}{r}_{Kj}|^2 = |\underset{\sim}{r}_K|^2 + |\underset{\sim}{r}_j|^2 - 2|\underset{\sim}{r}_K||\underset{\sim}{r}_j| \cos\phi_{Kj} \tag{17}$$

where ϕ_{Kj} is the angle between vectors $\underset{\sim}{r}_K$ and $\underset{\sim}{r}_j$.

$$\overline{I_S(h)} = I_e(h)\left(\sum_K f_K\right)^2\left\{1 - \frac{h^2}{3}\frac{\sum f_j|\underset{\sim}{r}_j|^2}{\sum f_K} - \frac{h^2}{3}\frac{\sum f_K|\underset{\sim}{r}_K|\sum f_j|\underset{\sim}{r}_j|\cos\phi_{Kj}}{\left(\sum f_K\right)^2}\right\} \tag{18}$$

As $h \to 0$:

$$\overline{I_S(h)} = I_e(h)\left(\sum_K f_K\right)^2\left(1 - \frac{h^2}{3}\overline{R_G^2}\right) \tag{19}$$

where $(\overline{R_G^2})^{1/2}$ is the root mean square radius of gyration of the particle.

It is important to realize that the equation for $\overline{I_S(h)}$ was obtained without any assumption concerning the dimensions of the particle in solution. Consequently, it is perfectly general and is applicable to every kind of dissolved particle.

At zero angle $\overline{I_S(h)}$ becomes

$$\overline{I_S(o)} = I_e(o)\left(\sum_K f_K\right)^2 = I(o)$$

where I(o) has been shown previously to be proportional to M_w in the limit of zero concentration. Therefore, $1 - \frac{h^2\overline{R_G^2}}{3}$ represents the interference function; P(h).

P(h) can be approximated in several different manners. Guinier chose to approximate P(h) as an exponential function where for small values of h

$$P(h) = 1 - \frac{h^2\overline{R_G^2}}{3} \simeq \exp\left(\frac{-h^2\overline{R_G^2}}{3}\right) \tag{20}$$

alternately,

$$P^{-1}(h) = \frac{1}{1 - \frac{h^2\overline{R_G^2}}{3}} \simeq 1 + \frac{h^2\overline{R_G^2}}{3} \tag{21}$$

Consequently, substituting into equation (11)

$$\frac{KC}{R(h)} = \frac{1}{M_w}\left(1 + \frac{h^2\cdot\overline{R_G^2}}{3}\right) + 2A_2C \tag{22}$$

or

$$\frac{KC}{R(h)} = \frac{1}{M_w} \exp\left(\frac{h^2\overline{R_G^2}}{3}\right) + 2A_2C \tag{23}$$

The former expression is the familiar Zimm equation, whereas the latter expression, equally valid at small values of $h^2\overline{R_G^2}$, is a modified version.

Debye (111,113) has extended this treatment of P(h) by considering the interference of a polymer coil, where the chain segment density is distributed about the center of gravity in a gaussian fashion.

In this case,

$$P(h) = \frac{2}{x^2}\left[e^{-x} - (1 - x)\right] \qquad (24)$$

$$\text{where } x = h^2\overline{R_G^2}$$

At small angles, this also reduces to the value obtained previously by simply expanding the exponential.

In a similar fashion, the same result can be obtained for neutron scattering. Benoit (76) has shown that for a mixture of labeled polymer A in a polymer B matrix the total intensity of scattering is given by

$$I(h) = N_A V \phi_o t T\left[\kappa^2 \frac{C_A}{m_A^2} M\, P(h) + \frac{C_A}{m_A} A_I^2 + \frac{C_B}{m_B} B_I^2\right] \qquad (25)$$

where N_A is Avogadro's number, V is the scattering volume, ϕ_o is the incident neutron flux (cm^{-2} sec^{-1}), t is the counting time for an experiment, T is the trans mission coefficient, C_A and C_B are the concentrations (g/cm^3) of components A and B, m_A and m_B are the molecular weights of monomers A and B, κ^2, A_I^2 and B_I^2 are the coherent scattering cross section and the incoherent scattering cross-sections of A and B. P(h) is the value of the interference function normalized to $P(0) = 1$.

Since the solvent scattering is represented strictly by the total incoherent scattering level, then we have

$$I(h)_{solv} = N_A V\, {}_o Tt\left[\frac{C_A}{m_A} A_I^2 + \frac{C_B}{m_B} B_I^2\right] \qquad (26)$$

As can be seen from the right side of this equation, $I(h)_{solv}$ is really not a function of h and is a constant. Therefore, the excess scattering due to the presence of a dilute quantity of labeled material is given by

$$I(h)_{ex} = I(h) - I(h)_{solv} \tag{27}$$

$$= N_A V \phi_o t T [\kappa^2 \frac{C_A}{m_A} MP(h)] \tag{28}$$

Therefore,

$$\frac{I(h)}{\phi_o V t T} = N_A \kappa^2 \frac{C_A}{m_A} MP(h) = \frac{I(h) r^2}{I_o V} = R(h) \tag{29}$$

This is identical to the Rayleigh Factor $(I(h)r^2/I_o V)$ employed in light scattering and x-ray scattering. Rewriting in terms of R(h) results in the familiar Zimm expression at h = 0.

$$\frac{KC}{R(h)} = \frac{P(h)}{M} \quad \overset{\rightarrow}{h=0} \quad \frac{1}{M} \tag{30}$$

where

$$K = N_A \kappa^2 / m_a = N_A Z \left| B_P - B_S \frac{V_P}{V_S} \right|^2 / m_A^2 \tag{31}$$

and the parameters have been defined previously.

There are several precautionary notes that must accompany the use of the preceding equations for light, x-ray and neutron scattering. These precautions are centered around several assumptions that have been made. Firstly, the system must be dilute, that is, each scatterer must be randomly located in a system and must act as an independent scatterer. The question of 'How dilute is dilute?' will be treated later. Secondly, the interpretation of the second virial coefficient

in the Flory-Huggins sense for a polymer-polymer mixture may be subject to some error, as will be discussed later. Thirdly, the approximations made require that experiments be carried out within a particular angular range. This will be discussed shortly. The final assumption made in a sense implicitly is that these equations are for monodisperse systems and not for a system with a polydisperse molecular weight distribution. This does cause an effect and will be discussed shortly. Only when these limitations are strictly met can the equations outlined above be used correctly.

Each of these limitations will be treated below under separate headings to amplify the restrictions placed on this type of analysis.

A. Angular limitations. The angular limitations in this analysis arise in the assumptions made in equations (16)-(19) and in equations (20) and (21). The first assumption involves the truncation of a power series expansion for the sine function in the second term. Consequently, it is assumed that

$$\frac{\sin x}{x} \simeq 1 - \frac{x^2}{6}$$

The second assumption involves either assuming that

$$\frac{1}{1-x} \simeq 1 + x$$

or

$$\frac{1}{1-x} \simeq \exp(-x)$$

Both of these assumptions are strictly valid only at $x = 0$. However, since $x = h^2\overline{R^2}$ this will be the case only where $h = 0$ or a measurement

is made at zero scattering angle. Because of this upper limits have been set on the range of applicability of these equations (112). Normally, the limitation is that $h^2R^2 < 1$ or $h < 1/R$ (some feel the approximations are valid for $h^2R^2 < 3$). We shall look at three dilute macromolecular solutions containing molecules of $\overline{R}$ = 5 nm, 10 nm, and 20 nm. These require that $h < 0.2$, 0.1, and 0.05 nm^{-1}, respectively. Due to the wavelength dependency of h the angular limitation will vary for the different radiations. Table 1 lists four different wavelengths of equipment now in use along with the angular limitation of each.

It is quite evident that as the wavelength of the radiation is increased the angular range in which data can be legitimately collected increases. Inversely, as the wavelength decreases, the minimum angular resolution must increase. This is particularly problematic with x-rays, where high resolution is required, thus making the use of a Kratky or a Bonse-Hart apparatus mandatory. Spectrometers at Oak Ridge and Grenoble can easily reach the desired resolution with a fairly large range of angles for data collection. For light scattering this really does not create a problem. However, as enumerated by Tabor (114), other problems limit this technique.

B. Effect of polydispersity. Consider the Debye coil interference function for a monodisperse system of Gaussian coils with a degree of polymerization N. The interference function shown previously can be rewritten as

$$P(h) = \frac{2}{N^2U^2}\{NU - 1 + \exp(-NU)\} \qquad (32)$$

TABLE 1

ANGULAR LIMITATIONS OF ANALYSIS

SOURCE	WAVELENGTH (nm)	MAXIMUM VALUES OF h AND θ FOR DATA COLLECTION								
		5.0 nm = R			10.0 nm = R			20.0 nm = R		
		h (nm)	θ (deg)	θ (rad)	h (nm)	θ (deg)	θ (rad)	h (nm)	θ (deg)	θ (rad)
Light	540	0.2	180	6.3	0.1	180	6.28	0.05	180	6.28
		h (nm)	2θ (deg)	2θ (rad)	h (nm)	2θ (deg)	2θ (rad)	h (nm)	2θ (deg)	2θ (rad)
X-rays (2θ)	0.15	0.2	0.3	0.005	0.1	0.13	0.002	0.05	0.07	0.001
Neutrons (2θ)	0.50	0.2	0.9	0.02	0.1	0.5	0.008	0.05	0.2	0.004
	1.0	0.2	1.8	0.03	0.1	0.9	0.02	0.05	0.456	0.008

where $U = h^2b^2/6$ and b is a length of the statistical element of the chain.

Zimm (67) and later Benoit (68) expanded this to include the effect of polydispersity. Letting f(N) be the number of chains with a degree of polymerization N the scattering is given by

$$P(h) = \frac{1}{\int_o^\infty Nf(N)dN} \int_o^\infty Nf(N)P_N(h)dN \qquad (33)$$

where $P_N(h)$ represents the interference function of a coil with a DP = N. The number, weight, and Z-average moments of f(N) are given by

$$\langle N_N \rangle = 1/(\int_o^\infty \frac{f(N)}{N} dN) \qquad (34)$$

$$\langle N_W \rangle = \int_o^\infty Nf(N)dN \qquad (35)$$

$$\langle N_Z \rangle = \frac{1}{\langle N_W \rangle} \int_o^\infty N^2 f(N)dN \qquad (36)$$

When the appropriate substitutions are made and P(h) is expanded as before, then

$$P(h)^{-1} = 1 + \langle N_Z \rangle U/3 \qquad (37)$$

This effectively means that the radius of gyration measured is characteristic of the Z-average and not the weight average value.

Consequently, the radius of gyration determined must be corrected to reduce it to the weight average value. Zimm (67) and, later,

Schultz and coworkers (115) have presented the appropriate correction factor for a polymer whose molecular weight distribution can be approximated by

$$f(N) = (y^{i+1}/Z!)n^{Z}e^{-yn} \tag{38}$$

where $f(N)$ is the number of molecules of molecular weight N, $Z = (\langle N^2\rangle/\langle \Delta N^2\rangle) - 1$, $\langle N\rangle$ is the weight average molecular weight, ΔN is the distributions dispersion and $y = \langle N\rangle/\langle \Delta N^2\rangle$. This ultimately leads to an equation to obtain $\overline{R_W}$ from $\overline{R_Z}$:

$$\overline{R_W} = \left(\frac{\overline{M}_W/\overline{M}_N}{2\overline{M}_W/\overline{M}_n - 1} \right)^{1/2} \overline{R}_Z \tag{39}$$

For a monodisperse chain, this says that $\overline{R}_W = \overline{R}_Z$ and that the broader the distribution, the greater is the correction factor.

C. Effect of concentration. A very important assumption was made when the form of the interference function was being discussed. It was assumed that each molecule was randomly located in the medium and was acting as an individual scattering entity. No account was made for interferences between the coils. This brings up the question of the maximum concentration where this dilute approximation can be made.

Cotton et al. (116) have defined a critical concentration, C*, at which the molecules begin to overlap as

$$C^* = M/N_A R_G^3 \tag{40}$$

So, for example, a polystyrene molecule with a molecular weight of 10^5

and a corresponding radius of gyration of 10 nm (10^{-6} cm) produces a $C^* = 0.17$ g/cm^3. Similar calculations were performed for poly(ε-caprolactone), where $M_W = 45{,}000$ and $\overline{R}_g = 5$ mm (5×10^{-7} cm), yielding a $C^* = 0.6$ g/cm^3. It was felt that these concentrations were much too high for there not to be significant chain overlapping. Consequently, an alternate approach was used to define the limits of the dilute solution approximation.

Eight molecules were placed at the corners of a cube and the chain displacement lengths were assumed to be given by a Gaussian (32)

$$W(r)dr = (\beta/\pi^{1/2})\ 4\pi r^2 e^{-\beta^2 r^2} dr \qquad (41)$$

where $W(r)dr$ defines the probability that a chain displacement length in between r and r + dr and $\beta^2 = \frac{1}{2}\overline{R_g^2}$. The dimensions of the cube were varied until the molecules' density distributions overlapped by 5%. This was taken to define a dilute solution and for a molecule with $\overline{R}_g = 5$ nm a concentration of 1.5×10^{-2} g/cm^3 was found. This definition of dilute was retained throughout this study.

Another approach to this problem of interferences arising between chains is to include the interferences in the analysis. Rather than having the normal Zimm equation of

$$\frac{KC}{R(h)} = \frac{P(h)}{M_W} + 2A_2C \qquad (42)$$

an alternate equation obtained by Albrecht (117) can be used

$$\frac{KC}{R(h)} = \frac{P_1(h)}{M_W} + 2A_2CQ(h) \qquad (43)$$

where $Q(h) = P_2(h)/P_1^2(h)$, $P_2(h)$ is the interference function of a single chain and $P_2(h)$ is related to the root mean square distance between the centers of gravity of pairs of molecules. In subsequent work by Picot (118) and Hyde and Taylor (119,120,121) over wide ranges of concentrations marked curvature was found in plots of $Kc/(I - I_{solv})$ vs. C as well as a change in the slope of $KC/(I - I_{solv})$ vs. $\sin^2(\theta/2)$. These studies indicate the possible concentration dependencies of A_2 or what may be termed the apparent molecular weight and the radius of gyration. Figure 3 shows a copy of these results and it can be seen that deviations from linearity are strong at concentrations $> 5 \times 10^{-2}$ g/cm^3 but even at lower concentrations there is still curvature. Both works indicate that the higher the concentrations are, the more difficult it is to perform the necessary extrapolations to obtain the desired molecular parameters.

D. Interpretation of the second virial coefficient. It will be assumed that the second virial coefficient, A_2, obtained from either the Zimm analysis or the modified Zimm analysis has been obtained from the initial slope of $KC/R(o)$ vs. C as $C \to 0$. Using this value, the effects of interchain interferences as discussed previously will be neglected and the value of A_2 reflects the interactions occurring in one molecule.

Before entering into a discussion of the interpretation of A_2 in a binary system it will be useful to review some classical lattice statistics to examine the origin of A_2. The lattice will be treated in a general fashion so that the final expression for A_2 can be interpreted for binary mixtures of molecules of any molecular weight.

Consider a binary mixture of two molecules, each occupying r_1 and r_2 lattice sites so that they completely fill a lattice of $N_1r_1 + N_2r_2$ sites. As shown by Flory (33,122) and Huggins (39), the free energy of mixing, ΔG_m, is given by:

$$\Delta G_m = kT(N_1r_1 + N_2r_2)\left(\frac{\phi_1}{r_1}\ln\phi_1 + \frac{\phi_2}{r_2}\ln\phi_2 + \phi_1\phi_2\chi\right) \quad (44)$$

where ϕ_1 is the volume fraction of component 1 and is given by $\phi_1 = 1 - \phi_2 = N_1r_1/(N_1r_1 + N_2r_2)$. χ is the interaction parameter and can be written in terms of the potential energy of component 1 - component 2 contacts as (41,123,124)

$$\chi = (Z/2)(\varepsilon_{11} + \varepsilon_{22} - 2\varepsilon_{12})/kT \quad (45)$$

where Z is the coordination number of the lattice, T is the absolute temperature, and k is Boltzmann's constant.

The chemical potential of component 1, $\Delta\mu_1$, is given by

$$\Delta\mu_1 = (\partial\Delta G_m/\partial N_1)_{N_2,T,P} \quad (46)$$

Therefore,

$$\Delta\mu_1/RT = \ln\phi_1 + (1 - r_1/r_2)\phi_2 + r_1\chi\phi_2^2 \quad (47)$$

Similarly,

$$\frac{\Delta\mu_2}{RT} = \ln\phi_2 + (1 - r_2/r_1)\phi_1 + r_2\chi\phi_1^2 \quad (48)$$

Expanding $\ln\phi_1$ in equation (47), we get:

$$(\Delta\mu_1/RT) = -\{(r_1/r_2)\phi_2 + (1/2 - r_1\chi)\phi_2^2 + \phi_2^3/3 + \ldots\} \quad (49)$$

The osmotic pressure, π, is related to $\Delta\mu_1$ by

$$\pi = -\Delta\mu_1/\bar{V}_1 = \{(RT/V_1^o)(\frac{r_1}{r_2}\phi_2 + (1/2 - r_1\chi)\phi_2^2 + \phi_2^3/3 + \ldots\} \quad (50)$$

For dilute solutions

$$\phi_2 = \frac{r_2N_2}{r_1N_1+r_2N_2} \simeq \frac{r_2N_2}{r_1N_1} \quad (51)$$

and

$$N_2 = \frac{C_2V}{M_2} \simeq \frac{C_2N_1V_1^o}{M_2} \quad (52)$$

where C_2 is the concentration of component 2, M_2 its molecular weight, and V is the volume of the solution ($\simeq N_1V_1^o$). V_1^o is the molar volume of component 1. Therefore

$$\phi_2 = \frac{r_2}{r_1}\frac{C_2V_1^o}{M_2} = \frac{V_2^o}{V_1^o}\frac{C_2V_1^o}{M_2} = \frac{V_2^oC_2}{M_2} = C_2/\rho_2 \quad (53)$$

where ρ_2 is the density (g/cm^3) of component 2.

Substituting this into equation (31),

$$\pi/RT = C_2(\frac{1}{M_2} + (1/2 - r_1\chi)C_2/\rho_2V_1^o + \ldots) \quad (54)$$

The virial expansion of van't Hoff's Law in terms of the concentration is

$$\pi/RT = C_2\left(\frac{1}{M_2} + A_2C_2 + \ldots\right) \tag{55}$$

By comparison,

$$A_2 = (1/2 - r_1\chi)/\rho_2{}^2V_1{}^o \tag{56}$$

This type of analysis has been used countless times in the past to assess the type and magnitude of interactions occurring in solutions of a polymer molecule in a low molecular weight solvent. For this type of a system is it readily seen that the value of the second virial coefficient is the dominant term in the expansion. For example, a typical polymer molecular weight is 10^5 with the concentrations being of the order of 10^{-2}, $\rho_2 \simeq 1$. Therefore, slight change in χ will have a dramatic effect upon the slope of the KC/R(1) vs. C line. Consequently, meaningful values of χ can be determined with a fair amount of accuracy.

From this equation it is seen that A_2 can be positive, negative or zero when $r_1\chi$ is less than, greater than, or equal to 0.5, respectively. Thermodynamic significance of these values is found when the stability limits of a mixture are considered. In order for a mixture to be stable

$$\left(\frac{\partial\Delta\mu_1}{\partial\phi_1}\right) > 0 \tag{57}$$

Upon performing the appropriate differentiation we get

$$\chi_1 = r_1\chi < 1/2\left\{\frac{1}{\phi_1} + \frac{r_1}{r_2\phi_2}\right\} \tag{58}$$

Now

$$\frac{r_1}{r_2\phi_2} \simeq \frac{1}{(10^5)(10^{-2})} \simeq 0 \tag{59}$$

$$1/\phi_1 \simeq 1 \tag{60}$$

Consequently, $\chi_1 < 1/2$. This result is certainly not new but it basically states that when $\chi_1 < 1/2$ the mixture is stable, i.e., one phase. Flory has defined the θ-point as the critical miscibility point or mathematically the θ-point is defined by $\partial\Delta\mu_1/\partial\phi_1 = 0$. In terms of a phase diagram this defines the spinodal line. For the polymer low molecular weight solvent case in dilute solution is given by $r_1\chi = 1/2$ or when $A_2 = 0$. At the θ-point the polymer molecules are in the unperturbed state where repulsive and attractive forces are completely balanced. Finally, the onset of phase separation or precipitation occurs when $\partial\Delta\mu_1/\partial\phi_1 < 0$, i.e., $\chi < 1/2$ or $A_2 < 0$.

Turning our attention to a polymer-polymer mixture the exact same criteria define the stability limits as in the polymer-low molecular weight solvent case. Before we analyze the value of χ_1, i.e., $r_1\chi$, the accuracy in the determination of A_2 should be examined. Let's consider a system of two polymers both of molecular weight 10^5 with the solute in a concentration of 10^{-2}. At first glance it appears as if nothing has changed and this case is a reiteration of the previous case. However, we still have V_1^o, the molar volume of the solvent to consider and

$$V_1^o = M_1/\rho_1 \tag{61}$$

Substituting this into the expression for Kc/R(0)

$$Kc/R(0) = \frac{1}{M_2} + (1/2 - \chi_1)C_2\rho_1/M_1\rho_2^2 \qquad (62)$$

Using the numbers stated above $1/M_2 \simeq 10^{-5}$ whereas the second term is $(1/2 - \chi_1)10^{-7}$. Quite clearly we see that χ_1 would have to be on the order of $\pm 10^2$ before it really begins to affect the slope of this line to any detectable extent. A value of $\chi_1 = \pm 10^2$ is quite ludicrous and is basically indicating that the dilute solution coherent scattering technique applied to polymer-polymer mixtures will not yield information concerning χ_1 and second virial coefficients of zero will always be obtained provided one is not observing clustering or other such phenomena.

For argument's sake we can still look at the stability criteria for a polymer-polymer mixture. After differentiating $\Delta\mu_1$ with respect to ϕ_1 for a stable solution we get

$$\chi_1 = r_1\chi < 1/2\left(\frac{1}{\phi_1} + \frac{r_1}{r_2\phi_2}\right) \qquad (63)$$

Now $r_1/r_2 \simeq 1$ and

$$\chi < \frac{1}{2\phi_1\phi_2} \qquad (64)$$

For immiscibility or phase separation

$$\chi > \frac{1}{2\phi_1\phi_2} \qquad (65)$$

and for the θ-point (if $\phi_1 = \phi_2$):

$$\chi = 2 \qquad (66)$$

Considering just the θ-point and substituting this back into the expression for Kc/R(0) we get

$$\frac{Kc}{R(0)} = \frac{1}{M_2} + (\frac{1}{2} - 2)C_2/\rho_2{}^2V_1{}^o \qquad (67)$$

Clearly, even if a value of χ could be obtained the interpretation of this would be most difficult even for a θ solvent. One would not expect a simple linear dependence of Kc/R(0) on C_2. Consequently, interpretation of A_2 in terms of molecular interactions must be done with strong reservations.

3. Concentrated Amorphous Blends

Having treated the scattering from dilute solutions of one polymer in a matrix of another polymer it was emphasized that intermolecular interference effects were not considered. Consequently, this approach is not applicable to concentrated systems where chain overlap is extensive. An alternate approach to characterizing the heterogeneities or fluctuations in the system is to use correlation function theory proposed by Debye and Bueche (125).

In general the scattering from an isotropic amorphous polymer blend is given by

$$R(h) = K\eta^{-2} \int_o^\infty \gamma(r) \frac{\sin(hr)}{hr} r^2 dr \qquad (68)$$

where R(h) is the Rayleigh factor as defined previously, h is the magnitude of the scattering vector and K is a constant depending on the type of radiation used.

The correlation function, $\gamma(r)$, describes the size and shape of the heterogeneities and is given by

$$\gamma(r) = \langle \Delta\eta_i \Delta\eta_j \rangle_r / \overline{\Delta\eta^2} \tag{69a}$$

where η_i is the difference between the i^{th} scattering volume element and the average scattering power of the system. The symbol $\langle\rangle_r$ denotes the average overall volume elements separated by a distance r. $\overline{\Delta\eta^2}$ is the mean square fluctuation of the contrast in the system. For light scattering η signifies the refractive index, for x-rays η is the electron density and for neutrons η is the scattering length. $\overline{\Delta\eta^2}$ is defined for a two phase system with infinitely sharp phase boundaries as

$$\overline{\Delta\eta^2} = \phi_1\phi_2(\eta_1 - \eta_2)^2 \tag{69b}$$

where ϕ_1 and ϕ_2 are the volume fractions of the two phases with corresponding scattering powers of η_1 and η_2 respectively.

In qualitative terms the value of the correlation function at a particular r value simply defines the probability that if one considers all pairs of points separated by a distance, r, what is the probability that η_i and η_j will be equal. Therefore, if $r = 0$, then $\eta_i = \eta_j$ and $\gamma(r) = 1$. If $r = \infty$ then there is no correlation between η_i and η_j and $\gamma(r) = 0$. Various correlation functions can be used to describe different systems. For example, in the dilute scattering case the correlation function for an isolated sphere (112) could have been chosen where

$$\gamma(r) = 1 - \frac{3}{4}(r/R) + \frac{1}{16}(r/R)^3 \tag{70}$$

where R is the radius of a sphere. Upon substitution into equation (68) and integration we would have arrived at the same relation as before.

In concentrated systems Debye, Anderson and Brumberger (126) have shown that for a random two phase system

$$\gamma(r) = \exp(-r/a) \tag{71}$$

where a is the correlation distance defining the size of the heterogeneity and upon substitution into equation (68)

$$R(h) = K\bar{\eta}^2 \int_0^\infty e^{-r/a} \frac{\sin(hr)}{hr} r^2 dr \tag{72}$$

$$= K\bar{\eta}^2 a^3/(1 + h^2a^2)^2 \tag{73}$$

Quite clearly the correlation distance in such systems can be obtained from plats of $R(h)^{-1/2}$ vs. h^2 and the correlation distance is given by

$$a = \left(\frac{\text{Slope}}{\text{Intercept}}\right)^{1/2} \tag{74}$$

For concentrated systems it is rather difficult to interpret the correlation distance directly. Kratky (127) has shown that the correlation distance is related to the average chord length by

$$\bar{\ell}_1 = a/\phi_2 \qquad \bar{\ell}_2 = a/\phi_1 \tag{75}$$

where $\bar{\ell}_1$ or $\bar{\ell}_2$ is the average length of chords drawn through phase 1 or 2 respectively.

The correlation distance can also be related to the specific internal surface, O/V, which is the area of the phase interface divided

by the volume of the system. The relationship is (126)

$$\frac{O}{V} = \frac{4\phi_1\phi_2}{a} \tag{76}$$

Using the specific internal surface Porod (128,129) defined the average chord length of a phase as

$$\bar{\ell}_1 = \frac{4\phi_1}{O/V} \quad \text{and} \quad \bar{\ell}_2 = \frac{4\phi_2}{O/V} \tag{77}$$

Combining these last two equations it is easily seen that

$$\frac{1}{a} = \frac{1}{\bar{\ell}_1} + \frac{1}{\bar{\ell}_2} \tag{78}$$

and

$$\bar{\ell}_1 = \frac{a}{\phi_2} \quad \text{and} \quad \bar{\ell}_2 = \frac{a}{\phi_1} \tag{79}$$

as indicated previously.

4. Concentrated Semicrystalline Blends

Polymer blends can also exist in the semicrystalline state where either one or both of the components can crystallize. Systems where components can crystallize can get quite complex in that there are at least two if not more phases present. In addition to the crystalline phase there is an amorphous phase that can contain any number of separate phases depending upon the mixing characteristics of the amorphous blends. For this work, however, we shall be concerned only with a system that contains two phases. These phases are a crystalline phase

possessing a distribution of lamellar thicknesses and an amorphous phase composed of a homogeneous mixture of two amorphous polymers. In other words, this blend system behaves as a normal semicrystalline polymer and the scattering arising from this system can be treated as one would treat the scattering from a polyethylene specimen, for example.

Currently, there are at least four different theoretical models to account for the scattering from semicrystalline polymers. These include the Tsvankin-Buchanan model (130), the Vonk correlation function (131), the Hosemann paracrystalline lattice (132), and the interface distribution function approach of Ruland (133). Each of the models will be discussed below, however, the original works or several recent reviews (134,135,136,137) dealing with the models should be consulted if the reader desires a more in-depth treatment.

A. Tsvankin-Buchanan. The Tsvankin-Buchanan model consists of a disordered one dimensional infinite lattice where the projection of the electron density onto a line perpendicular to the lamellar surface is considered (138,139). The thickness distribution of the amorphous phase was taken to be Gaussian whereas the crystal thickness distribution was rectangular. The model includes a linear transition zone thickness where the electron density increases from the amorphous electron density, ρ_a, to the crystal electron density, ρ_c. This basically results in a trapezoidal electron density profile along the lattice. This model is quite appealing in the sense that for any symmetric width distribution parameter and transition zone length both the width of the scattering peak (a measure of the disorder) and the position of the

scatterint maximum (a measure of the distribution asymmetry) are uniquely related to the crystallinity of the sample. This permitted the construction of a set of calibration curves where one could measure the peak position and the full width at half maximum of the scattering maximum and, automatically, the degree of crystallinity and lattice statistics were specified. The simplicity of this model and its ease of use are far outweighed by the fact that the model does not describe the true scattering profile for some quite common polymers. Some unpublished results of this worker (140) and later Warner et al. (135) have shown that this model yielded relatively poor fits to the experimentally determined scattering profile and quite often yielded results that contradicted results obtained by other methods. Consequently this analysis was not used.

B. Vonk correlation function. This model is essentially an extension of the analysis used by Debye et al. (126) on a system containing a random arrangement of voids in a matrix. In the Vonk model (131) a line is drawn through a stack of lamellae perpendicular to the lamellae surfaces. Two points a distance r apart on this line are considered and the deviations of the electron density from the mean are determined. The product of these deviations are averaged over all positions on this line. By dividing this by the average at r = 0, i.e., $\Delta\eta^2$, the correlation function is obtained. Therefore, the normalized one dimensional correlation function is given by

$$\gamma(r) = \frac{\gamma^1(r)}{\gamma^1(0)} = \frac{\int_0^\infty \Delta\eta(x + r)\Delta\eta(x)dx}{\int_0^\infty (\Delta\eta(x))^2 dx} \tag{80}$$

According to Guinier (112), the intensity of scattering in one dimension, i(s), can be written in terms of $\gamma^1(r)$ by

$$i(s) = 2V \int_0^\infty \gamma^1(r) \cos 2\pi rsdr \tag{81}$$

Fourier transformation of i(s) yields

$$\gamma^1(r) = \frac{1}{2V} \int_0^\infty i(s) \cos 2\pi rsds \tag{82}$$

and

$$\gamma^1(0) = \frac{1}{2V} \int_0^\infty i(s)ds \tag{83}$$

Since the scattering obtained experimentally, I(s)/V, is characteristic of a three-dimensional system i(s) must be corrected. Several authors (141,142,137) have shown that this reduces to multiplying I(s) by s^2. Consequently

$$\gamma(r) = \frac{\int_0^\infty s^2 I(s) \cos 2\pi rsds}{\int_0^\infty s^2 I(s)ds} \tag{84}$$

The correlation function calculated from the experimental scattering

profiles display a series of maxima and minima where the position of the first maximum corresponds approximately to the long period.

Considering a two phase system of alternating layers of high electron density, ρ_c, e.g., crystalline, and low electron density, ρ_a, e.g., amorphous, Vonk and Korleve (131), extended the work by Debye, Anderson and Brumberger (126). The thicknesses of the crystalline and amorphous layers, r_c and r_a respectively, are distributed around their mean values of C and A according to the distributions $p_c(r_c)$ and $p_a(r_a)$. Both are normalized to unity when integrated over all possible values of r. The volume fraction of crystallinity is related to C and A by $\phi_C = C/(C + A)$.

If rods of length, r, are randomly placed in a system the probability that the ends of the rod are in two crystalline or high electron density regions is given by p_{CC}. The probabilities p_{CA}, p_{AC} and p_{AA} can be defined in similar fashions. These various probabilities are related by

$$p_{CC} + p_{CA} = 1 \tag{85}$$

$$p_{AA} + p_{AC} = 1 \tag{86}$$

$$\phi_C p_{CA} = (1 - \phi_C) p_{AC} \tag{87}$$

It has been shown that (112,126)

$$\int_0^\infty \Delta\eta(x)^2 dx = \gamma^1(0) = \phi_C(1 - \phi_C)(\rho_C - \rho_A)^2 \tag{88}$$

and

$$\int_0^\infty \Delta\eta(x)\Delta\eta(x+r)dx = (1-\phi_C)p_{AA}(\rho_A - \bar{\rho})^2 + \phi_C p_{CC}(\rho_C - \bar{\rho})^2$$

$$+ (1-\phi_C)p_{AC}(\rho_A - \bar{\rho})(\rho_C - \bar{\rho})$$

$$+ \phi_C p_{CA}(\rho_A - \bar{\rho}) \times (\rho_C - \bar{\rho}) \qquad (89)$$

where $\bar{\rho}$ is the average electron density. It follows that

$$\gamma(r) = \frac{\gamma^1(r)}{\gamma^1(0)} = (p_{CC} - \phi_C)/(1-\phi_C) \qquad (90)$$

The probability p_{CC} can be rewritten in terms of the probability that the ends of the rod are in the same crystalline phase. p_C, or in different crystalline regions separated by a specified number of amorphous layers, p_{CAC}, p_{CACAC}, etc. Therefore

$$p_{CC} = p_C + p_{CAC} + p_{CACAC} + \ldots$$

p_C can only be considered if $r \leq r_C$ where r_C is the crystal thickness and is given by

$$p_C = \frac{1}{\phi_C(C+A)} \int_r^\infty (r_C - r)p_C(r_C)dr_C \qquad (91)$$

Calculation of p_{CAC} involves the thickness distribution of a crystal-amorphous-crystal stack and is obtained by convoluting the distributions of the individual phases. Vonk has shown that

$$p_{CAC}(r) = \phi_C(C+A)Q(r_1)p(r_a)Q(r_2) \qquad (92)$$

and

$$Q(r_1) = Q(r_2) = \frac{1}{\phi_C(C + A)} \int_{r_1}^{\infty} p_C(r_C)dr_C \qquad (93)$$

where the subscripts refer to layer number in the stack. Substituting these into equation (88) results in

$$\gamma(r) = \frac{\phi_C}{1 - \phi_C} \left[\frac{1}{\phi_C^2} \int_o^{\infty} (r_C - r)p_C(r_C)dr_C + p_{CAC} + \ldots -1 \right] \qquad (94)$$

The distributions used to define p_C and p_a can be assigned any desired shape and width (143). Care must be exercised however to avoid a high probability of very thin lamellae. Renormalization of the distributions must be taken into account, as well, since there will always be a finite amount of the distribution that is negative.

Consequently, the calculation of the theoretical correlation function contains ϕ_C, and the characteristics of the amorphous and crystalline distribution functions as adjustable parameters.

This approach has proved to be quite useful in describing the morphology of several systems (131,143,144). However, caution must be exercised with broad distribution parameters where a high probability of small crystals is present. This is unrealistic and points at an inherent drawback. In addition to this, at low values of r the correlation function approach is sensitive to the tail end of the scattering curve where experimental error is inherently high. This can have serious effects on the value of ϕ_c since ϕ_c is related to the first intercept on the r axis (149). Finally, as discussed by Warner (135),

the assumption of an infinite lattice may be questionable.

C. Hosemann paracrystalline lattice. This approach and subsequent modifications by Brämer (145,146) and Wenig (147,148) generalizes the Tsvankin-Buchanan model. The problem of an infinite lattice is circumvented by considering a finite lattice where the crystalline and amorphous layers are arranged according to paracrystalline statistics. Also, included in this model is a finite transition zone between the crystalline and amorphous phases. The experimentally determined scattering profile is fit with a theoretical function given by:

$$I(s) = \frac{K}{s^2} R_e \left[\frac{N(1 - F_a)(1 - F_c)}{(1 - F_d)} + F_c \left[\frac{1 - F_a}{1 - F_d} \right]^2 (1 - F_D^N) \right] \cdot Z_1(s) \tag{95}$$

where K is a normalization factor, F_a and F_c are the amorhpous and crystalline structure factors defined by the distribution

$$F_i = \int_o^\infty H_i(x) \exp(-2\ isx) dx \tag{96}$$

and $F_D = F_a - F_c$.

$H_i(x)$ are distribution functions for the amorphous and crystalline phases and typically these are taken to be of Guassian shape where

$$H_i(x) = \frac{1}{(2\pi i(\Delta x_i)^2)} \exp\left[\frac{-(x - x_i)^2}{2(\Delta x_i)^2} \right] \tag{97}$$

The term $Z_1(s)$ in the intensity function incorporates the effect

of the finite transition zone thickness, E, by

$$Z_1(s) = \frac{1}{(2\pi is)^2 E} \left| 1 - \exp(-2\pi isE) \right|^2 \qquad (98)$$

In I(s), the parameter N essentially defines the number of parallel lamellae averaged over all the assemblies of the lamellae in the entire system. It is not uncommon for very low values of N to be used. In several studies values of N less than or equal to 2.0 have been reported (134,135,148). It is rather difficult to envision a stack of lamellae containing less than two lamellae which has led to several different interpretations. Baczek (134) has suggested that N represents the equivalent number of perfectly parallel lamellae whereas Wenig et al. (148) consider N as a measure of the degree of angular disorder in a lamellar stack.

In addition to providing a value for N, the explicit parameters required to fit a scattering curve are the crystal, amorphous and transition zone thicknesses and the widths of the crystal and amorphous distributions. This particular model has been used with a high degree of success in polymer systems but the interpretation of the N parameter is still unresolved.

D. Ruland interface distribution approach. A very recent approach to analyzing the scattering from polymers was discussed by Ruland (133). In this analysis a correlation function analysis is applied to the first derivative of the electron density function. This magnifies the interfacial zone thickness which Ruland feels is more suitable for obtaining

spacings and crystal and amorphous distributions. However, as with the Vonk correlation function approach the Fourier transform of the scattering profile is analyzed and not the original curve. Consequently, errors can be propagated in the Fourier inversion calculation.

In view of the above discussions the methods of Vonk and Hosemann were used in the study. The method of Ruland was not employed simply due to the date when the model was developed. It would be interesting however to perform this analysis and compare it to the other techniques.

5. Total Integrated Scattering and Porod's Law

Aside from the angular dependence of scattering additional information can be obtained from the total amount of energy scattered. Without making any a priori assumptions concerning the morphology of the system one can write as shown by Debye et al. (125,126)

$$I(h) = 4\pi \overline{\eta^2} V \int_0^\infty \gamma(r) r^2 \frac{\sin(hr)}{hr} dr \qquad (99)$$

Fourier inversion of this equation yields

$$r\gamma(r) = \frac{2}{\pi} \int_0^\infty \frac{hI(h)}{4\pi\overline{\eta^2}V} \sin hr \, dh \qquad (100)$$

$$\gamma(r) = \frac{1}{2\pi^2\overline{\eta^2}V} \int_0^\infty h^2 I(h) \frac{\sin hr}{hr} dh \qquad (101)$$

Evaluation at r = 0 results in

$$\int_0^\infty h^2 I(h)dh = 2\pi^2 \overline{\eta^2} V \qquad (102)$$

This demonstrates that the total integrated scattering is related to the mean square fluctuation in the electron density. For a two phase system with infinitely sharp phase boundaries, $\overline{\eta^2}$ can be rewritten as (126)

$$\overline{\eta^2} = \phi_1\phi_2(\rho_1 - \rho_2)^2 \qquad (103)$$

where ϕ_i is the volume fraction of phase i with electron density, ρ_i. $\overline{\eta^2}$ is only obtained however when one determines the absolute level of scattering. Similarly, for a three phase system with infinitely sharp phase boundaries, we get

$$\overline{\eta^2} = \phi_1\phi_2(\rho_1 - \rho_2)^2 + \phi_1\phi_3(\rho_1 - \rho_3)^2 + \phi_2\phi_3(\rho_2 - \rho_3)^2 \qquad (104)$$

Experimentally, the determination of the invariant involves integration of the entire scattering profile from 0 to ∞. Physically intensity curves can be measured only up to a finite value of 2θ of 5 to 7° (for a Kratky apparatus). This introduces the problem of performing the integration. Porod, however, has thoroughly investigated a wide variety of systems ranging from dilute suspensions of spheres, rods, etc., to concentrated systems (128,129). It was found that for any shape of a scattering entity provided the electron density profile was rectangular, i.e., no transition zones, the limiting intensity was given by

$$\lim_{h\to\infty} s^4 I(s) = K \qquad \text{(Porod's Law)}$$

where the constant K is related to the specific inner surface of the scattering system, O/V, by

$$O/V = \frac{2\pi^2 \phi_2 K}{Q} \tag{105}$$

Consequently, this affords a means of determining Q from the experimental data. The total integral can be broken into

$$Q = \int_o^\infty I(s)s^2 dh = \int_o^{s_{pp}} I(s)s^2 ds + \int_{s_{pp}}^\infty I(s)s^2 ds \tag{106a}$$

The first integral extends from s = 0 to the value of s where Porod's Law is obeyed and this is evaluated numerically. Since the intensity in the second integral obeys Porod's Law it is proportional to s^{-4} and

$$\int_{s_{pp}}^\infty \frac{K}{s^4} s^2 ds = \frac{-K}{s} \Bigg|_{s_{pp}}^\infty = K/s_{pp} \tag{106b}$$

In this manner Q is experimentally evaluated. However, rarely do systems possess a rectangular electron density profile. Typically within each phase there are thermal density fluctuations of the electron density as well as a transition zone where there is a gradual change of the electron density from one phase to the next.

The effect of a finite transition zone has been treated by Hosemann (132), Vonk (149), Ruland (150), Hashmioto (151,152), and

Koberstein (153). It has been shown that the effect of a finite transition zone can be represented by a convolution of ideal (rectangular) electron density distribution with a function describing the profile of the interface. Considering the electron density along a line in the x-direction we get

$$\Delta\rho_{real}(x) = \Delta\rho(x)_{ideal} * h(x) \tag{107}$$

where * indicates the convolution product given by

$$\Delta\rho(x)_{ideal} * h(x) = \int_{-\infty}^{\infty} \Delta\rho(y)h(x - y)dy \tag{108}$$

After incorporation of this function into the scattering equations the intensity is modified by

$$I(s)_{obs} = I(s)_{ideal} H^2 \tag{109}$$

where H is the Fourier transform of the interface profile function, h. The function, h, has been evaluated for various interface profiles. Vonk (149) has shown that for a linear transition zone

$$h(x) = \begin{cases} 1/t & 0 \leq x \leq t \\ 0 & t < x \end{cases} \tag{110}$$

$$H(s) = \left(\frac{\sin Es}{Es}\right)^2 \simeq 1 - 2\pi^2E^2s^2 \tag{111}$$

Substituting this into equation (109)

$$I(s)_{obs} = I(s)_{ideal}\left(1 - \frac{2\pi^2E^2s^2}{3}\right) \quad (112)$$

$$= \frac{K}{s^4}\left(1 - \frac{2\pi^2E^2s^2}{3}\right) \quad (113)$$

Therefore, a plot of $I(s)s^4$ vs. s^2 can be used to obtain the interface thickness, E.

Hashimoto (151,152) has solved the case of a Gaussian transition zone where

$$h(x) = 2\pi\sigma^2 \exp(-x^2/2\sigma^2) \quad (114)$$

$$H(s) = \exp(-4\pi^2\sigma^2s^2) \quad (115)$$

$$\simeq 1 - 4\pi^2\sigma^2s^2 \quad (116)$$

Therefore,

$$I(s) = \frac{K}{s^4}(1 - 4\pi^2\sigma^2s^2) \quad (117)$$

Similarly, plots of $I(s)s^4$ vs. s^2 yield a slope to intercept value of $4\pi^2\sigma^2$ and $E = \sqrt{3/2}\,\sigma$.

In these fashions one can incorporate the effect of a finite transition zone of an arbitrary shape on the observed scattering intensity. Recently, however, Koberstein et al. (153) have critically examined these methods and have concluded that the values of E determined can be quite different from the real values of E in the system. Basically the problem arises in the approximations made in the expansion. Terms beyond s^2 have traditionally been neglected without proper justi-

fication and can be shown to be quite significant. In addition to this, Koberstein et al. (153) have shown that the final value of E determined will depend upon the range of s where extrapolations are made. The reader is referred to this work (153) for a more in-depth discussion of this topic.

As shown, a finite transition zone leads to a negative deviation from Porod's Law. The second distortion of the electron density profile is the thermal density fluctuations occurring within a phase and this leads to a positive deviation. Provided the fluctuations occur randomly in three dimensions the scattering arising from these fluctuations is nearly angularly independent and can be approximated by a constant, C. This modifies the intensity equation by

$$I(s) = \frac{K}{s^4} + C \tag{118}$$

So a plot of $I(s)s^4$ vs. s^4 will yield the value of C from the slope at large values. This line should intersect the origin. Bonart (154) has considered cases where non-zero intercepts were obtained and treats these as a fraction of the phases that have an infinitely sharp phase boundary. However, this could easily be a result of curvature in the intensity profile.

In summary, the experimentally determined scattering profile can be represented by

$$I(s) = \left(\frac{K}{s^4}\right)\left(1 - \frac{2\pi^2 E^2 s^2}{3}\right) + C \tag{119}$$

where the linear transition zone approximation has been used as an example. Before analysis with any of the models and before the invariant is obtained, the effects of E and C must be taken into account.

6. Smearing Effects

The theoretical expressions up to this point are correct for radiation scattered from a sample where the incident source is a point. Realistically, however, such experiments are only feasible when both the incident beam intensity is very intense and all (2θ) and azimuthal angles can be collected simultaneously as for example with a film technique or an area detector (155). Consequently, most experiments are performed with a line source to increase the power and, in some cases (156,157,158) increase the resolution. The scattered radiation is smeared as a result of this and collimation corrections must be applied before the data is analyzed. An alternate approach, though less commonly used, is to smear the theory and treat the experimentally obtained data.

Numerous treatments of this problem have been discussed in the literature. Guinier (159,160) has shown that for an incident beam of arbitrary height but of negligible width the smeared intensity, J(h), is given by

$$J(h) = \int_0^\infty W(x) I(\sqrt{h^2 + x^2})\, dx \qquad (120)$$

where x is the variable of integration and W(x) is the weighting function describing the shape and length of the incident beam. This is

normalized so that

$$\int_0^\infty W(x)dx = 1 \qquad (121)$$

The simplest case of J(h) is when W(x) is constant. This occurs when the beam is effectively of infinite length. In order to illustrate this consider a system where the receiving slit length is ℓ_C and the length of the beam at the receiving slit is ℓ_B. If the entire scattering profile occurs within an angular range corresponding to $\ell_B - \ell_C$ then a beam of infinite length would yield the same result. Consequently, the term infinite height is used. When this assumption is applicable several theoretical analyses previously discussed can be easily smeared. For example, consider Porod's Law where $I(h) \propto 1/h^4$. Substituting this into the smearing integral we get

$$J(h) = K \int_0^\infty \frac{1}{(h^2 + x^2)^2}\, dx = \frac{\pi K}{2h^3} \qquad (122)$$

Therefore, the smeared intensity for a system with infinitely sharp phase boundaries is proportional to h^{-3}. In a similar manner Guinier's Law where $I(h) = Ae^{-h^2R^2/3}$ can be treated

$$J(h) = A \int_0^\infty e^{-(h^2 + x^2)R^2/3}\, dx = Be^{-h^2R^2/3} \qquad (123)$$

where B is a constant different from A. Consequently, smearing with an infinitely long beam has no effect on the angular dependence of Guinier's Law. Finally, the invariant, $Q = \int_0^\infty I(h)h^2dh$, can be examined.

$$\int_0^\infty hJ(h)dh = \int_0^\infty \int_{-\infty}^\infty hI(\sqrt{h^2 + y^2})dhdy \qquad (124)$$

Letting $y = z \sin\alpha$ and $h = z \cos\alpha$, making the appropriate substitutions and solving we get

$$\int_0^\infty hJ(h)dh = 2\int_0^\infty h^2 I(h)dh \qquad (125)$$

These relationships between the smeared and desmeared intensities can be used only in the above framework of the infinite height assumption. In general this assumption cannot be applied. Shaffer and Hendricks (172) discussed this assumption and provided a series of equations that defined an upper and lower angular limit to this assumption. In almost all small angle x-ray scattering studies the collimation effects must be considered.

Procedures for treating a beam of finite length have been discussed where the weighting function in equation (120) is used and the experimentally determined scattering profile is analyzed numerically. The calculation of the weighting function has been treated by Hendricks (161), Buchanan and Hendricks (162), and Hendricks and Schmidt (163). Considering the collimation parameters of the camera and assuming a uniform beam intensity and detector sensitivity calculations are presented where the weighting function can be determined for most of the commonly used SAXS cameras. With the exact weighting function determined (either experimentally or theoretically) numerical procedures of Lake (164), Hossfeld and Schelten (165), Glätter (166,

167), or Deutsch and Luban (168) can be used to perform the desmearing operation. Schmidt and coworkers (169,170,171) have presented procedures where the weighting function can be approximated by a Gaussian.

In addition to the slit length smearing there is also an effect on the scattering profiles by the slit width. Kratky, Porod and Kahovec (70) have discussed this problem. For most cases this effect is negligible but can be incorporated into the smearing equations. Considering both of these effects, the measured scattered power, P(h), is related to the scattered intensity from the sample, I(h), in electron units per scatterer, by (172).

$$P(h) = \frac{A_w A_\ell}{L_o^2 L^2} I_o(\text{cosec}\,\xi)\, i_e N_v t e^{-\mu t} \int_{-\infty}^{\infty} W_w(v) F(h - v)\,dv \qquad (126)$$

with

$$F(h) = \int_{-\infty}^{\infty} W_\ell(v) I(\sqrt{h^2 + v^2})\,dv \qquad (127)$$

where

L = specimen to detector distance

L_o = specimen to focal spot distance

I_o = focal spot power per unit area per steradian

N_v = number of scatterers per unit volume

t = sample thickness

μ = linear absorption coefficient

i_e = Thompson scattering factor

ξ = take off angle from the focal spot

A_ℓ, A_W = normalization constants of $W_L(v)$, $W_W(v)$

$W_L(v)$, $W_w(v)$ = slit length and width weighting functions

I(h) can only be extracted from the measured scattering profile after P(h) has been treated properly according to the above equations.

In the work performed here the infinite height assumption was employed due to the narrow length of the receiving slit and relatively large homogeneous section of the beam. The procedures outlined by Schmidt et al. (169,170,171) were used with the proper modifications.

7. Absolute Intensity Measurement

In order to interpret the invariant in SAXS the intensity must be placed on an absolute scale. By definition (173,174) the absolute intensity is the ratio of the number of particles scattered into a unit solid angle per second per scattering entity to the intensity of the incident beam and has units of cm^2/scatterer. Experiments can be placed on an absolute level by either measurement of the incident beam intensity or by use of a secondary standard (175). The latter method has been used in this study with a Lupolen standard (176-180) kindly supplied by Professor O. Kratky. The scattering, I_s, of this sample (designated "17/4") at an angle of $2\theta = 0.59°$ is related to the power of the incident beam after attenuation by the sample, P_s, by

$$P_s = K I_s a A \qquad (128)$$

where K is the calibration constant (K = 68.7 for this sample), a is the sample to detector distance and A is the attenuation factor of the

sample. Consequently the absolute smeared invariant can be obtained and

$$Q(s) = \int_0^\infty sJ(s)ds = \frac{i_e \lambda N_A P_s t \overline{\eta^2}}{2\pi a} \qquad (129)$$

where all the terms have been previously defined.

Hendricks (174) has pointed out that the use of the Lupolen standard is valid only when the infinite beam height assumption is made. If this is not the case then the difference in the weighting functions must be considered. The correction is quite straightforward but is neglected in many studies without justification.

In addition to this, Pilz (180) found a significant temperature dependence of the Lupolen scattering. This correction is supplied with the standard sample and takes the form

$$I_s = I_{s,meas}/(1 + 0.0077\ \Delta T) \qquad (130)$$

where $I_{s,meas}$ is the measured intensity of the standard and $\Delta T = T - 21.0°C$ where T is the temperature of the measurement.

8. Infrared Spectroscopy

In an N-atomic molecule there are 3N normal vibrations including rotations and translations of the molecule as a whole. For a polymer molecule where N can be quite large the total number of normal vibrations can be enormous. However, the actual absorption spectrum for most polymers is relatively simple. This can be understood by considering first the repeat unit of the polymer molecule. A normal coordinate analysis can be performed predicting the characteristic

absorption frequencies of the groups in an isolated repeat unit. Now when the repeat unit is considered as a part of the polymer molecule the normal vibrations are affected by a coupling with neighboring repeat units. The effect of these interactions is normally small for characteristic group frequencies whereas vibrations that predominantly involve the main chain are appreciably affected. This problem of vibrational interactions has been thoroughly treated by several authors (183,184,185). Consequently, with a known polymer specimen it should be possible to identify the absorption frequencies of characteristic groups in the repeat unit.

In a polymer-polymer blend band assignments can lead to valuable information concerning the specific interactions occurring in the mixture. The interactions between two polymers sholud be local interactions promoting a segmental mixing of the two chains. These local interactions will affect the bond strength of the groups involved and consequently should cause an effect on the characteristic frequency of groups. Provided the interactions are strong enough they should be experimentally observable and, consequently, lead to possible causes for mixing. If there are no interactions occurring then the absorption frequency should not be affected and the spectrum of a blend should be calculable from the spectra of the pure components.

For a given characteristic frequency a molar extinction coefficient can be defined as (185)

$$\varepsilon_M = \frac{M}{Cb} \log I/I_o \qquad (131)$$

where M is the molecular weight of the absorbing group, C its concentration (g/liter), b is the pathlength (cm), and I is the transmitted energy after absorption of the primary energy I_o. This can be written in terms of the more familiar Beer-Lamber Law

$$A = \varepsilon b C \tag{132}$$

where ε is the extinction coefficient (ε_M/M) and A is the absorbance. (Note for a polymer molecule M is the monomer molecular weight and C is the monomer mole fraction.)

For a multicomponent system with interactions then equation (132) becomes

$$A = \Sigma A_i = \Sigma \varepsilon_i b C_i \tag{133}$$

where the subscripts refer to the individual species present. Therefore, the absorption from a two component system is given by

$$A_{blend} = A_1 + A_2 = b(\Sigma \varepsilon_i C_i) = b(\varepsilon_1 C_1 + \varepsilon_2 C_2) \tag{134}$$

Since C_i represents the monomer mole fraction of component i, then

$$\Sigma C_i = C_1 + C_2 = 1 \tag{135}$$

Therefore, equation (134) can be rewritten as

$$A_{blend} = b(\Sigma \varepsilon_i C_i) = b\left[(\varepsilon_2 - C_1)C_2 + \varepsilon_1\right] \tag{136}$$

and

$$\frac{dA_{blend}}{db} = (\varepsilon_2 - \varepsilon_1)C_2 + \varepsilon_1 \tag{137}$$

If there are no interactions occurring in the blend, then the change in the absorption as a function of pathlength is given by the extinction coefficients in the pure components. Alternately, (dA_{blend}/db) can be determined as a function of C_2. If there are no interactions occurring then this should yield a straight line. Deviations from a straight line will indicate local interactions in the blend.

A much more elegant approach to this technique is to use Fourier transform infrared spectrometers (186) where the entire spectrum of the pure compounds can be stored, summed in an appropriate manner, and subtracted from the blend spectrum. As shown by Coleman et al. (26,27) this advance in infrared spectroscopy has proven to be quite useful in the area of polymer blends.

CHAPTER III

EXPERIMENTAL

1. Purification of Materials

All materials used in this investigation were purified to remove any gross impurities and impurities soluble in the solvents used. As will be seen, in the polyvinylchloride/poly(ε-caprolactone) blend all of the experiments performed on the blend were drastically affected by the purification process. Therefore, it is felt that a detailed discussion of the purification procedures employed in this study, beginning with the solvent purification and glassware cleaning, is in order. These procedures must be followed if an experimenter wishes to work on these materials to ensure that the results obtained are not characteristic of an impurity or a gel content as in polyvinylchloride.

A. Cleaning of glassware. All the glassware used in this study was cleaned thoroughly prior to use. This was done simply to eliminate the possible presence of any unwanted polymer or foreign matter from previous usage. In most cases the procedure outlined below need not be followed. However, since very small blend concentrations were being used and since small effects were being examined it was felt that the elimination of the uncertainty, however small it may be, was justified. Glassware was placed in a warm chromic acid solution overnight and rinsed thoroughly with tap water. It was then scoured with alconox

and again rinsed thoroughly. It was finally rinsed twice with distilled water and allowed to drip dry inverted on a bench top.

This was found to be adequate for all glassware except that used in the preparation of the polyvinylchloride blends. In that case, the glassware was first allowed to soak in tetrahydrofuran saturated with sodium hydroxide. This dehydrohalogenated the PVC (187) and allowed subsequent cleaning with the chromic acid.

B. Solvent purification.

i. Tetrahydrofuran (THF). It has been shown (188) that in the absence of stabilizers THF decomposes and forms peroxides. In lieu of this THF is commercially available (189) but contains 0.025% (w/v) of hydroxytoluene as a stabilizer. This stabilizer must be removed when solution casting materials from THF. It is clearly evident that if a 2% (w/v) solution of a polymer or a polymer blend is prepared in 200 ml of non-purified THF and subsequently cast into a film, then the film contains ca. 2.5% (by weight) of hydroxytoluene. This is quite high and can affect the properties of the blend. In addition to the necessity of removing the stabilizer the THF must be used immediately or stored such that peroxides do not form. Films cast from purified THF containing small amounts of peroxides were found to be useless. Being non-volatile some of the peroxide exuded to the film surface forming an opaque crystalline layer. As a consequence of these various effects enumerated above the following procedure was followed (190).

Approximately one liter of commercially available THF was placed in a two liter ground glass distillation flask. Using a micro-

spatula, finely powdered lithium aluminum hydride ($LiAlH_4$) was added. The $LiAlH_4$ removes any peroxides present, stabilizes the THF during distillation and acts as a drying agent for the THF. Addition of the $LiAlH_4$ should be slow since with each addition the slurry foams. This is continued until there is no more frothing when the $LiAlH_4$ is added. The distillation flask is then placed on a distillation apparatus and the THF is distilled under a nitrogen blanket. A fore run of ca. 25 ml was collected and discarded. A main fraction of 800 ml was then collected for use in the blend preparation. Since the entire 800 ml would not be used immediately, the distillate was purged with dry nitrogen for fifteen minutes and stored under nitrogen in a brown glass bottle. Upon subsequent use of the THF the bottle was opened under a nitrogen flow and the THF was again purged with dry nitrogen before resealing. These procedures produced a pure THF that was dry and very suitable for casting purposes.

ii. Toluene. Although toluene does not require a stabilizer it still requires purification to remove gross impurities. Filtration through a fine sintered glass funnel was not found to be adequate. Therefore, all the toluene used was distilled using a simple distillation apparatus. The toluene was distilled in one liter quantities and stored in a glass bottle for future use.

iii. Methanol. During the precipitation procedures used rather massive quantities of methanol were required. This necessitated setting up a continuous distillation apparatus for the methanol. Upon each addition of a fresh volume of methanol a forerun of approximately 25 ml was collected. After the distillation of approximately eight liters of

the methanol the distillation pot was emptied and fresh boiling chips were added. Although this was not necessary it prevented the buildup of large concentrations of impurities in the pot.

iv. Benzene. The benzene used in the preparation of the neutron scattering specimens was spectral grade benzene and was used without further purification.

C. Polymer purification.

i. Poly(ε-caprolactone). Despite the fact that specification sheets of the poly(ε-caprolactone) used in this study stated that the material was pure PCL-700 (191) the material as received had a distinct yellowish color and was quite odorous. In a subsequent infrared study of the polyvinylchloride/poly(ε-caprolactone) blends Cooper and Hubbell (192) make mention of this discoloration but did not take measures to eliminate it. The discoloration strongly suggests the presence of low molecular weight impurities as well as the possibility of other extraneous matter. Therefore the material was purified with particular care being taken to remove the lower molecular weight material.

Approximately 20 grams of the PCL-700 was placed in 1 liter of purified THF. The mixture was allowed to reflux for five hours under a nitrogen blanket. After cooling, ten aliquots of this solution were separately filtered through a medium porosity sintered glass funnel and placed into a two liter beaker. With continuous stirring approximately 1.2 liters of distilled methanol were added to the PCL solution to precipitate the polymer. After completing the addition of the methanol the slurry was vigorously stirred for fifteen minutes and then allowed

to settle. Quite surprisingly there were two distinct layers of precipitates. The first fraction which was clustered and somewhat tacky floated on or near the surface whereas the second fraction appearing fluffy was suspended near the bottom of the beaker. Both fractions were white and were not discolored to any extent. The two were easily separated and were filtered through a Buchner funnel. They were then thoroughly washed with methanol and dried under vacuum at 50°C. The two fractions were analyzed using gel permeation chromatography (GPC). The two chromatograms were overlaid along with the chromatograms of the PCL-700 as received and a PCL-300, a lower molecular weight PCL. These are shown in Figure 4. The presence of both PCL-700 and PCL-300 is indicated. In further support of this the intrinsic viscosites of the two fractions were measured in THF at 30°C. These data are shown in Figure 5. This distinctly shows the two different molecular weight fractions present. According to Koleske these intrinsic viscosities yielded weight average molecular weights of 23,000 and 43,000 which correspond approximately to the values of PCL-300 and PCL-700, respectively. Therefore it is quite clear that the PCL-700 as received contained a fair quantity of the PCL-300, as well as some additional lower molecular weight PCL. The second fraction containing the predominant amount of the polymer was indeed a higher molecular weight fraction. From the relative amounts of the precipitates the ratio of PCL-300:PCL-700 in the as received material was approximately 1:9. This, however, does not explain the yellowish color nor the odor present in the material. The only possible explanation for these two effects is that there was some monomer present. It was found during a subsequent polymerization

of PCL that ε-caprolactone possessed a similar discoloration and odor before distillation. It is therefore felt that although previous workers (29,192,194) did not purify the PCL a purification was necessary in order to properly investigate the material as characterized by Union Carbide (191) as PCL-700.

ii. Polyvinylchloride (PVC). PVC is a rather complicated polymer. As was discussed previously whether or not the material is completely amorphous or if there is any microstructure present is still an open question. However, it is quite certain that there is a significant gel fraction in PVC (195,196,197) and recently Keller et al. (198) and others (199,200,201) have managed to crystallize the gel. On account of the various complications that the gel content can cause it was eliminated from the PVC used in this study by the following procedure.

Approximately 25 grams of the PVC (as received QYTQ-387) was placed in 1.5 liters of purified THF. It was very evident that there was a significant gel content in the PVC at this point because the material did not dissolve completely. The material first swelled and partially dissolved leaving behind nearly transparent particles that were visible only when held up to a light. As a consequence of this the contents were refluxed under nitrogen overnight and separated into several fractions. Each aliquot was filtered through a medium sintered glass funnel. It proved to be impossible to use a fine porosity funnel due to clogging of the pores with the gel. Even the medium pore funnel filtered with difficulty. The filtrate was added to approximately 1.5 liters of vigorously stirred, distilled methanol by dropwise addition

from a separatory funnel. The precipitate, allowed to settle overnight, was collected in a Buchner funnel, washed several times with methanol, and dried for three days at 40°C to remove residual solvents. Chromatograms of the as received and purified PVC are shown in Figure 6. Care must be taken not to expose the purified PVC to extreme temperatures >90°C for long periods of time (202,203) since the purification process removes the stabilizers used to commercially produce PVC. Also, in the non-stabilized state PVC is light sensitive (204) and can undergo photodegradation quite readily. Therefore, the dried polymer was stored under vacuum in a dessicator painted completely with flat black paint. The purified material was very fluffy and was not discolored.

iii. Polystyrene (a-PS). Atactic polystyrene (a-PS) was twice purified by dissolving the polystyrene (5% (w/v)) in distilled toluene and filtering through a medium porosity sintered glass funnel. The filtered solution was precipitated in vigorously stirred methanol by a dropwise addition from a separatory funnel. A ratio of 1:12 of toluene to methanol dictated the amount of methanol used in the precipitation. The precipitate was allowed to settle and was collected in a Buchner funnel. The contents in the funnel were washed thoroughly with methanol and dried in vacuum at 75-80°C for three to four days.

iv. Polyphenyleneoxide (PPO). As received PPO is partially crystalline. For the purposes of this work both the crystalline and foreign matter were removed by a double purification. The process used was identical to that used for the purification of a-PS. Even after the second purification of the PPO there was a definite yellow tint in the material. It is unknown at this time what the origin of this discolora-

tion was. However, previous workers (46,56) experienced this same problem. Upon meltpressing the PPO discolored even more. Therefore, minimal exposure to heat treatments was desired.

v. Poly(p-iodostyrene). Poly(p-iodostyrene) (PpIS) is not available commercially and had to be prepared from pure a-PS. The method of Braun (205) was used to perform the iodination. The iodination occurs strictly in the para position of the phenyl ring by the following reaction:

$$5RH + 2I_2 + HIO_3 \longrightarrow 5(RI) + 3H_2O$$

R in this equation represents the styrene monomer unit. A procedure for the reaction is given below.

1.9533 g of a-PS (Pressure Chemicals, M_w = 100,000, $M_w/M_n \leq 1.04$) was placed into 50 ml of reagent grade nitrobenzene in a round bottomed flask. In a separate flask 0.6767 g of recrystallized (206) iodic acid (HIO_3) and 1.9533 g of sublimed iodine (I_2) were dissolved in 25 ml of nitrobenzene. The two flasks were mixed at room temperature with the addition of 0.2 ml of sulfuric acid (H_2SO_4) and the contents were mechanically stirred. A condenser topped with a drying tube was placed on the flask containing the reaction mixture. The reaction mixture was heated to 90°C for 12 hours and the contents were then slowly poured into 1.5 liters of distilled methanol. The iodinated styrene immediately precipitated from the solution and the contents were collected.

The iodinated styrene appeared to be off-white even after repeated washing with methanol. It was assumed that this was the

"gelbich" color referred to by Braun (205). The polymer was then dissolved in purified toluene and precipitated into methanol. The material was collected in a Buchner funnel with repeated washings with methanol. The iodinated styrene was placed in a jar coated with aluminum foil and placed under vacuum at 60°C to dry.

Two samples of the PpIS were taken from the dried stock. One specimen was subjected to an iodine analysis yielding 48.1% iodine by weight. This translates into iodination of 87.5% of the phenyl rings during the reaction. The second specimen was dissolved in distilled toluene and a film was cast on a potassium bromide salt plate. An infrared spectrum was taken of the PpIS and compared to that of pure a-PS. This comparison is shown in Figures 7 and 8. Bands throughout the entire spectrum of the PpIS indicate that there is iodine substitution on the phenyl ring in the para position. This spectrum is in very good agreement with that shown by Braun.

vi. Poly(o-chlorostyrene). Poly(o-chlorostyrene) is another polymer that was not available commercially and was prepared by a radical polymerization of the monomer in solution.

25 grams of o-chlorostyrene were placed in a 100 ml round bottomed flask. The flask was attached to a vacuum distillation apparatus with the receiving flask cooled in an ice bath. The system was evacuated to 7 mm Hg from a floor pump connected to the system through a dry ice/acetone trap. A forerun of 1 ml was discarded and a main run of 15 ml was collected. Under this vacuum the o-chlorostyrene boiled at 50°C. The vacuum was broken using a stream of nitrogen and the flask containing the distillate was immediately capped with a bleached serum

stopper. 10 ml of the o-chlorostyrene were removed from the flask with a syringe and were placed in a 150 ml round bottom flask similarly capped and purged with nitrogen. 0.065 g of azobisisobutyronitrile (AIBN) dissolved in 8.5 ml of distilled toluene were then added to the flask via a syringe. The flask containing the monomer and AIBN initiator was placed in a water bath thermostadted at 60°C and continuously agitated. After 2 hours the flask was removed from the bath and the contents were diluted to 125 ml with the addition of toluene. The flask was then cooled to room temperature by passing cold tap water over the flask.

The entire 125 ml of solution was filtered through a medium sintered glass funnel and then poured into a clean separatory funnel. By a dropwise addition the poly(o-chlorostyrene) was precipitated in 1.5 liters of vigorously stirred methanol. After the addition of the full 125 ml, the stirring was continued for 0.5 hours. The precipitate was allowed to settle overnight before collection in a Buchner funnel. After separation the polymer was rinsed thoroughly with methanol and dried under vacuum at 75°C for four days.

vii. Poly(p-chlorostyrene). Purified poly(p-chlorostyrene) (PpClS) was kindly supplied by P. Alexandrovich. A full description of the preparation of this material can be found in his thesis (56).

viii. Deuterated polystyrene. A deuterated polystyrene (d-PS) (M_w = 114,000; M_w/M_n < 1.1) (207) was kindly supplied by Dr. Claude Picot. The material was used as received in the sample preparation.

2. Polymer Characterization

All the materials mentioned in the purification section were characterized with respect to molecular weights. Table 2 indicates the various polymers used along with the M_w, M_n, and M_z as supplied by the manufacturer or as determined experimentally. Wherever possible the method used to determine the various distribution moments are indicated. Also, the manufacturers' designations are included on the polymers that were supplied commercially.

3. Blend Preparation

Since a variety of experimental techniques was used to investigate the blends mentioned, there is no one set format for sample preparation. Each experiment requires the use of samples specifically designed for that experiment. In lieu of this the sample preparations will be treated under the individual experiments in order to facilitate comparison to the experimental results.

A. Infrared spectroscopy. Infrared spectroscopy studies were performed on blends of PVC and PCL throughout the entire composition range. One problem that is immediately evident is that above 50 weight percent of PCL the blends are crystalline. This hinders the investigation of possible interactions in three ways. First, the crystals could scatter the infrared (IR) radiation giving rise to a false absorbance reading. Second, the crystals in the blends are known to be pure PCL crystals (29,193,194) thereby removing PCL from the amorphous phase where the interactions are occurring. In addition to this the degree

TABLE 2

POLYMER CHARACTERIZATION

POLYMER	MANUFACTURER SPECIFICATION	ABBREVIATION	M_N	M_W	M_Z	M_W/M_N	$\frac{M_W/M_N}{2(M_W/M_N-1)}$
Polyvinylchloride	QYTQ-387	PVC[b]	38,000	78,000[c]	---	2.05	0.661
Poly(ε-caprolactone)	PCL-700	PCL	23,200	45,000[ac]	---	1.94	0.674
Polystyrene	HH101	PS[b]	90,000	260,000[c]	470,000	2.92	0.603
Polyphenyleneoxide	---	PPO	16,800	51,500	96,900	3.07	0.597
Poly(o-chlorostyrene)	---	PoClS[b]	107,000	220,000[c]	360,000	2.06	0.660
Poly(p-chlorostyrene)	---	PpClS[b]	63,500	130,000[c]	212,000	2.05	0.662
Poly(p-iodostyrene)	---	PpIS	374,000	397,000[a]	---	1.06	0.945
Deuterated Polystyrene	---	d-PS	~104,000	114,000[a]	---	1.1	1.00

[a]Light scattering.

[b]GPC.

[c]Viscosity.

of crystallinity can only be measured to an accuracy of ±5% by any technique. Consequently, an unnecessary error is introduced in determining the concentration of PCL in the amorphous phase. Finally, the spectrum of crystalline PCL is significantly different from the amorphous PCL (26,27,140) and only serves to complicate the spectrum of the blend. Therefore, it was necessary to work with films above the melting point of the PCL crystals.

Appropriate quantities of PVC and PCL were weighed into an Erlenmeyer flask and purified THF was added to make a 2% (w/v) solution. The solution was purged with nitrogen, sealed with a stopper and stirred for 24 hours to ensure good mixing. Using a Pasteur pipette the solution was carefully placed on a pre-weighed sodium chloride salt plate of known dimensions so that the entire surface was covered with the solution. THF was allowed to evaporate under a stream of nitrogen with further drying being performed under vacuum at 60°C for 2 hours and at 40°C for 4 hours. The films were then kept under vacuum for an additional 18 hours to completely evaporate the solvent. This procedure yielded a uniform film coating on the surface of the salt plate only 50% of the time with 50% of the films being either non-uniform or not entirely coating the surface. If the latter occurred the salt plate was cleaned and polished and the film was discarded.

Acceptable film and salt plate laminates were then weighed. The difference between the weights of the laminate and the salt plate yielded the weight of the polymer films. Since the density of the polymer blend was known from density gradient work, the thickness of the film was calculated by:

$$t_f = \frac{W_B}{\rho_B A_s} \tag{138}$$

where

t_f = film thickness

W_B = weight of the blend

ρ_B = density of the blend

A_s = area of salt plate face

It is estimated that the film thickness (on the order of microns) calculated by this method was accurate to within only 30%. In order to increase the thickness of the film the technique was repeated using various volumes of the casting solvent. It should be noted that the salt plates and the salt plate film laminates should be stored in a dessicator to prevent water absorption on the plates.

In order to perform an IR scan at the elevated temperatures an additional salt plate was placed directly on the film. This essentially made a sandwich of the film between the two salt plates. A hole was bored into this second salt plate for the placement of a thermocouple. The hole should be positioned such that it does not extend into the beam path and is as near to the film as possible. With an iron-constantin thermocouple the temperature of the sample was accurately recorded to within ±0.5°C.

The sandwich arrangement was placed into an asbestos heating cell designed to fit into the Perkin-Elmer model 283 IR spectrometer. Heating was accomplished with nichrome wire embedded in furnace cement within the heating cell. Coils of the wire were placed before and

after the sample chamber to ensure a uniform heating of the salt plates and, consequently, the sample. A diagram of the heating cell is shown in Figure 9. Throughout the course of the experiments the instrument was purged with dry nitrogen and a constant flow was maintained throughout the collection of a spectrum. Individual spectra were collected over a 60 minute period at a slit setting of 3. According to the instrument specifications this yields a resolution of ca. 1.0 cm^{-1} (E28). All spectra were collected with the above specifications in the absorbance mode. At least five spectra were collected for blends of identical composition but with a variation in the thickness.

B. Density. For the measurement of a sample density by the gradient column method (see, for example, 29, 194, 208), the samples used must be prepared with the desired thermal treatment and, more importantly, must be void free. This was easily accomplished by casting a 2% (w/v) solution of a preweighed mixture of PCL and PVC in purified THF onto flat bottomed Petri dishes (194). The dishes were then covered with perforated aluminum foil and appropriately sized beakers. This allows for a slow evaporation of the solvent (24-48 hours) since the atmosphere within the beaker is saturated with gaseous THF. The films deposited on the dishes are characteristically quite uniform in texture and thickness (if the dishes were previously leveled). The films (~40-80μ thick) were dried at 40°C under vacuum for 3 days followed by 2 days at room temperature. The films either lifted easily from the dishes or the perimeter of the film was sliced with a scalpel and covered with distilled methanol. Within 12 to 24 hrs the film floated

to the surface of the methanol. If the latter technique was used, an additional 3 days of drying under vacuum at 40°C was required to ensure removal of the methanol.

Strips of the film were placed between microscope coverslips shimmed such that contact with the film was just being made. This was sealed in a rubber container (i.e., a cleaned balloon), emersed in a water bath at 90°C for 30 minutes and then quickly transferred to a water bath thermostadted at 30 ± 0.1°C. The films were kept in the crystallization bath for different times depending on the crystallization rates established by Ong (29). The total amounts of time were set at twice the time for the establishment of the maximum degree of crystallinity. The reason for this is that the PCL is known to undergo a secondary crystallization (217) and this will vary depending on the temperature. Therefore, it was felt that the most consistent results would be obtained in this fashion.

The samples were then removed from the bath and examined to determine if the seals were broken during the crystallization. If so, they were discarded since PCL can absorb water quite readily (191) and this will ultimately affect the overall crystallization. The samples were then removed from between the coverslips and cut into ~0.5 x 0.5 mm^2 pieces for use in the density measurements. As will be seen, this procedure produced very reproducible results.

C. DSC. The requirements of the sample preparation for DSC experiments are not as stringent as they are for density work. Therefore, sections of the sample used in the density work were used in the DSC experiments

as well.

D. Light scattering. The procedure used in the preparation of samples for light scattering experiments was nearly identical to that used for the density work. The only differences were that the shims between the coverslip were removed and a slight pressure was applied on the surface of the coverslips with two small clamps. It was hoped that this would yield specimens with good adherency between the coverslips and the film. This was found only 20-25% of the time and, consequently, refractive index fluids had to be used when performing the scattering experiments.

E. SAXS--Concentrated semicrystalline blends. Films of the PCL/PVC were prepared as discussed in the density section. After all the solvent was removed and the films were dry they were cut with a scalpel into strips approximately 1 mm in width. The strips were then layered over a slot in a mold specifically designed for the Kratky SAXS apparatus. The stainless steel molds contained a slot with dimensions of 0.75 x 3.5 cm^2 and a depth being dictated by the desired sample thickness. The sides of the slot were cut at an angle to facilitate the removal of the specimen. The mold with the layers of the blend film was placed on a sheet of teflon coated aluminum foil, aluminum side facing the sample. This was placed on the lower platen of a Carver press heated to 90°C. The sample was melted and additional strips of the blend were placed over the slot to completely fill it and to provide a reasonable amount of flash when pressing. A second sheet of teflon foil, again aluminum side to the sample, was placed over the

mold containing the sample and the press platens were closed down. Five to six cycles of pressure ranging from 0 to 10,000 psi were applied on the sample over the course of 5 minutes. After the final cycle the pressure was kept at 10,000 psi for 5 minutes and the sample was removed and cooled to room temperature. When the material was cool the aluminum foil was removed to examine the specimen for voids. If the specimen was voidy, it was discarded and re-pressed. Otherwise, the sample and mold were placed between two sheets of teflon coated foil as before, placed between the platens and quickly pressed with a minimal amount of pressure. This was done only to get the aluminum foil adhering to the film.

The aluminum foil was crimped closed around its four sides and sealed completely with a rubber cement. A coverslip was placed over the slot and a pressure was exerted on the coverslip with two clamps. The sample was then melted at 90°C for 30 minutes and rapidly placed in a water bath thermostadted at 30 ± 0.1°C. Crystallization was performed for the same lengths of time as in the density section. After crystallizing the samples were removed from the mold and stored at room temperature in a dessicator.

F. SAXS--Concentrated amorphous blends. The PVC/PCL blends below 50 weight percent PCL do not crystallize. This simplifies matters greatly. In addition to this the mass absorption coefficient of the blend is increasing with the higher chlorine content. This dictates the use of thinner specimens. As mentioned previously films of uniform thickness were easily prepared by casting the blends from solution onto leveled,

flat-bottomed Petri dishes. Therefore, films dried as before were used in the scattering studies. If the films were too thin they were stacked to obtain the desired thickness of material. These stacks were easily mounted onto the specimen holder.

G. SAXS--Dilute mixtures.

i. PVC/PCL. These specimens were prepared in a fashion identical to that used in the preceding section on the concentrated amorphous blends.

ii. Other systems. Five other blend systems were prepared in very similar fashions. The only variable that changed to any degree was the pressing temperature and these are listed in Table 3. The five systems investigated were PoClS and PpClS dilute in both PS and PPO and a dilute mixture of PpIS in PS.

Preweighed quantities of the materials were dissolved in purified toluene to make a 2% (w/v) solution. The blends were then precipitated by dropwise addition of the solution into vigorously stirred purified methanol of a volume at least twelve times that of the toluene used. The precipitant was allowed to settle overnight and was collected in a Buchner funnel. The contents of the funnel were emptied into a glass jar, covered with perforated aluminum foil and placed under vacuum at 75°C for three days. According to Hayashi et al. (74) the PpIS/PS blends were dried at 50°C for a period of 5 days. The dried blends werethen pressed into 1 mm thick molds similar to those used for the concentrated semicrystalline PVC/PCL blends. The temperature and pressure used for pressing these blends is specified in Table 3. It

TABLE 3

SAMPLE PRESSING CONDITIONS

BLEND	DILUTE COMPONENT	DRYING TEMPERATURE (°C)	PRESSING CONDITIONS		
			TEMPERATURE (°C)	TIME (min)	PRESSURE (psi) x 10^{-3}
PoClS/PS	PoClS	75	180	5.0	10
PoClS/PPO	PoClS	75	260	2.5	20
PpClS/PS	PpClS	75	180	5.0	10
PpClS/PPO	PpClS	75	260	2.5	20
PpIS/PS	PpIS	75	140	5.0	15

should be noted that five to six cycles of pressure from zero psi to the pressure listed in Table 3 were conducted over the time period indicated to produce a relatively voidfree specimen. The samples were then quenched to room temperature and stored.

H. WAXD. The samples used in the SAXS experiments were used directly in the wide angle x-ray apparatus in both the photographic and scanning modes. No alterations were necessary.

I. Neutron scattering. The system investigated by neutron scattering was a dilute mixture of deuterated polystyrene (d-PS) in a hydrogenated PoClS. Preweighed quantities of d-PS and PoClS were dissolved in benzene to make a 1% solution. The solutions were rapidly frozen in liquid nitrogen and placed on a freeze-drying apparatus. The solutions were kept frozen by submersion of the flasks in an ice bath. The system was completely evacuated and the benzene was evaporated from the solution and trapped in a container submersed in a dry ice/acetone bath. After five hours all the benzene was removed from the solution leaving sheets of powdered blend in the flasks. The blends were removed, crushed to a fine powder and placed under vacuum at 75°C for three days. The dried powder was then pressed at 140°C under vacuum in an apparatus shown in Figure 10. The device was specifically designed for this experiment with the 1 mm thick molds containing a hole slightly larger than 1 cm in diameter. This produced a specimen large enough to be used at the Oak Ridge Research Reactor.

4. Equipment Employed

A. Density measurement. Densities of the PVC/PCL blends were determined by the density gradient column technique (208). Details of the construction of the columns will not be given here. Two separate columns were constructed to measure the densities of the 100-50% PCL blends and the 50-0% PCL blends. The first series of blends were measured in a column linear from 1.16-1.28 g/cc and the second in a column linear from 1.25-1.43 g/cc. Calibration of the columns were obtained with Scientific Glass Apparatus Company density floats calibrated at 23°C. The columns were maintained at 23 ± 0.05°C through the use of a Haake circulating bath Model N15 and a Neslab Batch Cooler PBC-2 refrigerating unit. The columns prepared from potassium iodide solutions were stable for only 6 hours even with the isothermal conditions. The heights of the beads' and samples' centers were determined with a cathetometer whose eyepiece was leveled before each reading. At least seven different samples were used for each blend composition to ensure an accurate average.

B. Differential scanning calorimetry (DSC). DSC measurements were performed on a Perkin-Elmer DSC II. The semicrystalline blends were examined from 25 to 100°C at scanning rates of 2 and 10°C per minute. Standard tin and indium samples were used to calculate the degrees of crystallinity from the areas of the endotherms. The weights of the samples, measured on a Perkin-Elmer AD-2 Autobalance, were varied so that the area under the melting profile was approximately equal. This essentially keeps the error in the measurement of the area constant.

The areas were measured by both planimetry and weighing techniques.

C. Wide angle x-ray diffraction. Wide angle x-ray diffraction experiments were conducted with nickel filtered copper radiation produced on a Philips x-ray tube and generator operated at 35 Kv and 20 milliamperes. Measurements were made using flat plate film and, also, a step scanning detector. The detection system consisted of a solid scintillation detector equipped with a sodium iodide crystal doped with tellurium. The detector was mounted on a goniometer with an automated $\theta/2\theta$ scanning motor. The diffracted radiation was first nickel filtered and then energy discriminated using previously determined energy levels. The exiting pulses were recorded on a Canberra counter and hard copies and tapes were produced on a teletype. All interactions with the diffraction unit were performed from a teletype by sending various commands to a PDP8 minicomputer.

The data collected were used to calculate degrees of crystallinity as described by Ruland (209). The photographs collected from a pinhole geometry were only used as a guide in the diffraction experiments.

D. Small angle light scattering (SALS). SALS experiments were performed on a system equipped with a Spectra Physics HeNe laser (λ = 632.8 nm). Scattering patterns were recorded on Polaroid film with the distance between the specimen and the film being variable. This apparatus has been described elsewhere in more detail (210,211) and will not be discussed further. The primary use of this technique was to obtain the average spherulite size from the position of the maximum

occurring at a 45° azimuthal angle. Stein and Rhodes (212) have shown this to be given by

$$4.1 = \frac{4\pi R_s}{\lambda} \sin(\theta_{max}/2) \qquad (139)$$

where λ is the wavelength of light in the medium, θ_{max} is the angle measured within the medium where the maximum in the scattering occurs and R_s is the average spherulite size.

This experiment was performed strictly for comparison with previous work and shall not be discussed in any greater depth. The interested reader is referred to the literature (213,214,215,216) for further detail.

E. Small angle x-ray scattering (SAXS). SAXS experiments were performed on three different pieces of equipment, namely: the Oak Ridge two dimensional position sensitive detector (2DPSD) facility, the Oak Ridge one dimensional position sensitive detector (1DPSD) facility, and the Kratky step scanning facility at the University of Massachusetts. Each of the three pieces of equipment is considered separately below.

i. ORNL--2DPSD. Only a short description of this apparatus will be given here. Further details on the apparatus can be obtained from a recent article by Hendricks (155). Beginning from the source, x-rays are generated by a 6 Kwatt Rigaku-Denki rotating anode. The x-rays are then diffracted down a 5 meter evacuated chamber by a graphite monochromator. Pinholes within this chamber collimate the beam before impinging upon the sample. The radiation is scattered by the sample and the scattered radiation passes through another evacuated

chamber with a length variable from 1.2 to 5 meters before being collected by the two dimensional detector. Electronically the pulses are discriminated and position encoded with the resulting data being printed on a Dec-writer and/or displayed on a video terminal.

ii. ORNL--1DPSD. A detailed report on the characteristics, operation, and performance of this instrument is given in Appendix I. Quite briefly, x-rays were produced in a Kratky-Siemens Ag 4ö/2 copper target x-ray tube powered by a General Electric XRD-6 generator operated at 35 Kv, 20 ma. From the tube the x-rays were filtered with a piece of nickel and entered the front slit of a Kratky camera. After the initial collimation the beam passed through a beam monitor and was finally collimated by the bridge. (From just before the bridge to the detector the beam was in a vacuum of 10 microns of mercury.) The finely collimated beam impinged on the sample and the scattered photons were collected on a 1DPSD ca. 1.5 meters from the sample. The pulses were then energy discriminated, position encoded and displayed on a multichannel analyzer (MCA). The MCA output was recorded on paper tape via a teletype.

iii. Step scanning Kratky apparatus. Again, only a brief discussion of this apparatus will be given here. A detailed report on the alignment, performance and operation of the apparatus assembled in this laboratory is given in Appendix II.

A Kratky Siemens Ag 4ö/2 copper target x-ray tube in conjunction with a Philips-Norelco generator operated at 40 Kv, 20 ma, was used to produce x-rays. In a similar fashion, the x-rays were filtered and collimated. However, in the commercially available equipment, the

specimen chamber was not evacuated. So there were at least two additional windows (vacuum-air interfaces) that the beam must traverse. In addition to this, the apparatus did not contain any sort of beam monitoring device. The receiving slits were located at the end of an evacuated chamber, 21.4 cm from the sample. These slits allowed a discrete solid angle to be viewed. The slits were of variable width so that the size of the solid angle could be varied if desired. A detector, identical to that used on the WAXD apparatus, was positioned just behind the receiving slits. Similarly, the pulses were energy discriminated and collected in a Canberra counter/timer. Hard copies of the data and/or paper tapes were recorded by a teletype. All interactions with the system were performed through the teletype. Since the system was not equipped with a minicomputer, individual commands had to be continually transmitted to the system.

During the course of this study a 39 micron entrance slit coupled with a 60 micron receiving slit provided a resolution of 150 nm. This was adequate for all the experiments conducted.

F. Small angle neutron scattering (SANS). Dilute mixtures of d-PS in PoClS were investigated by neutron scattering using equipment at the ORNL Research Reactor in the Oak Ridge National Laboratory. A rough schematic diagram of the equipment is shown in Figure 11. Neutrons, emitted in all directions from the core, are collected by a wave guide pointed away from the core. This is done so that the fast neutrons emerging from the core can be thermalized or slowed down by making numerous collisions with the moderator (D_2O) around the core. Before

entering the graphite monochromator system the neutrons are characterized by a Maxwellian distribution (219):

$$\nu_\lambda = \frac{2N_1}{\lambda} \left(\frac{E}{KT}\right)^2 e^{-E/KT} \qquad (140)$$

where N_1 is the total number of neutrons of all velocities emerging per second, E is the energy of a neutron of wavelength λ, K is Boltzmann's constant, T is the equilibrium reactor temperature, and ν_λ is the number of neutrons at a wavelength λ. The neutrons are then difracted by paired pyrolitic graphite crystal monochromators yielding a beam with a narrow wavelength distribution where $\Delta\lambda/\lambda = 0.1$. The spectrum of neutrons is compared to spectra of an x-ray source in Figure 12 where characteristic lines predominate the spectrum.

For this study neutrons of wavelength 0.48 nm were used. Collimation of the beam was achieved by two boron impregnated cadmium pinholes (1 cm in diameter) separated by 7.3 meters. An incident beam monitor was placed just prior to the second pinhole. After being collimated the beam impinged upon the sample with a flux of 10^4 neutrons/cm^2sec. The scattered neutrons passed through an evacuated chamber sealed with two aluminum windows before being collected on the two dimensional area detector 4-8 meters from the sample. Pulses from the detector were energy discriminated, position encoded and the results were stored on tape as well as being printed out on a Dec-writer.

The resolution and collimation characteristics of the ORR facility are given in Table 4 (219).

TABLE 4

ORR SANS APPARATUS

RESOLUTION	$\Delta\kappa$ (nm^{-1}) x 10^4	κ_{min} (nm^{-1}) x 10^4	κ_{max} (nm^{-1}) x 10^3	FLIGHT PATH (m)	PINHOLE DIAMETERS (mm)
High	1.9	3.9	3.5	4.8	10
Low	10.0	30.0	15.3	1.2	20

C H A P T E R I V

RESULTS AND DISCUSSION

In order to facilitate the treatment of the results obtained in this work this chapter has been divided into two major sections. The first section involves the investigation of compatibility in concentrated mixtures of PVC and PCL by several techniques. These results will be compared to previous work performed on the same two polymers by a number of other workers. The second section consists of SAXS and SANS studies performed on dilute solid solutions of PCL in PVC, PoClS, and PpClS in PS and PPO, PpIS in PS and d-PS in PoClS. These results will be compared to solution studies performed on these systems and conclusions concerning the conformation of polymers in bulk blends will be made. Although these two sections deal with the subject of compatibility the approaches involved are distinctly different and warrant individual treatment.

1. Concentrated PVC/PCL Blends

A. Discussion of blend status. The results of Ong (29), Khambatta et al. (144,194), Koleske et al. (193), Hubbell and Cooper (192), and Zarian et al. (24) all indicate that the concentrated mixtures of PVC and PCL are compatible throughout the entire composition range. However, a rather disturbing factor elucidated by the x-ray studies of Khambatta et al. (149,194) was that the amorphous phase contained

domains on the order of 10 nm. These domains were not pure PCL or pure PVC but consisted of a mixture of the two. This, however, would only indicate a partial miscibility of the two polymers and, consequently, two glass transition temperatures would be expected characterizing the composition of each phase. Only one glass transition is observed (29,193) which indicates that the phases are too small to be observed dynamic mechanically or the composition of the two phases is not significantly different or there is some heterogeneity present that would exhibit a separate T_g but is out of the range of the temperatures measured.

The concept of having two separate phases is rather disturbing since results of Ong on melting point depression and crystallization kinetics (29) and the infrared results of Zarian and Coleman (27) indicate that mixing is occurring on the segmental level. The results in both of these studies would have been dramatically affected by the presence of two separate phases. Indeed, two separate phases possessing different compositions would be expected only on the binodal where a tie line in the phase diagram would dictate the composition in the two phases.

Insight can be gained into this problem if the SAXS profile of PVC obtained by Khambatta (193) is examined (see Figure 13). A discrete maximum is clearly seen after desmearing and reducing the data to a one dimensional profile. This clearly indicates that there is some scattering entity present in the pure PVC. The scattering maximum or shoulder persists throughout the entire composition range of the amorphous blends (<50 weight percent PCL) and shifts to smaller and smaller

angles as PCL is added to the blend indicating a separation of these domains. From 50 weight percent PCL and above the scattering is predominated by the crystal-crystal interferences but the effect of this domain is still present as is evidenced by the calculation of the SAXS invariant. This indicated the presence of "more than two but less than three" phases and, consequently, the concept of a third phase with extremely broad transition zone thickness was introduced.

From the SAXS results on PVC it seems evident that this third phase is not a consequence of the compatibility between PVC and PCL but results from the presence of some foreign material in the PVC. The origin of this foreign material most probably lies in the commercial synthesis and stabilization of PVC. PVC is generally emulsion polymerized which requires the use of emulsion stabilizers to support the growing polymer molecule. In addition to this PVC is thermally unstable and readily undergoes a dehydrohalogenation upon heating leading to conjugated unsaturation in the chain and consequent discoloration. Therefore, radical scavengers are placed in the PVC to retard the degradation. Aside from these possible origins of foreign matter, PVC is known to readily branch and gel. This gel, as shown by Keller and others (197,198) is readily crystallizable and these crystals could possibly give rise to the scattering maximum as discussed by Wenig (220).

Regardless of the origin of the impurity in PVC its presence can only hinder the investigation of the mixing behavior between PVC and other polymers. For example, if we consider a suspension polymerized PVC where the molecular weight of the individual suspension par-

ticles is such that on the surface of the particle there is a high molecular weight crosslinked PVC and on the interior of the particle the PVC is present as a linear or slightly branched material. If this is mixed with PCL, for example, then it is quite possible that the PCL will mix with the PVC within the particle but not with the high molecular weight material. This is not unreasonable since molecular weight is known to affect even the compatibility of homopolymeric mixtures. If the materials are mixed in solution the PCL will readily diffuse into the PVC particle and PVC will diffuse out. This would inevitably lead to a system containing PVC and PCL mixed on the segmental level but randomly dispersed throughout this mixture would be the highly crosslinked shells of the emulsion particles. Provided the electron density of the shells is significantly different from the PVC and the PVC/PCL matrix then this could lead to the scattering profiles observed by Khambatta (143). Similar arguments can be used for emulsion stabilizers forming the particle shell where the stabilizer is not soluble in either PCL or PVC. Since the PVC is not detectably crystalline then some sort of explanation along these lines must be invoked to explain the discrepancy between the SAXS and the other experiments.

In lieu of these comments the PVC was purified as outlined in the experimental section of this work. Specific mention is made of the presence of a gel in the PVC. This gel, however, was not analyzed to determine the amount of crystallinity, molecular weight, stabilizer content, etc. As will be seen significant differences were observed in blends prepared using this purified material.

B. Density results. The effect of the purification of both PVC and PCL is readily seen from density measurements. Figure 14 shows the density of the PVC/PCL blends as a function of composition. This figure also contains the density of the nonpurified material as well as the density calculated assuming a simple volume rule (the dashed line includes the increase in density due to the presence of crystalline PCL). It is immediately obvious that the volume additivity relationship does not describe accurately the density of either the purified or nonpurified blend. This is not surprising since a negative volume of mixing, ΔV_M, and the densification of a glass below T_g (221) are both opposing a simple volume additivity. Secondly, the purified blend is characterized by higher densities than the non-purified materials. Provided the extent of the densification phenomenon is the same in both cases then the purified material exhibits a more negative ΔV_M and, consequently, greater mixing.

Above 50 weight percent PCL, there are PCL crystals present. If the density in excess of the amorphous density calculated by volume additivity is used to calculate a degree of crystallinity then it is found that this degree of crystallinity is anywhere from 5 to 20% higher than differential scanning calorimetric results and wide angle x-ray diffraction results. This is a further indication that the density is not simply additive. It also points to the possible magnitude of errors that can be obtained when calculating a degree of crystallinity for a polymer blend from density data.

C. Degree of crystallinity. The weight fraction of crystallinity in

the purified PVC/PCL blends (≥50% PCL) were obtained by both wide angle x-ray diffraction (WAXD) and differential scanning calorimetry (DSC). Photographs of the WAXD patterns along with their corresponding exposure times are shown in Figure 15. From a qualitative observation of these profiles it is clearly seen that the degree of crystallinity decreases as the concentration of PVC increases. This was placed on a quantitative scale by taking account of the sample thickness, attenuation factor and angle of diffraction and using a step scanning diffractometer to accurately record the intensity of each angle. After subtraction of a natural background the method of Ruland (2θ) was used to calculate the degree of crystallinity. These results are shown in Figure 17. These results confirm the qualitative observations made previously on the photographs.

DSC was used to confirm the WAXD results. Thermograms were obtained on six blends ranging from 50 to 100 weight percent PCL. The weight of the sample used was such that the area under the melting peak (endotherm) was relatively constant to optimize comparison. Sample specifications and experimental conditions are given in Table 5. and the thermograms are shown in Figure 16. The degree of crystallinity calculated from these curves is shown in Figure 17. As can be seen, good agreement was found between the two techniques.

The endotherms possessed a rather peculiar shape particularly in the 70-50 weight percent PCL range. Similar observations were made by Ong (29) on the non-purified blends. Consequently, it is felt that these profiles are characteristic of the blend and reflect a significant amount of crystals melting at lower temperatures. This could

TABLE 5

DIFFERENTIAL SCANNING CALORIMETRY DATA

WEIGHT % PCL	SCANNING RATE (°C/min)	WEIGHT (mg)	MELTING POINT (°C)	DEGREE CRYSTALLINITY
100	10	3.37	54.2	0.55
90	10	5.23	54.1	0.49
80	10	5.10	53.4	0.43
70	10	6.03	52.8	0.33
60	10	6.91	51.1	0.24
50	10	7.89	49.8	0.12

simply be the result of the increasing amount of PVC in the blend and its effect on the PCL crystals formed during isothermal crystallization.

In agreement with previous work, the degree of crystallinity was found to decrease from approximately 50 percent for pure PCL to nearly zero at a 50/50 mixture by weight. The cause of this reduction is two-fold. First of all the total amount of PCL capable of crystallizing is being reduced with the addition of PVC. More importantly, however, is the fact that the temperature envelope in which crystallization can occur is decreasing. This region of crystallization is dictated by the T_g and melting point of the system. For these blends this information is given in Figure 18 where T_m is the melting point of the blend and T_c is the temperature of crystallization (30°C). As can be seen, the difference between T_m and T_g continually decreases as PVC is added. Ong (29) investigated the overall rate of crystallization in the blends and found it to continually decrease in agreement with the narrower crystallization envelope. For blends with less than 50 weight percent PCL crystallization half times on the order of months to years (193) was also reported.

These facts point directly to the compatibility of PVC and PCL. If the two did not mix then the crystallization rate would not be affected to any extent since T_g would be that of the individual homopolymers. The degree of crystallinity would also be directly related to the amount of crystallizable component and the degree of crystallinity of that component in the bulk homopolymer. If the two were compatible at elevated temperatures and phase separated at the lower temperatures

then the crystallization rate and the rate of diffusion would have to be considered.

A closer examination of the melting point of the PCL also indicates good mixing. As seen in Figure 19 the melting point decreases as PVC is added to the blend. Melting point depression has been treated by Flory (32) but in order to use this theory and relate the depression to the interaction parameter the system must be at equilibrium. This requires performing the melting point experiments at different rates and extrapolating to zero heating rate to obtain the equilibrium melting point. This was not done for this system and, consequently, the results in Figure 19 can only qualitatively indicate compatibility.

D. Small angle light scattering (SALS). A dramatic difference was observed in the spherulite size between the purified and non-purified blend. Both cases yielded specimens volume filled with spherulites. However, spherulite radii determined by SALS were three times larger in the case of the purified materials than in the non-purified blend as shown in Figure 20. This can be attributed to the removal of heterogeneous nucleation sites in the form of impurities. In the non-purified blend the spherulite radius was found to reach a maximum value at 90 weight percent PCL whereas the radius remained constant to within experimental errors for the purified blend. The former case is easily explained by the addition of more impurities into the system providing more nucleation sites and, consequently, a decrease in the average spherulite size. The only explanation for the latter case is that impurities in the PVC balance the loss of nucleation sites in the PCL

due to the decreased PCL concentration. However, experimental errors were quite high and permit only a qualitative discussion at best.

A point that has not been discussed previously and warrants further attention is the fact that a spherulite morphology was not obtained from the blend unless the solution cast films were heated to 90°C or higher. If lower melting temperatures were used then a rod-like light scattering pattern was observed. This is due to the crystals melting but not being able to diffuse into the surrounding PCL/PVC matrix at temperatures below 90°C. Consequently, when the blend is crystallized crystallization occurs in the framework of the previously existing spherulite producing a rod-like morphology. When the temperature was raised above 90°C subsequent crystallization produced the expected spherulite morphology. This phenomenon was not observed in the non-purified material and could be due to the removal of the PCL-300, the lower molecular weight PCL, and other lower molecular weight material during the purification process. These materials would facilitate the diffusion process and, therefore, eliminate the effect noted above.

E. Small angle x-ray scattering (SAXS). As indicated in Chapter III, SAXS can be a valuable tool in the investigation of the morphology of semicrystalline and amorphous polymers. Khambatta (194) used this technique to elucidate the morphology of PVC/PCL blends and, consequently, was able to characterize the extent of mixing over the entire composition range.

In the semicrystalline blends SAXS provided information concerning the location of the PVC in the blend which is volume filled with

spherulites down to 50 weight percent PCL. The long period, i.e., the crystal center to crystal center distance, determined from model calculations of the scattering curve, was found to increase sufficiently to accommodate the PVC. In confirmation of this observation, the invariant indicated that the amorphous material between the PCL lamellae was not pure PCL but was composed of a mixture of the two polymers. Debye-Beuche analyses on the amorphous blends yielded an average heterogeneity length in the medium and, as previously discussed, this led to the conclusion that the amorphous material consisted of a mixed phase with diffuse heterogeneities on the order of 10 nm distributed throughout the matrix.

In view of these findings similar analyses were performed on the purified materials to determine if the differences observed in the macroscopic properties would be reflected in the scattering properties of the purified blends. Since there are two distinct morphologies present in the blends, i.e., completely amorphous and semicrystalline, they shall be treated separately because different models are used to describe the scattering.

i. Semicrystalline blends. SAXS profiles for the semicrystalline blends isothermally crystallized at 30°C were obtained on the step scanning Kratky apparatus. Sample specifications are given in Table 6. The scattering curves are shown in Figures 21 and 22 plotted against modular degrees where 1 modular degree corresponds to 0.936 mrad. The intensity profiles have been corrected for parasitic scattering and electronic noise and were normalized to the scattering from pure PCL. The normalized intensity is given by:

TABLE 6

CONCENTRATED PVC/PCL BLENDS--SAXS INFORMATION

WEIGHT % PCL	ATTENUATION FACTOR (I/I_o)	THICKNESS (mm)	MONITOR INTENSITY (cps)
100	0.464	1.13	9.73
89.6	0.529	0.467	10.13
79.8	0.366	0.529	10.04
69.6	0.237	0.521	10.04
59.8	0.441	0.243	10.92
50.4	0.273	0.473	10.34

$$I_{norm} = \frac{I_{m2} A_2 d_2}{I_{m1} A_1 d_1} I_1 \qquad (141)$$

where A_i is the attenuation factor of sample i, I_{mi} is the monitor counts (Lupolen intensity) for the scattering curve i, d_i is the thickness of sample i, and I_i is the intensity of sample i. I_{norm} is the intensity normalized to the scattering of sample 2 where 2 in this case is PCL.

Quite pronounced differences are seen in these data compared to that of Khambatta (193). In the latter case distinct maxima or shoulders were clearly evident. These are only readily seen in the pure PCL and the 90 percent blend. The remainder of the profiles could be characterized by a monotonically decreasing function.

The scattering of interest, however, is that due to lamellar interferences and, consequently, any contributions due to heterogeneities in the amorphous phase or from foreign matter must be eliminated from the scattering before application of any of the existing models. In order to arrive at these contributions the specimens were melted at 90°C and scattering profiles were taken on the molten materials. The scattering from these samples arises from dirt or foreign matter in the samples, as well as thermal density and concentration fluctuations. The scattering profiles, obtained on the one dimensional position sensitive detector (1DPSD) at Oak Ridge National Laboratory (see Appendix I) are shown in Figure 23. The curves, corrected for electronic noise and parasitic scattering, were subtracted from the scattering profiles of the semicrystalline blends after normalizing the profile

at very high angles where the intensity is flat and is predominated by fluctuation scattering from the amorphous phase.

Alternate procedures were available to perform this subtraction. For example, the thermal density fluctuations give rise to an angularly independent scattering. This can be determined by plotting $J(s)s^3$ against s^3 and determining the slope of the line at high angles. This scattering level can be subtracted from the overall scattering profile. However, contributions due to correlated fluctuations or foreign matter both of which are possible in polymer blends would not be removed.

In terms of fluctuation scattering a better method of subtracting the contribution to the total scattering from the amorphous phase would be to perform an experiment on a sample with the exact PVC/PCL concentrations as in the amorphous phase. If ϕ_C and ϕ_{PCL} are the volume fractions of crystallinity and PCL, respectively, then a melt scattering profile of a sample with a PCL concentration of $\phi_{PCL} - \phi_C$ should be performed. This profile, $I_{FL,A}$, should then be subtracted from the semicrystalline scattering, I_S, weighted by the volume fraction of the amorphous phase. Consequently, the corrected profile, I_{corr}, would be given by

$$I_{corr} = I_S - (1 - \phi_C)I_{FL,A} \tag{142}$$

A complicating factor arises in this procedure in that scattering from foreign matter is also included in this scattering from the molten material and this is characteristic of the blend regardless of

its degree of crystallinity. There is no method available for separating these two contributions. Therefore, the first method was used due to its simplicity and the availability of the sample. Errors involved in using this method will be small when considering the total integral. However, proper background subtraction is crucial for examining zero order scattering.

A point that should be made here concerning experiments on the molten samples is that sufficient time must be allowed to produce a homogeneous mixture. Before the experiment is performed, the PCL from the molten crystals must be allowed to diffuse into the PVC/PCL mixture in the amorphous phase. Otherwise an artificial fluctuation approximately the size of a lamella can be incorporated into the scattering profile. At least 20 minutes were allowed at 90°C for this to occur and for the size range of interest Gilmore (24) has shown that this is a sufficient time allotment.

The result of subtracting the liquid scattering and foreign matter scattering from the initial semicrystalline profiles is shown in Figure 24. In only three of the concentrations investigated was there sufficient excess scattering to analyze. Even in the 69 percent blend the errors on the scattering profile are relatively high. The profiles in Figure 24 were desmeared and reduced to profiles from a one dimensional system (multiplication by s^2) shown in Figure 25. Treatment of these profiles with the various scattering models will be discussed momentarily. However, a discussion of the total integrated scattering of these systems along with an explanation of the lack of scattering in some of the semicrystalline blends is necessary.

In order to correctly assess the value of the total integral the scattering was examined for deviations from Porod's Law. The data appearing in Figure 24 along with corresponding pinhole data obtained on the two dimensional position sensitive detector were used to assess deviations due to transition zone thicknesses. Plots were made of $J(h)h^3$ vs. h^3 and $I(h)h^4$ vs. h^4 for the smeared Kratky data, J(h), and the pinhole data, I(h). The plots from the pinhole data appear in Figures 26, 27, and 28. The transition zone, E, was found to be constant to within experimental errors over the entire composition range. Both the pinhole and smeared data yielded an E = 1.6 nm with errors for the pure PCL increasing from ±0.2 nm to ±0.4 nm for the 69 weight percent PCL. These data are tabulated in Table 7 and plotted as a function of concentration in Figure 29.

The intensity profiles in Figure 24 were corrected for the loss in intensity due to the transition zone by equation (119), and the invariant was calculated according to equations (106a,b) after placing the data on an absolute level by equation (129). The profiles were examined to ensure that Porod's Law was obeyed before calculation of the invariant. This is necessary to obtain a correct extrapolation to $s \to \infty$. The results of these calculations (tabulated as $\overline{(\Delta\rho)^2}$) are shown in Table 8 and are plotted as a function of PCL concentration in Figure 30.

As can be seen from Table 8 the errors listed range from ±10% for the pure PCL to approximately ±100% in the 69.6 blend. These enormous errors in the 69.6 percent result from the fact that the invariant was very small and the contribution to the invariant from the extrapola-

TABLE 7

TRANSITION ZONE THICKNESS DATA

WEIGHT % PCL	TRANSITION ZONE THICKNESS (nm)	ERRORS (nm)
100	1.6	±0.2
89.6	1.6	±0.1
79.8	---	---
69.6	1.5	±0.4
59.8	---	---
50.4	---	---

TABLE 8

MEAN SQUARE FLUCTUATION IN THE ELECTRON DENSITY

WEIGHT % PCL	$\overline{(\Delta\rho)^2}$ (mole $e^-/cm^3)^2 \times 10^4$	
	MEASURED	CALCULATED
100	6.70 ± 0.6	6.91
89.6	3.70 ± 0.8	2.64
79.8	---	0.34
69.6	0.60 ± 0.6	0.09
59.8	---	0.26
50.4	---	0.26

--- indicates that experimental values were not measurable.

tion of Porod's Law is nearly 70% of the total integral. In the 100 and 89.6 weight percent samples the Porod Law contribution is 25% and 38%, respectively.

Using the crystallinities obtained from DSC and WAXD measurements and the electron densities of crystalline PCL ($\rho_{C,PCL}$ = 0.6447 mole e^-/cm^3), amorphous PCL ($\rho_{C,PCL}$ = 0.592 mole e^-/cm^3) and polyvinylchloride (ρ_{PVC} = 0.721 mole e^-/cm^3) the mean square fluctuation can be calculated assuming a model. For simplicity it will be assumed that the electron density of the amorphous phase is given by

$$\rho_a = \phi_{a,PCL}\,\rho_{a,PCL} + \phi_{PVC}\,\rho_{PVC} \tag{143}$$

The mean square fluctuation in electron density for a two phase system given by equation (69b) can be written in terms of the crystal and amorphous phases by

$$\overline{(\Delta\rho)^2} = \phi_c\phi_a(\rho_c - \rho_a)^2 \tag{144}$$

These calculations were performed and are compared to the experimentally determined values in Figure 30. Even with the assumption of a volume additivity which according to the density measurements is not strictly correct the calculated value of $\overline{(\Delta\rho)^2}$ follows the same trend as the experimental value. These calculations also explain why no scattering was observed in some of the semicrystalline blends.

In essence, there are two parameters contributing to this lack of intensity. First, the invariant is proportional to ϕ_c which continually decreases for the blends as shown in Figure 17. Secondly, the

integrated intensity is given by the square of the electron density difference. This, however, goes to zero near 70 weight percent PCL because the electron density of the amorphous phase equals that of the crystalline phase. This is understood when the magnitudes of the electron density are considered. Initially, $\rho_c > \rho_a$ since both the phases are composed of PCL and $\rho_{c,PCL} > \rho_{a,PCL}$. However, since $\rho_{PVC} > \rho_{c,PCL}$ then as PVC is added to the amorphous phase ρ_a increases and obtains a value equal to ρ_c near 70 weight percent PCL. Further addition of PVC increases ρ_a even more making $\rho_a > \rho_c$ and, consequently, an increase in the intensity would be expected. However, the decreasing value of ϕ_c counteracts this and consequently only a slight rise is seen before returning to zero.

The interesting and important feature that this calculation demonstrates is that the PVC must be located between the lamellae to explain the observed invariants. This can be stated without even considering the long period. These calculations also indicate that the electron density difference can be explained in terms of a two phase model without the need of incorporating additional diffuse phases. Consequently, this behavior strongly indicates a well mixed amorphous phase.

The presence of PVC between the lamellae is reflected in the long period as well. Using Bragg's Law to roughly calculate the long period it is found to increase from 14.7 nm in the pure PCL case to approximately 26 nm in the 69.6 weight percent blend. As shown in Figure 31 the increase does not vary directly with the concentration of PVC. It is found to increase very slowly at first followed by a

rapid increase near 80 weight percent. Due to the absence of scattering the trend cannot be characterized to any further extent. This trend would not be expected if the degree of crystallinity of the PCL (based on total weight percent of PCL) remained constant. Therefore, this must be changing as a function of composition. Due to the absence of scattering the trend cannot be characterized to any further extent. Indeed, the errors in the determination of the scattering maximum for the 69.6 weight percent sample are magnified since the excess intensities are small. The increase in long spacing is definitely indicated but not as pronounced as that observed by Khambatta where the long period increased in proportion to the volume fraction of PVC.

The scattering profiles shown in Figure 29 were compared to theoretical curves calculated from the Vonk correlation function and the Hosemann paracrystalline lattice models.

Theoretical correlation functions were fit to the experimental correlation function using Gaussian crystal thickness distributions and log normal amorphous thickness distributions. Comparison of the theoretical and experimental curves are shown in Figures 32 and 33 for the pure PCL and the 90 percent blend with PVC. As can be seen, reasonable agreement was found between the two using the theoretical distribution shown in Table 9. These data indicate that the effect of adding ten percent PVC to the PCL does not dramatically alter the distributions of either phase. However, broader distribution parameters had to be used for the 69 percent blend. The crystallinities obtained by these calculations agree to within six percent of the values obtained by DSC or WAXD. This supports the fact that PVC resides between the lamellae

TABLE 9

SAXS MODEL PARAMETERS

V O N K

CONCENTRATION PCL	ϕ_C (DSC)	ϕ_C (SAXS)	β_c (Gaussian)	β_a (Log Normal)
100	.49	.55	0.25	0.05
90	.45	.40	0.25	0.09
69	.30	.35	0.30	0.31

H O S E M A N N

WGT % PCL	ϕ_C	C (nm)	A (nm)	N	g_c	g_a	E (nm)
100	50	7.5	7.5	2.0	0.15	0.33	1.5
90	46	7.3	8.7	1.7	0.20	0.32	1.6
69	39	10.1	15.9	1.9	0.31	0.30	1.5

and is not excluded from the interlamellar regions. If the latter were so, higher crystallinities would have been obtained by SAXS than other methods since the local crystallinity giving rise to SAXS would be higher than the overall crystallinity of the specimen.

Parameters used in the Hosemann paracrystalline lattice calculations are given in Table 9. Gaussian distribution statistics were used to describe both the amorphous and crystalline phases. Again it is seen that the distribution functions broaden as PVC is added to the PCL and that the crystallinity determined by this model agrees with the overall degree of crystallinity. The value of N, i.e., the number of lamellae per stack, is seen to be low. The only physical significance that can be given to this is that it represents the number of lamellae that are perfectly aligned with one another. Baczek (134) has discussed this point and the interested reader is referred to that work.

The precision to which a scattering curve can be described by a single set of distribution parameters and degree of crystallinity is quite good. However, this does not mean that they are the only set of parameters that can be fit to a scattering profile. Equally good fits could be obtained in the correlation function analysis using different parameters but, as in this case, either the crystallinities were absurd or the distribution parameters were too broad and yielded a high probability of very small crystals. In the Hosemann analysis, the value of N is always ambiguous in its physical meaning.

Even with these ambiguities it is still felt that the reasonable models for the blend were found. These models are consistent with the

idea of a compatible mixture in the amorphous phase with the long period increasing to accommodate the added PVC.

In addition to the above model calculations another piece of information can be obtained from the scattering profiles. Considering the initial smeared scattering profiles in Figures 21 and 22 mention was made of the fluctuation scattering at the tail end of the scattering curves. In this region the scattering is essentially angularly independent. In the pure PCL this scattering is characteristic of thermal density fluctuations in the amorphous phase whereas in the blends there are added contributions due to concentration fluctuations. Consequently, if the level of scattering is corrected for the amount of crystallinity present and the contributions due to thermal density fluctuations in the pure amorphous PCL are subtracted then this will yield a qualitative measure of the amount of fluctuation scattering attributable to concentration fluctuations. Therefore, the corrected scattering level, $I_{L,C}$, would be given by

$$I_{L,C} = I_{L,B} - I_{L,PCL}\left(\frac{\phi_{c,B}}{\phi_{c,PCL}}\right) \qquad (145)$$

where $I_{L,B}$ and $I_{L,PCL}$ are the liquid scattering levels of the blend and pure PCL, $\phi_{c,B}$ and $\phi_{c,PCL}$ are the volume fractions of crystallinity in the blend and pure PCL.

This excess liquid scattering is shown in Figure 34 to increase as PVC is added to the PCL indicating that the number or magnitude of the fluctuations is increasing. The former would be indicative of mixing in the amorphous phase in keeping with the invariant calculation.

This observation is only qualitative and can only be discussed in terms of other evidence.

ii. Amorphous blends. The scattering from the amorphous blends and the semicrystalline blends above the melting point is characterized by scattering arising from concentration and thermal density fluctuations. In addition to this scattering foreign matter and parasitic scattering are also present. Parasitic scattering is easily accounted for. However, as mentioned previously, the scattering from foreign matter is not easily obtained. Khambatta suggested one possible approach where the scattering from the two pure materials weighted by the volume fraction of the materials present can be subtracted from the scattering of the blend. This essentially assumes that the foreign matter in the blend is a weighted sum of that in the pure components. This assumption is most likely valid to within experimental errors and was used in this study. Any errors involved in improper subtraction will be reflected in deviations at small angles. Therefore, the corrected intensity I(h) is given by

$$I(h) = I_{BL}(h) - \phi_{PCL}\, I_{M,PCL}(h) - \phi_{PVC}\, I_{PVC}(h) \qquad (146)$$

where $I_{M,PCL}$ is the scattering from molten PCL, I_{PVC} and I_{BL} are the scattered intensities from pure PVC and the blend, respectively.

The corrected intensities were desmeared using the infinite height assumption and the resulting profiles were treated using an exponential correlation function as described previously in equation (71). Plots of $I(h)^{-1/2}$ against h^2 are shown in Figures 35 and 36 with the correlation distances given in Table 10. Since the fluctuations are

TABLE 10

CORRELATION DISTANCE DATA

VOLUME FRACTION PCL	CORRELATION DISTANCES (nm)		CHORD LENGTHS (nm)			
			ℓ_{PVC}		ℓ_{PCL}	
92*	1.05	(3.94)	1.15	(4.28)	18.2	(49.2)
74*	1.18	(4.15)	1.60	(5.60)	4.66	(15.9)
66*	1.64	(5.29)	2.49	(8.02)	4.84	(15.6)
56*	1.33	(7.54)	2.30	(13.5)	3.03	(16.4)
46**	1.70	(3.41)	3.70	(7.40)	3.15	(6.32)
24**	0.95	(2.23)	3.97	(9.31)	1.23	(2.94)

*Measured at 90°C.

**Measured at room temperature.

NOTE: Values in parentheses indicate correlation distances and chord lengths determined at the initial part of the scattering profiles.

due predominantly to concentration fluctuations the average chord lengths, defined previously, were calculated for both PVC and PCL. These are also shown in Table 10 and are plotted in Figure 37 as a function of concentration.

The most surprising result of these calculations is that the correlation distances are quite small and are smaller than the dimensions of a single chain. This was found to be true for the PVC and PCL chord lengths as well. Consequently, these results indicate that mixing must be occurring on the segmental level. If this were not the case then the correlation distances and the average chord lengths would have to be much larger. In previous studies on these materials, Khambatta found much larger chord lengths and arrived at the conclusion of the presence of partially mixed phases in the amorphous material. However, this may very well have been a result of the presence of impurities in the initial PVC.

Deviations from the Debye-Bueche analysis were seen at small angles. These deviations must be attributable to an improper subtraction of the background. Attempts can be made to eliminate these deviations, however, the procedure then loses physical significance and is basically force fitting the data to the analysis. In addition to this a straight line behavior was observed over a large angular region. Therefore, the deviations were ignored in the analysis.

F. Infrared spectroscopy. The results of the SAXS analysis clearly indicate that mixing is occurring in the blends throughout the entire composition range. IR was then undertaken to locate the specific in-

teractions in the blends. A parallel study by Coleman and Zarian (27) was undertaken on the same specimens using Fourier transform infrared techniques. The results of their study confirmed the results obtained in this work. The results from their investigation are more quantitative since they rely on a digital subtraction of the spectra (222,223) which circumvents the problems associated with the determination of film thicknesses. This was the source of the predominant error in this study.

Typical spectra obtained in this study for a series of sample thicknesses are shown in Figure 38. Only one composition (80 weight percent PCL) is shown for illustration purposes. The baseline used to obtain the absorbance at any given frequency is shown as a dotted line. The reason this baseline extends over the entire range of absorbances and is not restricted to a single absorption peak is that the total absorption arising from both components is of interest. Consequently, absorbance readings obtained from such a baseline will include overlaps from other bands in the same polymer and of the alternate component.

Plots of total absorbance as a function of thickness are shown in Figures 39, 40, 41, and 42 for several blends and the pure homopolymers. Several different frequencies are shown in each case and the assignments of these bands are given in Table 11. The assignments in PVC have been made by Krimm et al. (224) whereas the PCL assignments are characteristic group frequencies made by Holland-Moritz and coworkers (225,226) by a group frequency approach on a series of polyesters.

The slopes of the lines in the absorbance vs. thickness plots, shown in Tables 12 and 13, were plotted against monomer mole fraction in

TABLE 11

INFRARED SPECTROSCOPY ASSIGNMENTS AND RESULTS

FREQUENCY (cm^{-1})	ASSIGNMENT	POLYMER	DEVIATION FROM
1355	CH_2 wagging	PVC	No
1460	CH_2 bending	PVC	No
2835	CH stretching	PVC	No
960	CH_2 rocking	PVC	No
1200	CH_{am} wagging	PVC	No*
1240	CH_{am} deformation	PVC	No*
1255	CH_2 deformation	PVC	No
1100	COC stretching	PCL	No*
1165	CO stretching	PCL	Yes
1429, 1436	CH_2 deformation	PVC	Yes

*Extrapolate to extinction coefficient values for pure PCL that are too high.

TABLE 12

RESULTS OF ABSORBANCE VS. THICKNESS

WEIGHT % PCL	MONOMER MOLE FRACTION	SLOPES (= εC in cm^{-1} x 10^2) AT SPECIFIED FREQUENCY					
		1100 cm^{-1}	1165 cm^{-1}	1200 cm^{-1}	1240 cm^{-1}	1255 cm^{-1}	1335 cm^{-1}
100	1	3.96	11.68	6.78	7.22	5.66	2.91
89.6	0.826	5.53	16.93	3.07	11.40	9.64	1.02
80.1	0.687	5.88	13.93	9.83	9.26	7.41	3.85
69.9	0.559	5.89	13.64	9.44	8.92	10.03	4.37
59.7	0.448	5.91	16.69	9.61	10.70	9.84	4.48
49.8	0.353	.453	11.14	6.53	8.71	7.55	3.60
31.1	0.198	3.08	4.93	4.14	3.53	4.80	2.56
17.7	0.105	1.32	2.18	1.76	2.91	2.91	1.58
9.52	0.059	0.98	0.99	0.98	2.57	2.83	1.08
0	0	0.95	0.25	0.87	2.08	2.54	1.63

TABLE 13

RESULTS OF ABSORBANCE VS. THICKNESS

WEIGHT % PCL	MONOMER MOLE FRACTION	SLOPES (= εC in cm^{-1} x 10^2) AT SPECIFIED FREQUENCY					
		1356 cm^{-1}	1460 cm^{-1}	1436 cm^{-1}	1731 cm^{-1}	1736 cm^{-1}	2865 cm^{-1}
100	1	2.57	2.90	1.35	23.77	22.59	5.29
89.6	0.826	4.41	4.53	4.40	30.32	---	4.92
80.1	0.687	4.02	3.13	2.85	21.21	23.31	4.00
69.9	0.559	4.85	3.42	3.54	25.92	26.01	4.07
59.7	0.448	4.86	4.24	4.24	24.40	22.78	3.75
49.8	0.353	3.60	3.00	3.12	20.34	20.75	3.13
31.1	0.198	2.16	1.99	2.83	10.67	12.61	1.49
17.7	0.105	1.13	0.56	2.50	6.67	5.69	0.84
9.52	0.059	0.70	0.47	---	5.29	3.76	0.74
0	0	0.73	0.21	2.48	---	---	0.28

the blends and are shown in Figures 42-52 according to frequency. Table 11 lists frequencies where deviations from linearity were observed.

Strong deviations from linearity were observed at only two frequencies namely the 1165 cm^{-1} band due to a C-O-C bending and at 1429 cm^{-1} due to a CH_2 deformation. The band at 1165 cm^{-1} was also observed by Coleman and Zarian (27), however, the band at 1429 cm^{-1} was only observed to a small extent in their study.

Another type of deviation that was observed was that the extinction coefficient varied linearly as a function of PVC monomer mole fraction but did not yield the correct value for the PCL extinction coefficient. This type of deviation was found in the 1100 cm^{-1} C-O stretching frequency, the 1200 cm^{-1} C-H wagging frequency and in the 1240 cm^{-1} C-H deformation frequency. The first of these was not extremely pronounced but was in the last two cases. (These latter frequencies have been assigned to the amorphous component of PVC by Krimm (224).) Coleman and Zarian do not make specific mention of these bands but may likely be included in the minor changes they observed. In all of the cases above the extinction coefficient extrapolated to a value higher than that obtained for the pure components.

The carbonyl group in the PCL absorbs in the 1725-1740 cm^{-1} frequenty range. Coleman and Zarian (27) performed work on semicrystalline and molten PCL indicating that the crystalline carbonyl absorbs at 1724 cm^{-1} and the amorphous at 1737 cm^{-1}. Since this work was performed in the melt only the 1737 cm^{-1} band was observed. This was studied as a function of composition with the results being shown in Figure 53. As can be seen, the carbonyl peak shifts to lower frequen-

cies as PVC is added, indicating interactions are occurring. The shifting appears to be quite distinctive with a shift of over 5 cm^{-1} occurring. The shifting to lower frequency indicates a weakening of the carbonyl bond possibly due to hydrogen bonding with the proton opposite the chlorine in the PVC. This is illustrated schematically in Figure 54. Hallam (227) investigated the effect of hydrogen bonding on the carbonyl absorption frequency in some low molecular weight esters. In these studies downward shifts in frequency from 5 to 25 cm^{-1} in the carbonyl frequency. The greatest shifts in frequency occurred in solvents such as chloroform. In these cases the X-H bonds were only slightly affected. Given the structures of the two polymers, the type of interaction proposed in Figure 54 is not unreasonable when the work of Hallem is considered. The delocalization of the carbonyl bond will in turn have an effect on the C-O- C bond. This explains the deviations observed at 1165 cm^{-1}. This type of interaction can give rise to the peculiar behavior observed at the C-H wagging and deformation of 1200 cm^{-1} and 1240 cm^{-1}. Therefore, the infrared data is consistent with the schematic drawn in Figure 54.

Since sodium chloride salt plates were used the low frequency range could not be investigated. This region is of importance in the blend system because the conformations of the C-Cl bond can be examined. With the type of interaction drawn it would be expected that the C-Cl bond would be affected. Surprisingly, Coleman and Zarian's results do not indicate this. This region was completely removed when the spectra were subtracted. Consequently, if the C-Cl bond is involved in specific interactions the overall effect must be small.

G. Conclusions on concentrated PVC/PCL blends. The results of the various techniques employed in this study indicate that PVC/PCL blends mix on a finer scale than indicated previously by Khambatta et al. (144). SAXS correlation distances and specific interactions revealed by IR investigations indicate that the amorphous blends are mixed on a segmental level. No evidence was found for domains or heterogeneities on the 10 nm or molecular scale. Rather the heterogeneities were on the order of 2 nm which is on the segmental level for both materials. Consistent with these results the densities of the amorphous blends were not simply additive and indicated a negative volume of mixing. This is also supported by a single glass transition temperature found by others (29,193).

In the PVC/PCL blends at room temperature at PCL concentrations greater than fifty weight percent the PCL crystallizes. Consequently, the blends are phase separated into a pure PCL phase and an amorphous mixture of PVC and PCL. SALS and SAXS results indicate that the PVC resides between the PCL lamellae. Apparent melting point depression and SAXS invariant calculations further indicate that the two polymers are mixed on a segmental level. This conclusion is also supported by the observation of a single glass transition temperature.

Compatibility of the amorphous phase between the lamellae is really not too surprising when the relative concentrations of the two polymers are considered. Due to crystallization the composition of the amorphous phase is not the same as the overall mixing composition. If the volume fraction crystallinity is subtracted from the total volume fraction PCL it is seen that the concentration of PCL never exceeds

fifty weight percent in the amorphous phase. Specimens of this composition are easily investigated and are known to be compatible. Therefore, provided the presence of crystals does not drastically modify the PCL in the amorphous phase then the interlamellar regions should be well mixed.

The only observation that displays an abnormality along these lines is the glass transition temperature. Although only one glass transition temperature is seen it is characteristic of the overall composition and not the composition of the amorphous phase. It would be expected that the glass transition temperature would obey the behavior shown by the dotted line in Figure 91 rather than the observed (solid line) behavior. This may indicate that the crystals do affect the amorphous phase and the PCL chains are behaving in an anomalous manner. This is one point that needs further investigation to determine the reasons for this anomalous behavior.

2. Dilute Small Angle X-ray Scattering in the Bulk

Since a variety of systems were investigated by the dilute scattering technique they shall be discussed separately. The molecular weight specifications of the polymers used have been given in Table 2. Additional parameters necessary for calculations, for example, mass and electron density of the homopolymers and the excess number of electrons per gram for the various systems are shown in Tables 14 and 15. Tables 16 to 21 list the experimentally determined sample characteristics and scattering run specifications.

A. PCL/PVC. In order to work on the PCL/PVC system a

TABLE 14

HOMOPOLYMERS USED IN ZIMM SAXS

POLYMER	CHEMICAL COMPOSITION	MASS DENSITY (g/cm^3)	ELECTRON DENSITY (mole e^-/cm^3)	Z_e (mole e^-/g)
PVC	C_2H_3Cl	1.410	0.7219	0.512
PCL	$C_6H_{10}O_2$	1.090	0.5157	0.473
PpIS	C_8H_7I	~1.90	~1.09	0.573
PS	C_8H_8	1.048	0.5635	0.538
PpClS	C_8H_7Cl	1.226	0.6369	0.520
PoClS	C_8H_7Cl	1.245	0.6467	0.520
PPO	C_8H_8O	1.066	0.5680	0.533

TABLE 15

EXCESS ELECTRONS PER GRAM AND
ELECTRON DENSITY DIFFERENCES

MIXTURE	$\Delta\rho_e$ (mole e^-/cc)	$(\Delta\rho_e)^2$ (mole e^-/cc)^2	ΔZ_e (mole e^-/g)	$(\Delta Z_e)^2$ (10^3) (mole e^-/g)^2
PCL/PVC	0.2062	0.0425	0.039	0.152
PpIS/PS	0.5266	0.2772	0.036	0.130
PoClS/PS	0.0832	0.0069	0.018	0.033
PpClS/PS	0.0734	0.0054	0.018	0.033
PoClS/PPO	0.0787	0.0062	0.017	0.029
PpClS/PPO	0.0689	0.0048	0.017	0.029

TABLE 16

PVC/PCL SAMPLE SPECIFICATIONS--ZIMM ANALYSIS

$g \times 10^2$ PCL/cm^3 blend	COUNTING TIME (sec)	MONITOR COUNTS	THICKNESS (mm)	ATTENUATION FACTOR
PVC	16100	245819	0.226	0.616
0.75	10100	181420	0.122	0.643
1.039	19560	255924	0.139	0.650
1.209	10000	193843	0.096	0.731
1.239	10000	68558	0.302	0.496
2.60	13700	205887	0.276	0.635
3.85	10000	86548	0.175	0.621
6.16	10000	16240	0.127	0.636

TABLE 17

PpIS/PS SAMPLE SPECIFICATIONS--ZIMM ANALYSIS

WEIGHT PERCENT PpIS	COUNTING TIME (sec)	MONITOR COUNTS	THICKNESS (mm)	ATTENUATION FACTOR
PS	20735	317636	1.143	0.775
0.301	13500	287326	1.002	0.759
0.558	8500	177606	1.073	0.746
0.807	12000	258264	1.126	0.759
1.407	8300	177703	1.549	0.643
1.588	8000	168176	1.080	0.693
1.911	5000	115564	1.120	0.687

TABLE 18

PpClS/PS SAMPLE SPECIFICATIONS--ZIMM SAXS

WEIGHT PERCENT PpClS	COUNTING TIME (sec)	MONITOR COUNTS	THICKNESS (0.001 in)	ATTENUATION FACTOR
0.508	4000	82623	45.5	0.78
0.76	5000	143108	45.5	0.75
1.25	7600	143108	51.5	0.78
1.66	5100	104856	40.5	0.78

TABLE 19

PpClS/PPO SAMPLE SPECIFICATIONS--ZIMM SAXS

WEIGHT PERCENT PpClS	COUNTING TIME (sec)	MONITOR COUNTS	THICKNESS (mm)	ATTENUATION FACTOR
0.53	6000	111050	1.05	0.75
1.13	5600	109126	1.22	0.74
1.50	6000	125545	1.13	0.71
4.48	5500	172272	1.09	0.72

TABLE 20

PoClS/PPO SAMPLE SPECIFICATIONS--ZIMM SAXS

WEIGHT PERCENT PCL	COUNTING TIME (sec)	MONITOR COUNTS	THICKNESS	ATTENUATION FACTOR
0.54	5000	85507	1.04	0.707
0.84	5000	88585.	1.25	0.707
1.11	5000	103042	1.17	0.711
1.47	5280	110631	1.16	0.719
1.72	6300	118152	1.04	0.718
PPO	5100	102756	1.41	0.676

TABLE 21

PoClS/PS SAMPLE SPECIFICATIONS--ZIMM SAXS

WEIGHT PERCENT PCL	COUNTING TIME (sec)	MONITOR COUNTS	THICKNESS (mm)	ATTENUATION FACTOR
0.509	6100	127667	1.04	0.788
0.796	7600	148888	1.05	0.784
1.066	7300	133423	1.03	0.796
1.29	6000	113551	1.09	0.779
1.65	4100	77376	1.04	0.776
3.19	6400	118707	1.05	0.759

dilute amount of PCL was placed in a PVC matrix to investigate the conformation of the PCL molecule. If the picture of a compatible mixture is correct for this system it should be reflected in the radius of gyration of the single molecule.

Since the concentrations involved in these studies are small the total amount of scattering will be low as well. Consequently, any scattering that arises from the matrix material must be examined in detail. The matrix in this system is polyvinylchloride and the origins of scattering in this homopolymer are ill-defined to say the least. Previous discussions have dealt with order in amorphous materials and PVC can have the additional problem of a possible microcrystallinity. Numerous studies have been conducted on this material and still the conclusions drawn vary from laboratory to laboratory. Nearly all the scattering studies conducted on PVC have been performed on non-purified materials. Therefore, the PVC used in this study was purified in the described manner.

The smeared scattering profile obtained with the 1DPSD on a Kratky small angle x-ray apparatus is shown in Figure 55. The scattering monotonically decreases and to a constant value in the vicinity of 2-4 milliradians. No evidence was found for a shoulder or a discrete scattering maximum as was found by Khambatta (193) and Wenig (220). Using an infinite height assumption the desmearing procedure of Schmidt (170,171) was employed to reduce the data to that from a pinhole geometry. The data was placed on an absolute scale and compared to the data published by Straff and Uhlmann (91). This is shown in Figure 56. As can be seen the scattering for PVC obtained in this study is

in good agreement with their data although it lies slightly below their scattering curve. This can be expected due to the purification of the material in this study.

Straff and Uhlmann have described the origin of this scattering in terms of impurities in the PVC of a range of sizes and concentrations. The data obtained in this experiment can be described in a similar fashion by varying the concentrations of the impurities. Attempts to describe this scattering in terms of a superstructure were not successful. In addition to this wide angle x-ray diffraction did not display a measurable amount of crystallinity. Therefore, the picture drawn by Straff and Uhlmann (91) seemed to best describe the PVC in this study and their interpretation was used.

With the addition of PCL to this system the scattering profiles in Figure 57 were seen after normalizing the intensities by equations (141). As mentioned previously this scattering was assumed to be due solely to the PCL in the PVC matrix and was not affected by any possible structure in the PVC. In view of the results this conclusion seems to be borne out. The excess scattering was obtained by subtracting the scattering due to the PVC from the blend scattering. This excess scattering was analyzed with a Guinier analysis and is shown in Figure 58. According to Guinier (112), the slope of the plot at ($2\theta = 0$) is related to the Z-average radius of gyration according to equation (21). These values are listed in Table 22 for the various concentrations investigated.

Using an infinite height assumption the data was desmeared by the procedure of Schmidt (170,171). Again the intensities were sub-

TABLE 22

PCL/PVC DILUTE SAXS RESULTS

CONCENTRATION PCL ($g/cc \times 10^2$)	SMEARED RESULTS	DESMEARED RESULTS		
	$\langle R_g^2 \rangle_Z^{1/2}$ (nm)	$\langle R_g^2 \rangle_Z^{1/2}$ (nm)	$\langle R_g^2 \rangle_W^{1/2}$ (nm)	$KC/I(0) \times 10^5$ g^{-1}
1.055	12.6	15.1	10.1	0.77
1.462	12.9	15.2	10.2	4.231
1.700	13.5	15.4	10.3	1.713
1.742	13.1	15.4	10.3	1.713
6.16	12.9	15.4	10.3	2.343

$\langle R_g^2 \rangle_W / \langle R_g^2 \rangle_Z = 0.674$ $\quad [KC/I(0)]_{C=0} = 1.987 \times 10^{-4}$ g^{-1}

$(\langle R_g^2 \rangle_W^{1/2})_{C=0} = 10.3 \pm 2$ nm $\quad \langle R_g^2 \rangle_\theta^{1/2} = 6.6$ nm $\quad \bar{M}_W \simeq 50 \pm 15 \times 10^3$ g

$2A_2 = 0.43 \times 10^{-5}$ $cm^3 mole\ g^{-2}$ $\quad \chi_1 = 0.36 \pm 0.15$

jected to a Guinier analysis, shown in Figure 59, with the Z-average radius of gyration determined being given in Table 22. These were corrected by the method of Altgelt and Schultz (115) with the factor used to correct the radius of gyration being listed in Table 2 as $(M_W/M_N)/[2(M_W/M_N) - 1]$ (called F_M henceforth). The two types of radii are related by

$$\langle \overline{R_g^2} \rangle_W^{1/2} = (F_M)^{1/2} \langle \overline{R_g^2} \rangle_Z \qquad (147)$$

Koleske and Lundberg (228) have published the unperturbed dimensions of PCL (shown in Figure 60) and indicate that for a PCL molecule with a molecular weight of 45,000, $\langle \overline{R_g^2} \rangle_\theta^{1/2} = 6.6$ nm. It is quite evident that in the samples investigated the PCL is expanded by nearly 50% when the zero concentration value of 10.3 nm is compared to the unperturbed value. This is consistent with the fact that the PCL molecules are compatible with the PVC molecules.

One point that is disturbing is that Luzatti (229) has demonstrated that in an infinite height system the radius of gyration determined from the smeared and desmeared Guinier plots should be the same. This is illustrated by placing pinhole intensities obeying Guinier's Law into the smearing integral where the smeared intensity, J(h), is given by

$$J(h) = C \int_0^\infty \exp(-h^2R^2/3)\exp(-v^2R^2/3)dv \qquad (148)$$

$$= K \exp(-h^2R^2/3) \qquad (149)$$

Consequently, Guinier's Law should describe both types of data. However, deviations of approximately 16% were found in this study and are most likely a result of the deviations from Guinier's Law seen in the desmeared data. Since this law is a limiting law with more accurate values of $\overline{\langle R_g^2 \rangle}$ being obtained at smaller angles, the desmeared radius of gyration was used to compare to solution values. It should also be noted that the molecular wieght distribution was far from ideally monodisperse and $M_W/M_n = 1.94$. This will not necessarily affect the Guinier analysis but it necessitated a large correction factor to get $\overline{\langle R_g^2 \rangle}_W$. Nevertheless, even with these problems the data clearly indicate that the PCL is expanded.

The intercept of the Guinier plot at C = 0 has been shown to be relatable to the molecular weight at C = 0. After placing the data on an absolute level by equation (123) the data was analyzed by plotting KC/R(0) vs. concentration where the variables have been previously defined in equation (10). The advantage of doing this is that the slope of this line is twice the second virial coefficient. This analysis is shown in Figure 61 where the zero intercept was found to be 1.9×10^{-4} mole g^{-1} with a slope of $+0.44 \times 10^{-5}$ $cm^3 g^{-2}$ mole. This translates to a molecular weight of 50,000 ± 12,500 g/mole which is within 10% of the solution determined value. The interaction parameter, χ_1, was found to be 0.36 ± 0.15.

As can be seen from Figure 61 the precision of the individual intercepts is low with a best value of ±30% being obtained. Similarly, the value of the interaction can only be quoted to within 40% due to the spread in the values of the intercepts. These errors are rather

large and are due to the fact that R(0) is an extrapolated value. The errors in the individual scattering profiles are magnified during this extrapolation.

However, a reasonable value of the molecular weight was obtained indicating that the PCL molecules are molecularly dispersed in the PVC matrix. The value of the second virial coefficient is at best only slightly positive. As mentioned previously, a value of χ_1 can be assigned to a given system by scattering techniques but the analysis is severely limited in the investigation of bulk blends. Therefore, despite the slightly positive value of A_2 no conclusions can or should be made concerning the interaction parameter. Indeed unlike polymers in low molecular weight solvents, in polymer-polymer systems the radius of gyration, however insensitive it may be, is the more important parameter.

A question that requires an answer at this point is why a Zimm analysis was not employed in this study. Figure 62 displays an attempt at performing such an analysis where KC/R(0) is plotted as a function of $(2\theta)^2$. As can be seen a significant amount of curvature is seen in this plot. This curvature was unexpected and a satisfactory explanation of this behavior was not found. Normally curvature due to polydispersity causes a deviation in a direction opposite to that seen as discussed by Benoit and coworkers (68,69). The reason similar deviations were not seen in the Guinier analyses must rest in the different types of approximations made. Also, the use of a log scale will tend to deemphasize the errors present in the data.

B. PpIS/PS. The system of PpIS/PS was investigated strictly as a control system. The materials are known to be incompatible (74) and the presence of iodine will give rise to high amounts of scattering. This system was used simply to act as a check on the analysis to confirm the validity of the technique employed.

The scattering from the pure polystyrene homopolymer, i.e., the matrix material, is shown smeared in Figure 63. Desmearing produced the curve shown in Figure 64. As with the scattering from PVC, the PS scattering decreases monotonically with no indication of a superstructure or any other order in the system. These scattering profiles can be described in terms of a distribution of impurities of various concentrations similar to the PVC scattering. This agrees with the SAXS results of Renninger and Uhlmann (93) where similar conclusions were made. Transmission electron microscopy results of Thomas (230) indicate a similar lack of order in this amorphous polymer.

Upon addition of PpIS to the PS the scattering increased substantially with the normalized profiles of the various runs being shown in Figure 65. The excess scattering in these samples were treated in a Guinier fashion which is shown in Figure 66. The Z-average radii of gyration are listed in Table 23. The desmeared Guinier plots are shown in Figure 67 with both the Z-average and W-average radii of gyration being given in Table 23 (where $F_M = 0.945$).

Several features of these data are striking. The radius of gyration is shown in Figure 68 plotted as a function of composition. It is seen to increase as the concentration of PpIS increases. In addition to this the value of $(\langle \overline{R_g^2} \rangle_W^{1/2})_{C=0}$ is 31.5 nm which is larger than

TABLE 23

PpIS/PS DILUTE SAXS RESULTS

CONCENTRATION PpIS ($g/cc \times 10^2$)	SMEARED RESULTS	DESMEARED RESULTS		
	$\langle R_g^2 \rangle_Z^{1/2}$ (nm)	$\langle R_g^2 \rangle_Z^{1/2}$ (nm)	$\langle R_g^2 \rangle_W^{1/2}$ (nm)	$KC/R(0) \times 10^6$ g^{-1}
0.617	26.7	35.3	33.4	2.29
0.842	32.0	39.8	37.6	1.21
1.481	38.2	42.3	39.9	0.50
1.672	37.2	40.6	38.4	1.07
2.014	37.3	48.7	46.0	0.253

$\langle R_g^2 \rangle_W^{1/2} / \langle R_g^2 \rangle_Z^{1/2} = 0.945$ $\quad (\langle R_g^2 \rangle_W^{1/2})_{C=0} = 31.5 \pm 5$ nm

$[KC/R(0)]_{C=0} = 2.61 \times 10^{-6}$ mole/g $\quad \bar{M}_W \simeq 40 \pm 11 \times 10^4$ g/mole

$\langle R_g^2 \rangle^{1/2} = 24.0$ nm $\quad 2A_2 = -1.16 \times 10^{-4}$ $cm^3 mole/g^2$ $\quad \chi_1 = +8.6$

the value given by Brady et al. (206) of 24.0 nm for PpIS in a good solvent. Sense cannot be made of these results until the ($2\theta = 0$) intercepts are examined as a function of concentration. After placing the data on an absolute scale KC/R(0) was plotted against concentration and is shown in Figure 69. As can be seen the points decrease rapidly as the concentration increases indicating an incompatible system where the apparent molecular weight of the PpIS domains increases when the PpIS is added. If a line is drawn through the points a large negative value of $2A_2 = -1.16 \times 10^{-4}$ $cm^3 g^{-2}$ mole is obtained. This in turn translates into a ridiculously high interaction parameter of $\chi_1 = 8.96$. Therefore, what appears to be happening in this system is that as PpIS is added to the PS the PpIS phase separates or clusters causing an increase in the radius of gyration, as well as an increase in the molecular weight. Upon extrapolation to zero concentration using a linear least squares analysis a value of $M_W = 413{,}000$ and $R_g = 31.6$ nm in comparison to solution values of 373,000 and 24.9 nm, respectively, were obtained.

However, due to the large value of the radius of gyration the limitations placed on the Guinier type of analysis ($h < 1/R$) are quite severe and almost make this system inaccessible to experimental investigation. Because of this the errors involved (although quoted to only ±30%) can be very high and, consequently, may jeopardize the reliability of the data. This is also reflected in the differences between the smeared and desmeared values of the radius of gyration.

These analyses indicate that the materials are incompatible. Therefore, a more reasonable approach to this system would be the use

of the Debye-Bueche (125) correlation function analysis. This is shown in Figure 70 where $[I(h)]^{-1/2}$ is plotted as a function of h^2 in accordance with equation (71). Excellent straight line behaviors were seen for all compositions investigated and the correlation distances determined are shown in Table 24. According to equation (73) the chord lengths of the PpIS are obtained by dividing the correlation distance by the volume fraction of the PS. This was done and the results are presented in Table 24 and are plotted in Figure 71 as a function of composition.

The results agree with the conclusions drawn from the Guinier analyses in that the chord lengths of the PpIS increase rapidly as a function of composition indicating that the domains of PpIS are increasing in size as additional PpIS is added. This indicates that the materials are incompatible. It is important to realize that even in compatible cases an increase in the chord length is expected but it would not be the factor of two observed in this case. Assuming a random placement of the chains in the matrix a compatible system would yield a much less pronounced increase in the chord length.

C. PoClS/PPO and PpClS/PPO. In the two systems listed above polyphenylenoxide (PPO) is the matrix polymer. As indicated previously, the as received PPO contains some crystallinity which is removed by a purification. The scattering from the purified PPO is shown in Figure 72. As in the PVC and PS cases the scattering of the PPO decreases sharply with a gradual leveling at 10-12 milliradians with no indication of interferences arising from an ordered structure in the material.

TABLE 24

DEBYE-BUECHE ANALYSIS: PpIS/PS

WEIGHT % PpIS	CORRELATION DISTANCE (nm)	CHORD LENGTH (nm)
0.588	9.75	9.81
0.801	13.2	13.3
1.407	20.9	21.2
1.588	25.8	26.2
1.911	21.6	22.0

Again the intensity can be ascribed to impurities present in the PPO. However, in PPO degradation of the material had definitely occurred to some extent as was evidenced by a significant browning in the material after melt pressing. Degradation was even seen in the purified material before pressing since the material possessed a yellowish color. The contribution of this decomposition to the scattering from PPO is unknown.

The scattering profiles of the PoClS and PpClS blends with PS are shown in Figures 73 and 74, respectively. In both systems at concentrations ≤ 0.014 g/cm^3 no scattering in excess of the solvent scattering is observed. Excess scattering is observed in systems of higher concentration but it cannot be reduced readily by any of the previously indicated analyses. Upon closer examination of the scattering profiles the intensity abruptly increases near $2\theta = 1.1$ milliradians and quite possibly could be indicating that the focal spot was wandering during these runs. The reproducibility of these runs is unknown since time did not permit a rerun of these specimens. Consequently, results cannot be reported with any confidence.

If Guinier analyses are performed on the PpClS/PPO mixtures, Z-average radii of gyration of 18.7 nm and 24.0 nm are found for the 0.015 and 0.045 g/cm^3 mixtures, respectively. This increase in $\langle R_g^2 \rangle_Z^{1/2}$ tends to indicate compatibility but the reliability of these results is questionable.

D. PoClS/PS. The scattering profiles of PS and various blends of PoClS with PS are shown in Figure 75. As can be seen, all the data

superimpose on one scattering curve. Consequently, there was no excess scattering observable in this system at the concentration levels investigated. This system will be treated further in the neutron scattering section.

E. PpClS/PS. In lieu of the lack of results in the PoClS/PS system the PpClS/PS system surprisingly yielded some excess scattering power. The normalized profiles are shown in Figure 76. As can be seen, the intensity difference is quite small but it is definitely present. The excess intensity was desmeared and treated with a Guinier analysis as shown in Figure 77. The slopes of these plots listed in Table 25 at h = 0 were found to remain constant as a function of concentration of the PpClS as shown in Figure 78. These values extrapolated to an $(\langle R_g^2 \rangle_Z^{1/2})_{C=0}$ of 42.2 nm which reduced to 28 nm when $F_M = 0.662$. This value is nearly 1.5 times the value of the unperturbed dimension of 20 nm as given by Kawahara (231), Mohita (232, and Noguchi (233).

The zero intercepts in the Guinier plots were placed on an absolute level and were plotted in Figure 79 as KC/R(0) vs. concentration. The slope of this line was quite positive, $+5.4 \times 10^{-3}$ with a zero intercept of 9.31×10^{-6} mole/g. The molecular weight was found to be 107,000 in reasonable agreement with the value of 130,000 determined by solution methods and the interaction parameter, χ_1, from the second virial coefficient was -0.31.

On face value these results indicate that PpClS is compatible with PS. However, this is in direct disagreement with the results obtained by dynamic mechanical methods. There are two possible reasons

TABLE 25

DILUTE SAXS RESULTS FOR PpClS/PS

CONCENTRATION PpClS (g/cc x 10^2)	DESMEARED RESULTS		
	$\langle R_g^2 \rangle_Z^{1/2}$ (nm)	$\langle R_g^2 \rangle_W^{1/2}$ (nm)	KC/R(0) mole g^{-1} x 10^5
0.533	42.5	28.0	3.4
0.835	42.1	27.8	5.33
1.296	42.5	28.0	9.35

$\langle R_g^2 \rangle_W^{1/2} / \langle R_g^2 \rangle_Z^{1/2} = 0.662$ $\quad (\langle R_g^2 \rangle_W)_{C=0} = 28$ nm

$[KC/R(0)]_{C=0} = 9.31 \times 10^6$ $\quad \bar{M}_W = 107{,}000$

$\langle R_g^2 \rangle_W^{1/2} = 20$ nm (good solvent) $\quad 2A_2 = 5.4 \times 10^{-3}$ $\quad \chi_1 = -0.31$

for this discrepancy. The first is that the concentrations are so low that the PpClS has been compatibilized. This can be seen if the phase diagram in Figure 1 is considered. If for a given temperature the concentration is varied the system could be incompatible or phase separated over most of the composition range (where dynamic mechanical experiments are performed) but at low concentrations the binodal is passed through and the material is a compatible mixture at the dilute concentrations. If this is the case, then scattering should have been observed for the PoClS/PS system since the contrast factor is the same in both cases. A second possible reason for this scattering is that the system has phase separated and the particles are just too large to be visible by this technique. Consequently, only the tail of the intensity profile is being examined where the Zimm and Guinier analyses are not applicable. This could invalidate the results obtained by SAXS for this system. Light scattering and x-ray measurements are now being conducted to differentiate between these possibilities and to clarify this discrepancy.

3. Dilute Small Angle Neutron Scattering in the Bulk

SAXS investigations on PoClS in PS proved to be fruitless due to the insufficient contrast between the two polymers. However, use was made of neutron scattering to examine the conformation of a deuterated polystyrene (d-PS) in a protonated poly(orthochlorostyrene). Contrast in this system is obtained by using deuterium as a label on the polystyrene chain.

Before experimental results on this system are treated a brief

discussion of the calculation of neutron contrast factors will be given. Referring to equation (29) the magnitude of the contrast factor is governed by the quantity (called Δ here)

$$\Delta = 4\pi \left| B_P - B_S \frac{V_P}{V_S} \right|^2 \qquad (150)$$

where B_i is the scattering length of component i and V_i is the specific volume of component i. The factor of 4π results by projecting a sphere onto a plane. This can be written in terms of the scattering lengths of the individual atoms in the monomer units by

$$\Delta = 4\pi \left| \Sigma a_{i1} - \frac{\rho_2}{\rho_1} \Sigma ai_2 \right|^2 \qquad (151)$$

where a_{i1} is the scattering length of atom i in monomer unit 1. The values of the atomic scattering lengths can be found for example in Bacon (218). Values for scattering lengths typically used in polymeric systems are given in Table 26. Considering the system investigated in this study, i.e., d-PS (ρ_1 = 1.0 g/cm^3) dilute in PoClS (ρ_2 = 1.245), the differential scattering cross section is given by

$$\Delta = 4\pi \left[8(a_C) + 8(a_D) - \left(\frac{1.245}{1.0}\right)(8(a_C) + 7(a_H) + a_{Cl}) \right]^2 \qquad (152)$$

Using the values in Table 26 for a_i gives a value of Δ = 447.3 x 10^{24} cm^2 = 447.3 barns. Similar calculations were performed on the different combinations of PS in PoClS where either component is labeled. These calculations are shown in Table 27. For comparison's sake the

TABLE 26

ATOMIC SCATTERING CROSS SECTIONS

ELEMENT	a_{coh} (x 10^{12} cm)	σ_{total} (barns)	σ_{coh} (barns)
H	-0.378	81.5	1.79
D	+0.650	7.6	5.40
C	+0.661	4.9	4.50
O	+0.58	4.24	4.20
Cl	+0.89	15.0	12.2

COHERENT SCATTERING LENGTHS
FOR SOME SIMPLE COMPOUNDS

Compound	a_{coh} (x 10^{12} cm)
C_8C_8	2.264
C_8H_8	10.48
C_8H_7Cl	3.25
C_2H_3Cl	1.178
$C_6H_{10}O_2$	1.346

$$\sigma_{coh} = 4\pi(a_{coh})^2$$

$$\sigma_{total} = \sigma_{coh} + \sigma_{inc}$$

TABLE 27

DIFFERENTIAL SCATTERING CROSS SECTIONS FOR
VARIOUS PS/PoClS COMBINATIONS

SYSTEM	DILUTE COMPONENT	$a_1 = \Sigma a_{i1}$ ($\times 10^{12}$ cm)	$a_2 = \Sigma a_{i2}$ ($\times 10^{12}$ cm)	ρ_2/ρ_1	σ_{coh} (barns) $4\pi(\rho_2/\rho_1)^2$
PS/PoClS	PS	2.264	3.632	1.188	52.85
	PoClS	3.632	2.264	0.842	37.42
d-PS/PoClS	d-PS	10.488	10.828	1.188	70.92
	PoClS	10.828	10.488	0.842	50.12
PS/d-PoClS	PS	2.264	10.828	1.188	1411.9
	d-PoClS	10.828	2.264	0.842	1000.2
d-PS/PoClS	d-PS*	10.488	3.632	1.188	478.9
	PoClS	3.632	10.488	0.842	339.6
d-PS/PS	d-PS	10.488	2.264	1.00	849.9
	PS	2.264	10.488	1.00	849.9

*Indicates system used.

value of Δ for the well studied d-PS in protonated PS is 849.9 barns. Table 27 demonstrates that although the d-PS in PoClS does not provide the maximum contrast it is still of a comparable value. The choice of this system was mandated due to sample availability.

Samples of d-PS dilute in PoClS were prepared as described in the preparation section. Scattering experiments were conducted at the Oak Ridge National Laboratory (ORNL) reactor with the assistance of Dr. H.R. Child. Schematics of the apparatus are shown in Figures 11 and 80. Neutrons with an average wavelength of 0.4 nm were used in this study.

Sample specifications determined at the ORNL facility are given in Table 28. These values were used for normalizing the scattering profiles and placing them on an absolute level. The SANS scattering curves for a series of these blends are shown in Figure 81 where the intensity is plotted against κ ($\kappa = h = 4\pi/\lambda(\sin\varepsilon/2)$, $\varepsilon = 2\theta$). According to equation (25) the scattering from the PoClS matrix was subtracted from the blend to obtain the excess scattering. Letting $S_o(h)$ in equation (26) be given by

$$S_o(h) = \exp(-h^2R^2/3) \qquad (153)$$

the log of the excess intensity was plotted as a function of h^2 in Figures 82, 83, 84, and 85 with the limiting slope defining the Z-average radius of gyration. These values are tabulated in Table 29 along with the weight average values determined by the method of Altgelt and Schultz (115) where $F_M = 0.916$. Light scattering values of this d-PS were determined by Picot (207) with the unperturbed radius of gyration

TABLE 28

SAMPLE CHARACTERISTICS FOR SANS

CONCENTRATION PSD ($g/cm^3 \times 10^2$)	THICKNESS (mm)	TRANSMISSION FACTOR	NORMALIZATION CONSTANT
0.482	0.76	0.682	9.5303
1.235	0.82	0.76	11.4419
1.492	1.28	0.570	13.3955
2.322	0.815	0.70	10.4744
3.749	0.79	0.709	10.2836
4.399	0.66	0.788	9.5487
3.226	0.94	0.70	10.7957
5.872	0.82	0.784	17.5610
PoClS	0.82	0.69	10.3881

TABLE 29

NEUTRON SCATTERING RESULTS

CONCENTRATION PSD ($g/cm^3 \times 10^2$)	$\langle R_g^2 \rangle_Z^{1/2}$ (nm)	$\langle R_g^2 \rangle_W^{1/2}$ (nm)	KC/R(0) (g^{-1}mole $\times 10^5$)
1.492	14.2	13.0	1.096
2.322	14.4	13.2	1.188
3.226	14.1	12.9	0.968
3.749	13.8	12.6	0.820
4.399	13.9	12.7	1.031
5.872	13.0	11.9	1.405

$\langle R_g^2 \rangle_W^{1/2} / \langle R_g^2 \rangle_Z^{1/2} = 0.916$ $\quad\quad$ $\langle R_g^2 \rangle_{W,}^{1/2} = 9.0$ nm

$[\langle R_g^2 \rangle_W^{1/2}]_{C=0} = 12.6$ nm $\quad\quad$ D11 Result: $\langle R_g^2 \rangle_W^{1/2} = 11.5$

$A_2 \simeq 0$ $\quad\quad$ $\chi_1 = 0.5$ $\quad\quad$ $\bar{M}_W = 115{,}000$

$[KC/R(0)]_{C=0} = 8.63 \times 10^{-6}$

being 9.0 nm and the value of R_g in a good solvent was 13.2 nm. The results in Table 29 were plotted as a function of concentration in Figure 86 to yield $(\langle R_g^2 \rangle^{1/2})_{C=0}$. R_g was found to be independent of concentration within experimental errors. Therefore, $(\langle R_g^2 \rangle^{1/2})_{C=0}$ = 12.6 nm indicating that the d-PS was expanded in the PoClS matrix. Experiments were performed on the D-11 facility in Grenoble by Dr. J.S. Higgins on a specimen from this series. The results shown in Figures 87 and 88 yield an R_g = 11.5 nm and confirm the work conducted at the ORNL facility. These experiments were performed at room temperature but since the T_g of PoClS is near 120°C the conformations of the d-PS should have been frozen in at this temperature. Therefore, the results reflect the R_g at this temperature rather than the room temperature value.

Separate experiments were conducted on the 2.322 and 4.399×10^{-2} g PS/cm^3 samples as a function of temperature. No differences in R_g were found. This is most likely a result of the low d-PS concentrations used. If the phase diagram of Figure 1 is consulted it is seen that the binodal rises steeply in these regions and the system will remain compatible at the elevated temperatures. Consequently, the change in R_g could be small.

Attempts were made to place the data in Figure 81 on an absolute level using a vanadium standard. The incoherent scattering cross section of vanadium is well known and can normally be used to calibrate scattering experiments. However, being incoherent scattering the scattered intensity should be angularly independent. This was not found to be the case as shown in Figure 89. Consequently, absolute levels of scattering were not obtainable (see Note, next page).

However, the intercepts of the Guinier plots at (h = 0) were plotted in Figure 90 on a relative basis. The intercept at C = 0 was normalized to yield the correct molecular weight of the d-PS molecule. The normalized KC/R(0) values are given in Table 28. This provided a means of obtaining the second virial coefficient, A_2, on a "quasi" absolute scale. Fortunately, $A_2 = 0$ to within experimental errors and counterbalanced the problem of calibration.

Again the result of an expanded chain coupled with a zero second virial coefficient was obtained similar to the SAXS results on the PVC/PCL system. This emphasizes the points made earlier concerning the value of A_2 in relation to $1/M_W$.

In conclusion it is felt that at the glass transition temperature of PoClS (~120°C), d-PS is compatible with PoClS in the concentration region investigated. No conclusions can be drawn from A_2 concerning the value of χ_1, the Flory-Huggins interaction parameter, for this system. Due to the dilute conditions no change in $\langle R_g^2 \rangle^{1/2}$ was found as a function of temperature.

NOTE: The experiments at the D-11 facility were placed on an absolute level yielding an M_W = 124,000 in comparison to 113,000 from solution. This justifies the procedure used with the ORNL data.

CHAPTER V

CONCLUDING REMARKS

In the course of this study concentrated and dilute mixtures of polymers were investigated. An interesting point to be noted is that the concentrated studies on PVC/PCL blends revealed correlation distances less than the radius of gyration obtained from the dilute studies. These results are shown to be consistent in Figure 92 where a scattering curve for a Gaussian coil with an R_g = 4.5 nm was generated and the intensity was plotted in a Debye-Bueche fashion. The result yields a correlation distance of 2.3 nm. Similarly, with a scatterer obeying Guinier's Law (R_g = 4.5 nm) a correlation distance of 1.1 nm was found. This results from the fact that the Guinier and Debye analyses emphasize the initial part of the scattering profile (low h) whereas the Debye-Bueche analysis emphasizes the higher angular range. As can be seen in Figure 91 deviations from the Debye-Bueche plot similar to those in the PCL/PVC blends are also seen without the problems associated with background scattering. Consequently, it is felt that correlation distances smaller than the chain dimensions can be obtained and, therefore, the studies on the dilute and concentrated blends are in agreement.

C H A P T E R V I

SUGGESTIONS FOR FUTURE WORK

1. Small Angle Neutron Scattering

The SANS investigation of the PS/PoClS system should be expanded in two different manners. As is known the PS/PoClS system undergoes phase separation at elevated temperatures. This is difficult if not impossible to observe in the concentration range employed in this study. Consequently, the same type of analysis should be performed as in this work but only using a matrix composed of a protonated PS/PoClS mixture. Therefore, the overall composition of PS, i.e., PS-H and d-PS, is concentrated but the d-PS is dilute. This permits the investigation of the conformation of the d-PS in the concentrated blend. By varying the concentration of d-PS but retaining the total PS composition the same, Zimm analyses can be conducted for any desired composition permitting the necessary extrapolation to zero composition to obtain $(R_g)_{C=0}$, M_W and A_2. Each of these systems can be investigated as a function of temperature to investigate the conformation of the d-PS chain below and above the LCST.

It is important to realize that as the overall composition of PS increases the overall change in R_g will be diminished. This is due to the fact that d-PS is known to have θ dimensions in PS and if the concentration of PS is too high then θ or near θ conditions will be seen below and above the LCST. Therefore, initial investigations should

be performed on the high PoClS concentration side. These studies should be paralleled with SAXS and SALS experiments to characterize the overall morphological changes in the sample.

A second and equally important area is to examine the configurational changes occurring in the model. This utilizes the intermediate angular region of the scattering curve. Using Kratky plots the persistance length, related to chain flexibility, can be determined. In addition to this, the scattering profiles can be calculated from chain statistics to examine the detailed behavior of the polymer chain above and below the LCST.

2. Semicrystalline Blends

An interesting feature obtained in previous investigations of the PVC/PCL system was that the glass transition temperature varied according to the overall composition of the blend. This has been observed in several other systems as well.

This is rather surprising when the composition of the amorphous phase is not equal to the overall composition in semicrystalline materials. If the amorphous phase is a mixture then a T_g should be obtained that reflects a composition other than the total composition.

Although this may indeed be a minor point it is still unknown why this should occur. An in-depth study of the PVC/PCL or other such systems could yield some interesting information concerning either the phenomenon of the glass transition in polymer blends or the interpretation of mechanical spectra of semicrystalline polymer blends.

3. Concentrated Amorphous Blends

As a result of a discussion with Dr. I.C. Sanchez, the possible use of scattering in concentrated amorphous blends was proposed for determining the interaction parameter, χ. The absolute scattering at zero angle, R(0), is related to the osmotic pressure, π, and the chemical potential, $\Delta\mu_1$, by

$$KC/R(0) = (1/RT)(\partial\pi/\partial C_2) = (-1/RT)(\Delta\mu_1/C_2\bar{V}_1) \qquad (154)$$

where K is a contrast factor dependent upon the radiation used, C_2 is the concentration of polymer 2 (g/cm^3) and $\bar{V}_1$ is the partial molar volume of component 1.

In terms of Flory-Higgins lattice theory, $\Delta\mu_1$ can be determined in terms of the volume fractions of the components, ϕ, the degree of polymerization of the components, r (if one monomer unit occupies one lattice site), and the interaction parameter, χ. $\Delta\mu_1$ is given by

$$\Delta\mu_1 = -\frac{1}{RT}\left[\ln\phi_1 + (1 - r_1/r_2)\phi_2 + r_1\chi\phi_2^2\right] \qquad (155)$$

Therefore,

$$\frac{KC}{R(0)} = \frac{1}{C_2\bar{V}_1}\left[\ln\phi_1 + (1 - r_1/r_2)\phi_2 + r_1\chi\phi_2^2\right] \qquad (156)$$

Normally the approximations that $\bar{V}_1 = V_1^o$ and $\phi_2 = C_2/\rho_2$ are made for dilute solution scattering where V_1^o is the molar volume of component 1 and ρ_2 is the mass density of component 2. These approximations are not valid in concentrated systems.

Therefore, for a given concentration, R(0) and $\bar{V}_1$ will determine χ. An analytic expression for χ can be obtained if the scattering from the system can be described in terms of a particular interference function. For example, consider a system that can be described in terms of a Debye-Bueche correlation function, $\gamma(r)$, where the correlation function can be given in terms of an exponential as

$$\gamma(r) = \exp(-r/a) \tag{157}$$

The scattering for such a system is given by

$$R(h) = K_1 \overline{\eta^2}\, a^3/(1 + h^2a^2)^2 \tag{158}$$

and

$$R(0) = K_1 \overline{\eta^2}\, a^3$$

Substituting into equation (156) we get

$$\frac{KC}{K_1 \overline{\eta^2} a^3} = \frac{1}{C_2 \bar{V}_1} (\ln\phi_1 + (1 - r_1/r_2)\phi_2 + r_1\chi\phi_2^2) \tag{159}$$

Therefore, the intensity of scattering can be analytically described in terms of the interaction parameter. Similar types of equations can be obtained for other types of scatterers but it is important to emphasize the use of the scattering power at zero angle.

Consequently, using either equation (156) or (159) the interaction parameter can be determined. Once this is determined care must be exercised in its interpretation. For a polymer blend to be compatible,

$$\frac{\partial \Delta\mu_1}{\partial \phi_1} > 0 \qquad (160)$$

Using the Flory-Huggins expression for $\Delta\mu_1$, the interaction parameter is given by

$$r_1\chi = \chi_1 < \frac{1}{2\phi_1\phi_2} \qquad (161)$$

Consequently, χ_1 can be very large and positive for a compatible mixture. Also, it is seen to be concentration dependent with the variation being smaller at the intermediate compositions.

4. Interpretation of the Invariant

At present the interpretation of the SAXS invariant, Q, in concentrated solutions is given by

$$Q = \phi_1\phi_2(\rho_1 - \rho_2)$$

where ϕ_i is the volume fraction of phase i of electron density ρ_i. This requires the presence of two phases with infinitely sharp phase boundaries where the scattering profile can be corrected for diffuse phase boundaries as discussed previously. However, in a concentrated mixture of a compatible polymer the extent of inter-molecular penetration is high and, consequently, the idea of two separate phases is really not applicable. Therefore, it is felt that an interpretation of Q in terms of molecular parameters is necessary for application to compatible polymer blends. It has been shown that the invariant for dilute and semi-dilute solutions can be explained in terms of molecular parameters ( ).

Consequently, it is felt that extension of these ideas to concentrated solutions would be valuable for elucidating the molecular behavior in polymer blends.

5. Deformation Studies

Recently infrared dichroism was used to examine the deformation behavior of PVC/PCL blends (192). In this work it was concluded that PVC and PCL must be compatible because the orientation of both materials was equal. If the material was phase separated the authors stated that the orientation of the PVC would differ from that of the PCL.

However, this conclusion is not strictly correct since the orientation of a molecule will depend upon the statistical segment length in a polymer chain. If the statistical segment lengths of the chain are not equal then the orientation of the molecules will be different even in a compatible mixture. This can be visualized by considering a compatible mixture of a very stiff molecule with a very flexible one. Upon deformation the two will orient differently despite the fact that they are molecularly dispersed. This essentially invalidates the conclusions made concerning the equality of orientation necessitating compatibility.

The total birefringence, ΔT, is directly related to the number, N_i, of statistical segments of length ℓ_i by

$$\Delta T = \Sigma n_i \Delta_i \ell_i^2 / \Sigma n_i L_i^2 \qquad (162)$$

Consequently, birefringence and stress optical coefficient investigations of blends could yield some interesting results.

FIGURES

Figure 1. Illustration of a phase diagram for a binary mixture with the corresponding free energy curve at one particular temperature.

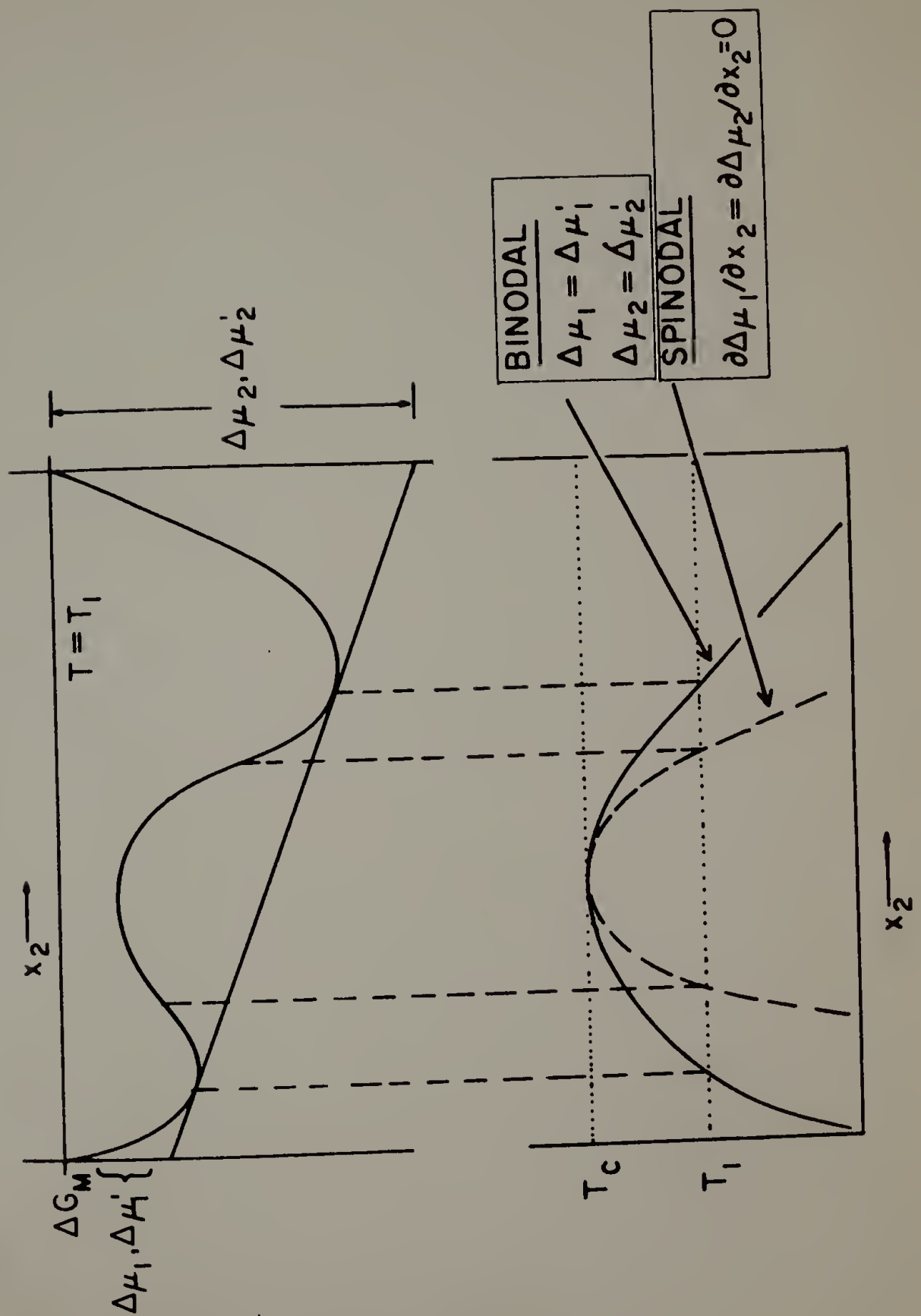
BINODAL
$\Delta\mu_1 = \Delta\mu_1'$
$\Delta\mu_2 = \Delta\mu_2'$
SPINODAL
$\partial\Delta\mu_1/\partial x_2 = \partial\Delta\mu_2/\partial x_2 = 0$
$\Delta\mu_2, \Delta\mu_2'$
$T = T_1$
x_2
ΔG_M
$\Delta\mu_1, \Delta\mu_1'$
T_c
T_1
x_2

Figure 2. Schematic diagram of phase separation processes.

MODES OF PHASE SEPARATION

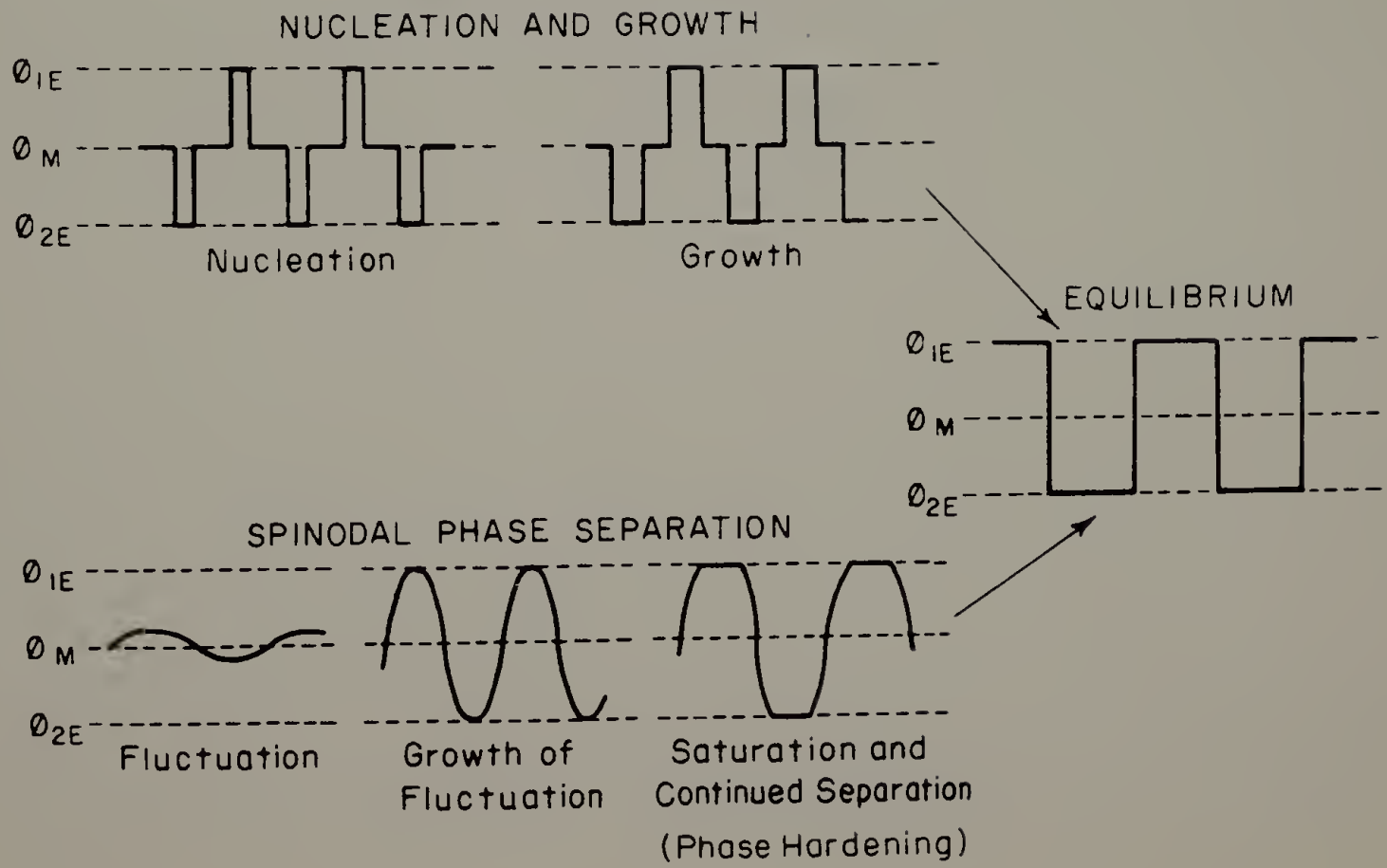

$\emptyset_M$ = Composition of mixture
$\emptyset_{iE}$ = Equilibrium composition of Phase i

Figure 3. Data illustrating possible deviations in scattering experiments at high concentrations.

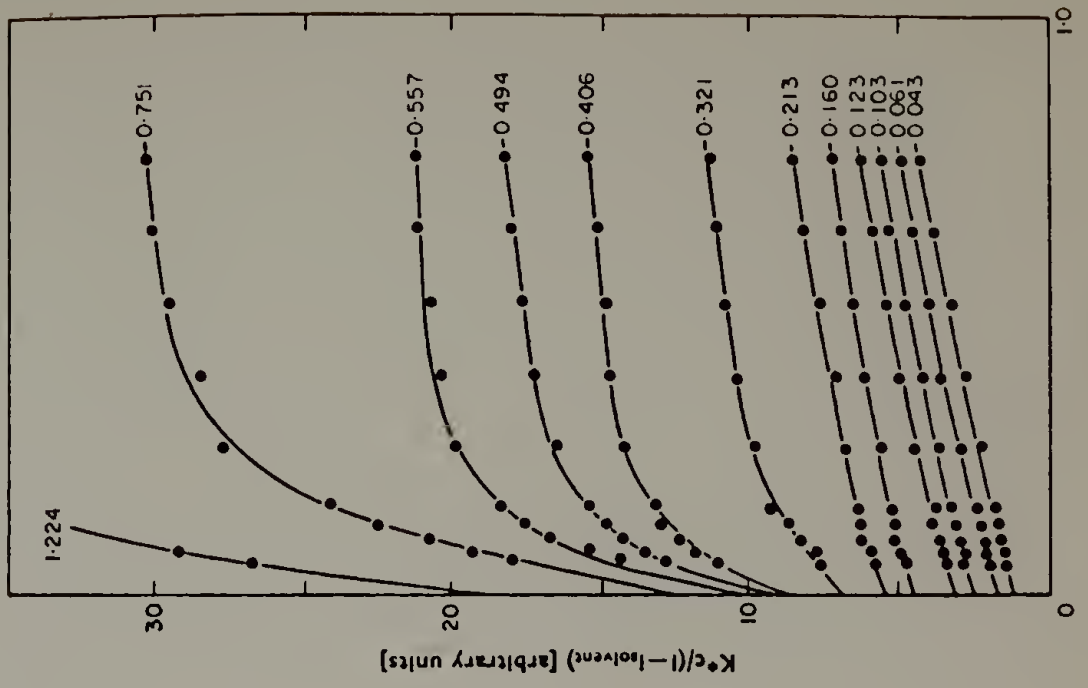
1·224
0·751
0·557
0·494
0·406
0·321
0·213
0·160
0·123
0·103
0·061
0·043
30
20
10
0
1·0
sin² (θ/2)
K*c/(I−I_solvent) [arbitrary units]

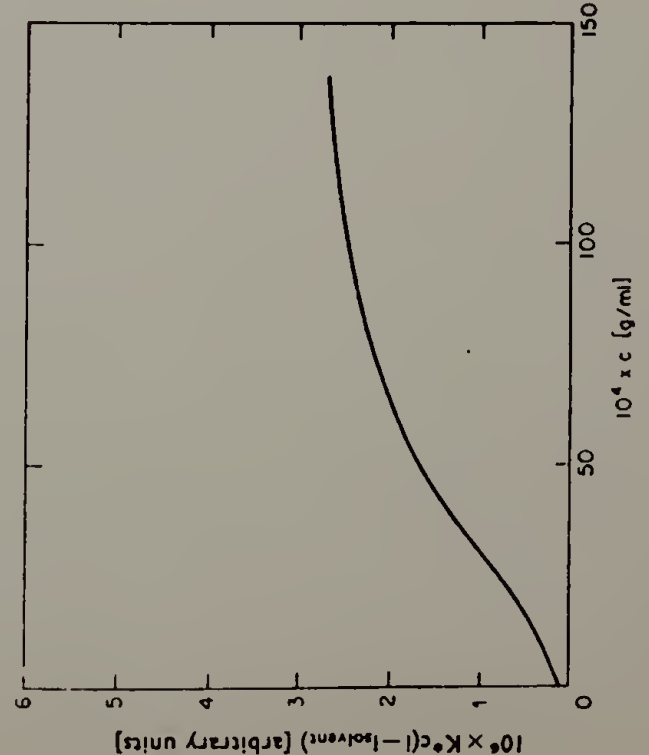
0
1
2
3
4
5
6
50
100
150
10⁴ x c [g/ml]
10⁶ × K*c(I−I_solvent) [arbitrary units]

Figure 4. Gel permeation chromatograms of various PCL samples demonstrating the effect of purification.

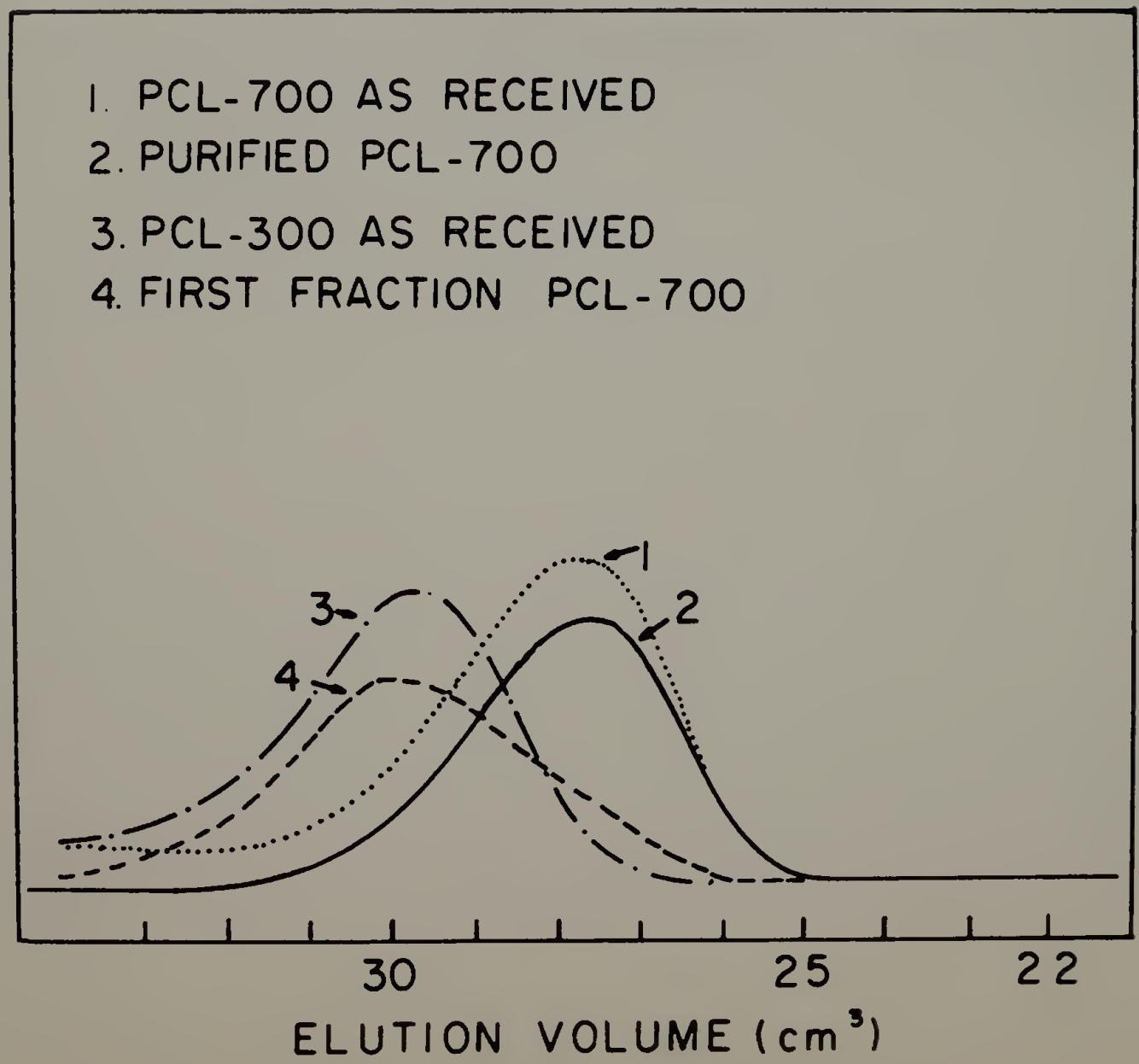
1. PCL-700 AS RECEIVED
2. PURIFIED PCL-700
3. PCL-300 AS RECEIVED
4. FIRST FRACTION PCL-700
1
2
3
4
30
25
22
ELUTION VOLUME (cm³)

Figure 5. Intrinsic viscosity data for the two PCL fractions and a PCL-300 sample.

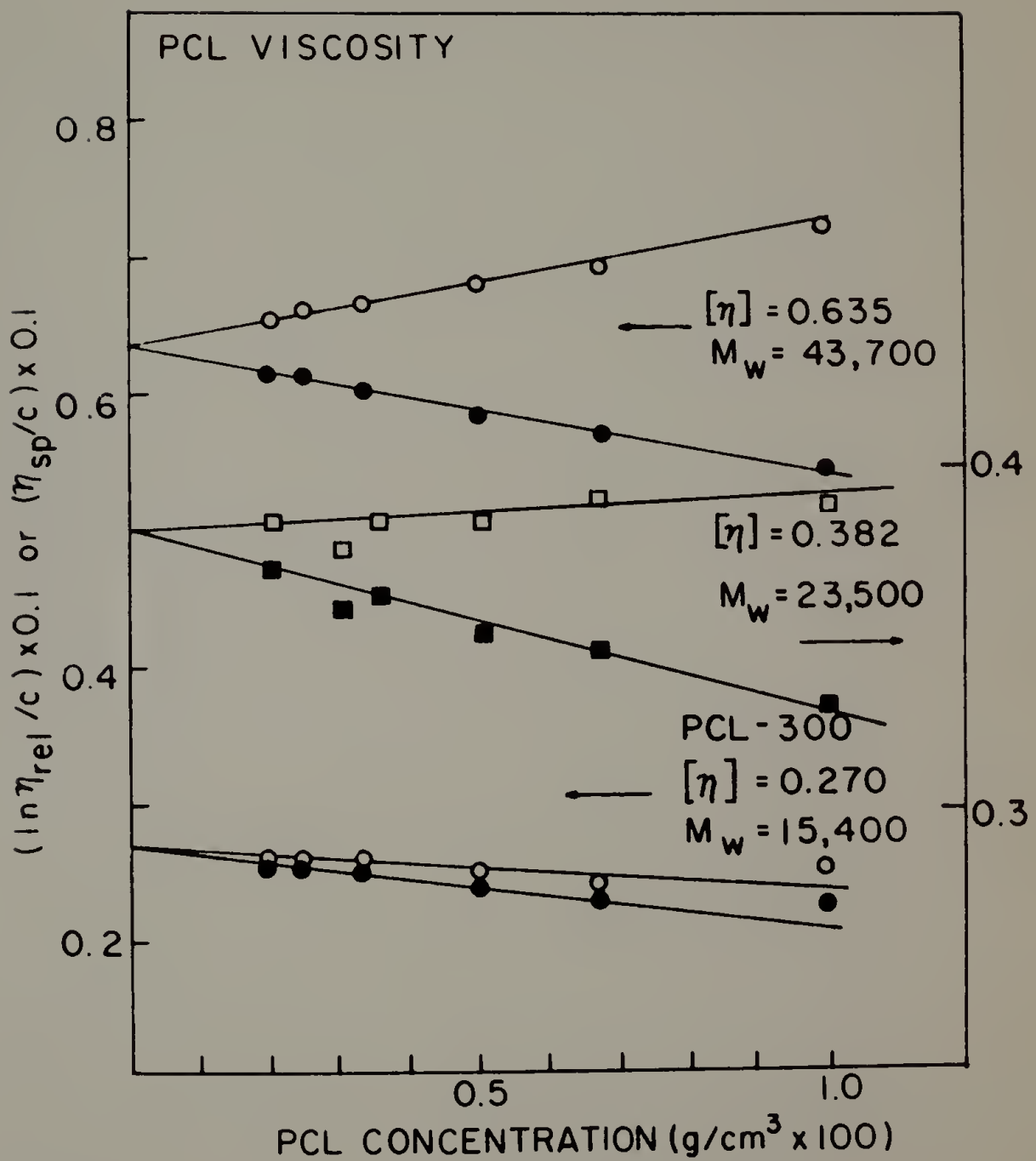
PCL VISCOSITY
0.8
0.6
0.4
0.2
0.4
0.3
$(\ln \eta_{rel}/c) \times 0.1$ or $(\eta_{sp}/c) \times 0.1$
$[\eta] = 0.635$
$M_w = 43,700$
$[\eta] = 0.382$
$M_w = 23,500$
PCL-300
$[\eta] = 0.270$
$M_w = 15,400$
0.5
1.0
PCL CONCENTRATION ($g/cm^3 \times 100$)

Figure 6. Gel permeation chromatograms of PVC as received and purified.

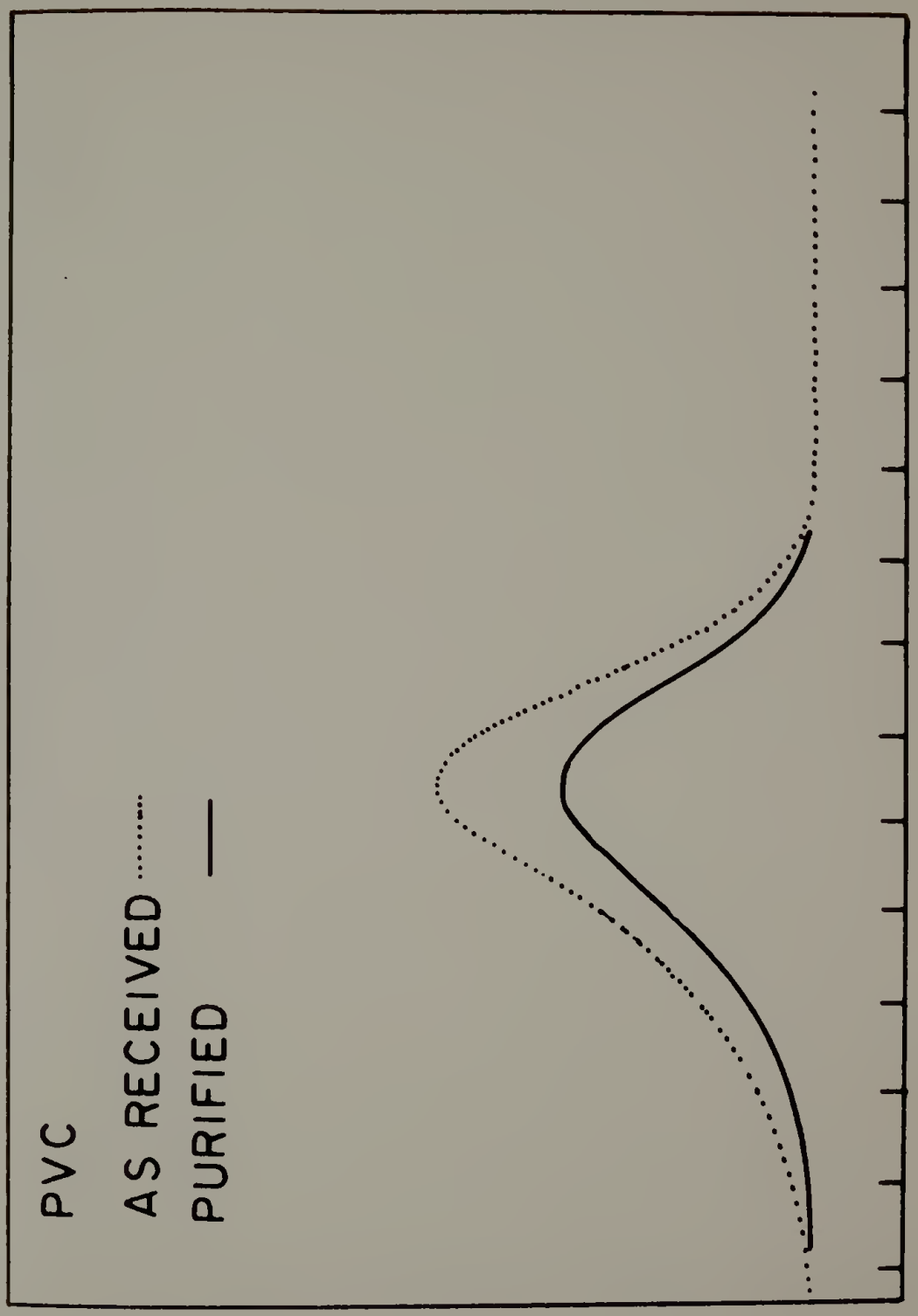
PVC
AS RECEIVED
PURIFIED
30
25
20
ELUTION VOLUME (ml.)

Figure 7. Infrared spectrum of PpIS and a-PS from 2.4 - 3.7 cm^{-1}.

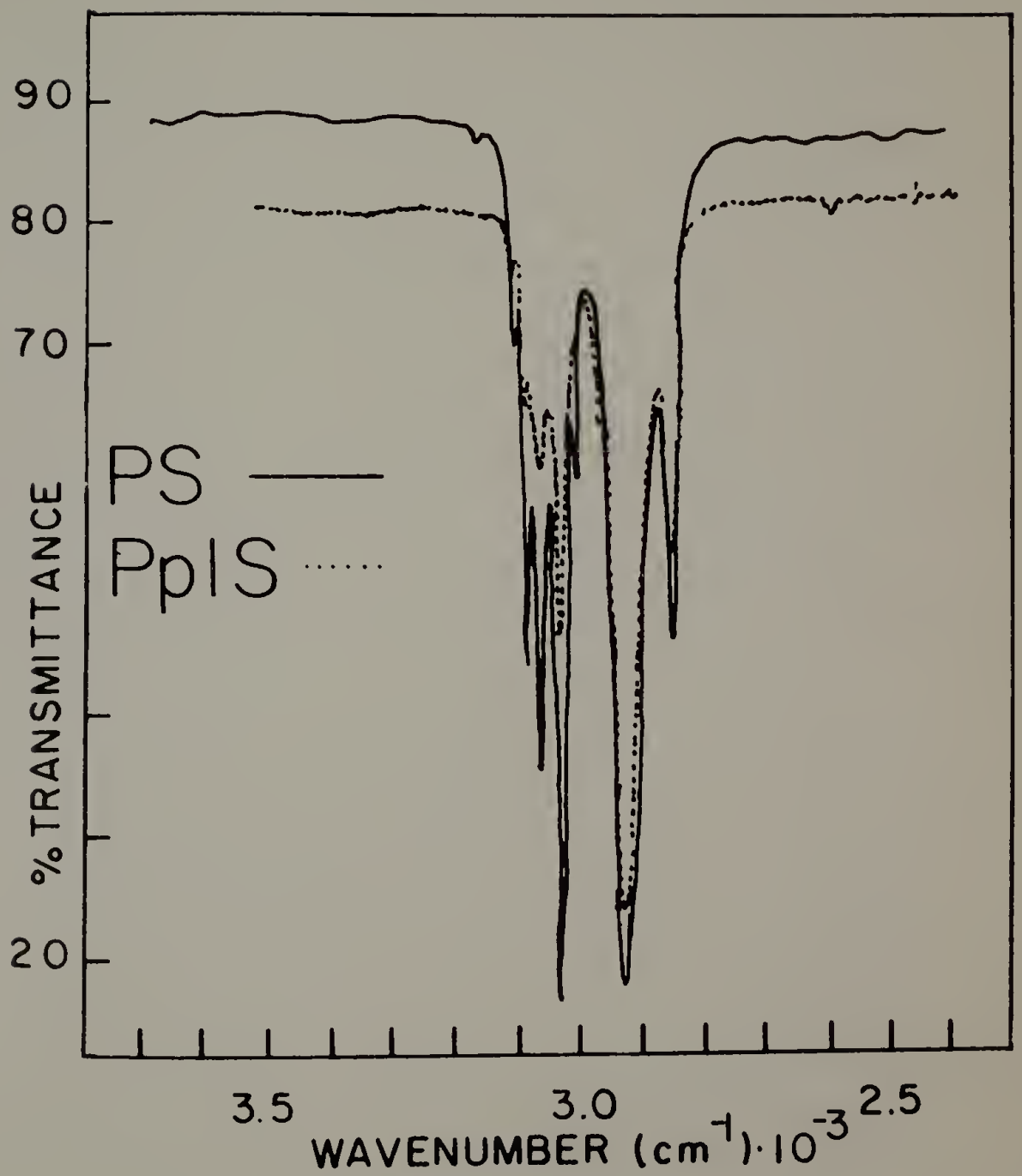
90
80
70
20
% TRANSMITTANCE
PS
PpIS
3.5
3.0
2.5
WAVENUMBER (cm^{-1})·10^{-3}

Figure 8. Infrared spectrum of PpIS and a-PS from 0.7 - 1.9 cm^{-1}.

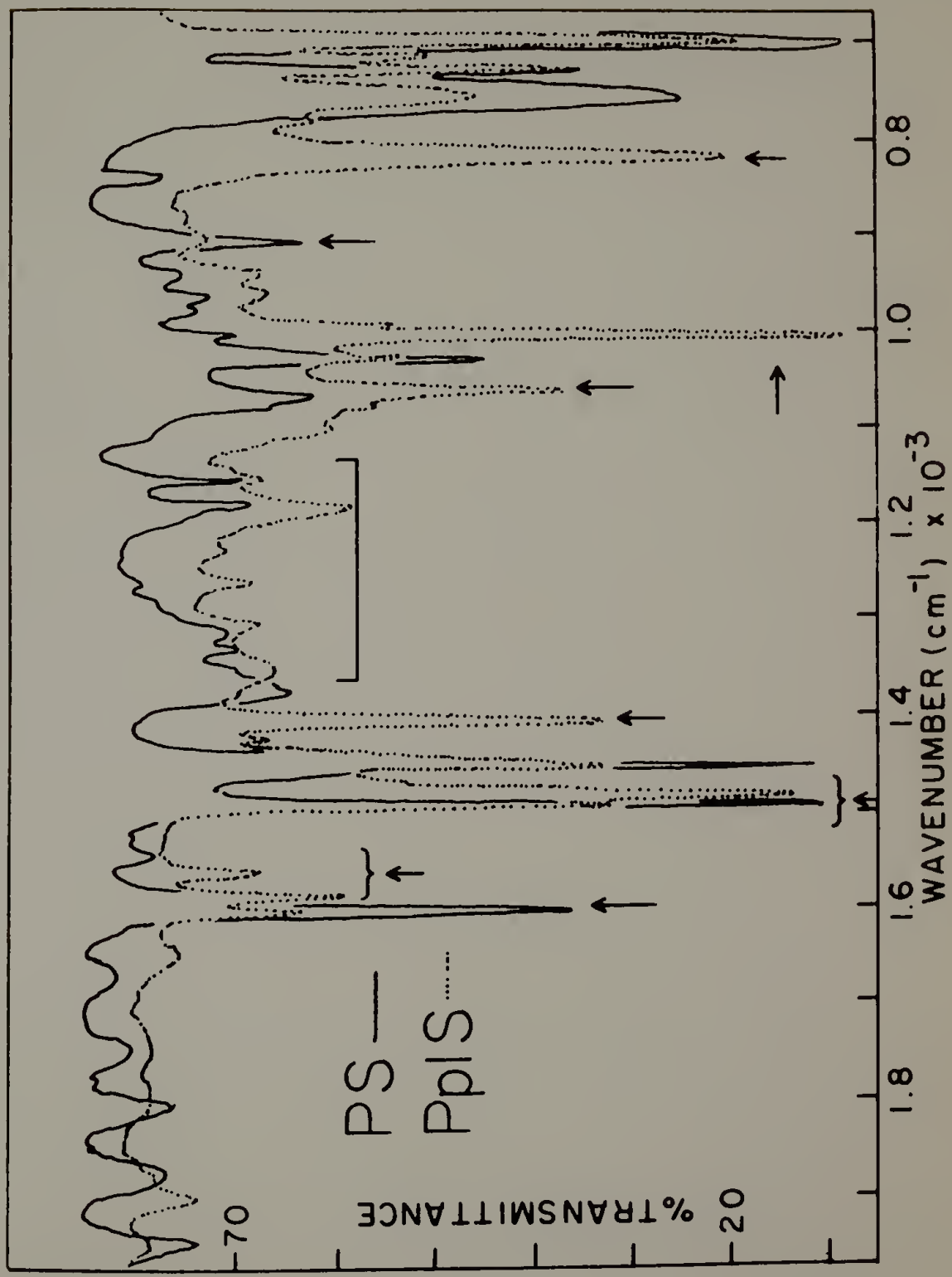
PS
PpIS
%TRANSMITTANCE
70
20
1.8
1.6
1.4
1.2
1.0
0.8
WAVENUMBER (cm^{-1}) x 10^{-3}

Figure 9. Heating cell for infrared spectroscopy experiments.

IR SAMPLE HOLDER / HEATER

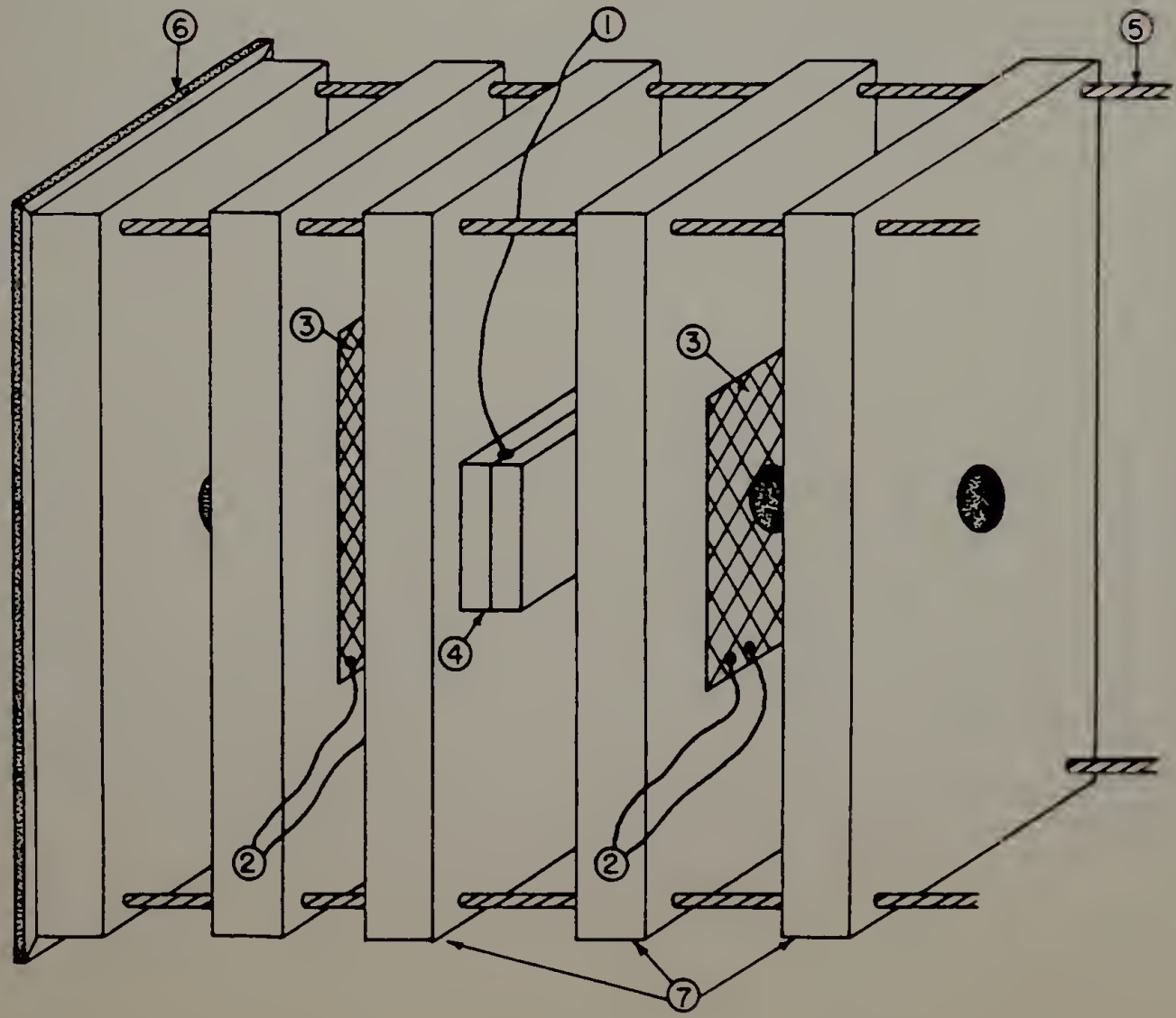

① Thermocouple
② Heater Leads
③ Heaters
④ Solt Plates
⑤ Mounting Bolts
⑥ Instrument Mounts
⑦ Asbestos Sheeting

Figure 10. Vacuum melt pressing device for preparation of neutron scattering specimens.

Vacuum Pressing Device

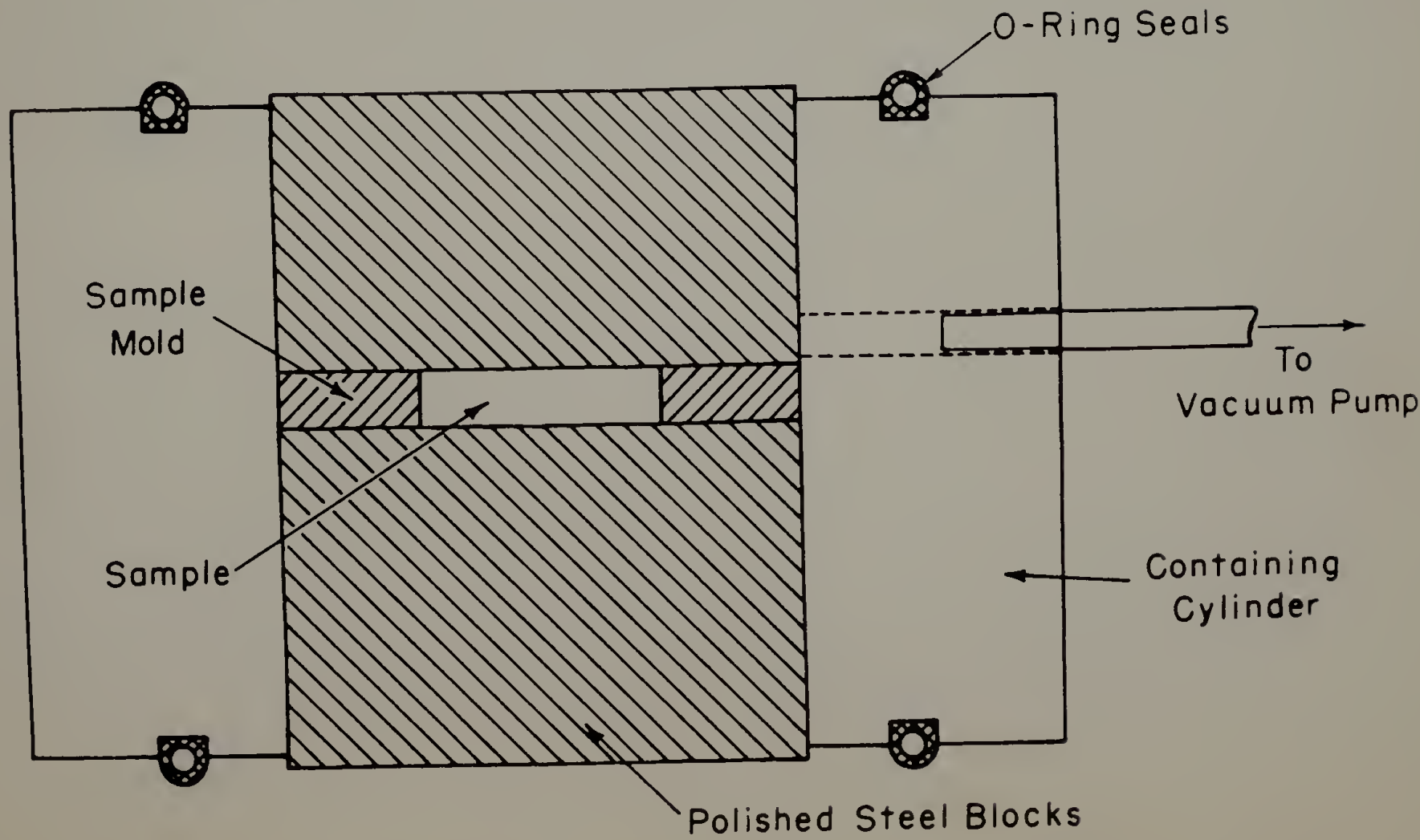

Figure 11. Small angle neutron scattering facility at the Oak Ridge Research Reactor. (Figure kindly supplied by Dr. H.R. Childe of ORNL.)

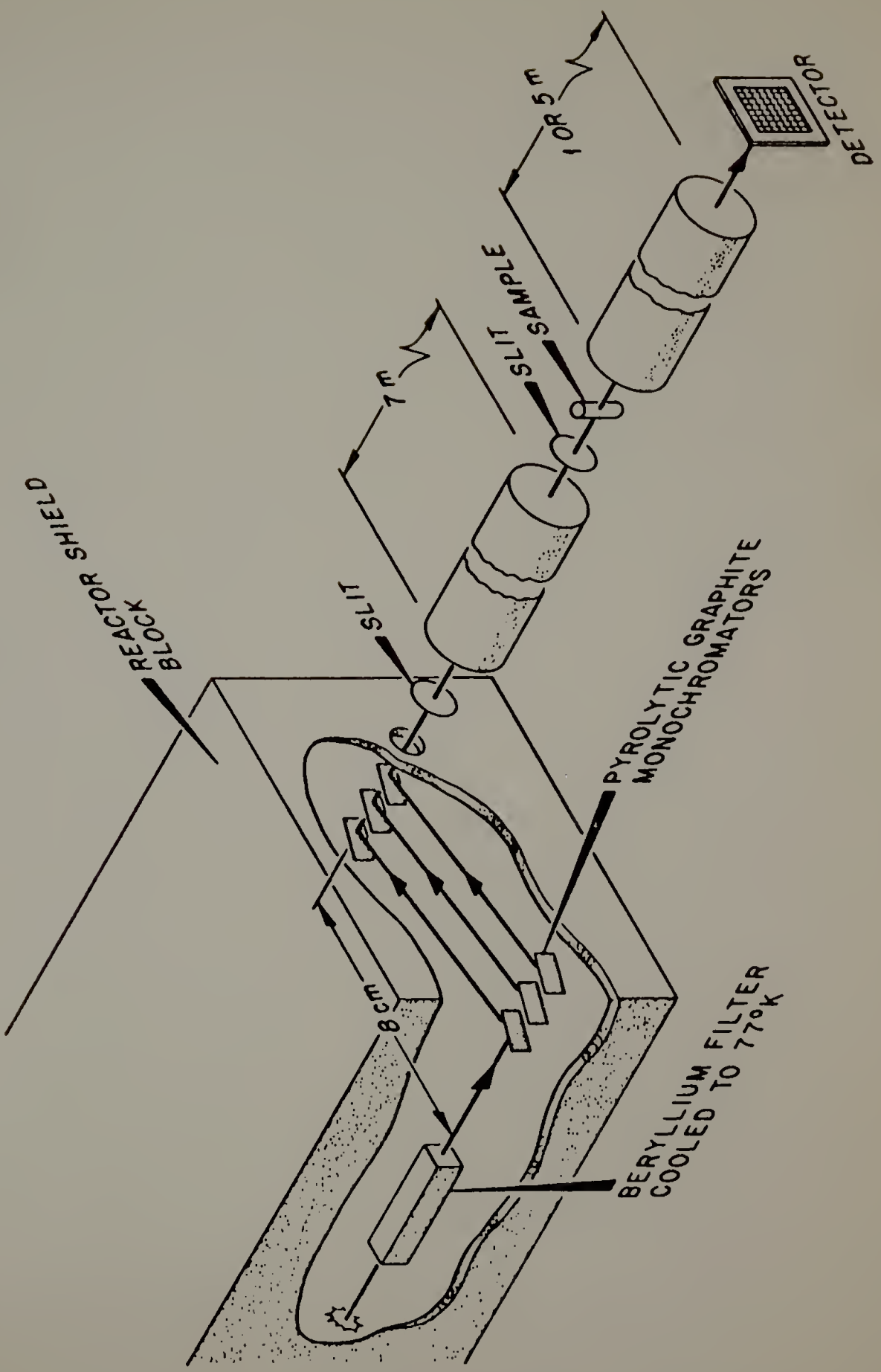
REACTOR SHIELD
BLOCK
SLIT
7 m
SLIT
SAMPLE
1 OR 5 m
DETECTOR
PYROLYTIC GRAPHITE
MONOCHROMATORS
8 cm
BERYLLIUM FILTER
COOLED TO 77°K

Figure 12. Comparison of the energy distributions for neutron and x-ray sources.

NEUTRONS

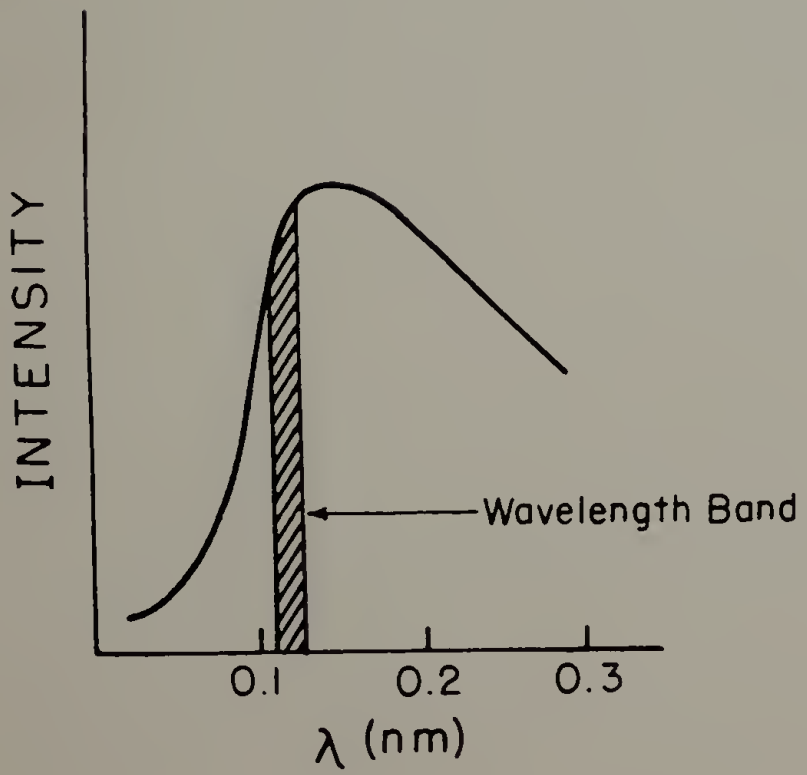

X-RAY

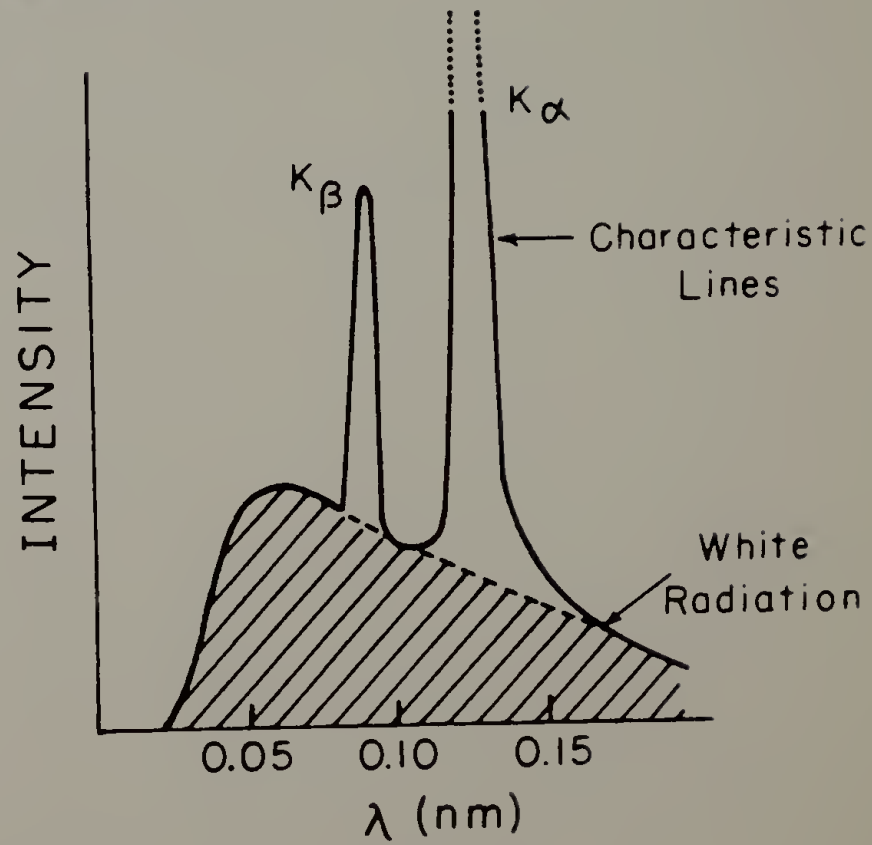

$$\gamma_\lambda = \frac{2N_1}{}\left(\frac{E}{kT}\right)^2 e^{-E/kT}$$

Figure 13. Small angle x-ray scattering profile of PVC obtained by Khambatta. (Data taken from F. Khambatta's dissertation.)

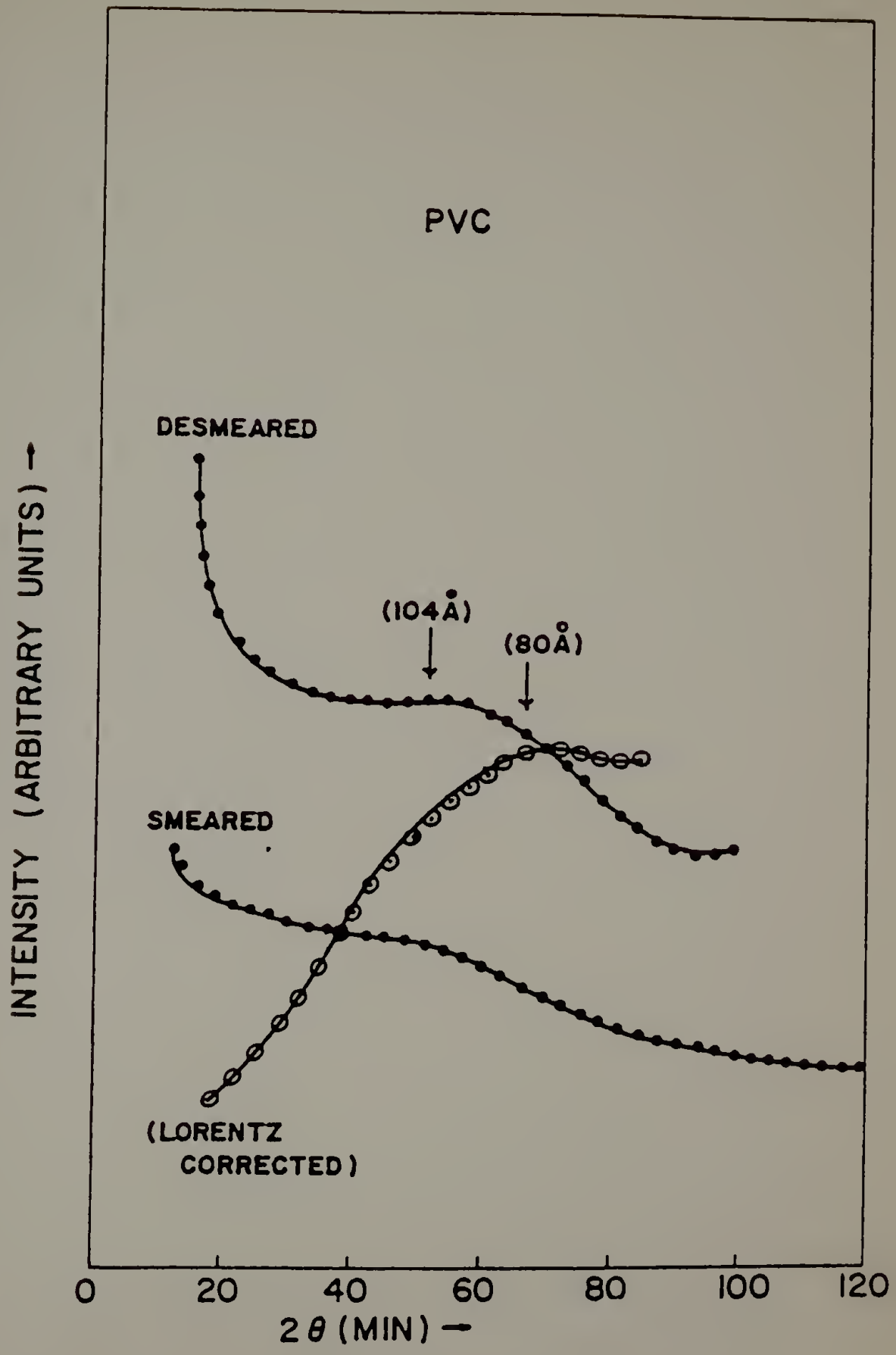
PVC
DESMEARED
(104Å)
(80Å)
SMEARED
(LORENTZ
CORRECTED)
INTENSITY (ARBITRARY UNITS) →
0
20
40
60
80
100
120
2θ (MIN) →

Figure 14. Mass density as a function of composition. Comparison of pure and impure specimens and the calculated density assuming volume additivity.

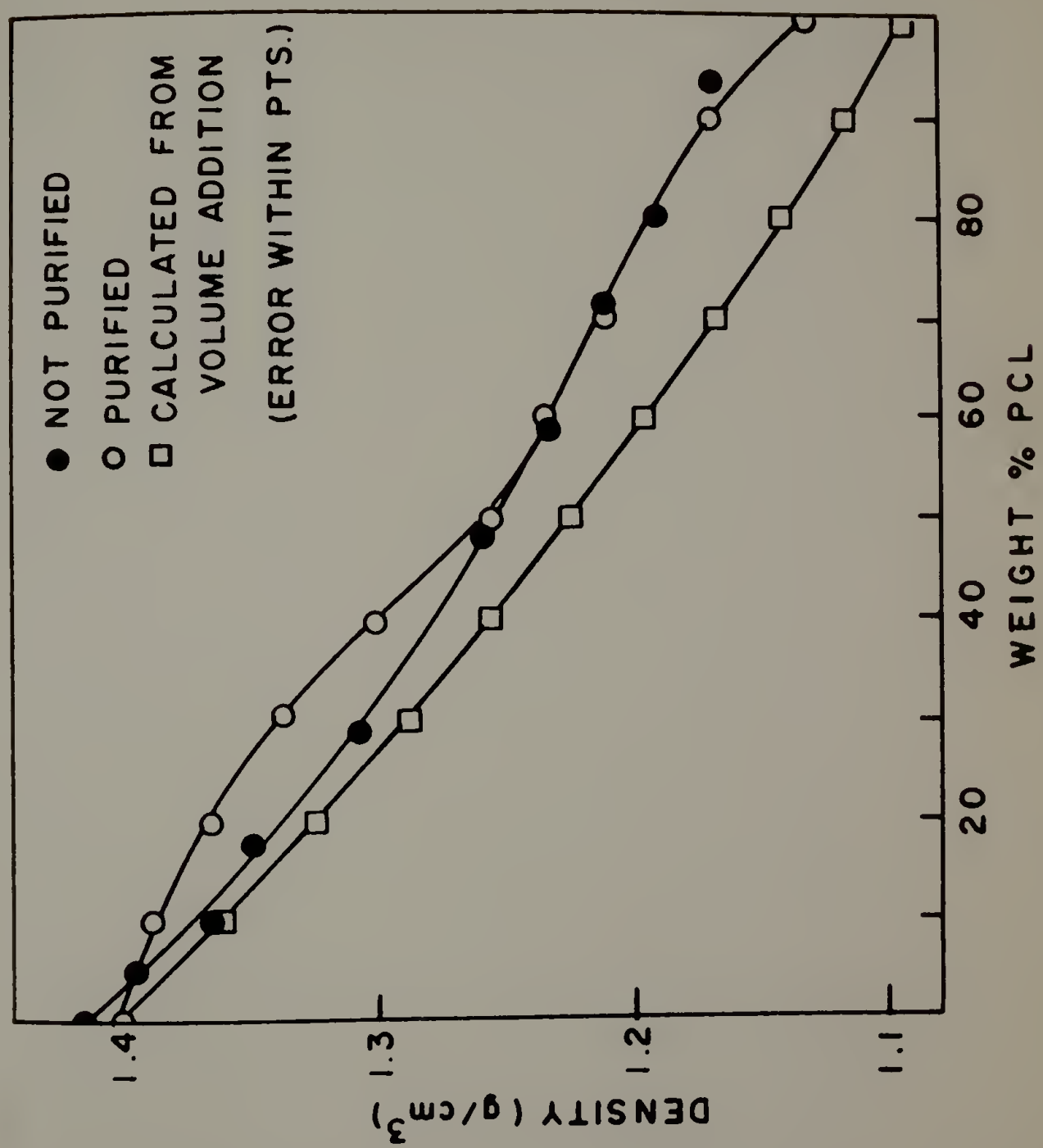
● NOT PURIFIED
○ PURIFIED
□ CALCULATED FROM VOLUME ADDITION
(ERROR WITHIN PTS.)
DENSITY (g/cm³)
1.4
1.3
1.2
1.1
20
40
60
80
WEIGHT % PCL

Figure 15. Wide angle x-ray diffraction photographs for various concentrations of PCL. Exposure times and concentrations are indicated.

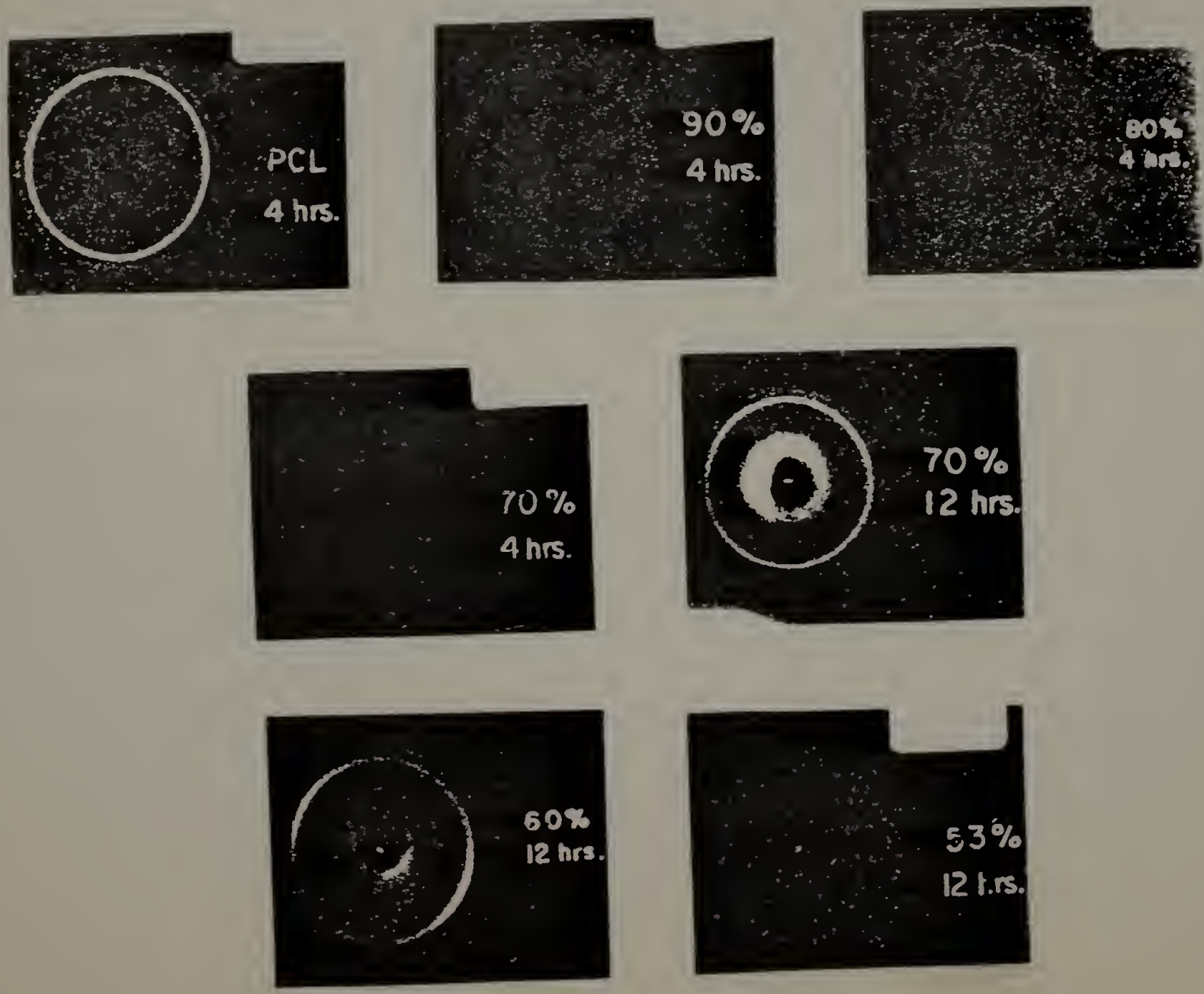
PCL
4 hrs.
90 %
4 hrs.
80 %
4 hrs.
70 %
4 hrs.
70 %
12 hrs.
60 %
12 hrs.
53 %
12 hrs.

Figure 16. Differential scanning calorimetry thermograms of various blend compositions.

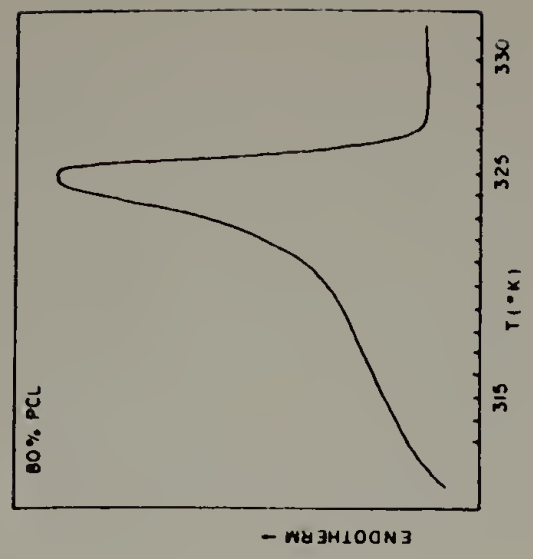
80% PCL
ENDOTHERM →
315
325
330
T(°K)

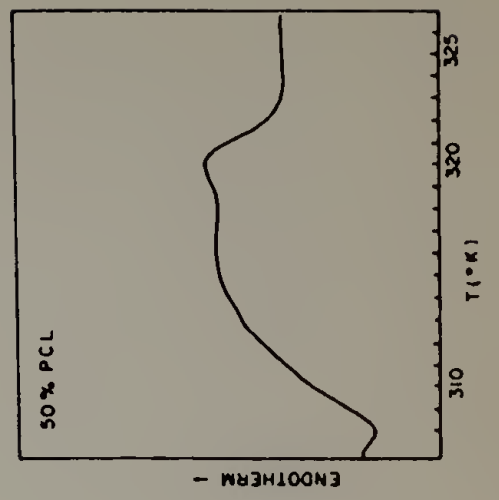
50% PCL
ENDOTHERM →
310
320
325
T(°K)

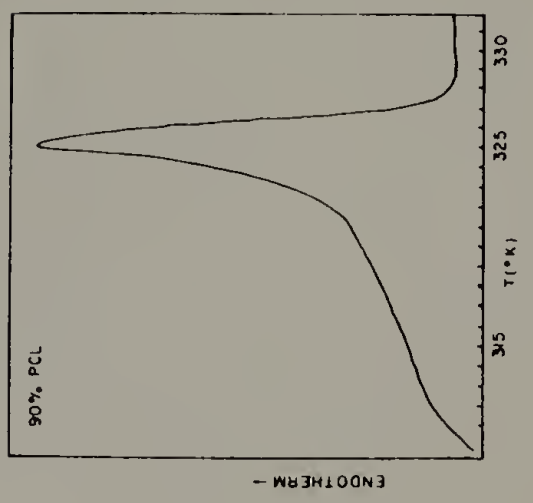
90% PCL
ENDOTHERM →
315
325
330
T(°K)

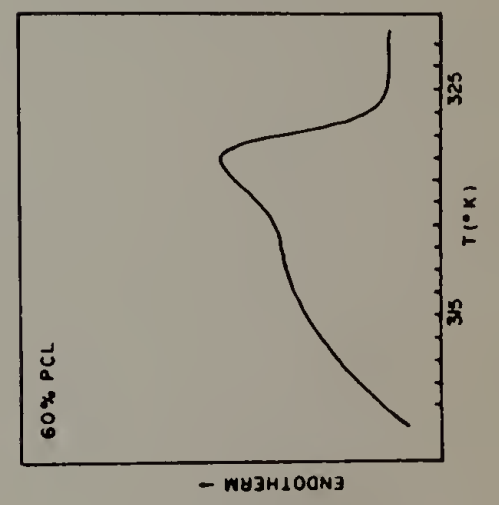
60% PCL
ENDOTHERM →
315
325
T(°K)

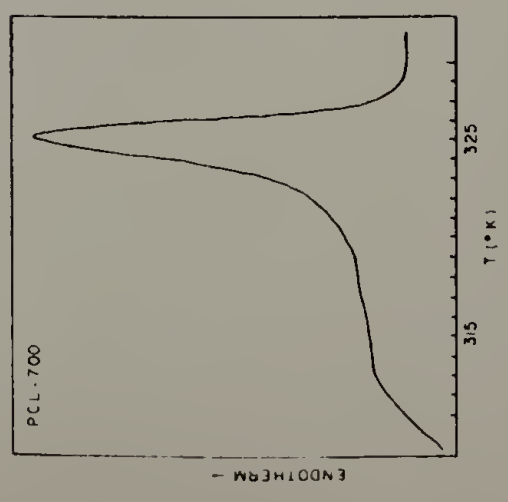
PCL-700
ENDOTHERM →
315
325
T(°K)

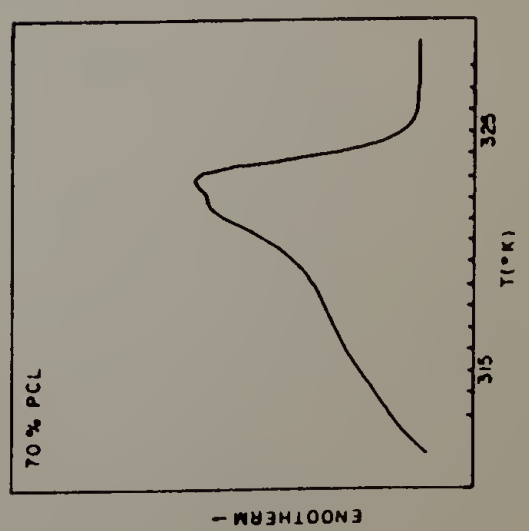
70% PCL
ENDOTHERM →
315
325
T(°K)

Figure 17. Degree of crystallinity as a function of composition. Results of density, DSC and WAXD experiments are shown.

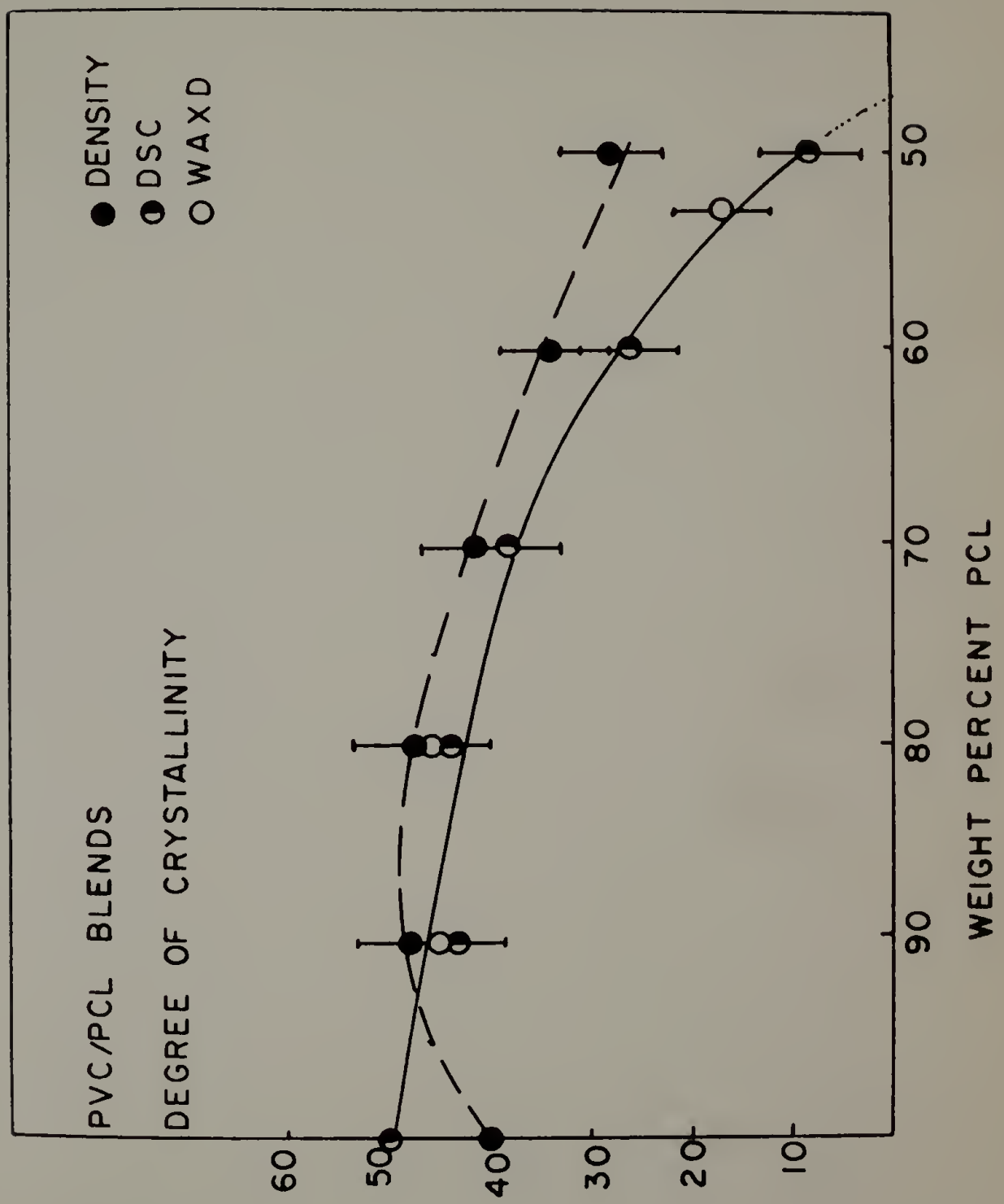
PVC/PCL BLENDS
DEGREE OF CRYSTALLINITY
● DENSITY
◑ DSC
○ WAXD
60
50
40
30
20
10
50
60
70
80
90
WEIGHT PERCENT PCL

Figure 18. Melting point (T_M), crystallization temperature (T_C), and glass transition temperature (T_g) of blends as a function of compositions.

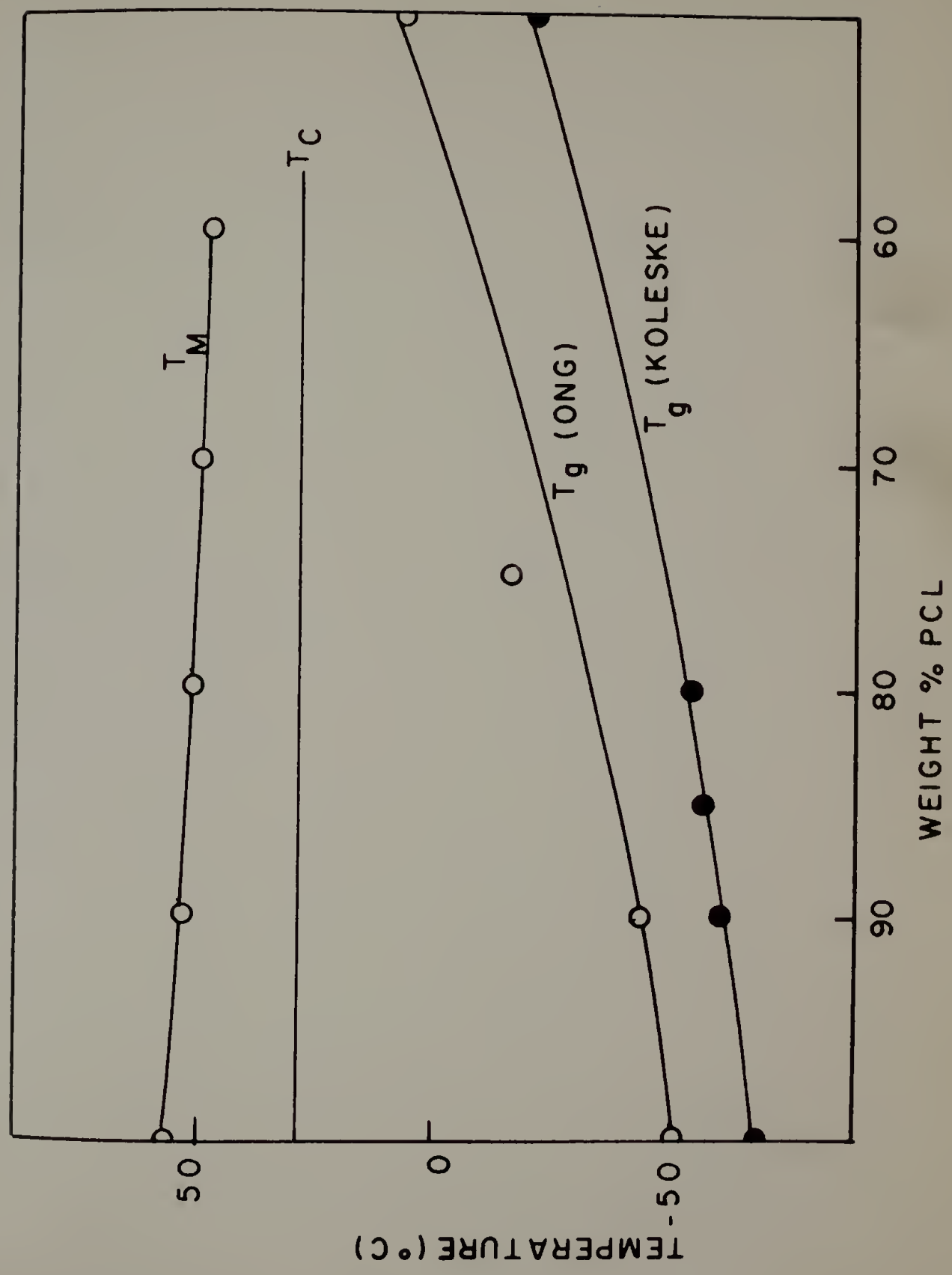
TEMPERATURE (°C)
50
0
-50
90
80
70
60
WEIGHT % PCL
T_M
T_C
T_g (ONG)
T_g (KOLESKE)

Figure 19. Melting point of PCL crystals as a function of compositions.

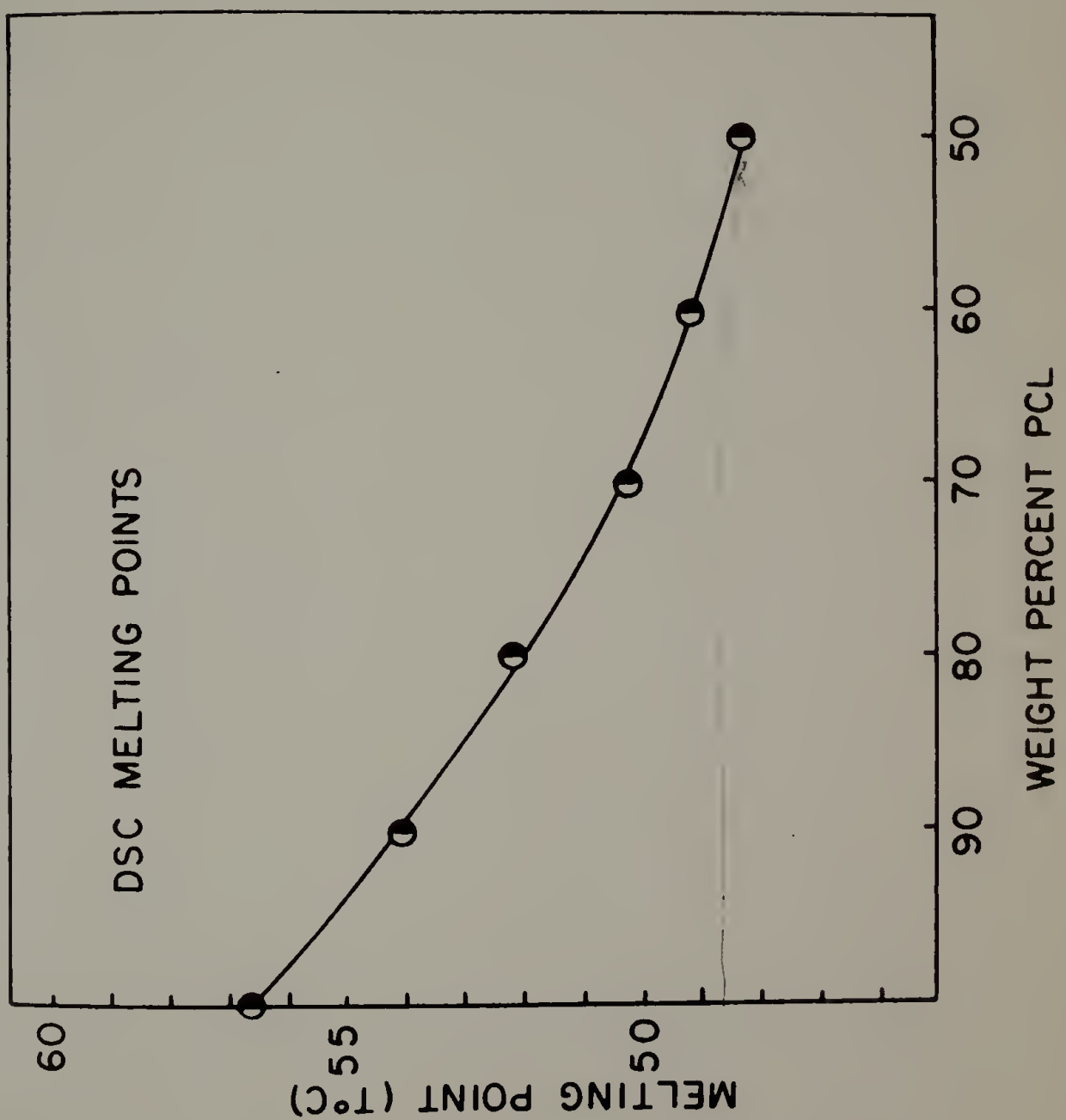
DSC MELTING POINTS
MELTING POINT (T°C)
60
55
50
90
80
70
60
50
WEIGHT PERCENT PCL

Figure 20. Spherulite radius for purified and nonpurified blends as a function of composition.

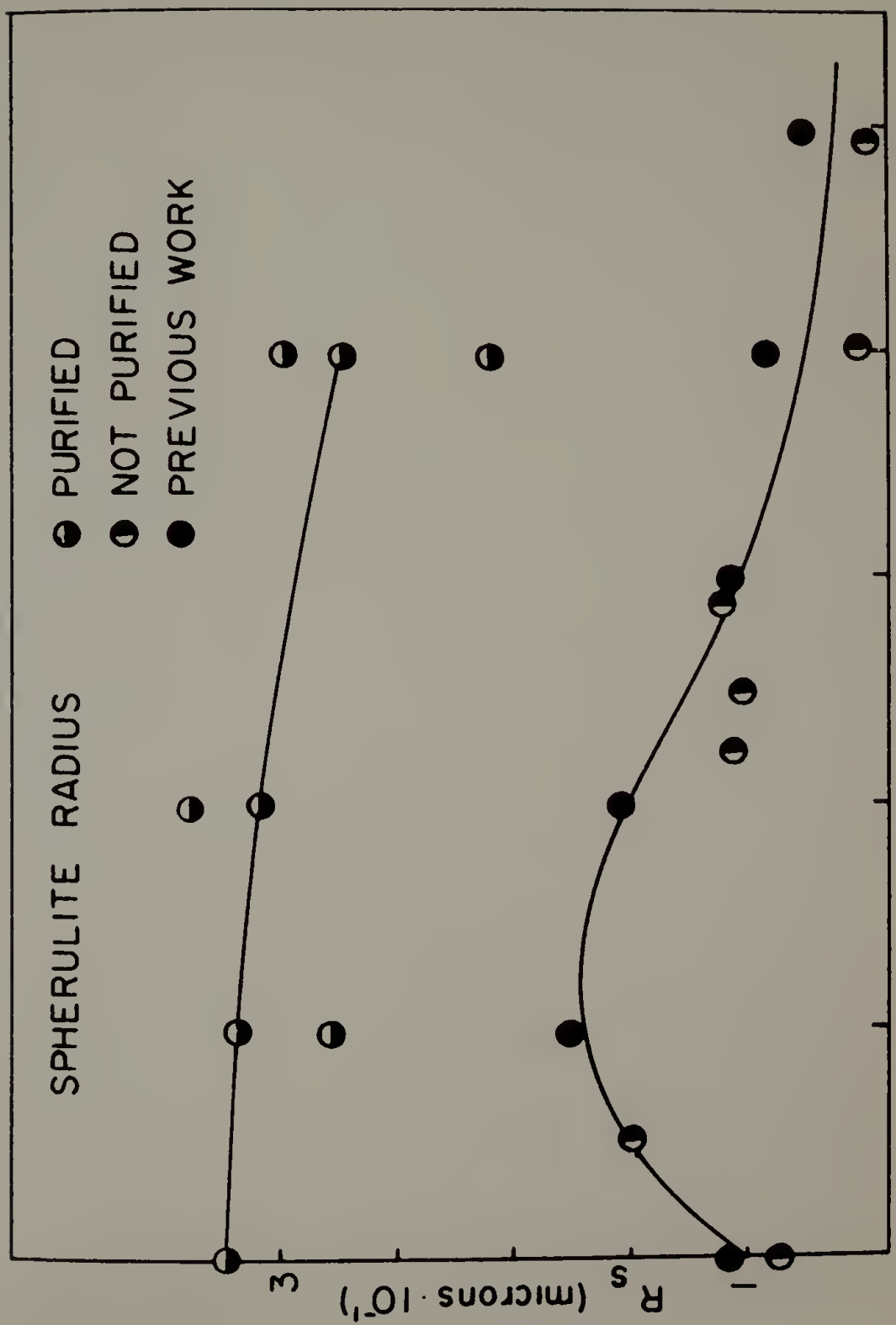
SPHERULITE RADIUS
PURIFIED
NOT PURIFIED
PREVIOUS WORK
R_s (microns · 10^{-1})
3
1
50
60
70
80
90
WEIGHT PERCENT PCL

Figure 21. Experimentally obtained small angle x-ray scattering profiles of PVC/PCL blends (pure PCL, 90%, 50%).

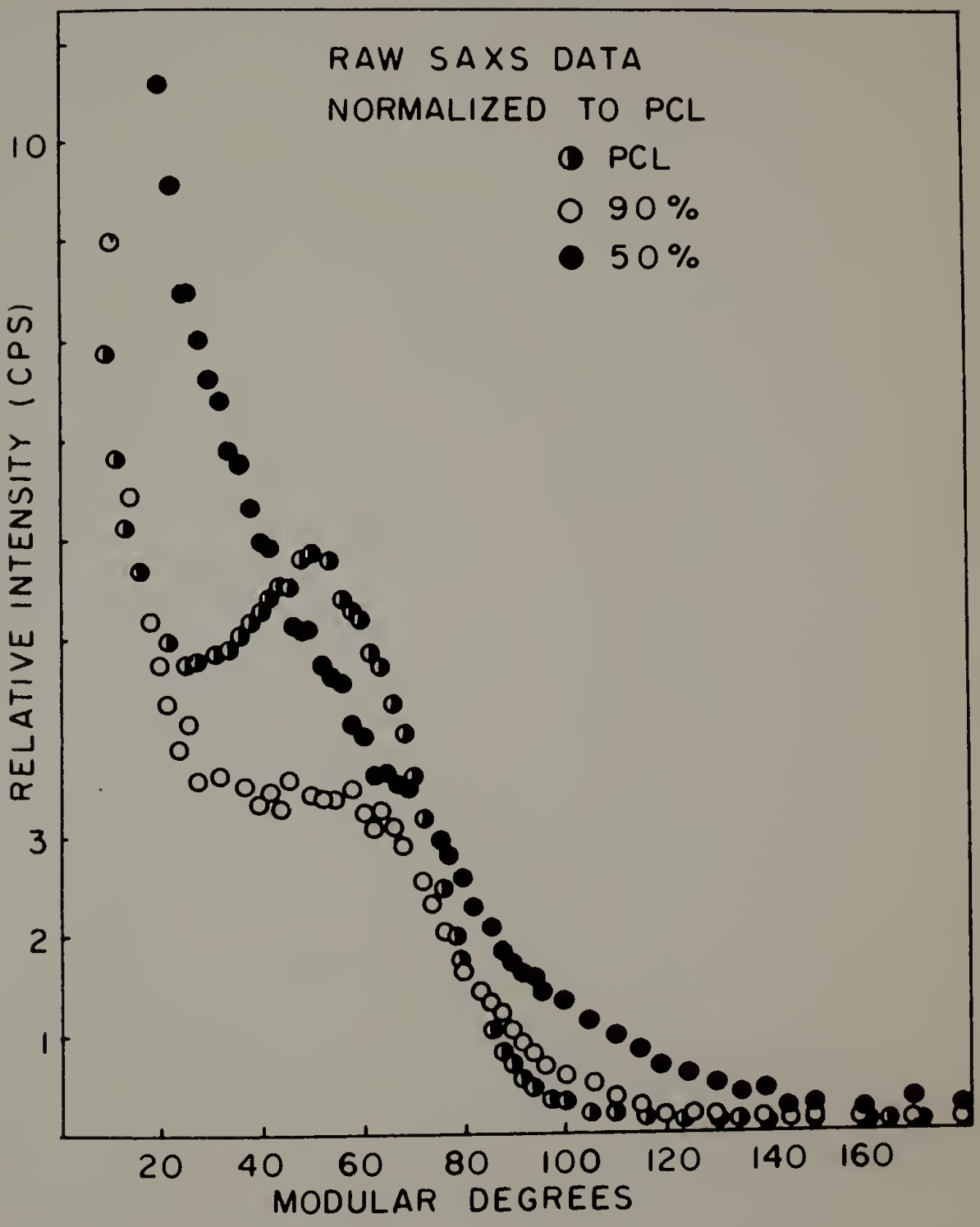
RAW SAXS DATA
NORMALIZED TO PCL
PCL
90%
50%
RELATIVE INTENSITY (CPS)
10
3
2
1
20
40
60
80
100
120
140
160
MODULAR DEGREES

Figure 22. Experimentally obtained small angle x-ray scattering profiles of PVC/PCL blends (69% and 59% PCL).

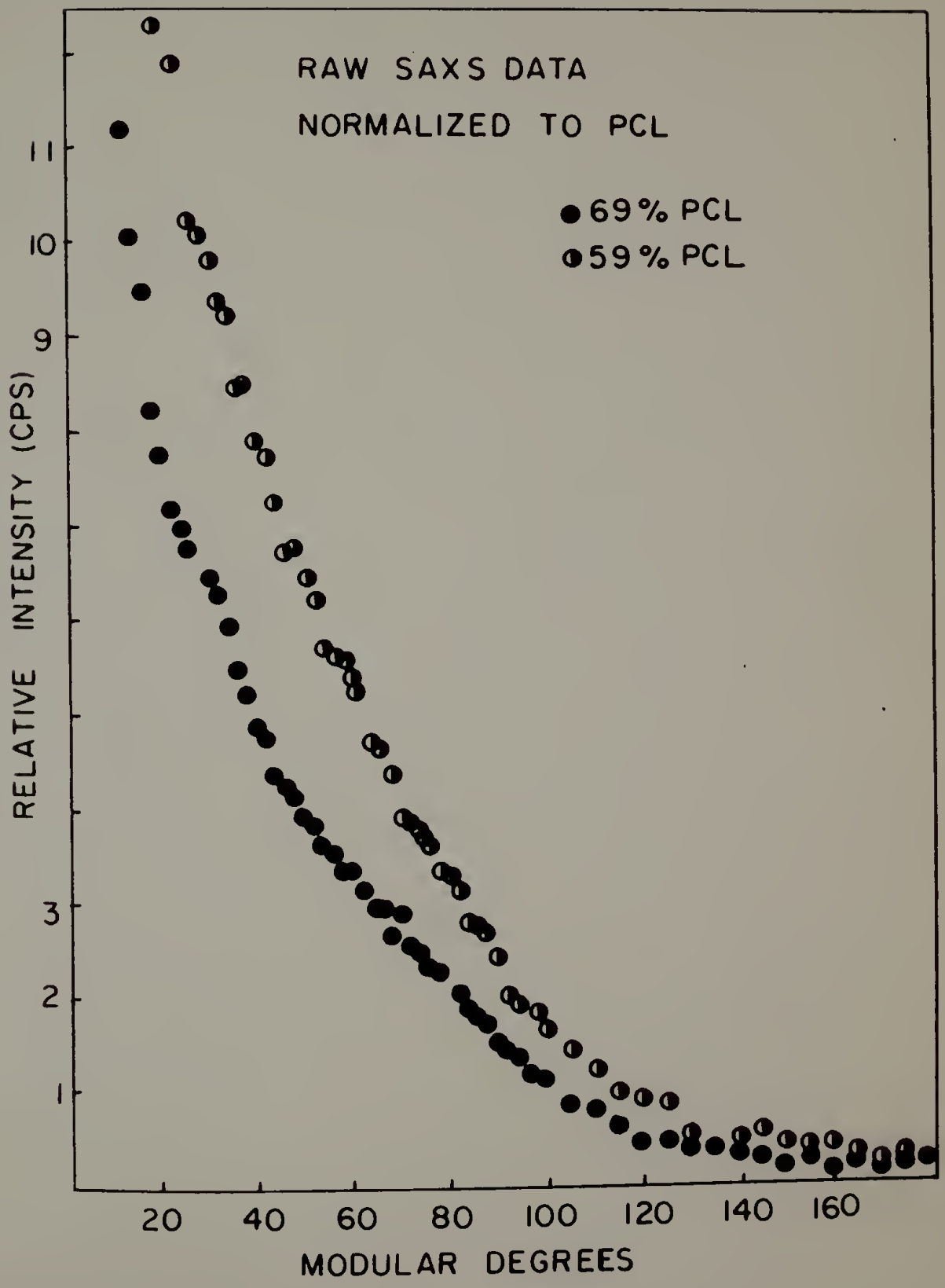
RAW SAXS DATA
NORMALIZED TO PCL
69% PCL
59% PCL
RELATIVE INTENSITY (CPS)
11
10
9
3
2
1
20
40
60
80
100
120
140
160
MODULAR DEGREES

Figure 23. Small angle x-ray scattering profiles of molten PVC/PCL blends (90%, 69%, 60%, and 50% PCL). (Data of Picot (118) and Hyde (119,120,121) taken from Huglin.)

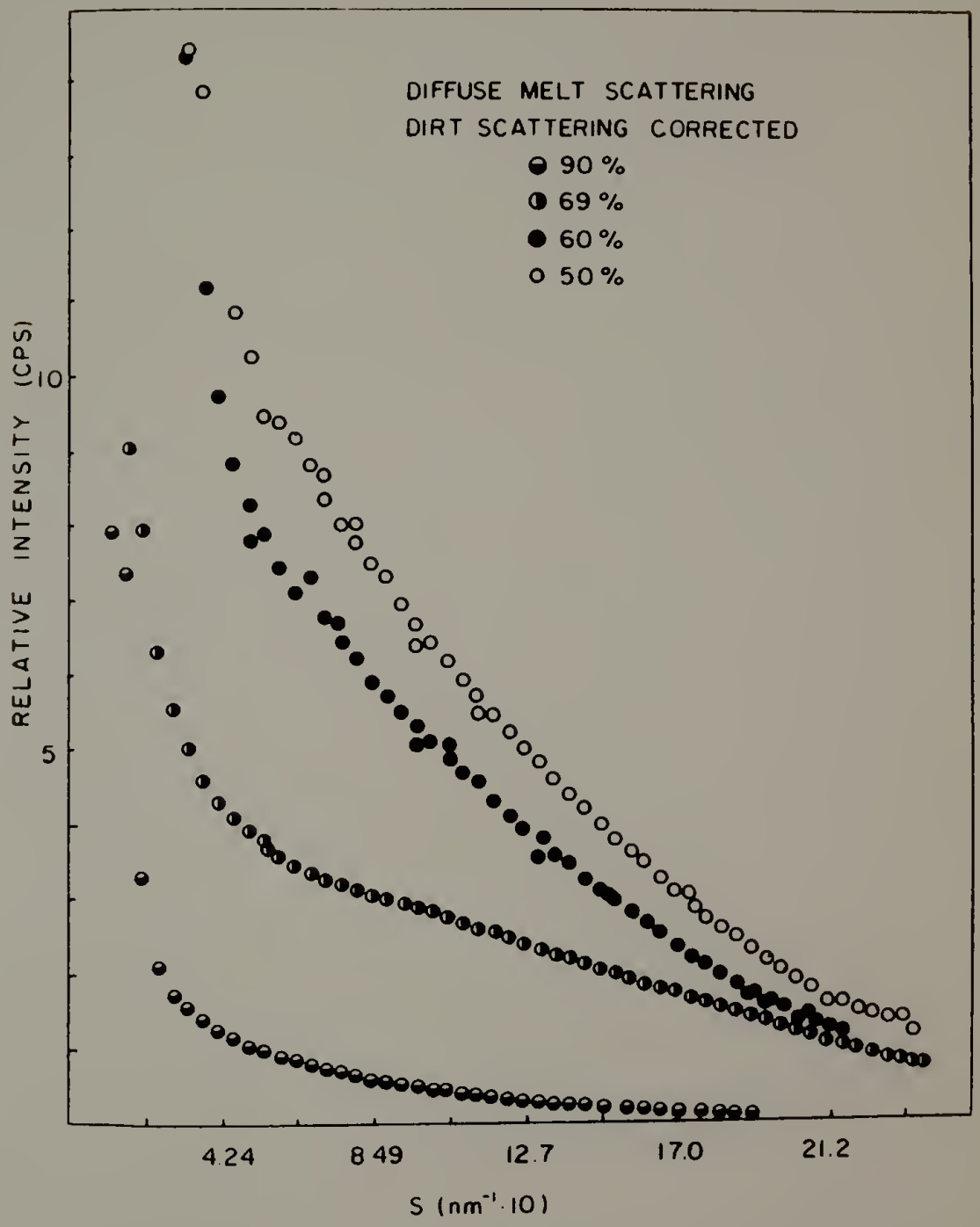
DIFFUSE MELT SCATTERING
DIRT SCATTERING CORRECTED
90 %
69 %
60 %
50 %
RELATIVE INTENSITY (CPS)
10
5
4.24
8.49
12.7
17.0
21.2
S (nm⁻¹·10)

Figure 24. Smeared small angle x-ray scattering profiles after correcting for liquid scattering.

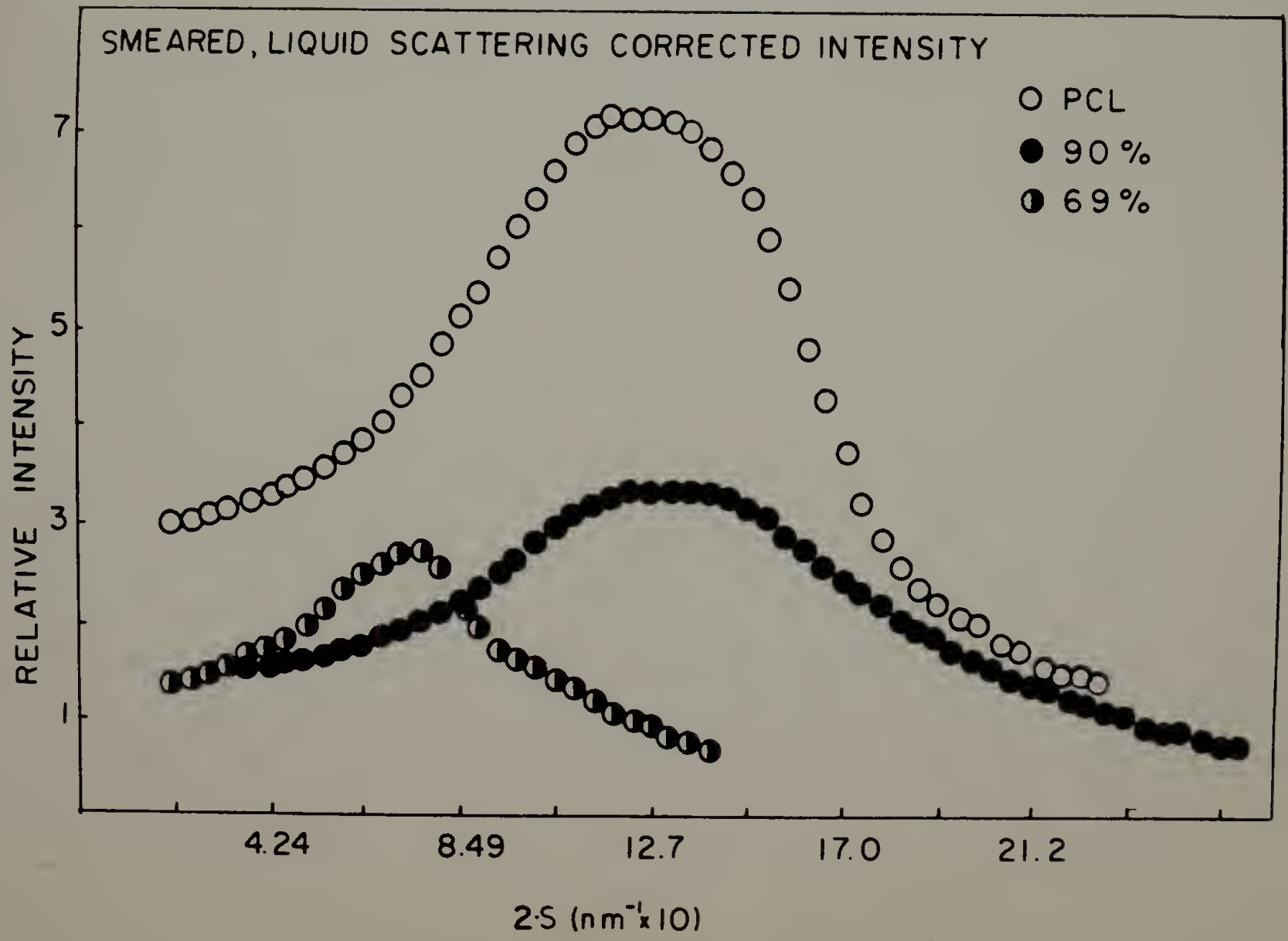
SMEARED, LIQUID SCATTERING CORRECTED INTENSITY
PCL
90 %
69 %
RELATIVE INTENSITY
7
5
3
1
4.24
8.49
12.7
17.0
21.2
2·S (nm⁻¹ x 10)

Figure 25. Desmeared small angle x-ray scattering profiles of PCL, 90% and 69% blends.

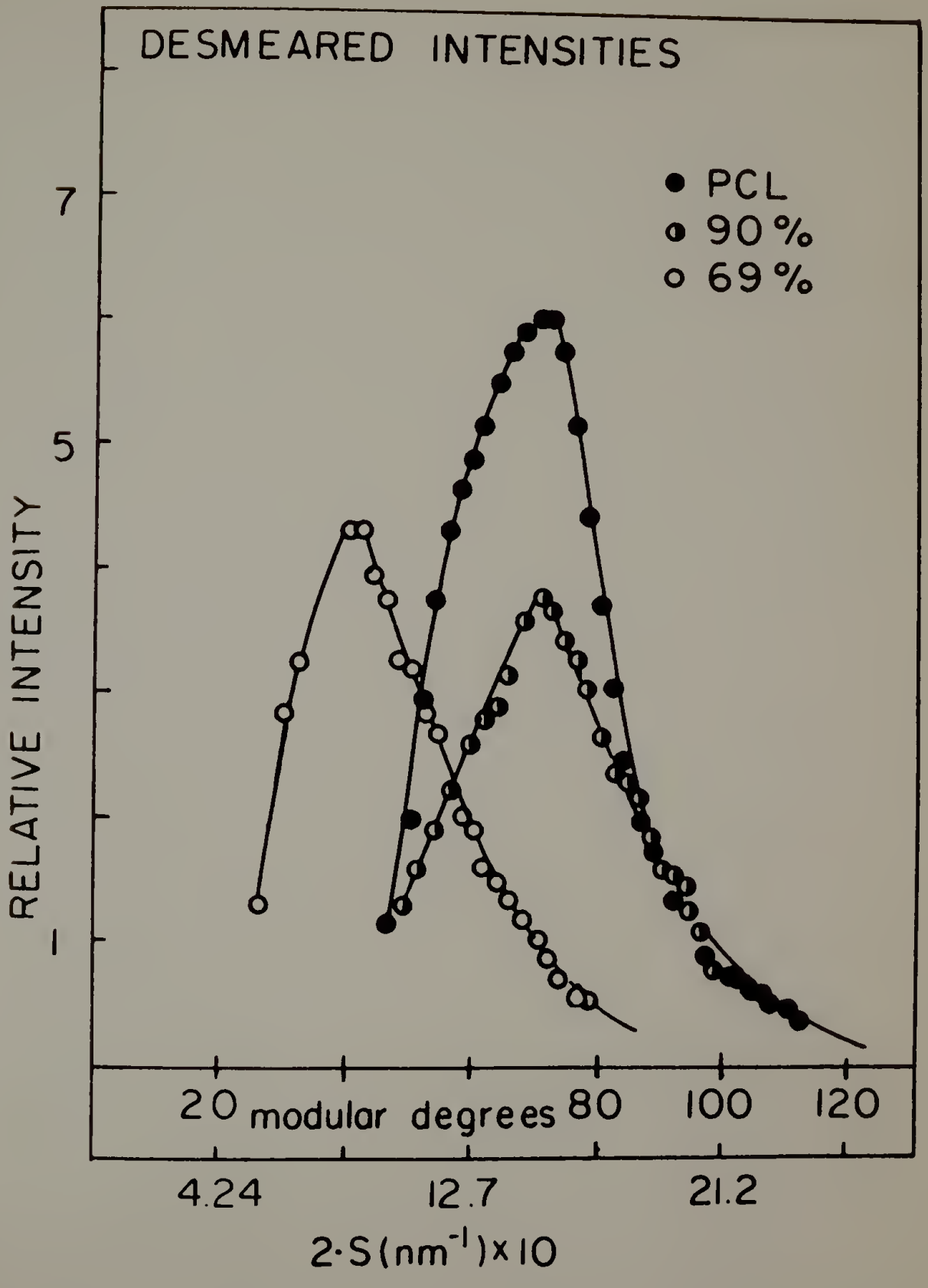
DESMEARED INTENSITIES
PCL
90 %
69 %
RELATIVE INTENSITY
7
5
1
20
modular degrees
80
100
120
4.24
12.7
21.2
2·S(nm⁻¹)×10

Figure 26. Plot of $I(h)h^4$ vs. h^2 for pinhole data of pure PCL.

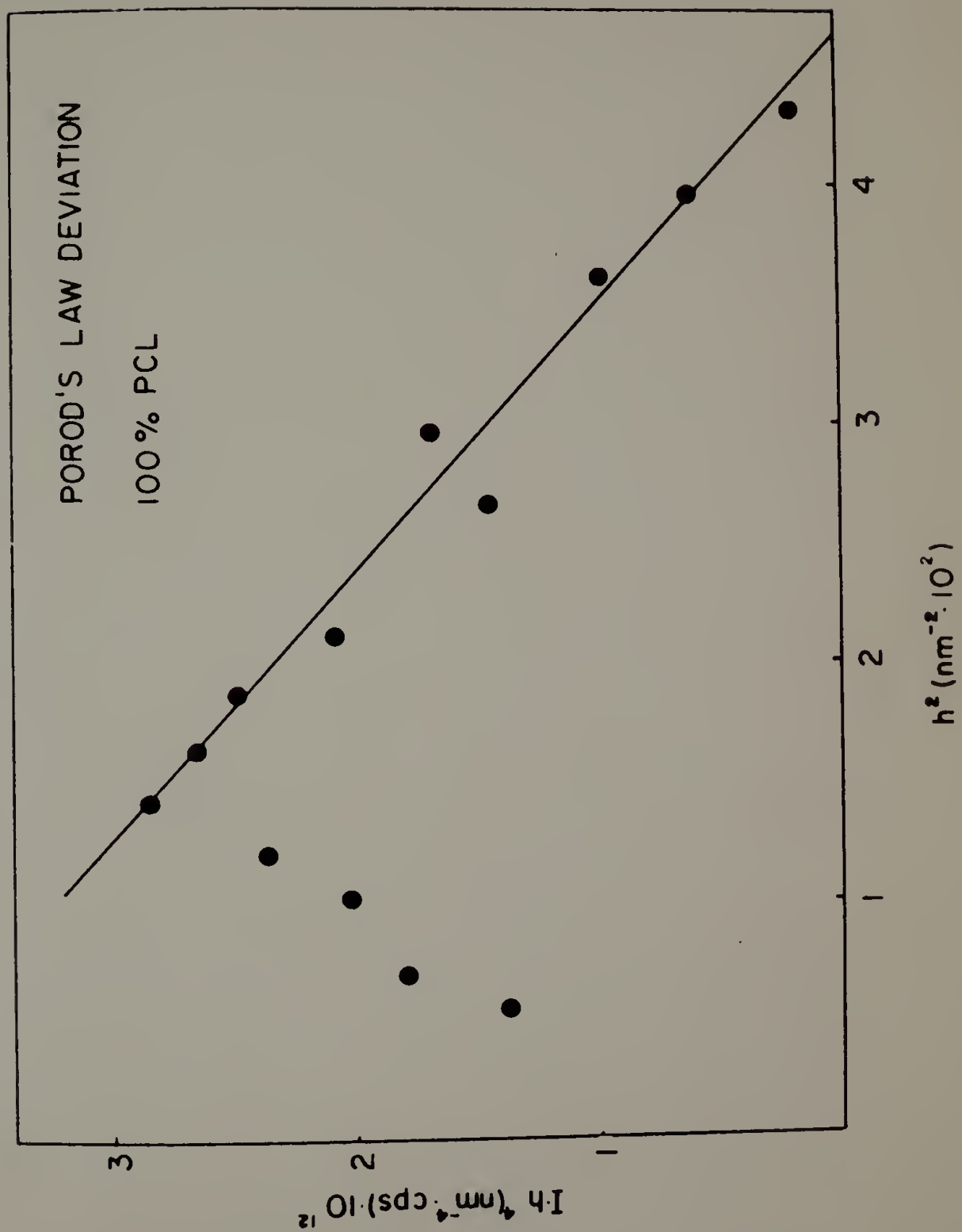
POROD'S LAW DEVIATION
100 % PCL
I·h⁴ (nm⁻⁴·cps)·10¹²
h² (nm⁻²·10²)
1
2
3
4

Figure 27. Plot of $I(h)h^4$ vs. h^2 for pinhole data of 90% PCL.

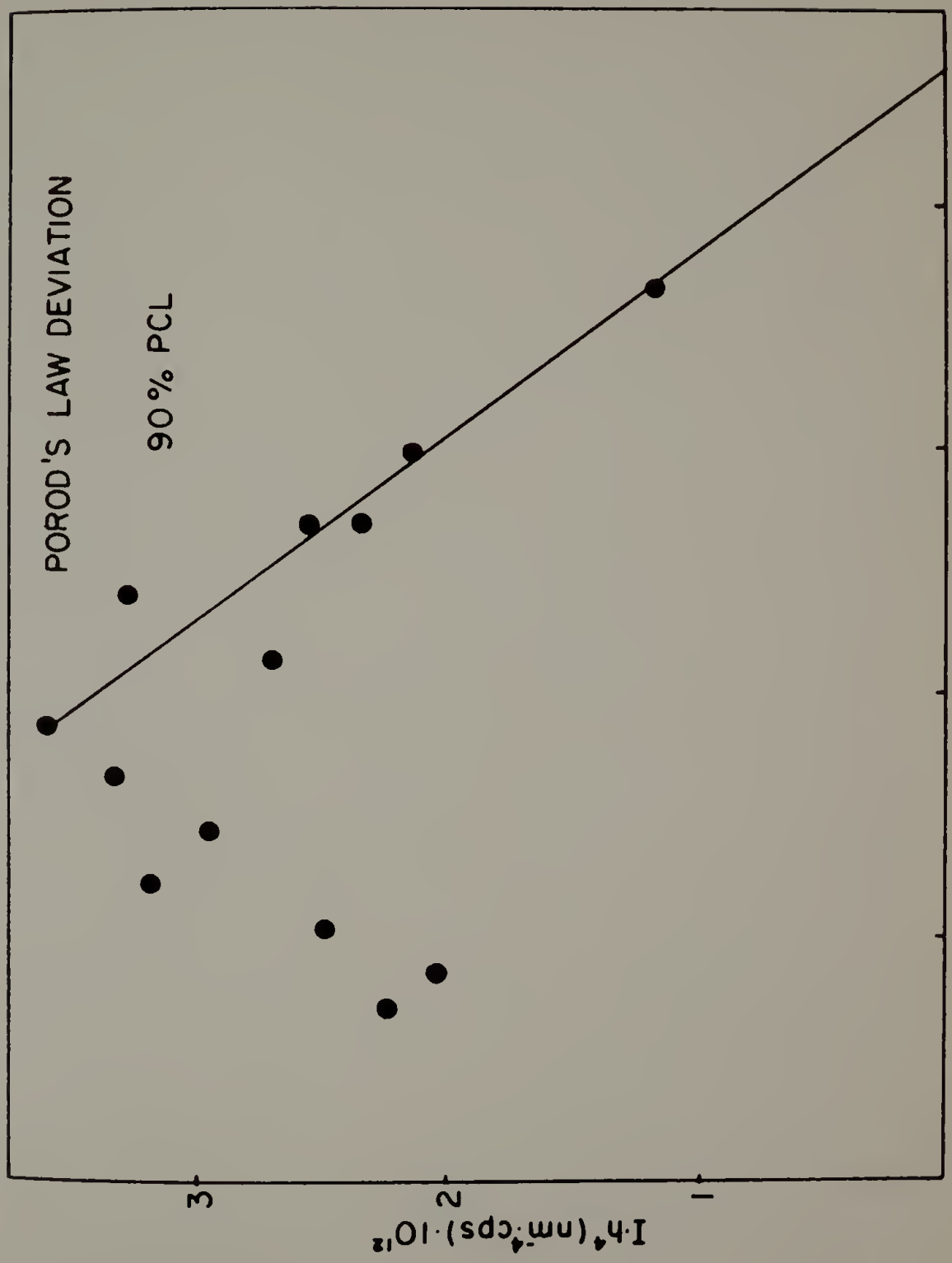
POROD'S LAW DEVIATION
90% PCL
$I \cdot h^4 (nm^{-4} \cdot cps) \cdot 10^{12}$
$h^2 (nm^{-2} \cdot 10^2)$
1
2
3
4

Figure 28. Plot of $I(h)h^4$ vs. h^2 for pinhole data of 69% PCL.

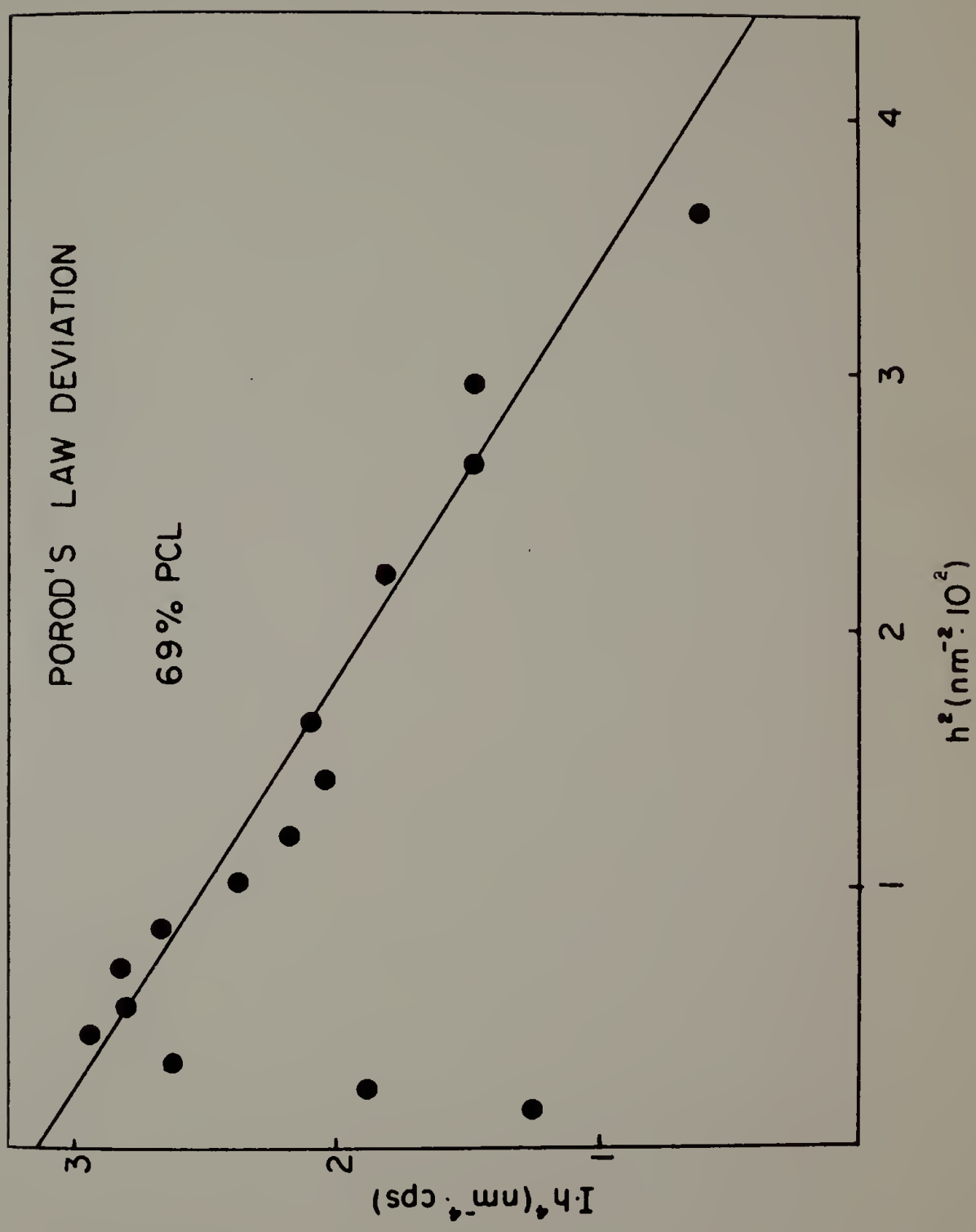
POROD'S LAW DEVIATION
69% PCL
I·h⁴(nm⁻⁴· cps)
h²(nm⁻²·10²)
1
2
3
4

Figure 29. Transition zone thickness as a function of composition for PCL/PVC blends.

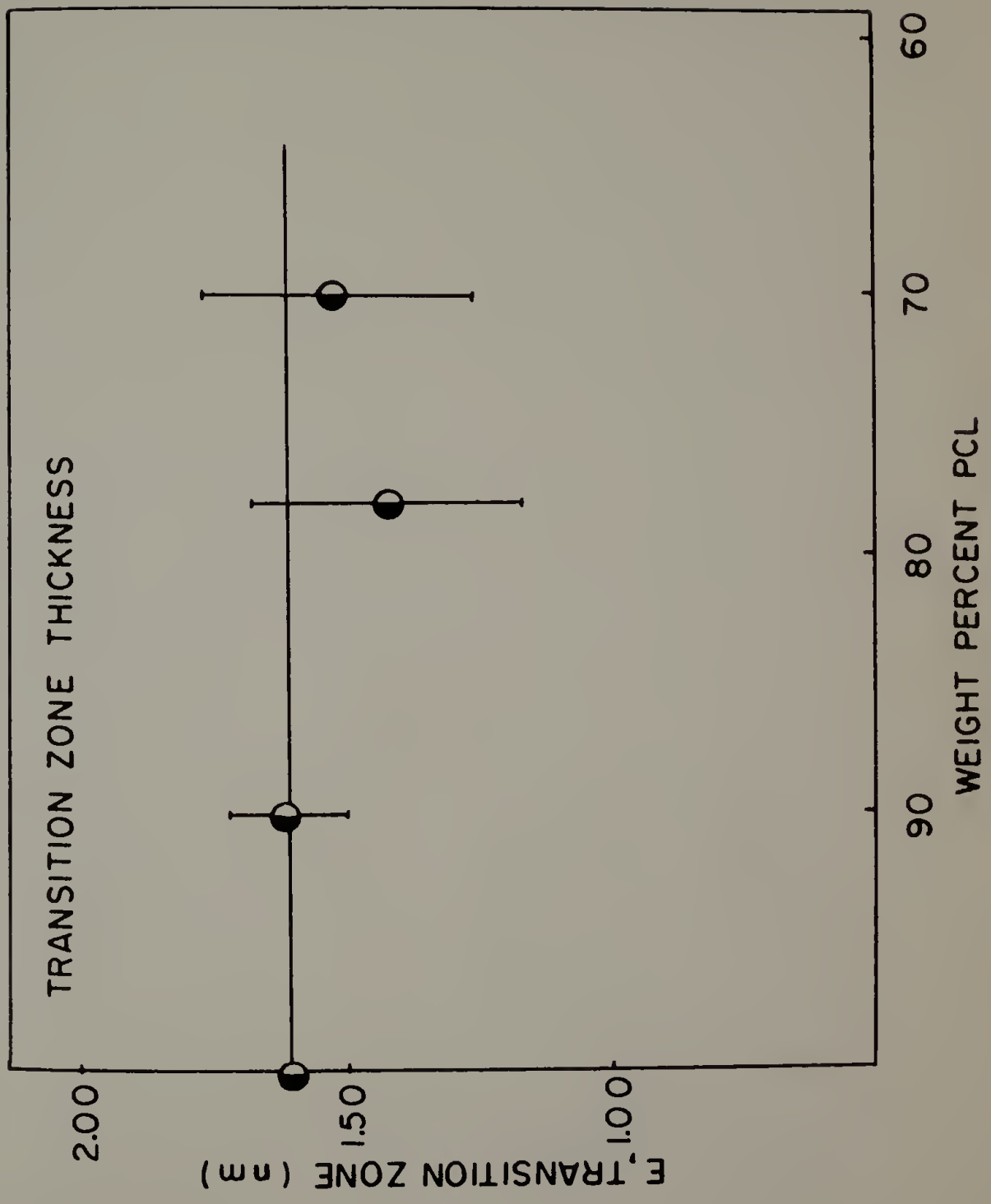
TRANSITION ZONE THICKNESS
E, TRANSITION ZONE (nm)
2.00
1.50
1.00
60
70
80
90
WEIGHT PERCENT PCL

Figure 30. Comparison of calculated and experimentally obtained fluctuations of the electron density.

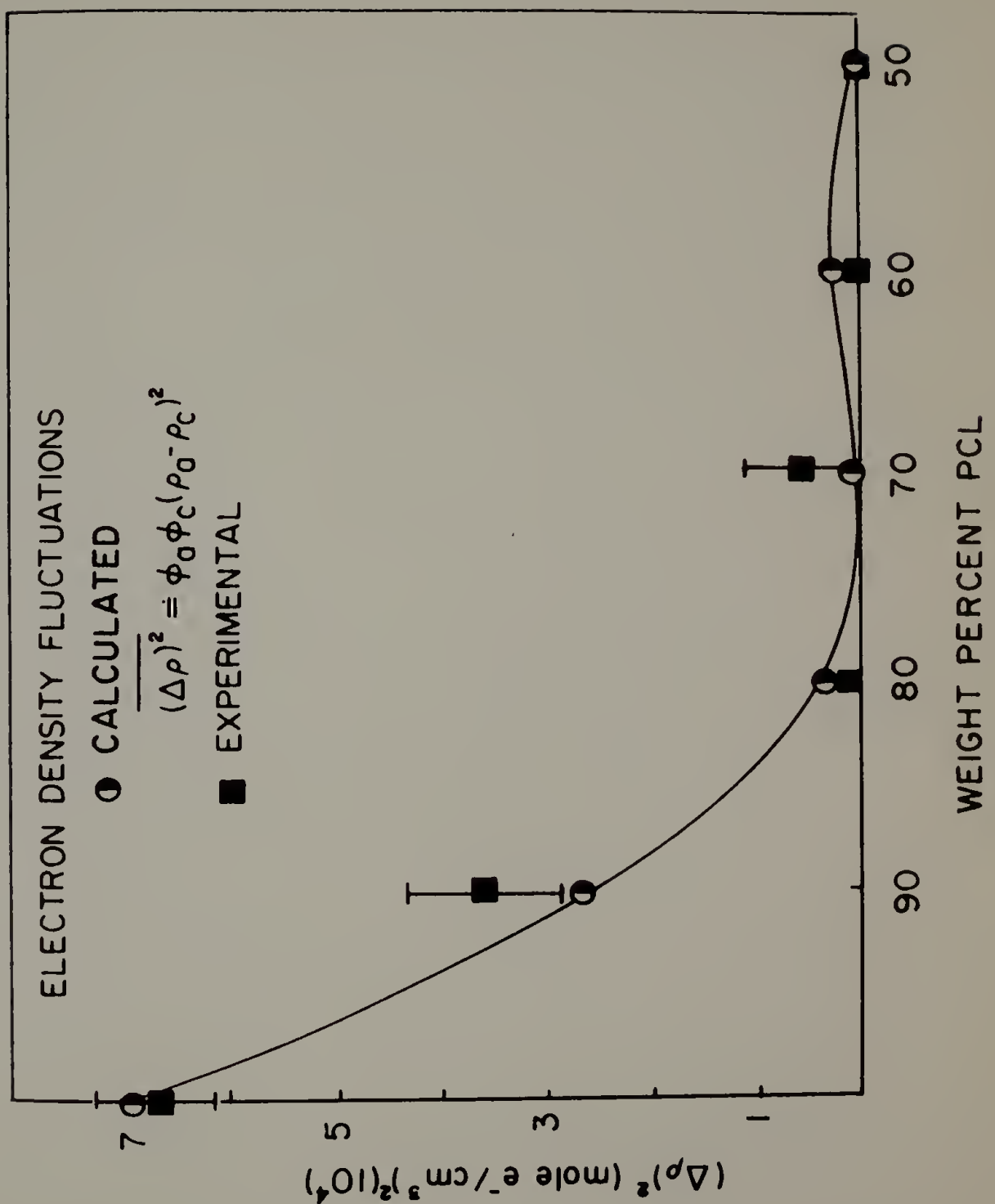
ELECTRON DENSITY FLUCTUATIONS
CALCULATED
$\overline{(\Delta\rho)^2} = \phi_a\phi_c(\rho_a-\rho_c)^2$
EXPERIMENTAL
$(\Delta\rho)^2$ (mole e⁻/cm³)²(10⁴)
7
5
3
1
90
80
70
60
50
WEIGHT PERCENT PCL

Figure 31. Long period as a function of composition.

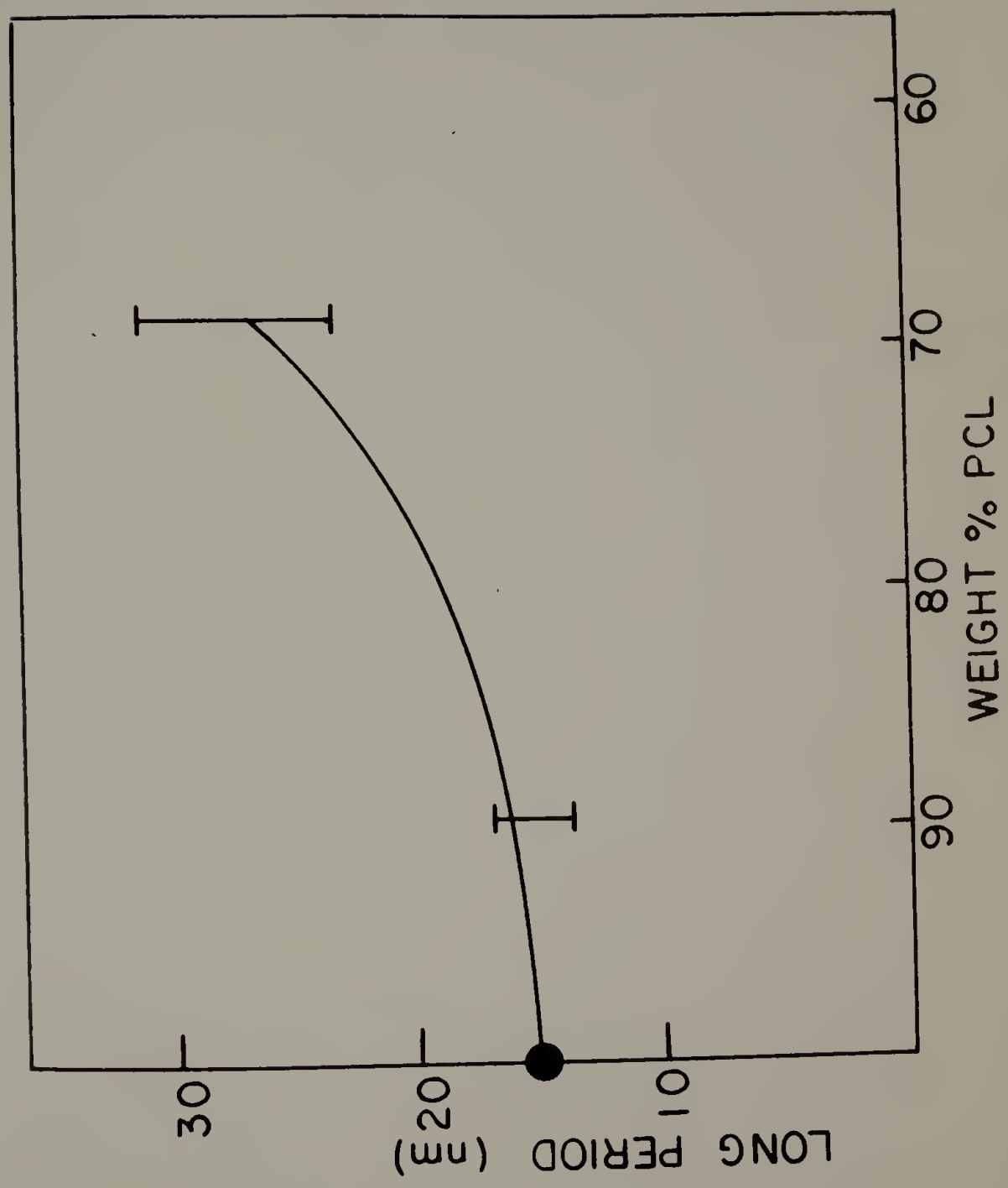
LONG PERIOD (nm)
30
20
10
WEIGHT % PCL
60
70
80
90

Figure 32. Calculated and experimental correlation functions of PCL.

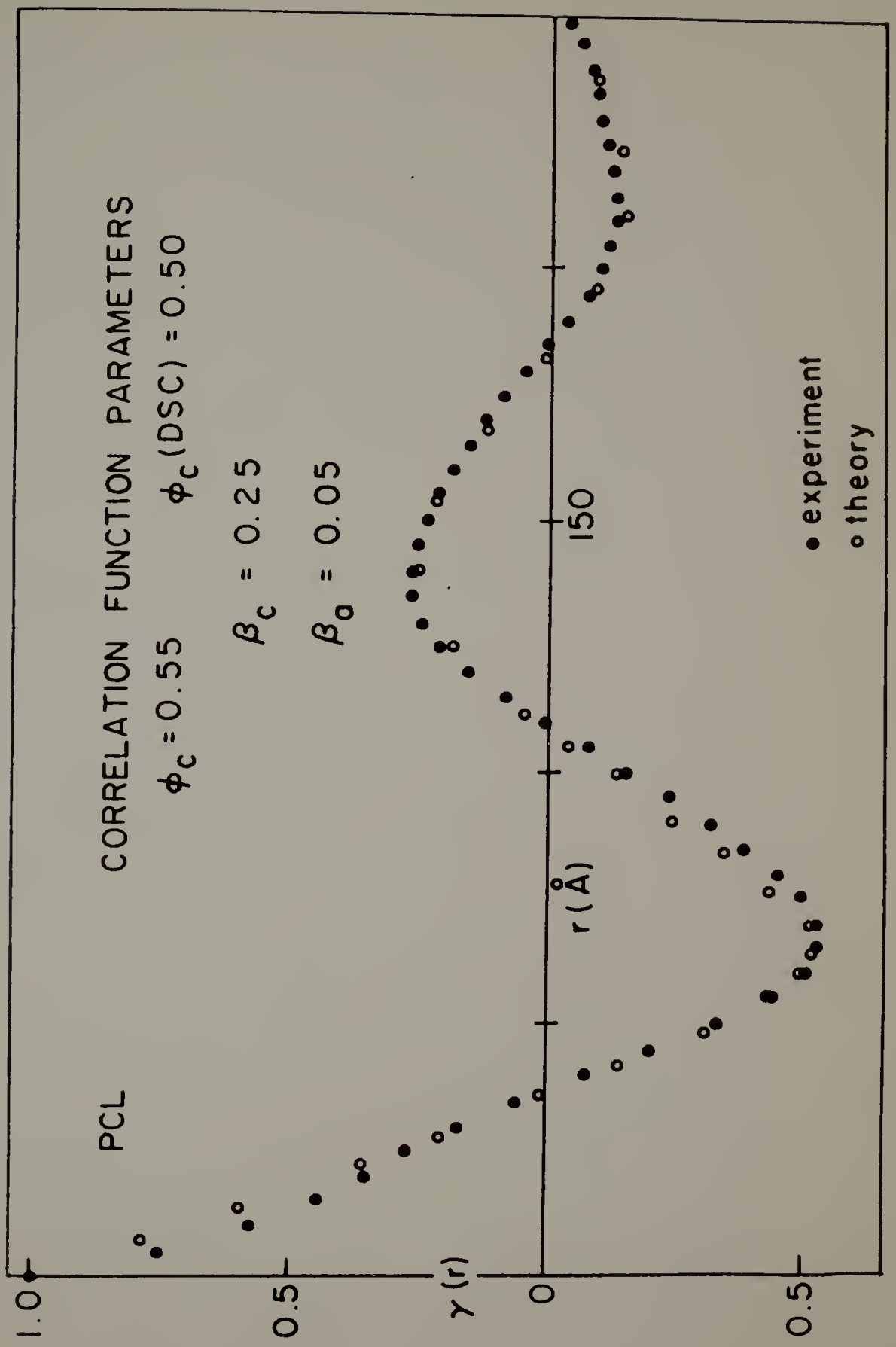
PCL
CORRELATION FUNCTION PARAMETERS
ϕ_c = 0.55
ϕ_c(DSC) = 0.50
β_c = 0.25
β_a = 0.05
1.0
0.5
0
0.5
γ(r)
150
r(Å)
• experiment
∘ theory

Figure 33. Calculated and experimental correlation functions of 90% PCL.

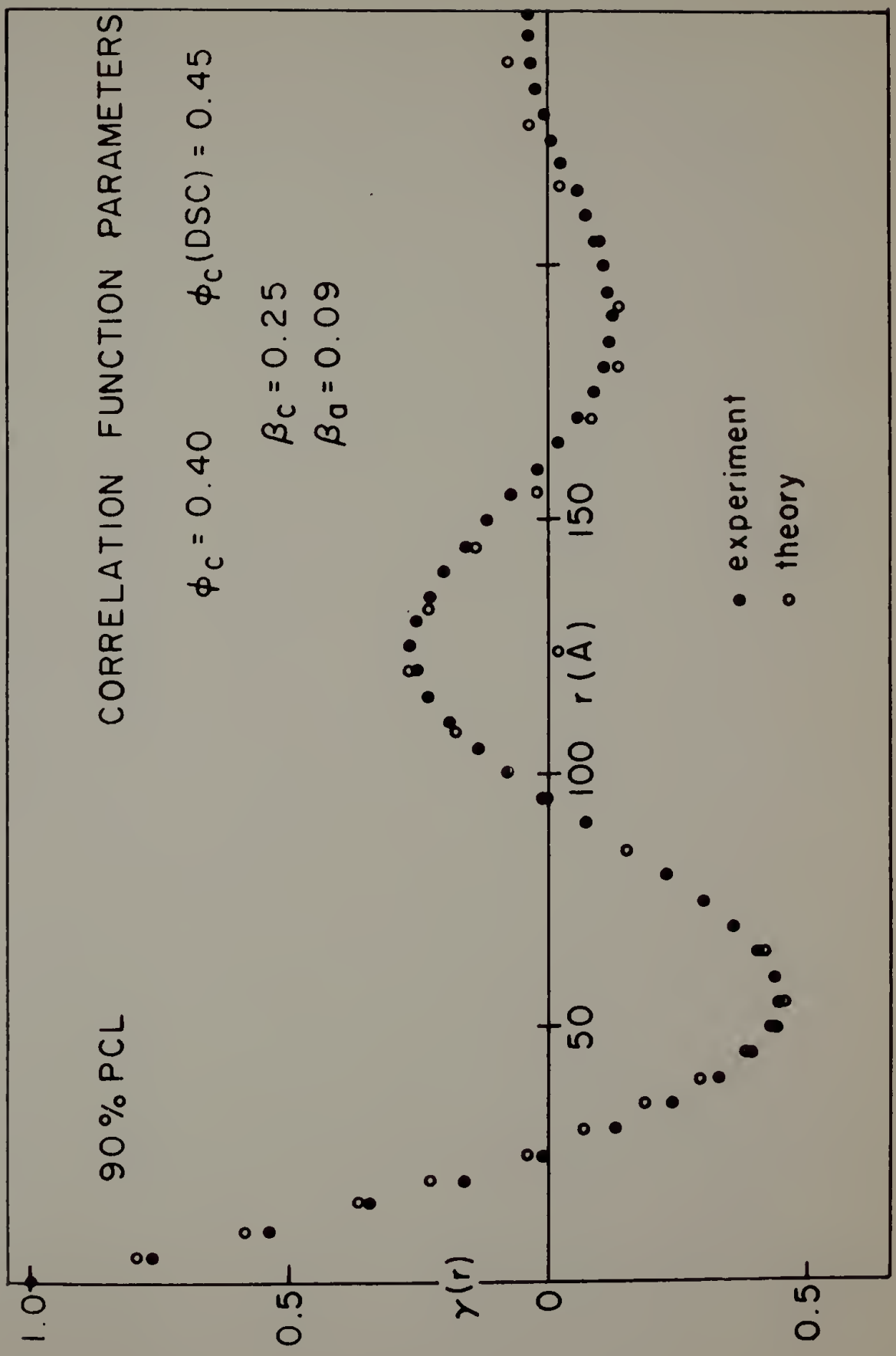
90% PCL
CORRELATION FUNCTION PARAMETERS
ϕ_c = 0.40
ϕ_c(DSC) = 0.45
β_c = 0.25
β_a = 0.09
• experiment
○ theory
1.0
0.5
0
0.5
γ(r)
50
100
150
r(Å)

Figure 34. Level of liquid scattering as a function of composition.

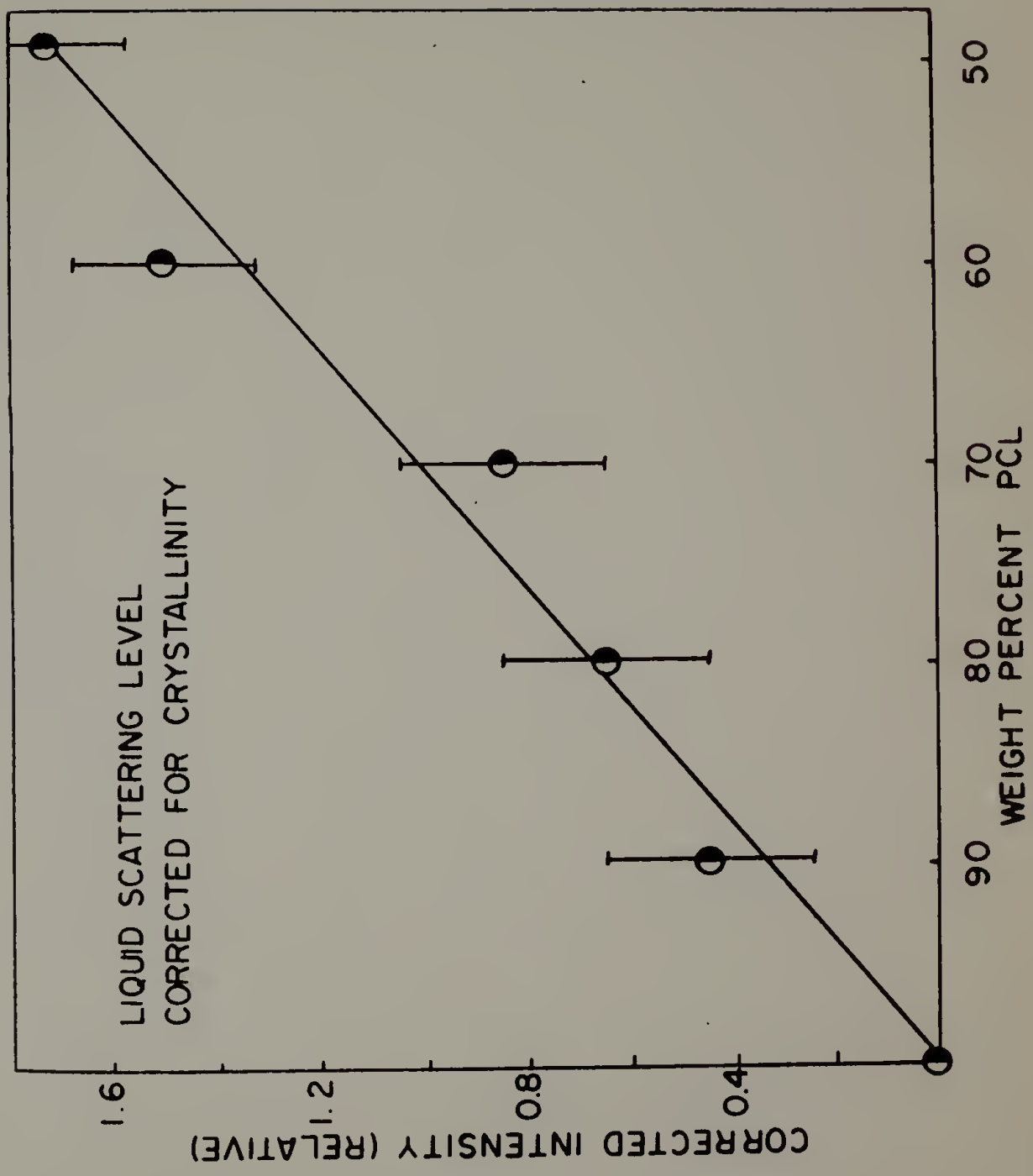
LIQUID SCATTERING LEVEL
CORRECTED FOR CRYSTALLINITY
CORRECTED INTENSITY (RELATIVE)
1.6
1.2
0.8
0.4
90
80
70
60
50
WEIGHT PERCENT PCL

Figure 35. Debye-Bueche analysis for molten samples of 90%, 69%, 59%, and 50% PCL blends.

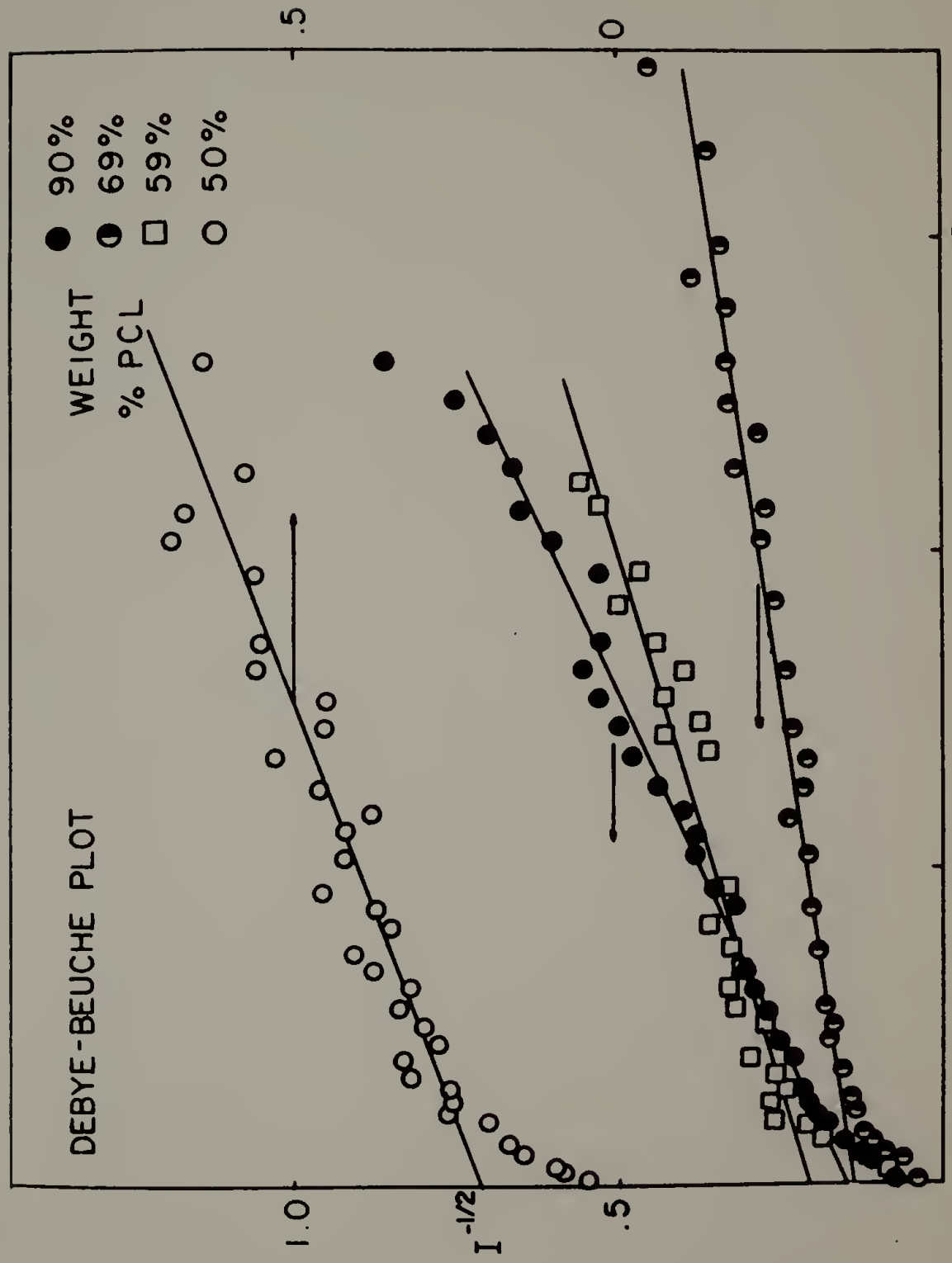
DEBYE-BEUCHE PLOT
WEIGHT % PCL
90%
69%
59%
50%
$I^{-1/2}$
1.0
.5
0
5
10
15
$h^2(10^1)\,nm^{-2}$

Figure 36. Debye-Bueche analysis for 40% and 20% PCL blends.

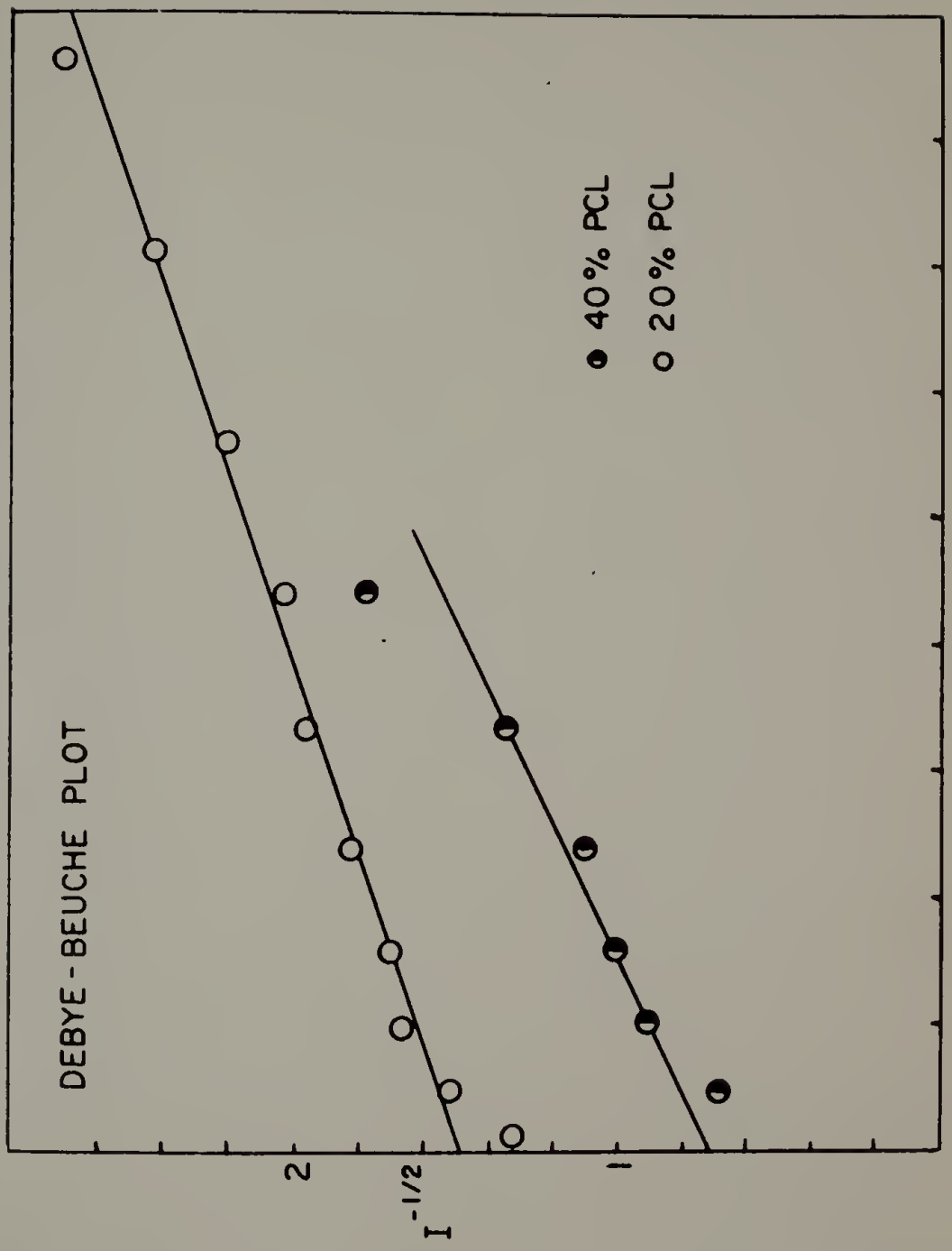
DEBYE-BEUCHE PLOT
● 40% PCL
○ 20% PCL
$I^{-1/2}$
2
1
20
40
60
80
$h^2(nm^{-2}\cdot 10^2)$

Figure 37. Chord lengths for PCL and PVC calculated from the correlation distances.

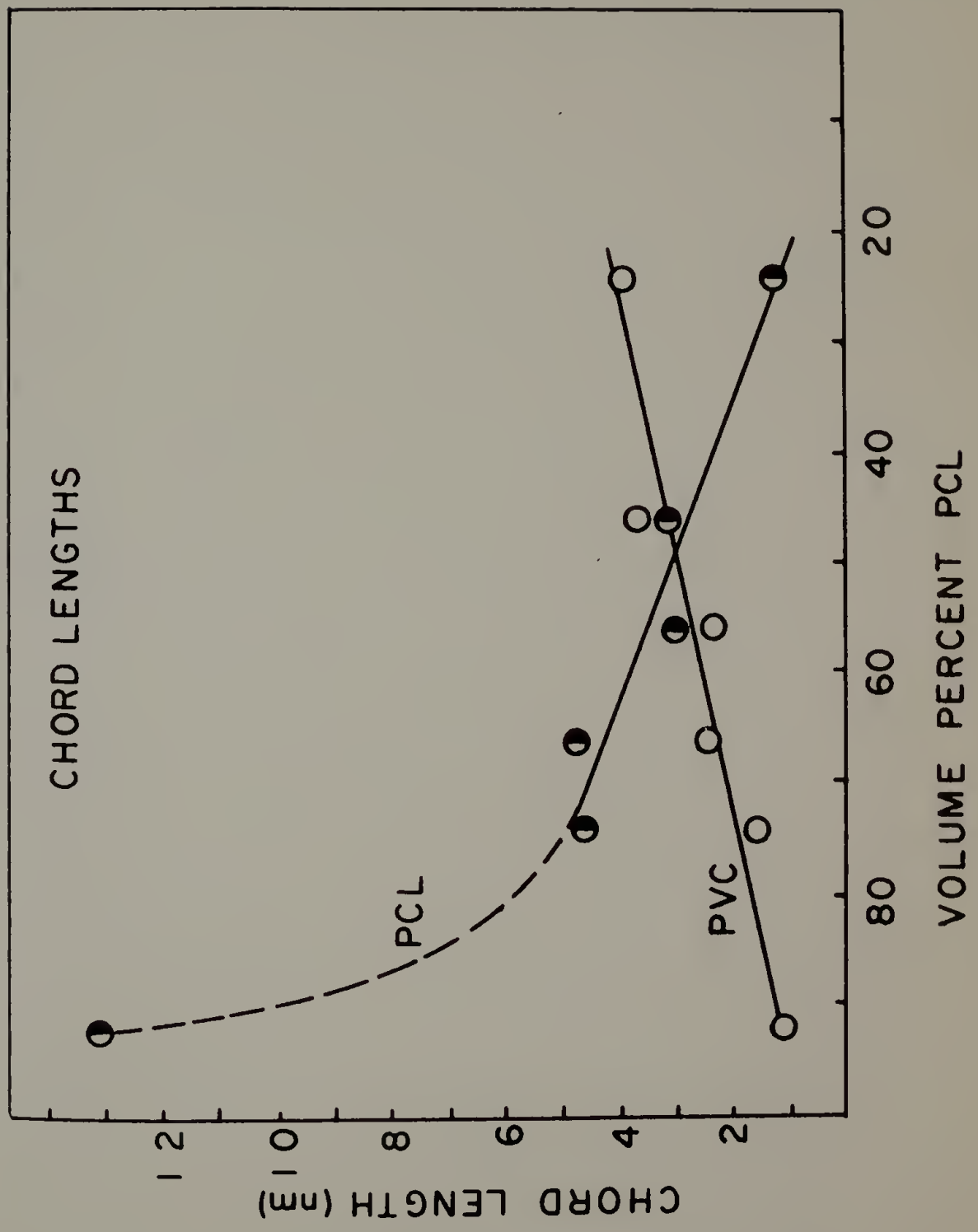
CHORD LENGTHS
PCL
PVC
CHORD LENGTH (nm)
12
10
8
6
4
2
20
40
60
80
VOLUME PERCENT PCL

Figure 38. Sample of a series of PVC/PCL blend infrared spectra as a function of film thickness.

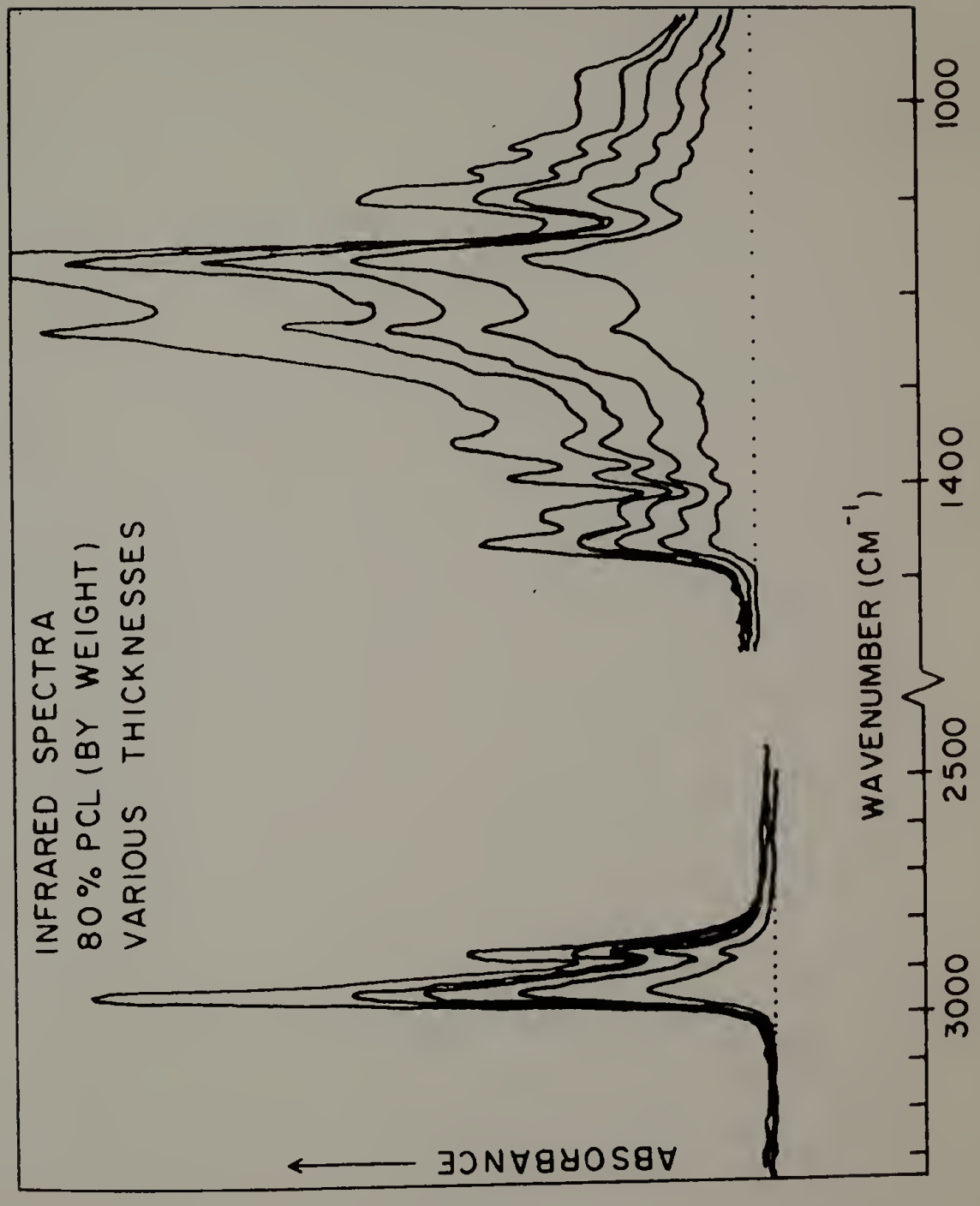
INFRARED SPECTRA
80% PCL (BY WEIGHT)
VARIOUS THICKNESSES
ABSORBANCE
WAVENUMBER (CM^{-1})
3000
2500
1400
1000

Figure 39. Absorbance as a function of film thickness for PVC at several different wavenumbers.

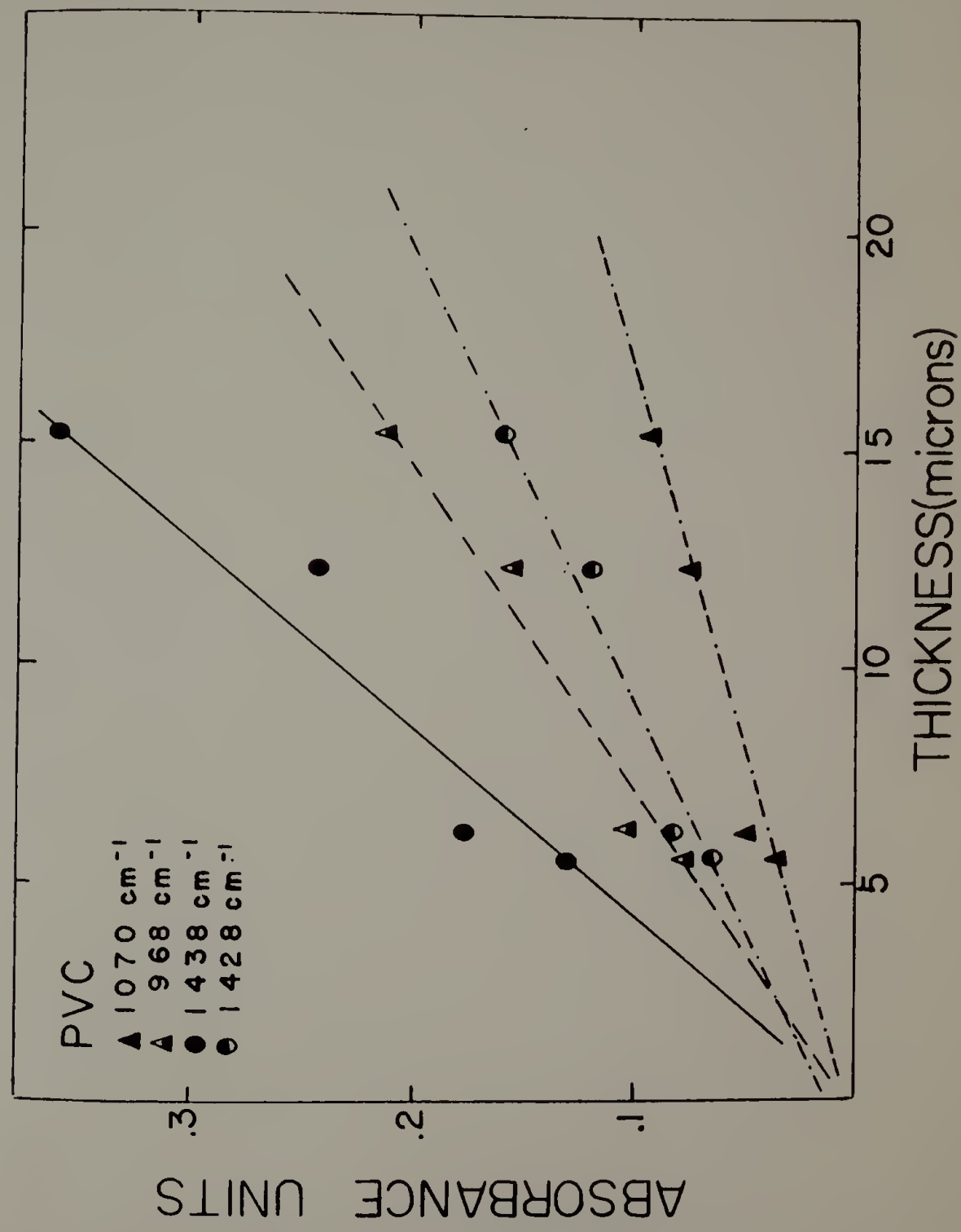
PVC
1070 cm⁻¹
968 cm⁻¹
1438 cm⁻¹
1428 cm⁻¹
ABSORBANCE UNITS
.3
.2
.1
5
10
15
20
THICKNESS(microns)

Figure 40. Absorbance as a function of film thickness for a 49.8% PCL blend at several different wavenumbers.

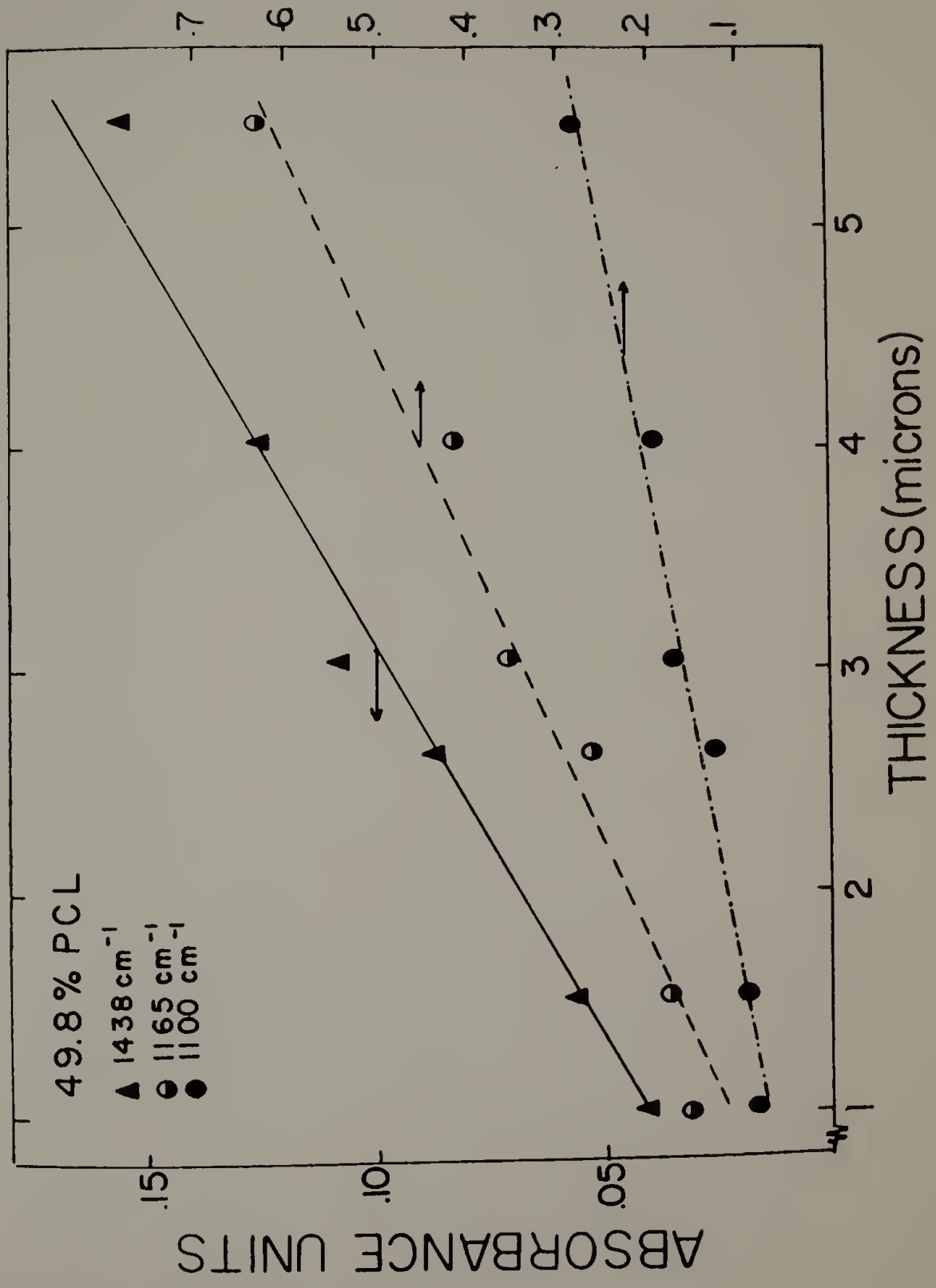
49.8% PCL
1438 cm⁻¹
1165 cm⁻¹
1100 cm⁻¹
ABSORBANCE UNITS
.15
.10
.05
THICKNESS (microns)
1
2
3
4
5
.7
.6
.5
.4
.3
.2
.1

Figure 41. Absorbance as a function of film thickness for an 89.7% PCL blend at several different wavenumbers.

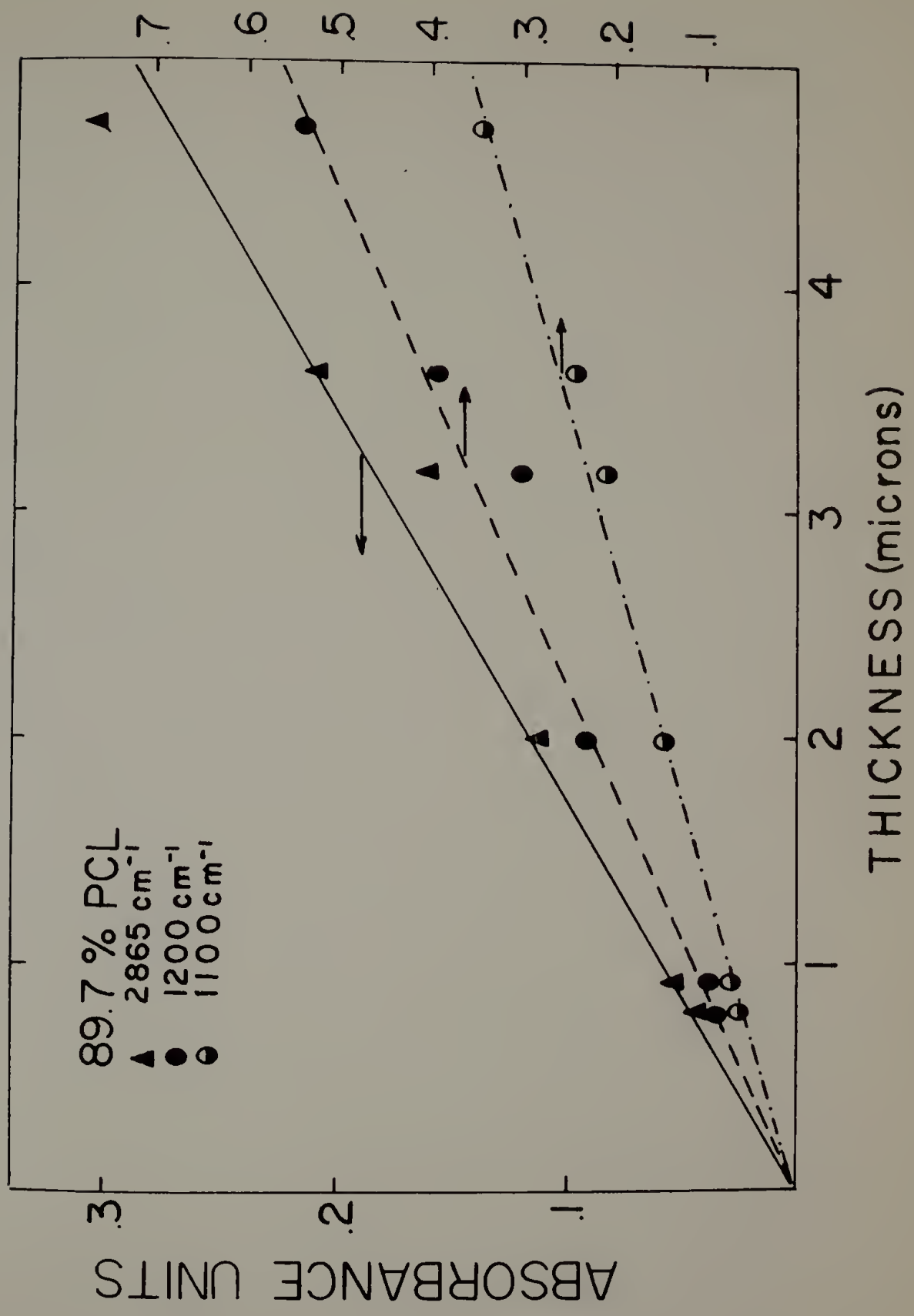
ABSORBANCE UNITS
THICKNESS (microns)
89.7 % PCL
2865 cm⁻¹
1200 cm⁻¹
1100 cm⁻¹

Figure 42. Absorbance as a function of thickness for pure PCL at several different wavenumbers.

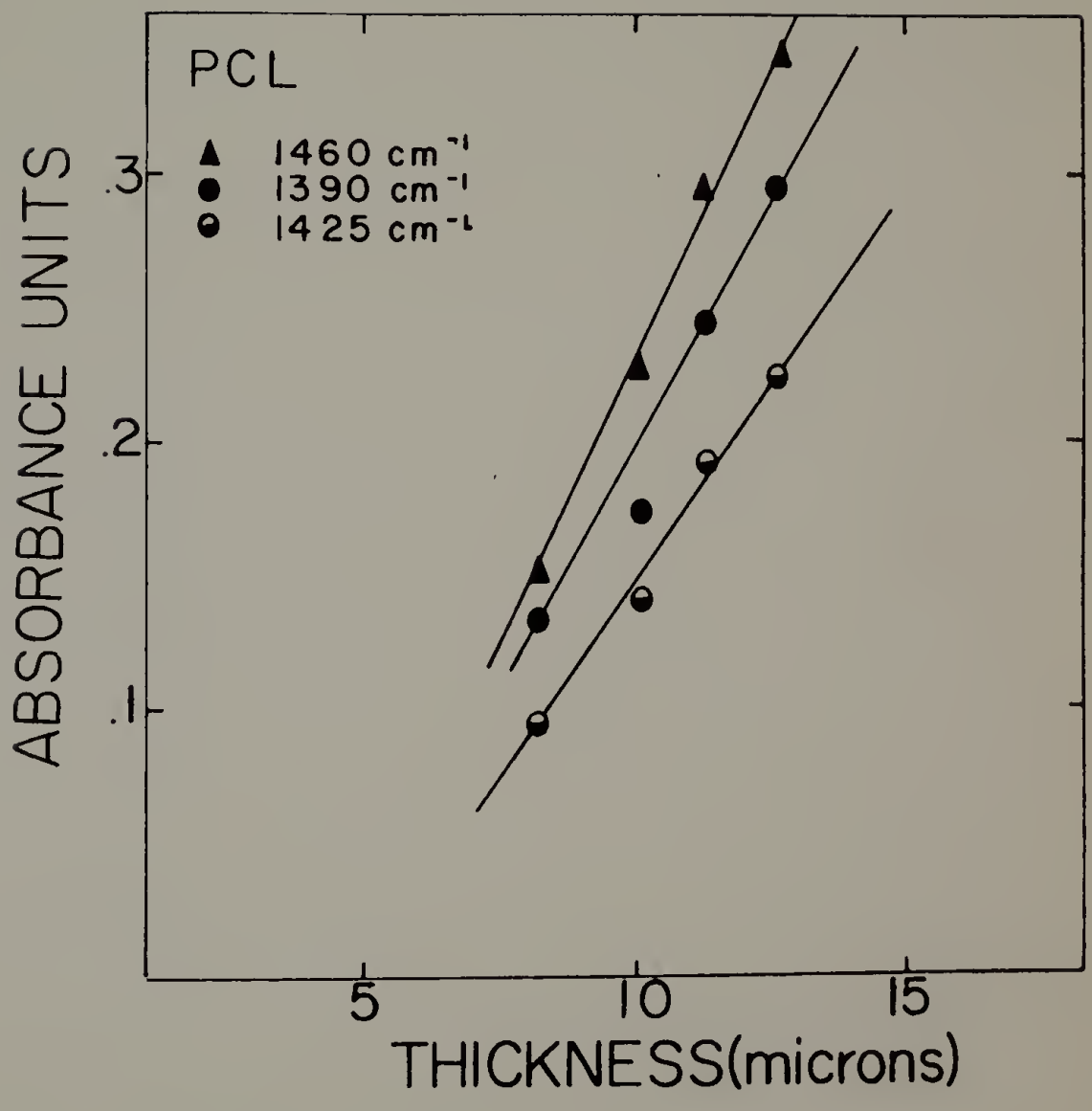
PCL
1460 cm⁻¹
1390 cm⁻¹
1425 cm⁻¹
ABSORBANCE UNITS
.3
.2
.1
5
10
15
THICKNESS(microns)

Figure 43. Extinction coefficient as a function of monomer mole fraction for the 960 cm^{-1} band.

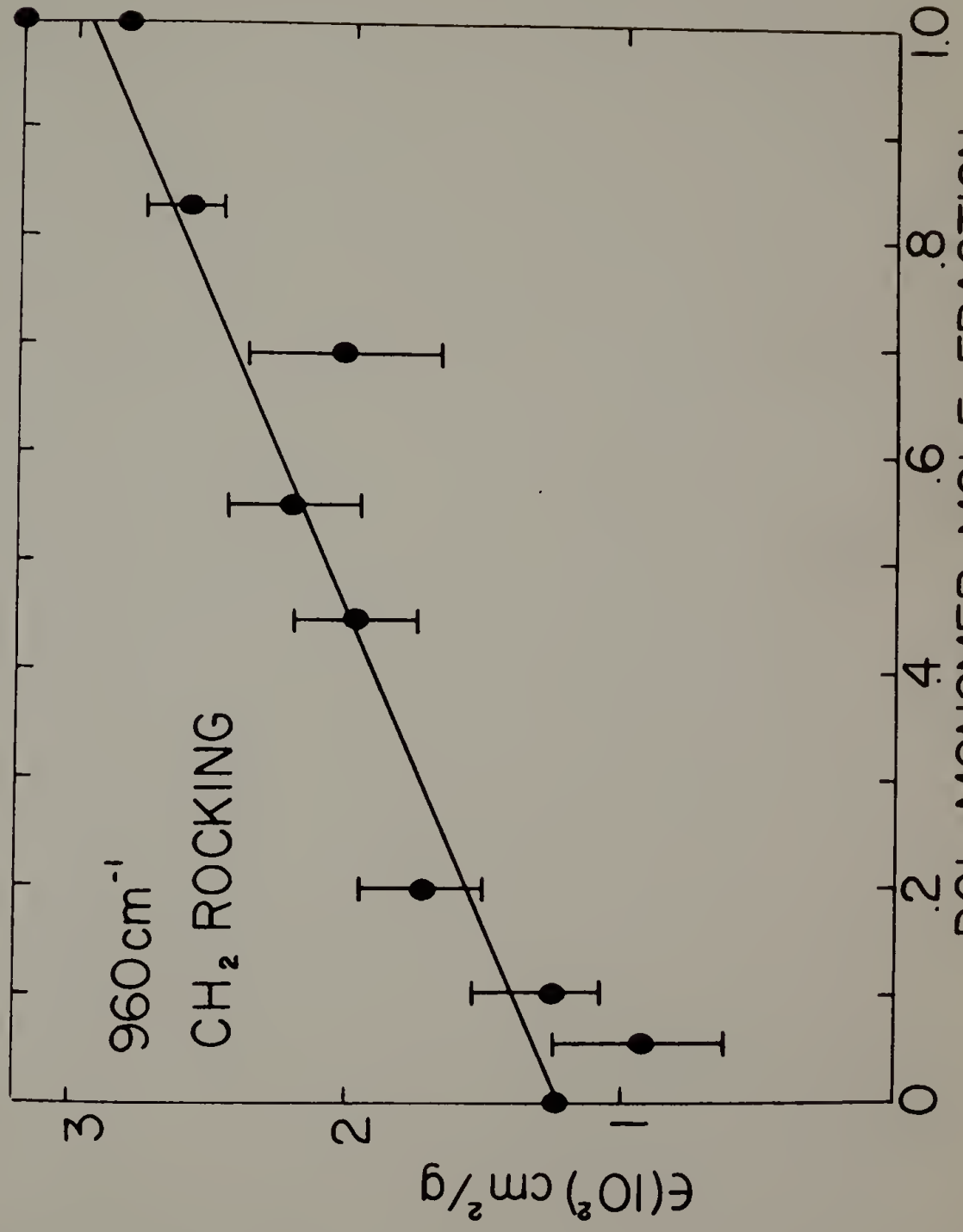
960cm⁻¹
CH₂ ROCKING
ε(10²) cm²/g
PCL MONOMER MOLE FRACTION
0
.2
.4
.6
.8
1.0
1
2
3

Figure 44. Extinction coefficient as a function of monomer mole fraction for the 1100 cm^{-1} band.

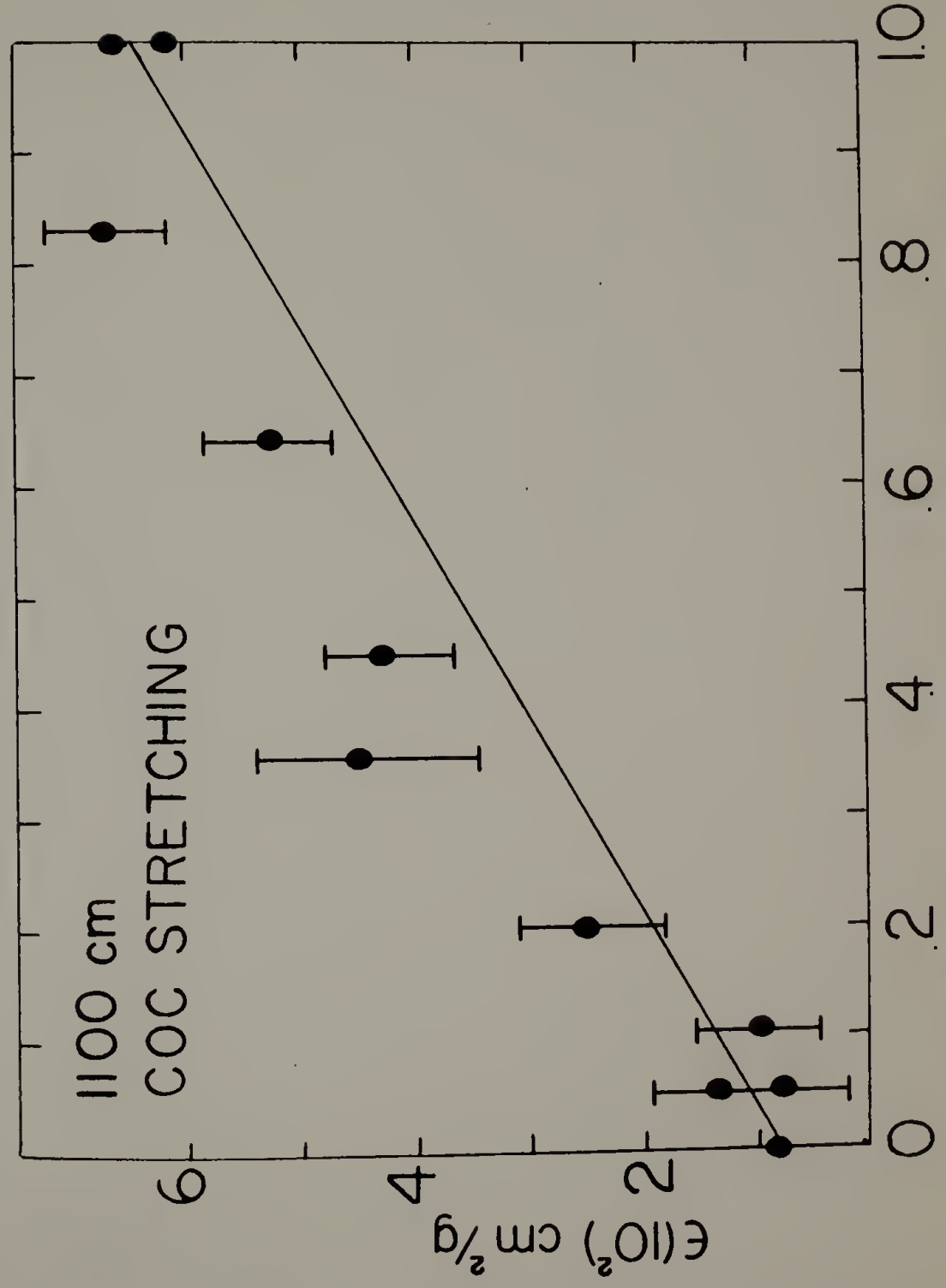
1100 cm
COC STRETCHING
ε(10²) cm²/g
0
2
4
6
.2
.4
.6
.8
1.0
PCL MONOMER MOLE FRACTION

Figure 45. Extinction coefficient as a function of monomer mole fraction for the 1165 cm^{-1} band.

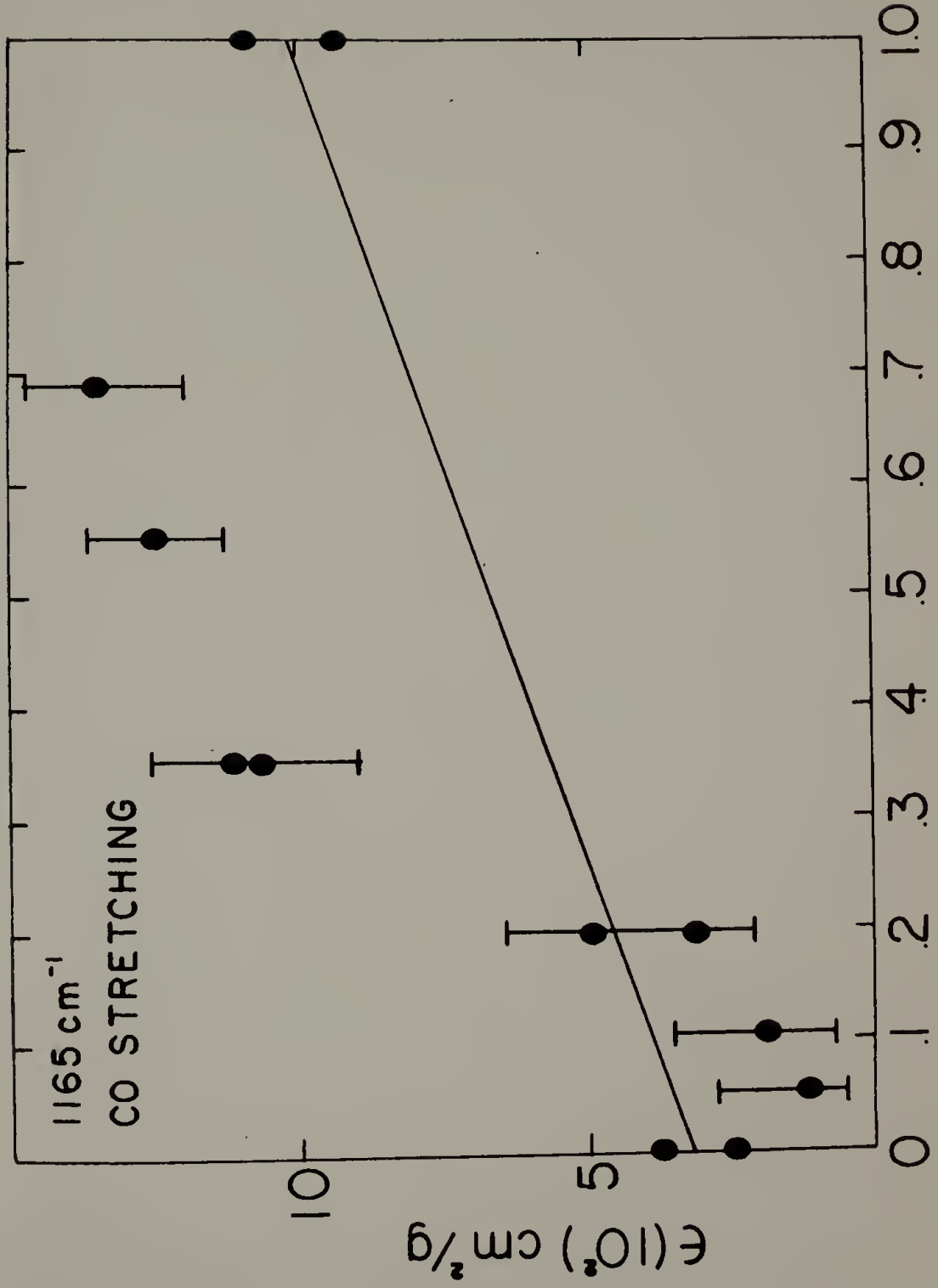
1165 cm⁻¹
CO STRETCHING
ε (10²) cm²/g
0
5
10
0 .1 .2 .3 .4 .5 .6 .7 .8 .9 1.0
PCL MONOMER MOLE FRACTION

Figure 46. Extinction coefficient as a function of monomer mole fraction for the 1200 cm^{-1} band.

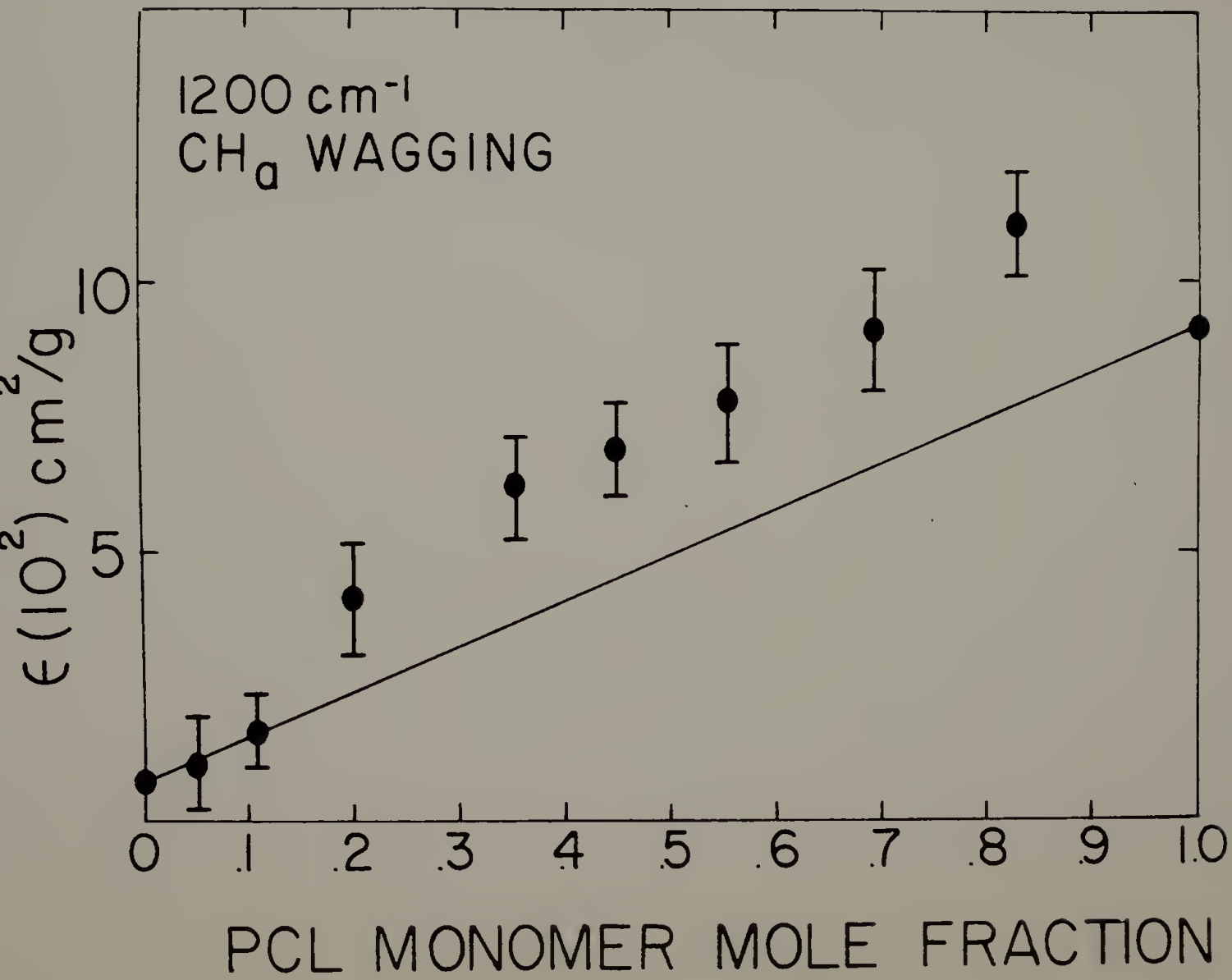
1200 cm⁻¹
CHa WAGGING
ε(10²) cm²/g
10
5
0
.1
.2
.3
.4
.5
.6
.7
.8
.9
1.0
PCL MONOMER MOLE FRACTION

Figure 47. Extinction coefficient as a function of monomer mole fraction for the 1240 cm^{-1} band.

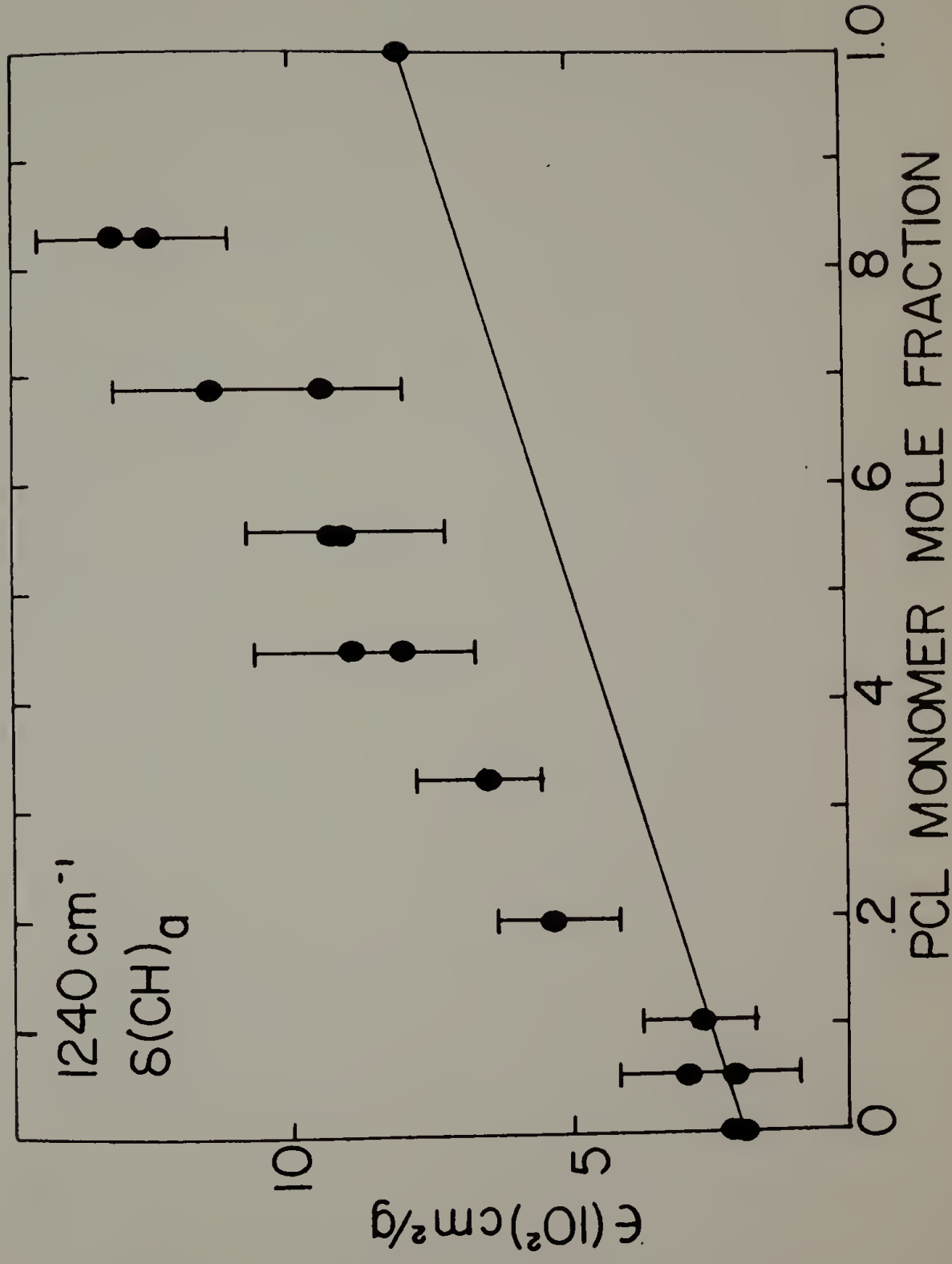
1240 cm⁻¹
δ(CH)a
ε(10²)cm²/g
10
5
0
.2
4
6
8
1.0
PCL MONOMER MOLE FRACTION

Figure 48. Extinction coefficient as a function of monomer mole fraction for the 1255 cm^{-1} band.

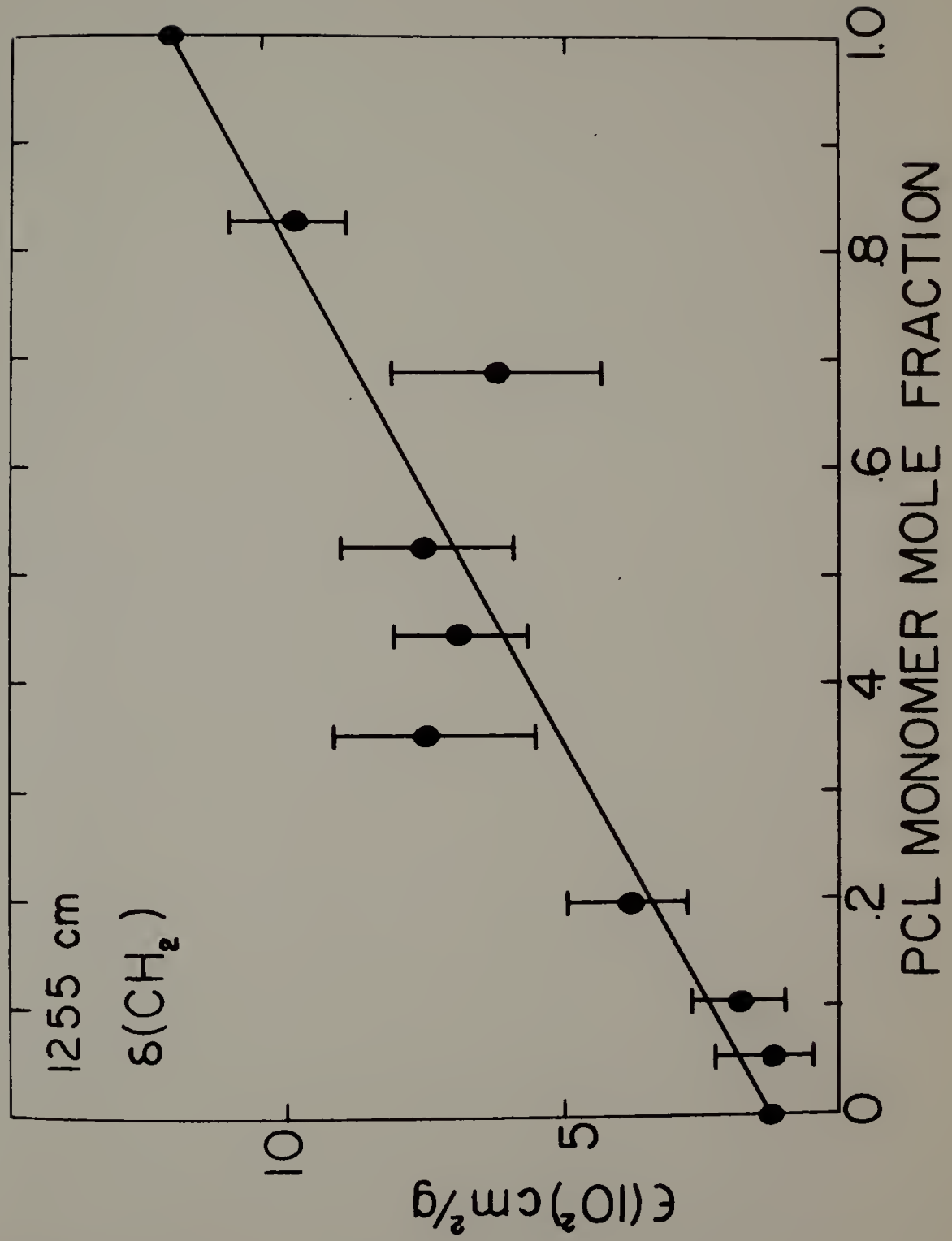
1255 cm
δ(CH2)
ε(10²)cm²/g
10
5
0
.2
.4
.6
.8
1.0
PCL MONOMER MOLE FRACTION

Figure 49. Extinction coefficient as a function of monomer mole fraction for the 1355 cm^{-1} band.

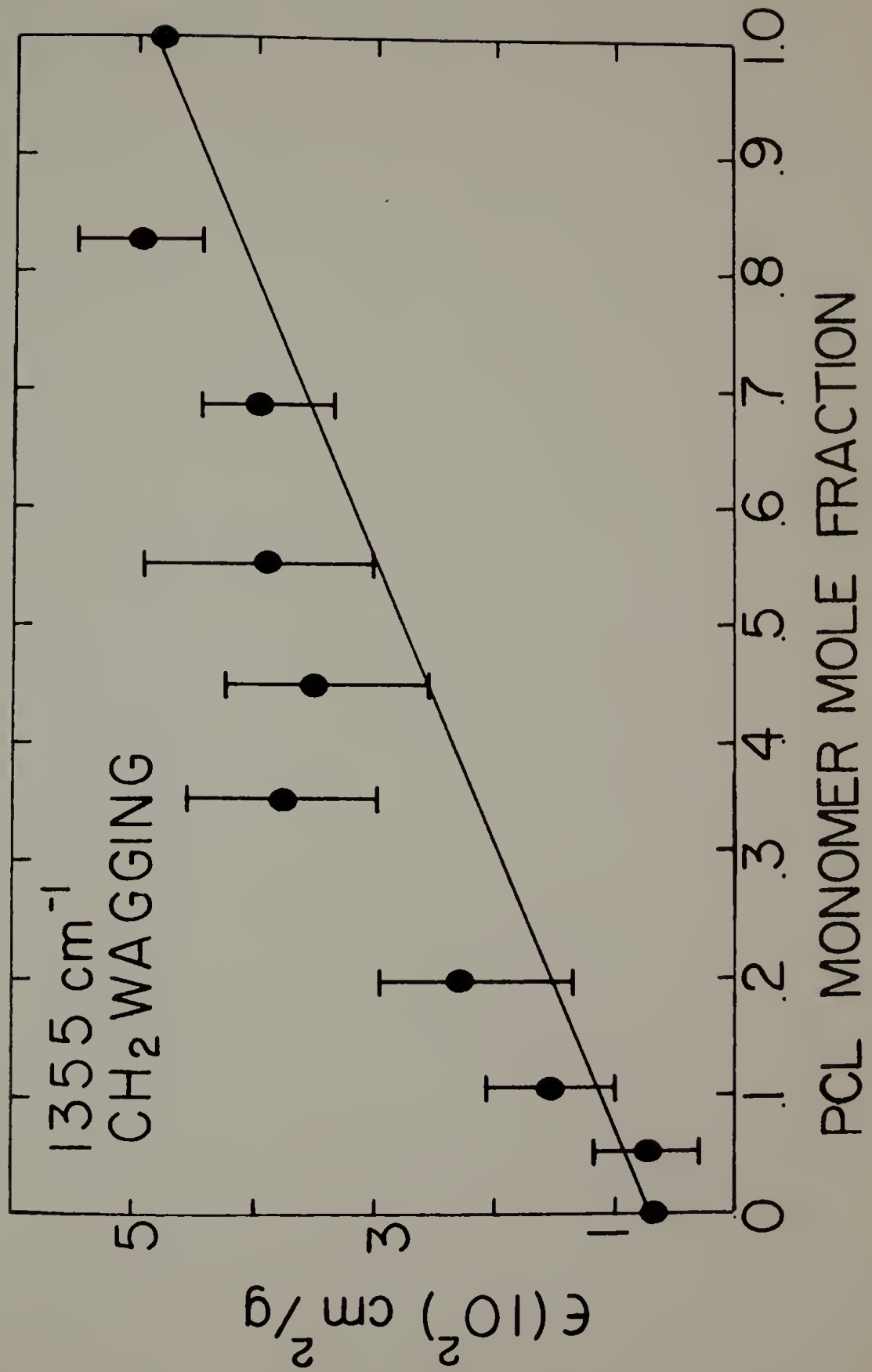
1355 cm⁻¹
CH₂ WAGGING
ε (10²) cm²/g
5
3
1
0
.1
.2
.3
.4
.5
.6
.7
.8
.9
1.0
PCL MONOMER MOLE FRACTION

Figure 50. Extinction coefficient as a function of monomer mole fraction for the 1436 cm^{-1} band.

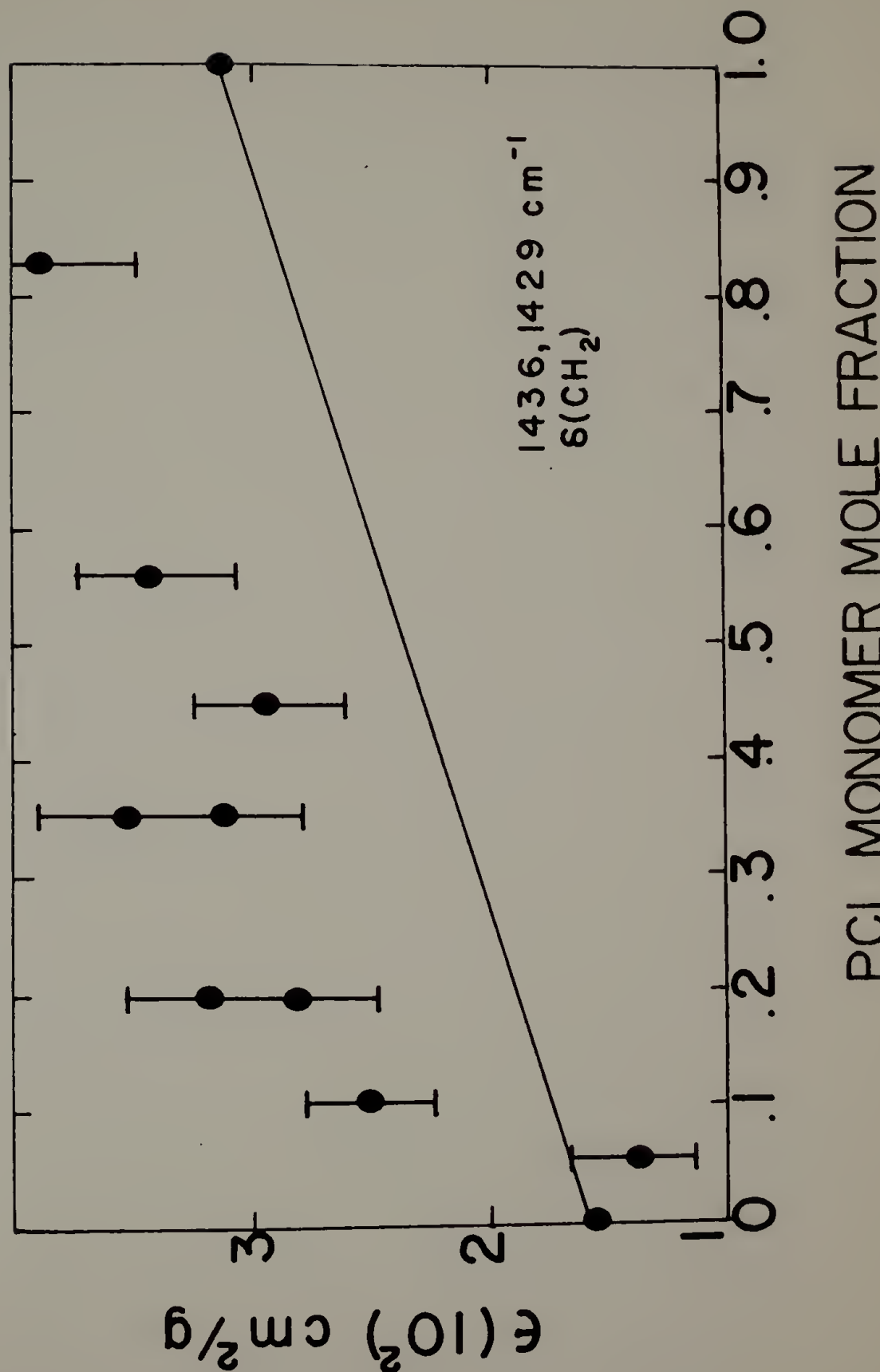
1436, 1429 cm⁻¹
δ(CH₂)
ε (10²) cm²/g
1
2
3
0
.1
.2
.3
.4
.5
.6
.7
.8
.9
1.0
PCL MONOMER MOLE FRACTION

Figure 51. Extinction coefficient as a function of monomer mole fraction for the 1460 cm^{-1} band.

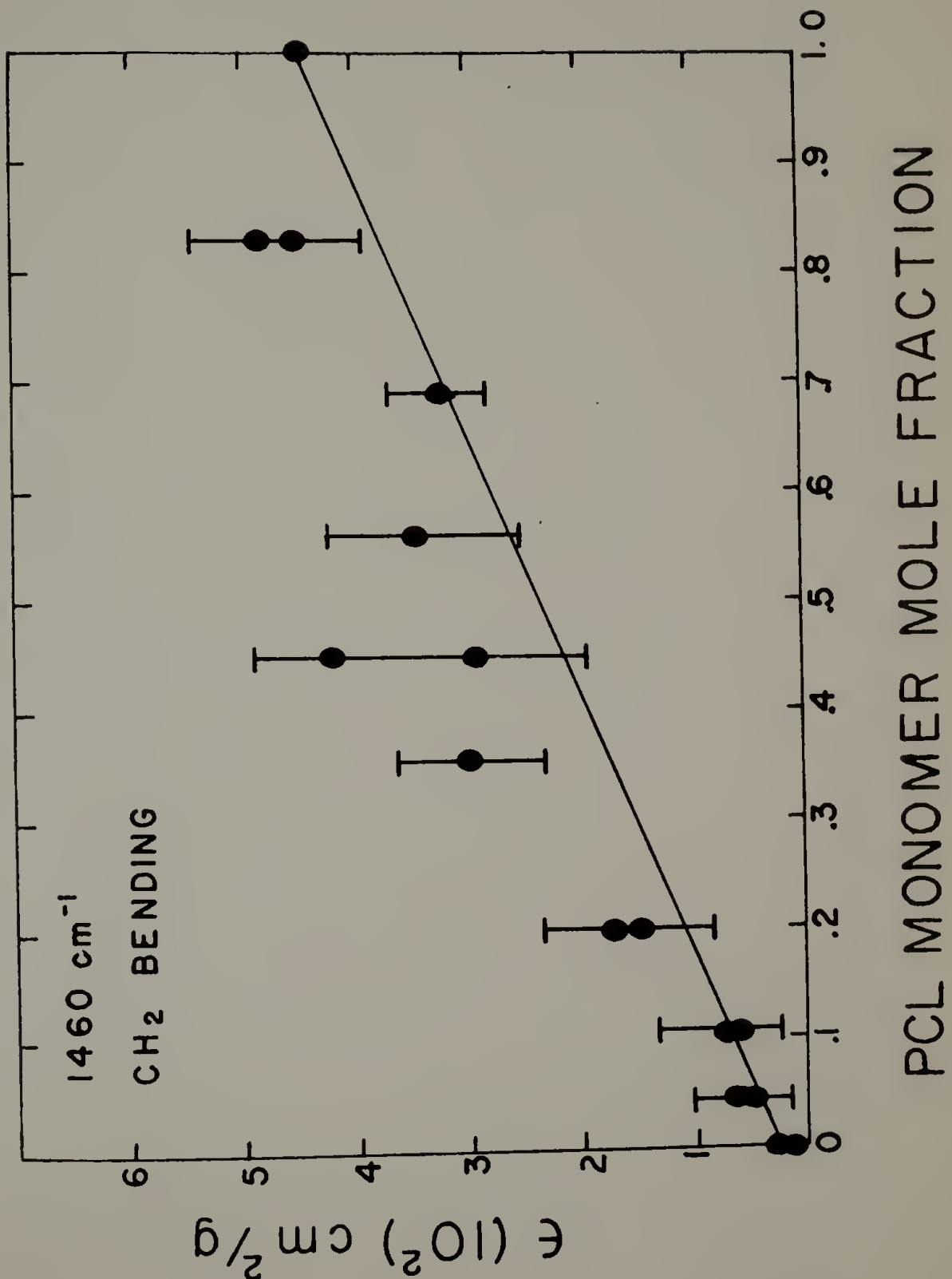
1460 cm⁻¹
CH₂ BENDING
ε (10²) cm²/g
0
1
2
3
4
5
6
.1
.2
.3
.4
.5
.6
.7
.8
.9
1.0
PCL MONOMER MOLE FRACTION

Figure 52. Extinction coefficient as a function of monomer mole fraction for the 2835 cm^{-1} band.

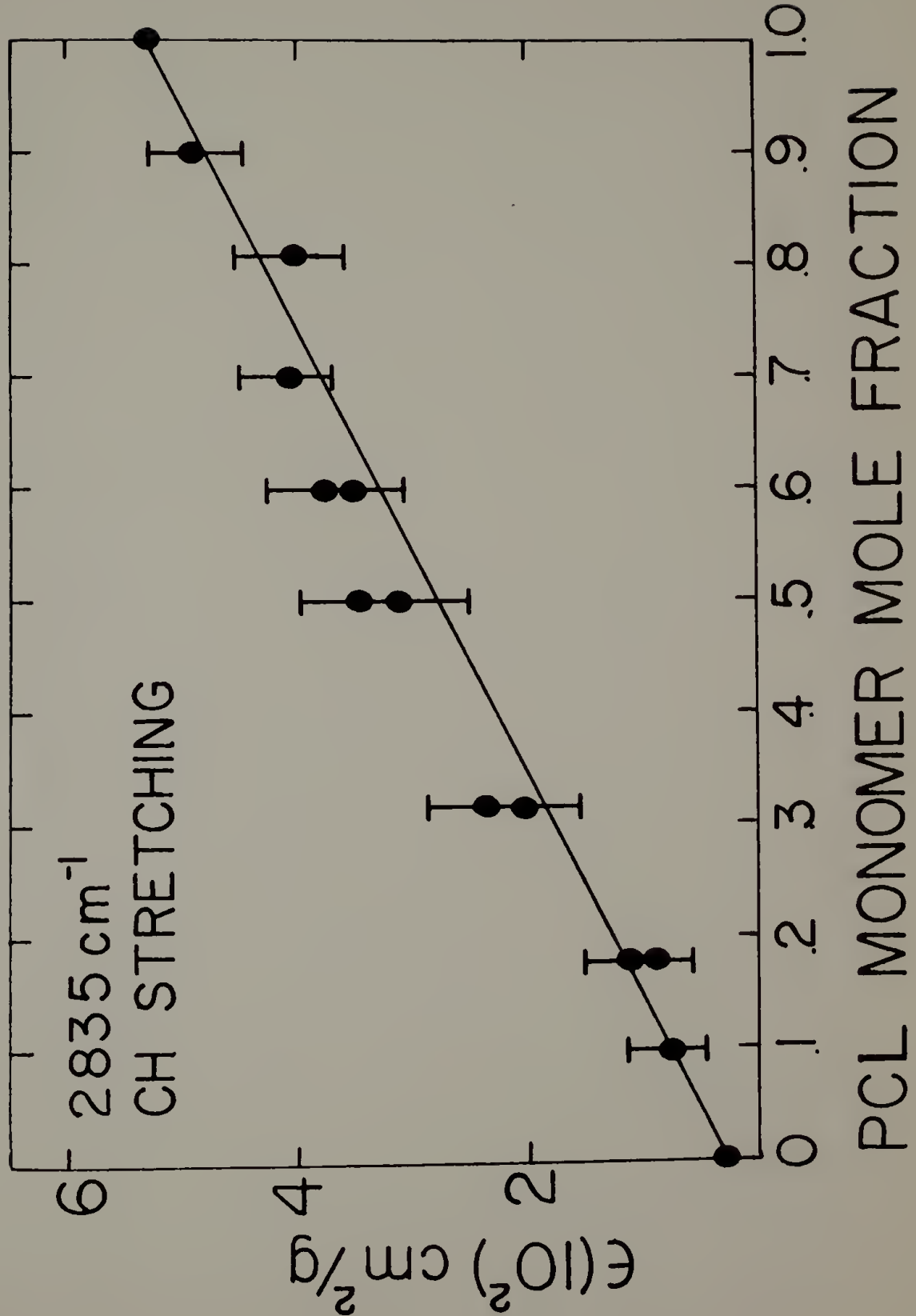
2835 cm⁻¹
CH STRETCHING
ε(10²) cm²/g
PCL MONOMER MOLE FRACTION
0
.1
.2
.3
.4
.5
.6
.7
.8
.9
1.0
2
4
6

Figure 53. Carbonyl stretching band as a function of composition.

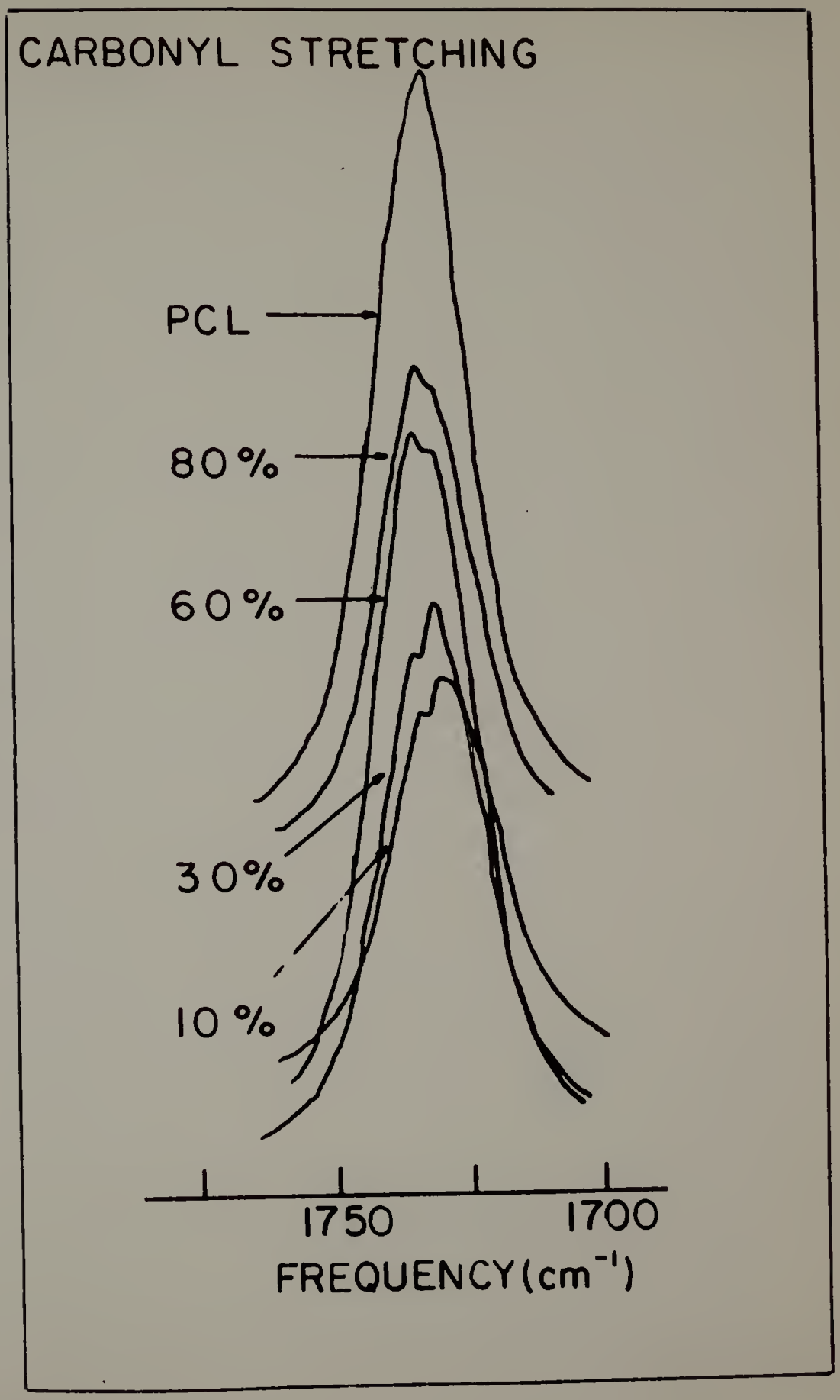
CARBONYL STRETCHING
PCL
80%
60%
30%
10%
1750
1700
FREQUENCY(cm⁻¹)

Figure 54. Schematic illustration of a possible interaction occurring in PCL-PVC blends.

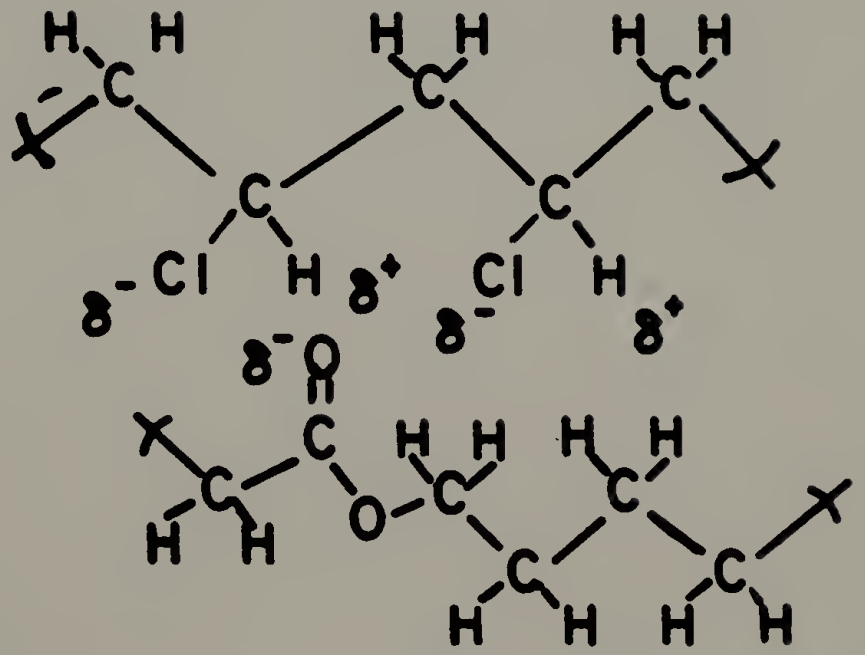

ONE TYPE OF INTERACTION
BETWEEN PVC AND PCL

Figure 55. SAXS profile of pure PVC.

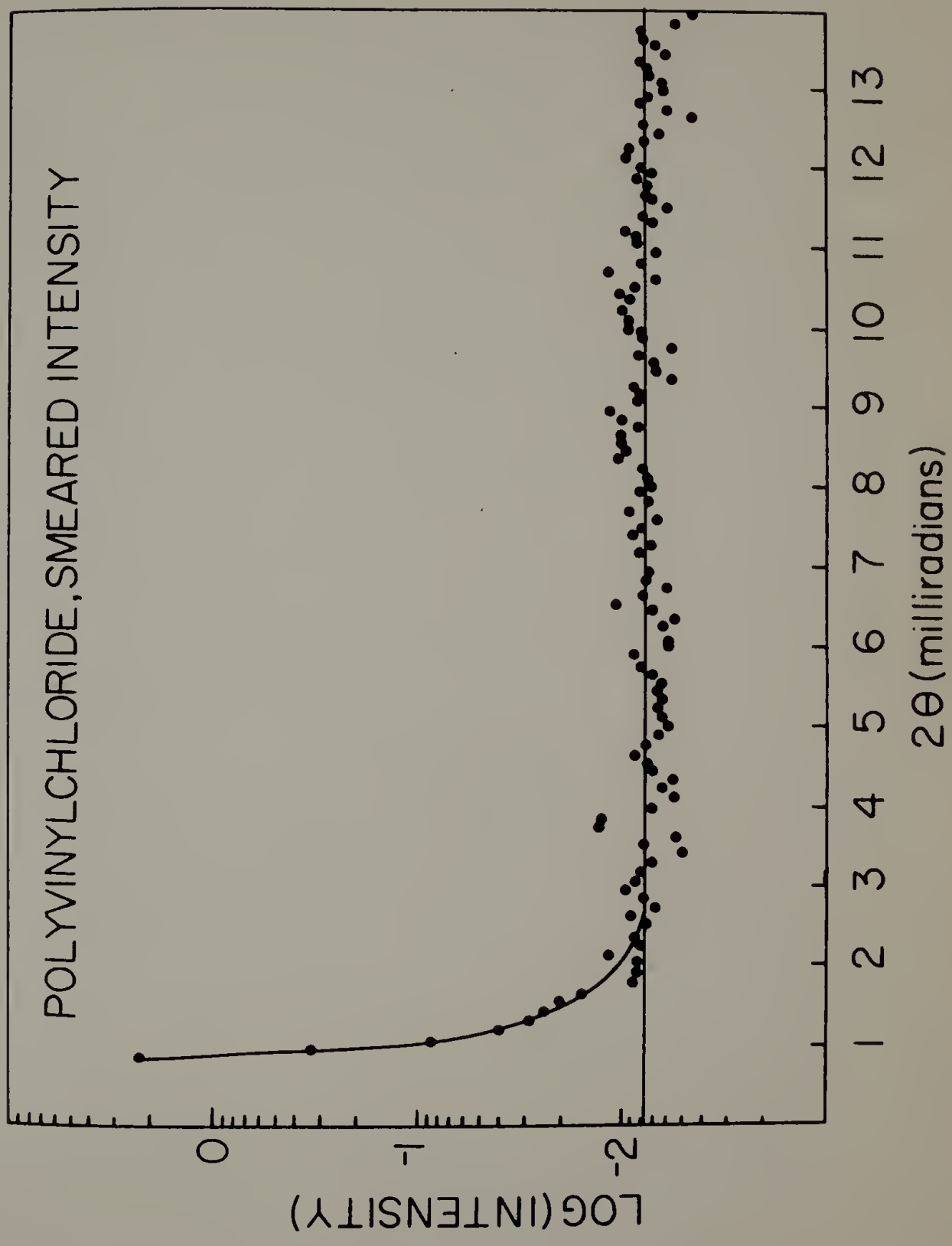
POLYVINYLCHLORIDE, SMEARED INTENSITY
LOG (INTENSITY)
0
-1
-2
1 2 3 4 5 6 7 8 9 10 11 12 13
2θ (milliradians)

Figure 56. Comparison of desmeared SAXS intensity of PVC with data of Straff and Uhlmann.

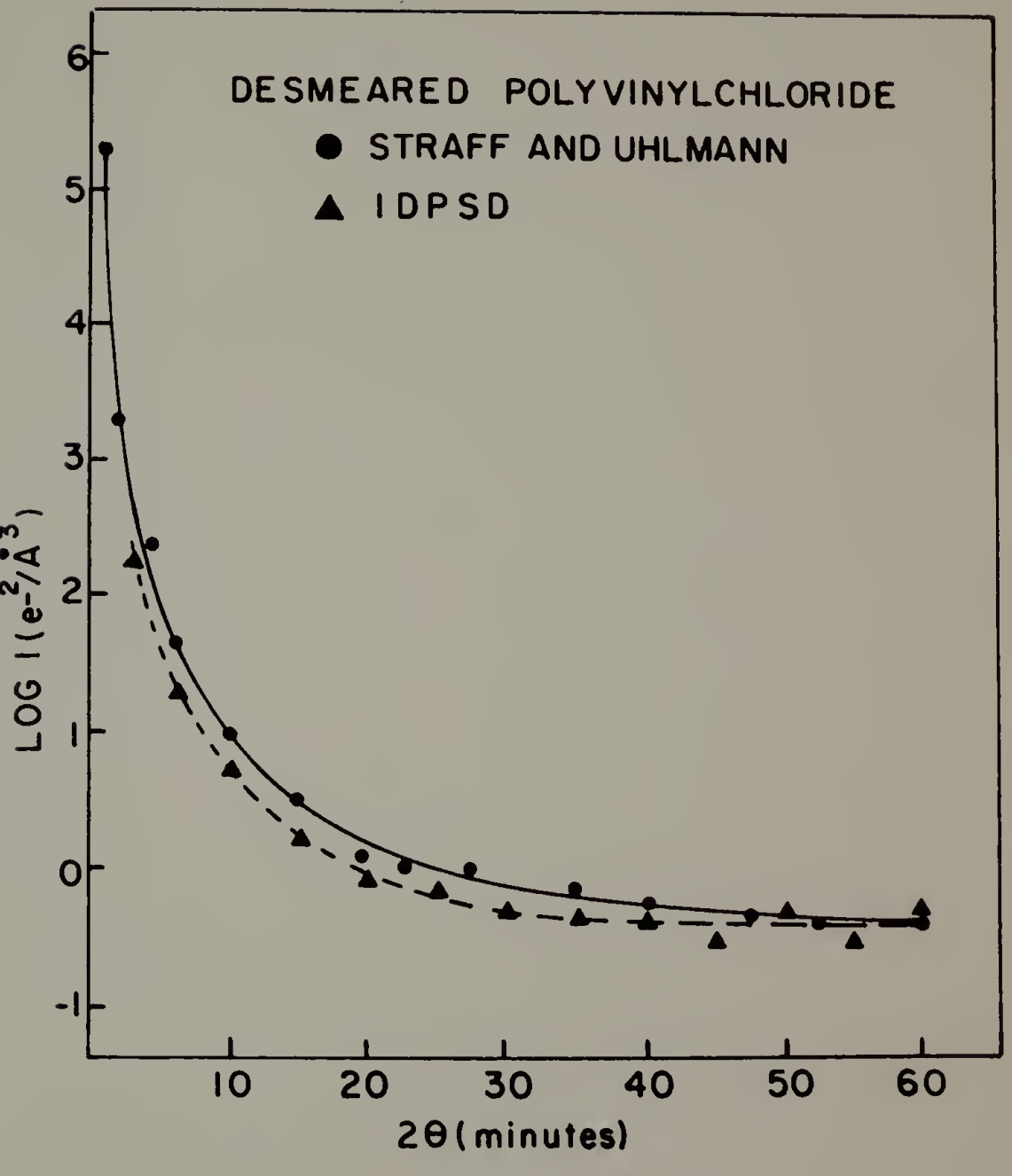
DESMEARED POLYVINYLCHLORIDE
STRAFF AND UHLMANN
IDPSD
LOG I (e⁻²/Å³)
6
5
4
3
2
1
0
-1
10
20
30
40
50
60
2θ (minutes)

Figure 57. SAXS intensities for dilute solid PVC/PCL solutions. Concentrations are in grams x 10^2 PCL/cm^3 solution.

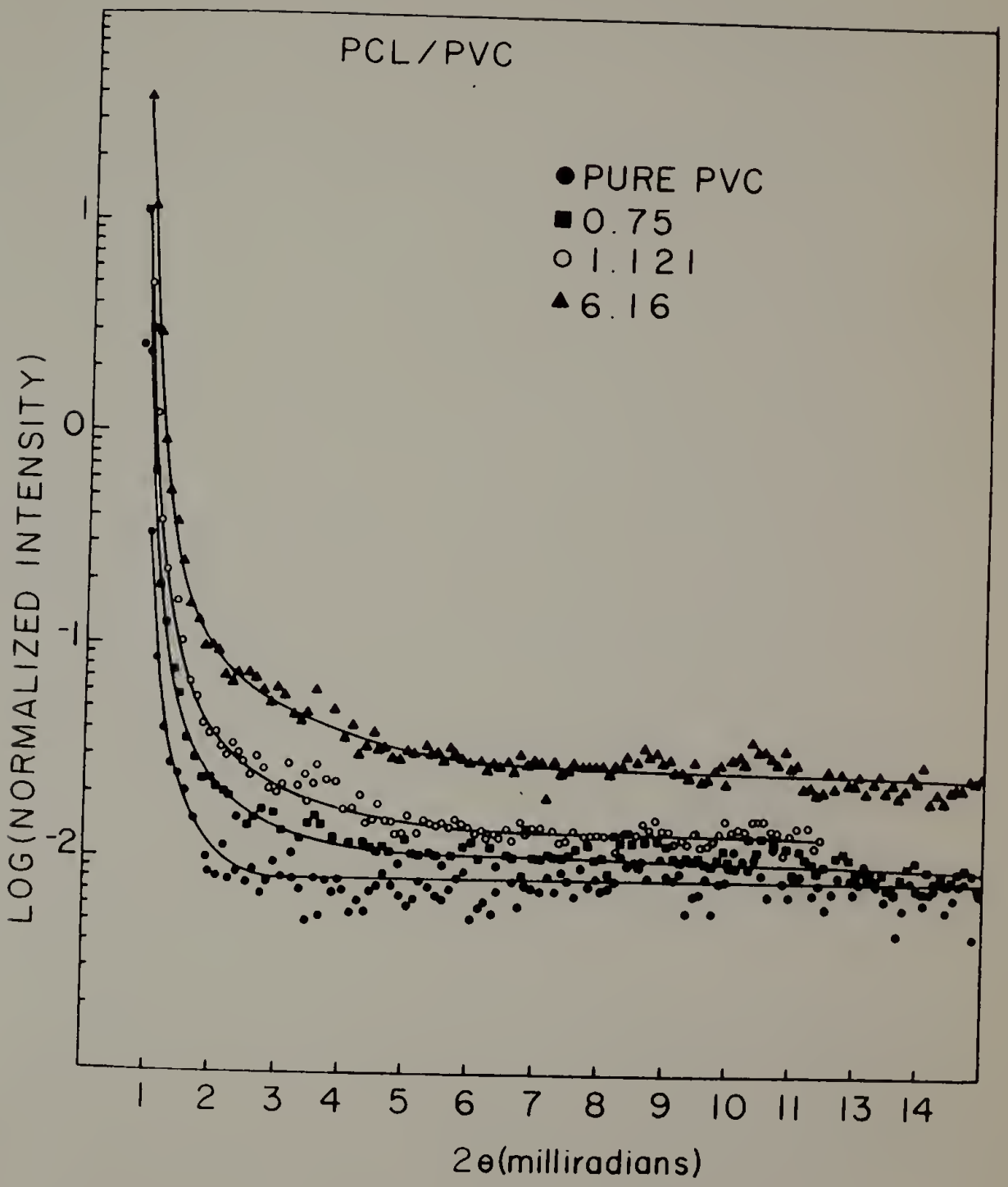
PCL/PVC
PURE PVC
0.75
1.121
6.16
LOG(NORMALIZED INTENSITY)
0
-1
-2
1
2
3
4
5
6
7
8
9
10
11
13
14
2θ(milliradians)

Figure 58. Guinier analysis of PVC/PCL blends using smeared intensities. Concentrations are in g x 10^2 PCL/cm^3 solution.

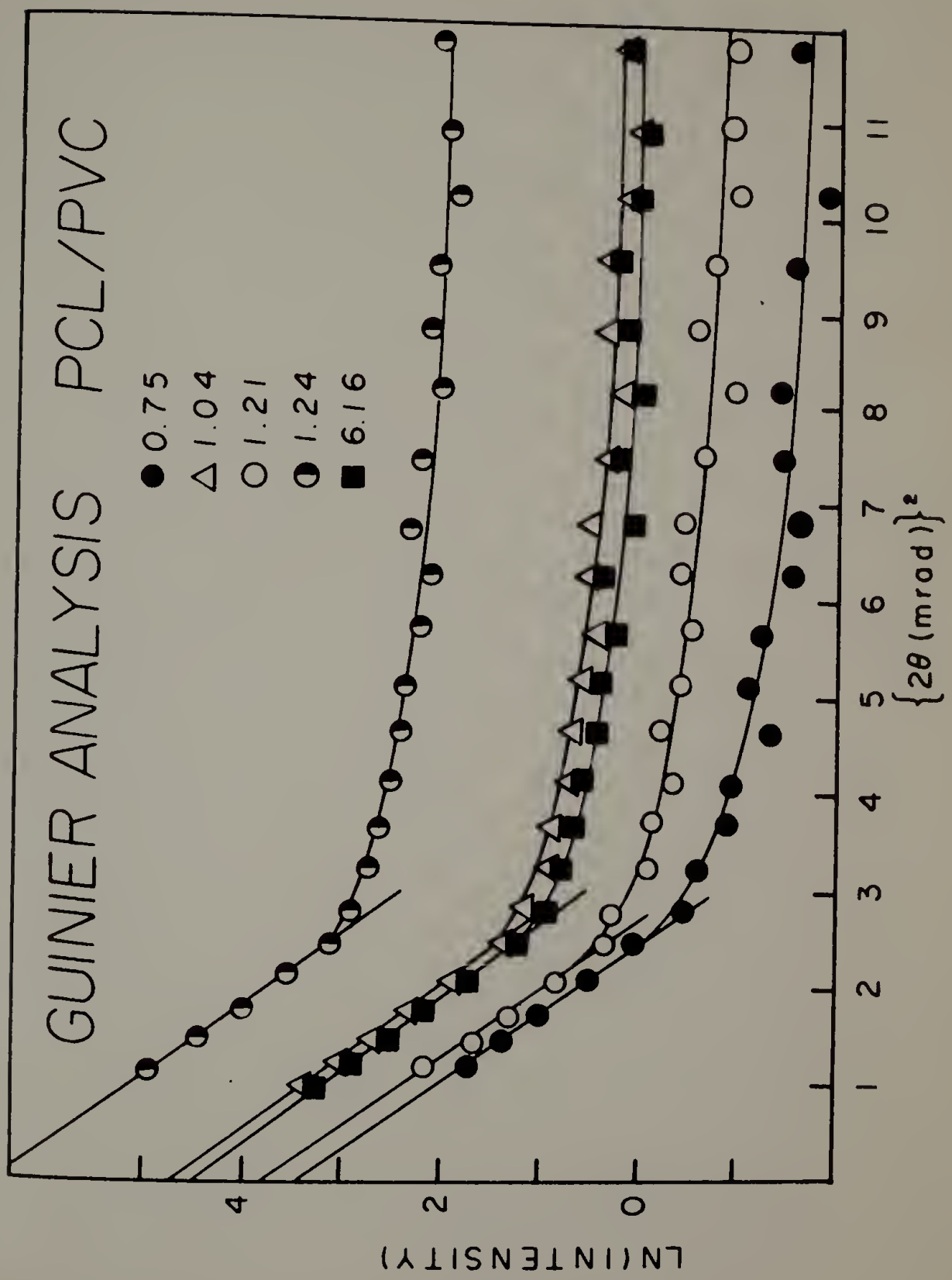
GUINIER ANALYSIS PCL/PVC
● 0.75
△ 1.04
○ 1.21
◑ 1.24
■ 6.16
LN(INTENSITY)
4
2
0
1
2
3
4
5
6
7
8
9
10
11
{2θ (mrad)}²

Figure 59. Guinier analysis of PVC/PCL blends using desmeared intensities. Concentrations are in g x 10^2 PCL/cm^3 solution.

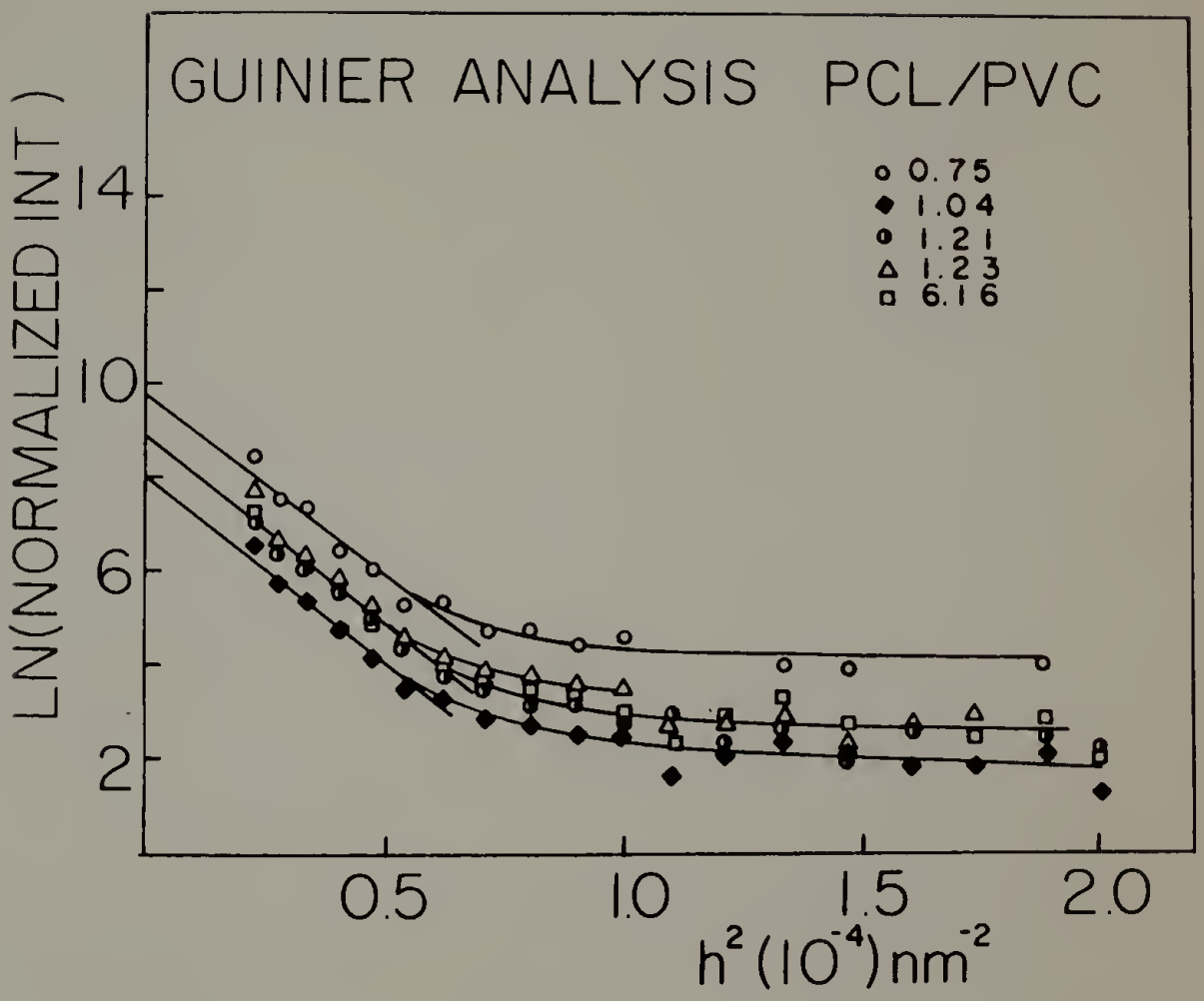
GUINIER ANALYSIS PCL/PVC
0.75
1.04
1.21
1.23
6.16
LN(NORMALIZED INT)
14
10
6
2
0.5
1.0
1.5
2.0
h² (10⁻⁴) nm⁻²

Figure 60. Dilute solution data of Koleske and Lundberg for PCL in DMF at 30°C.

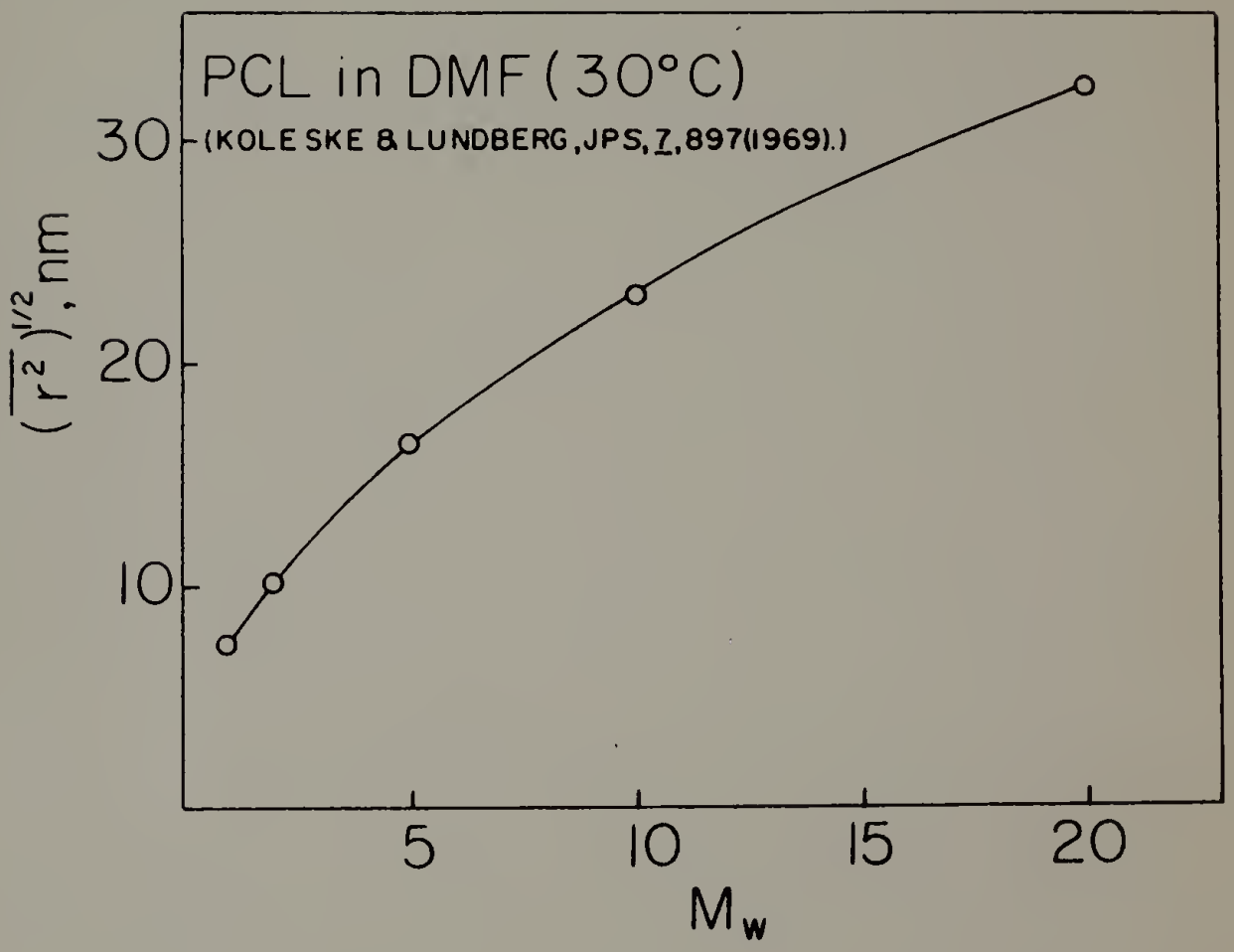
PCL in DMF (30°C)
(KOLESKE & LUNDBERG, JPS, 7, 897(1969).)
30
20
10
$(\overline{r^2})^{1/2}$, nm
5
10
15
20
M_w

Figure 61. Plot of KC/R(0) as a function of composition for PCL/PVC blends.

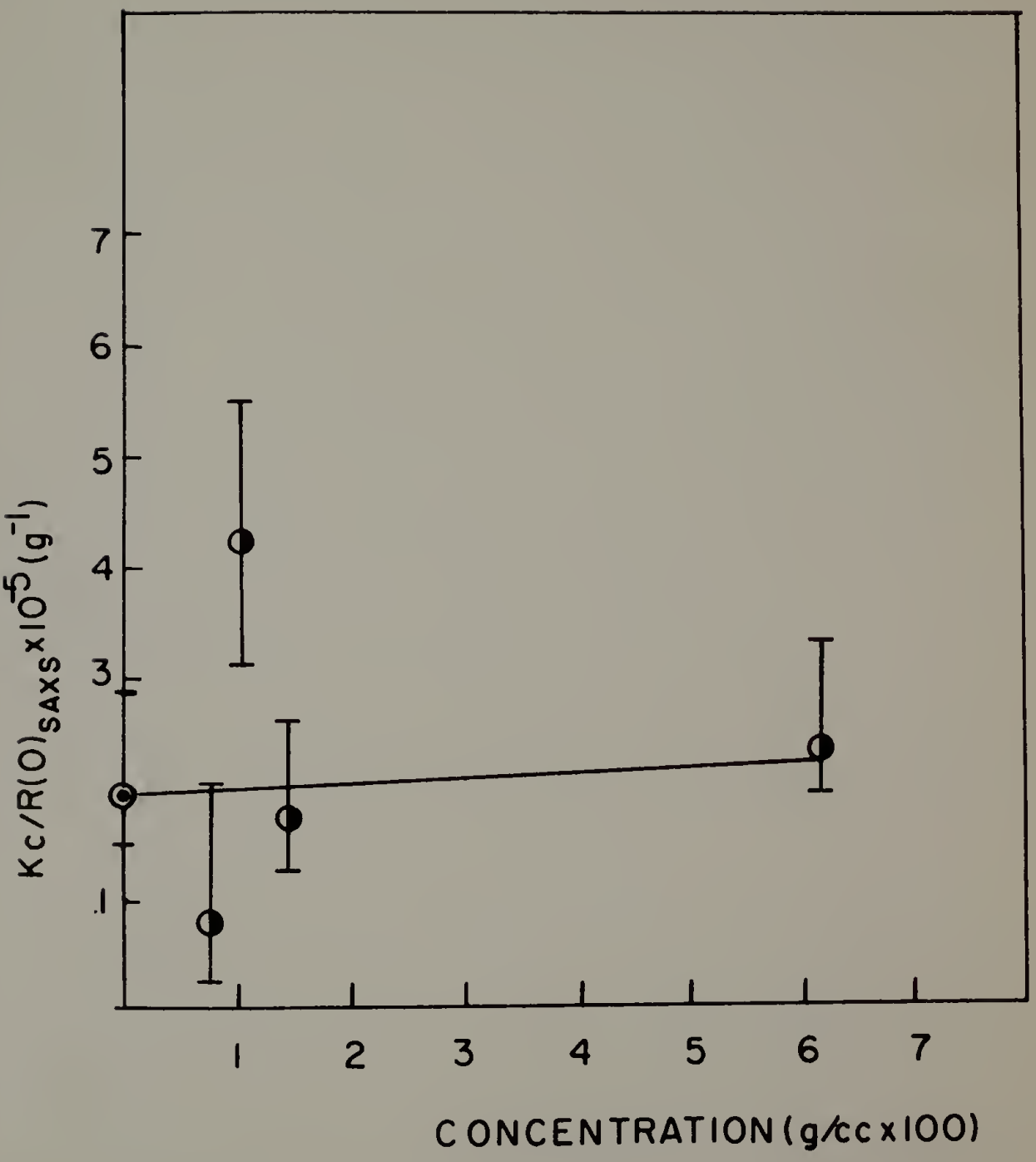
7
6
5
4
3
.1
1
2
3
4
5
6
7
$Kc/R(0)_{SAXS} \times 10^{-5} (g^{-1})$
CONCENTRATION (g/cc x 100)

Figure 62. Attempted use of a Zimm analysis in the PVC/PCL blends.

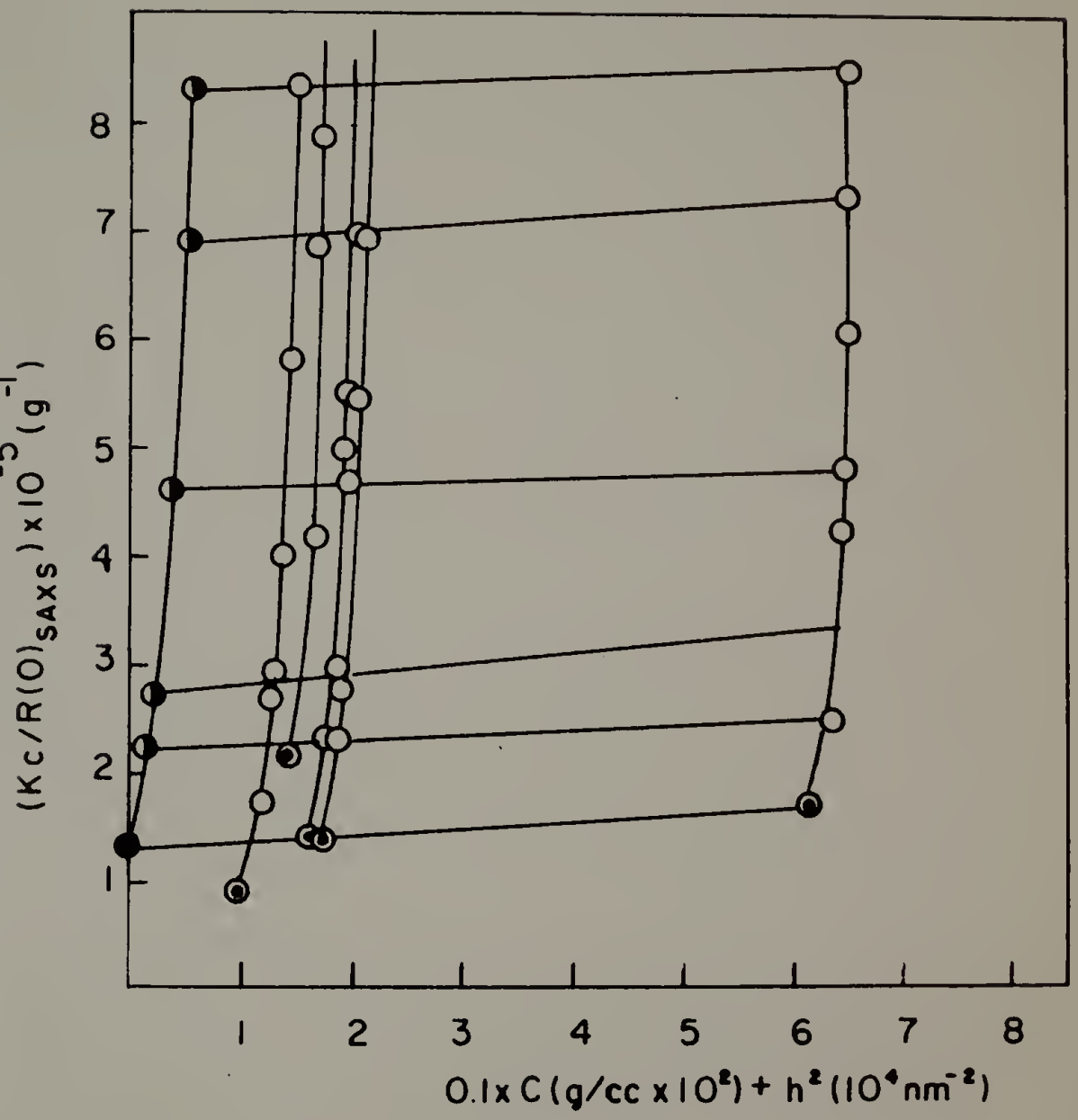
$(Kc/R(0)_{SAXS}) \times 10^{-5} (g^{-1})$
8
7
6
5
4
3
2
1
1
2
3
4
5
6
7
8
$0.1 \times C (g/cc \times 10^2) + h^2 (10^4 nm^{-2})$

Figure 63. Smeared SAXS profile of polystyrene.

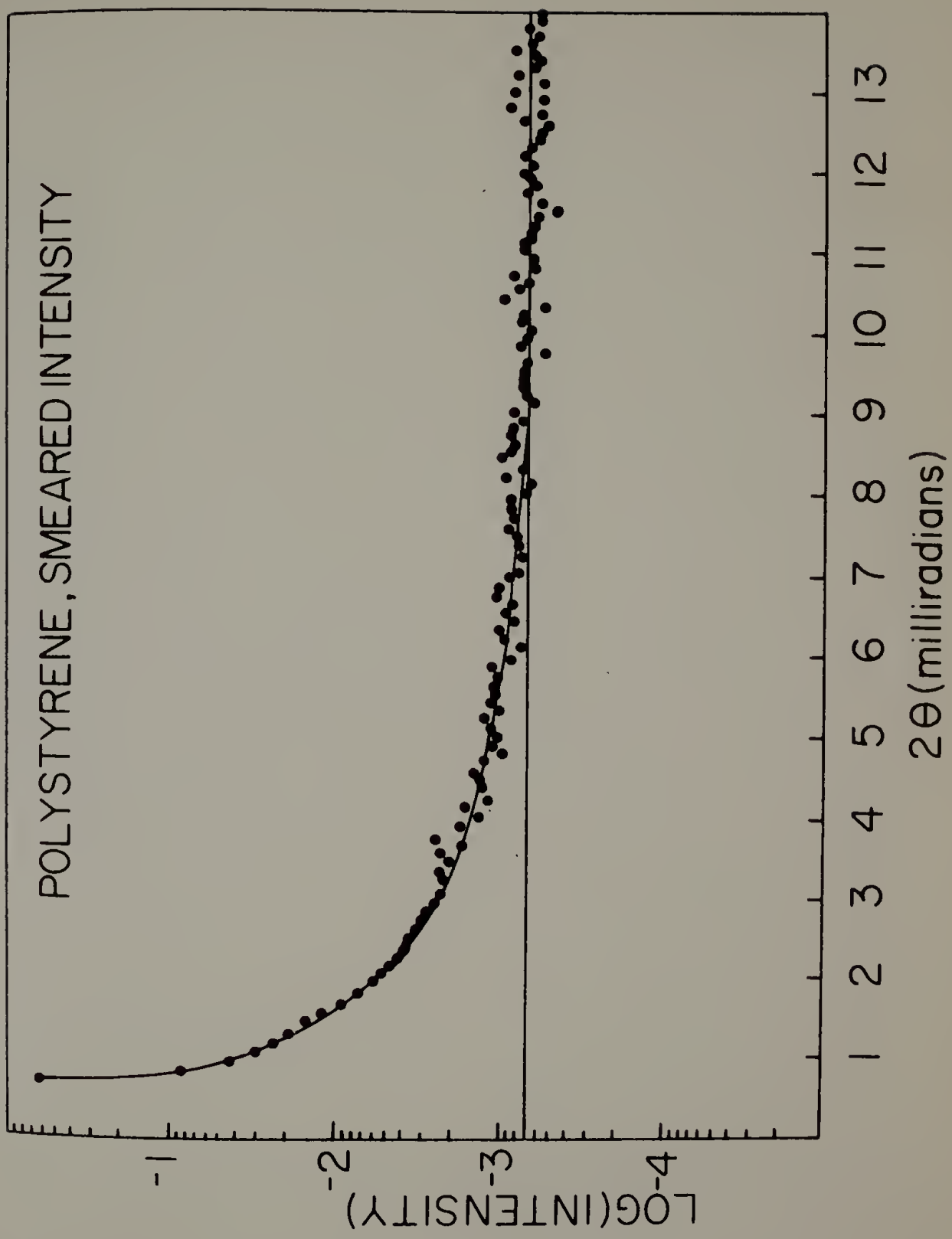
POLYSTYRENE, SMEARED INTENSITY
LOG(INTENSITY)
-1
-2
-3
-4
1 2 3 4 5 6 7 8 9 10 11 12 13
2θ(milliradians)

Figure 64. Comparison of smeared and desmeared scattering profiles of atactic polystyrene. Note that the initial slope is approximately constant.

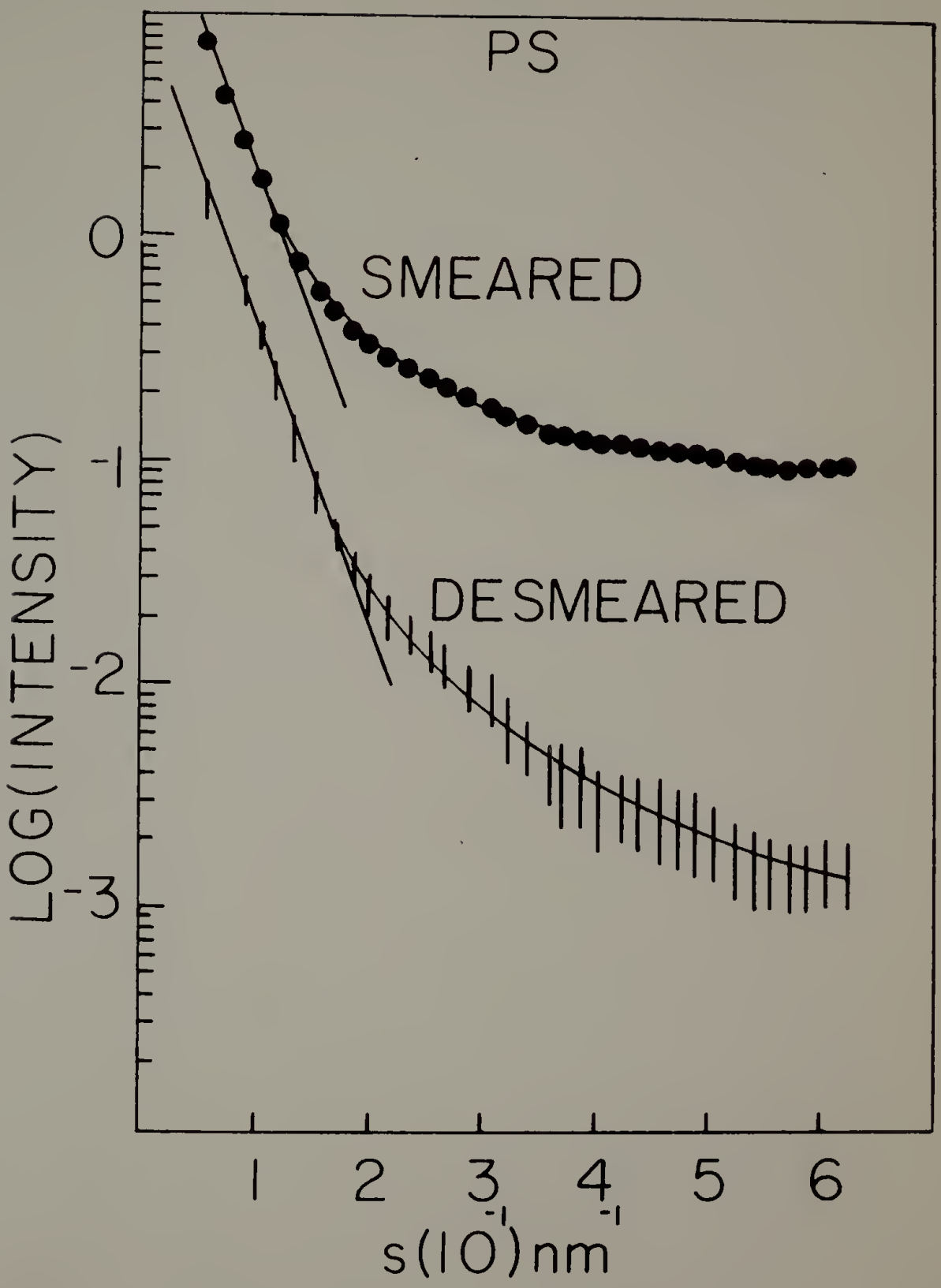
PS
SMEARED
DESMEARED
LOG(INTENSITY)
0
-1
-2
-3
1
2
3
4
5
6
s(10) nm⁻¹

Figure 65. SAXS data for PpIS/PS dilute solid solutions. Concentrations are in g x 10^2 PpIS/cm^3 of solution.

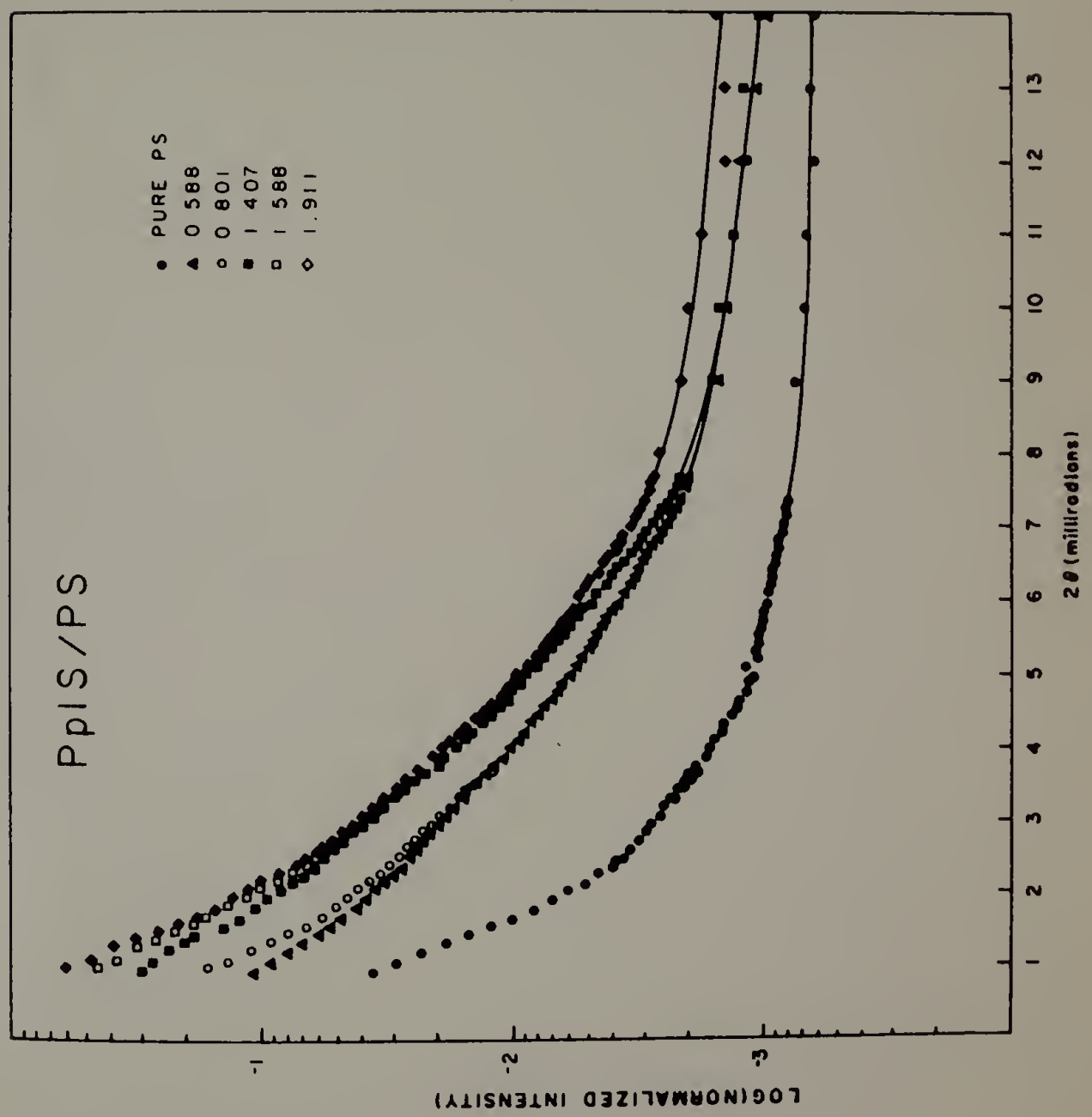
PpIS/PS
PURE PS
0 588
0 801
1 407
1 588
1.911
LOG(NORMALIZED INTENSITY)
-1
-2
-3
1
2
3
4
5
6
7
8
9
10
11
12
13
2θ (milliradians)

Figure 66. Guinier analysis on smeared PpIS/PS blend data.

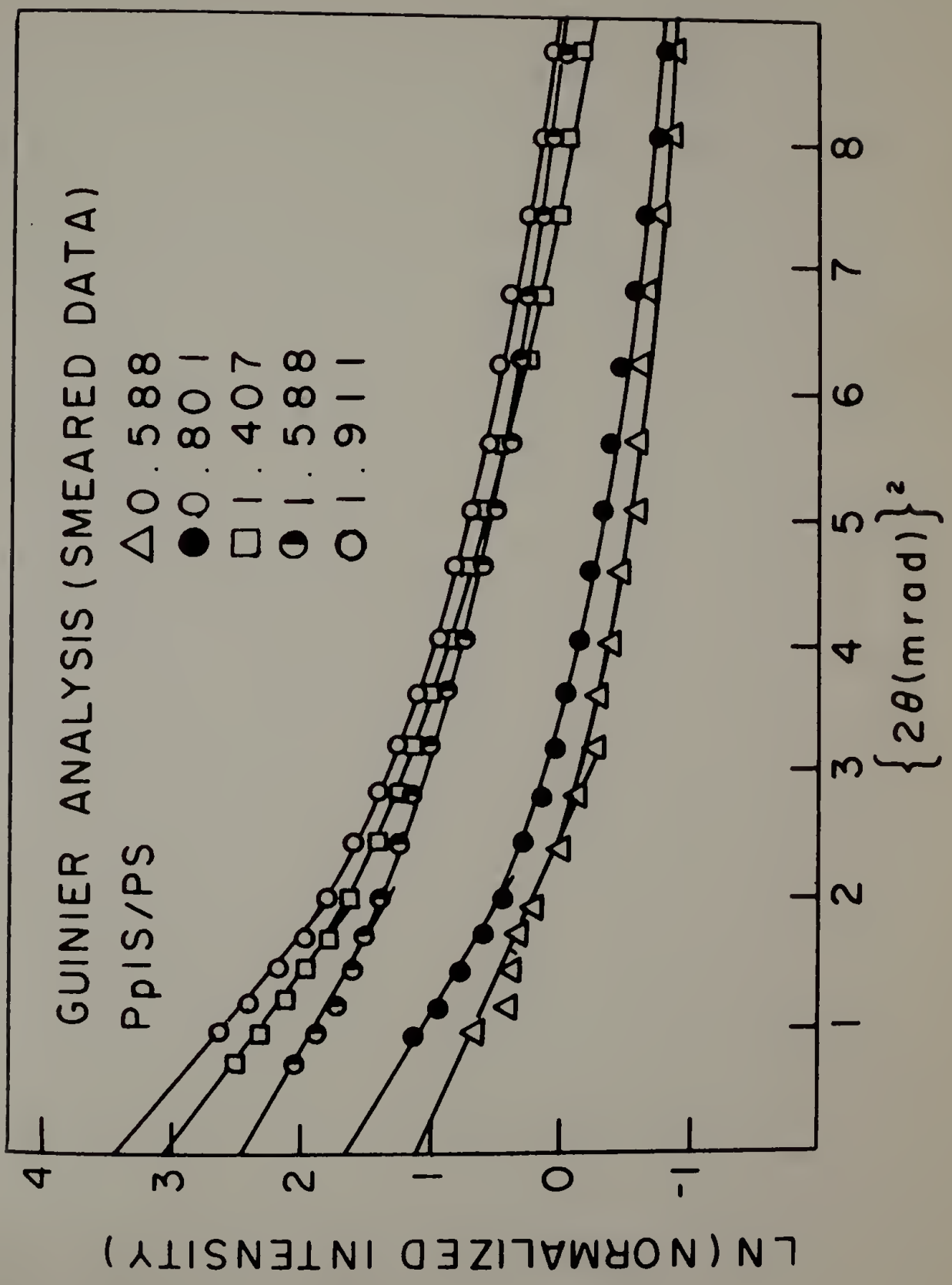
GUINIER ANALYSIS (SMEARED DATA)
PpIS/PS
△0.588
●0.801
□1.407
◑1.588
○1.911
LN (NORMALIZED INTENSITY)
{2θ(mrad)}²
4
3
2
1
0
-1
1
2
3
4
5
6
7
8

Figure 67. Guinier analysis on desmeared PpIS/PS blends.

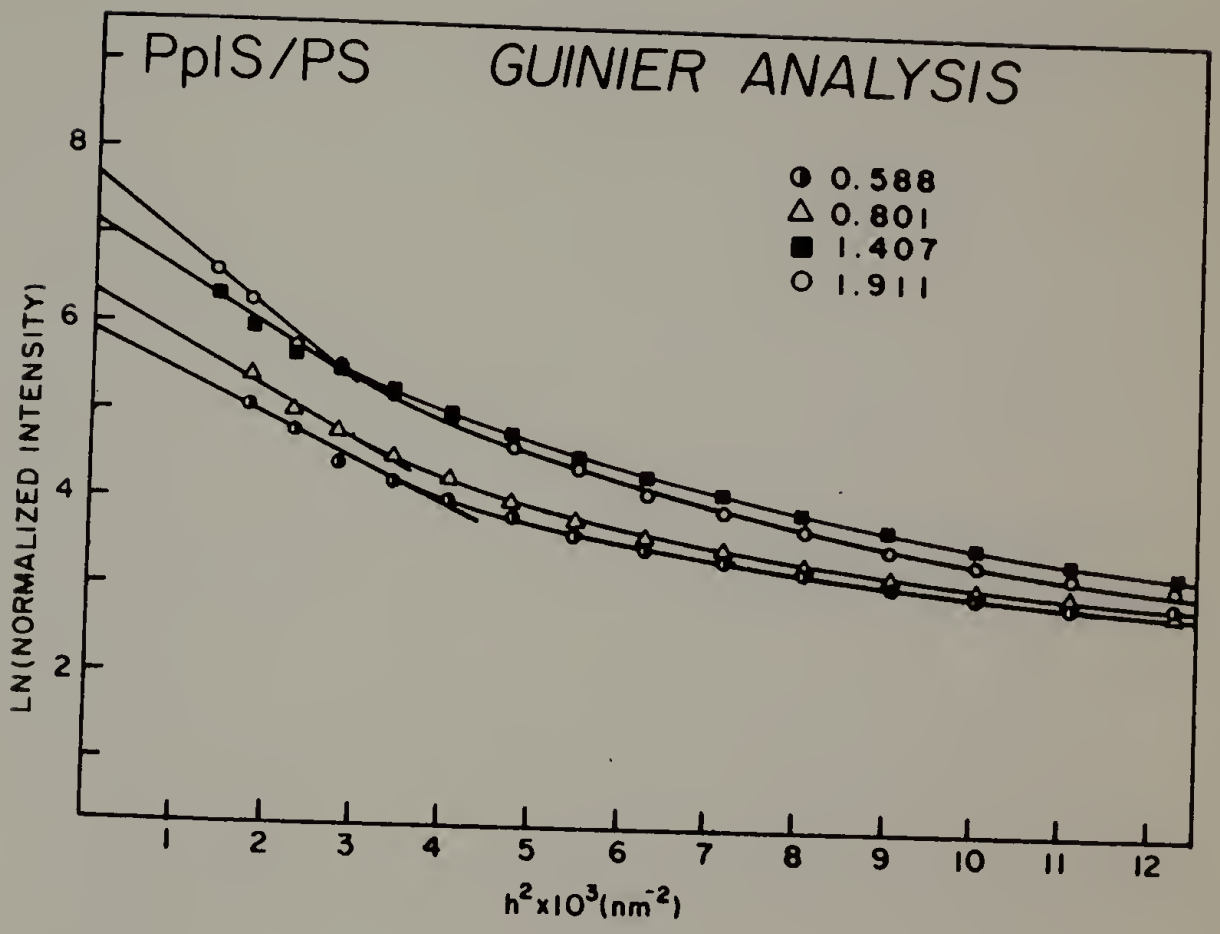
PpIS/PS
GUINIER ANALYSIS
0.588
0.801
1.407
1.911
LN(NORMALIZED INTENSITY)
8
6
4
2
1
2
3
4
5
6
7
8
9
10
11
12
h²x10³(nm⁻²)

Figure 68. Radius of gyration vs. concentration for PpIS/PS blends.

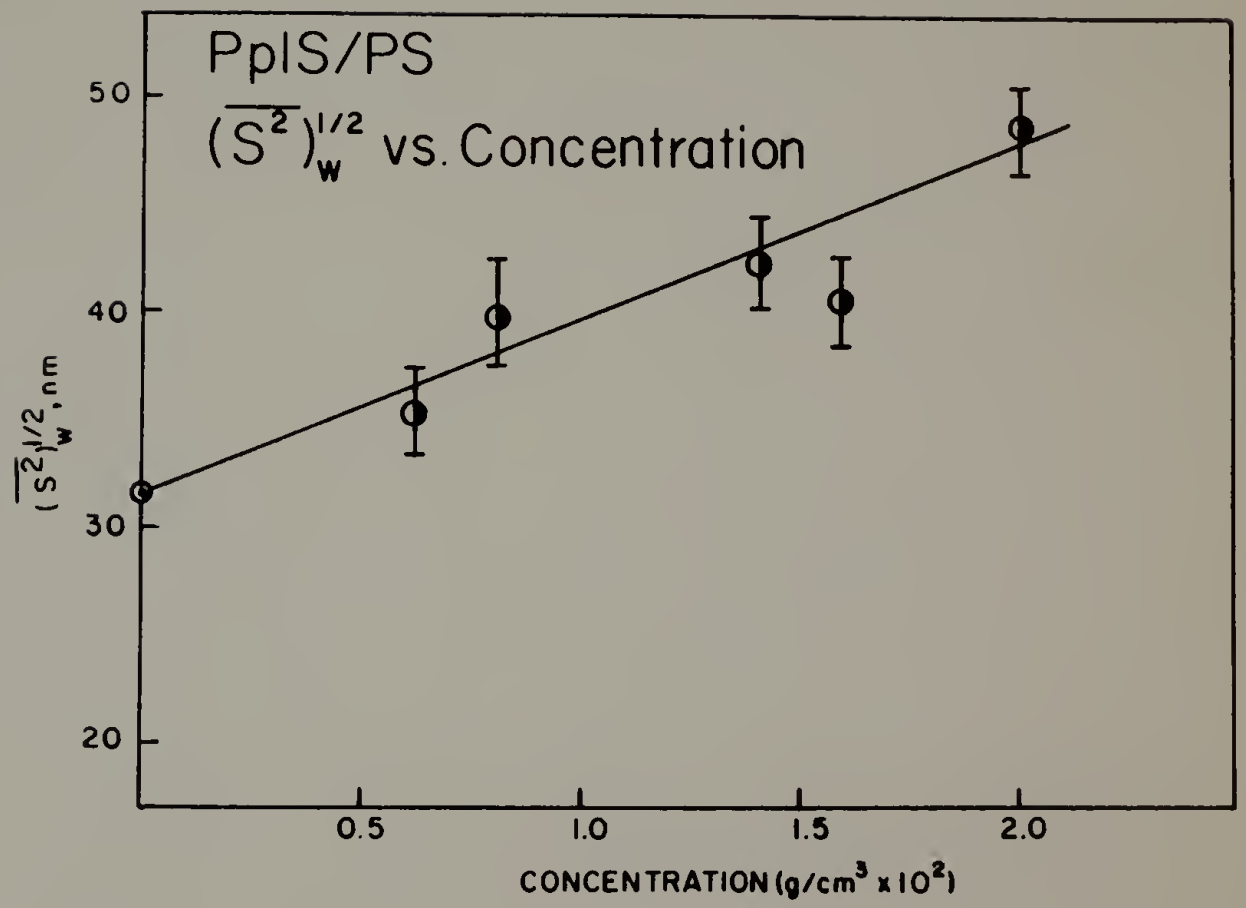
PpIS/PS
$(\overline{S^2})_w^{1/2}$ vs. Concentration
50
40
30
20
$(\overline{S^2})_w^{1/2}$, nm
0.5
1.0
1.5
2.0
CONCENTRATION (g/cm^3 x 10^2)

Figure 69. KC/R(0) for PpIS/PS blends as a function of composition.

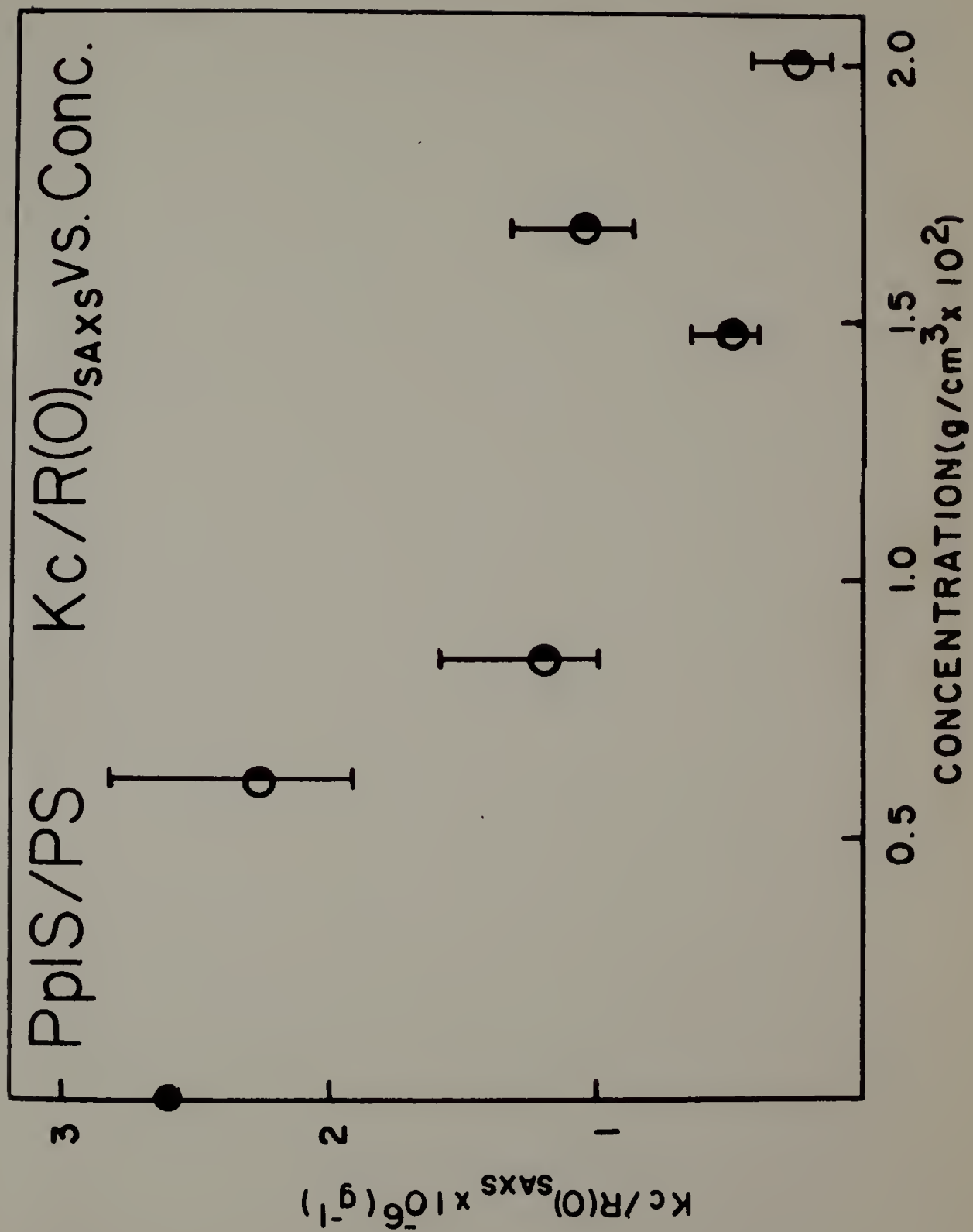
PpIS/PS
Kc/R(O)SAXS VS. Conc.
Kc/R(O)SAXS x 10⁻⁶ (g⁻¹)
3
2
1
0.5
1.0
1.5
2.0
CONCENTRATION(g/cm³x 10²)

Figure 70. Debye-Bueche plots for PpIS/PS blends. Concentrations in grams PpIS per cm^3 solution.

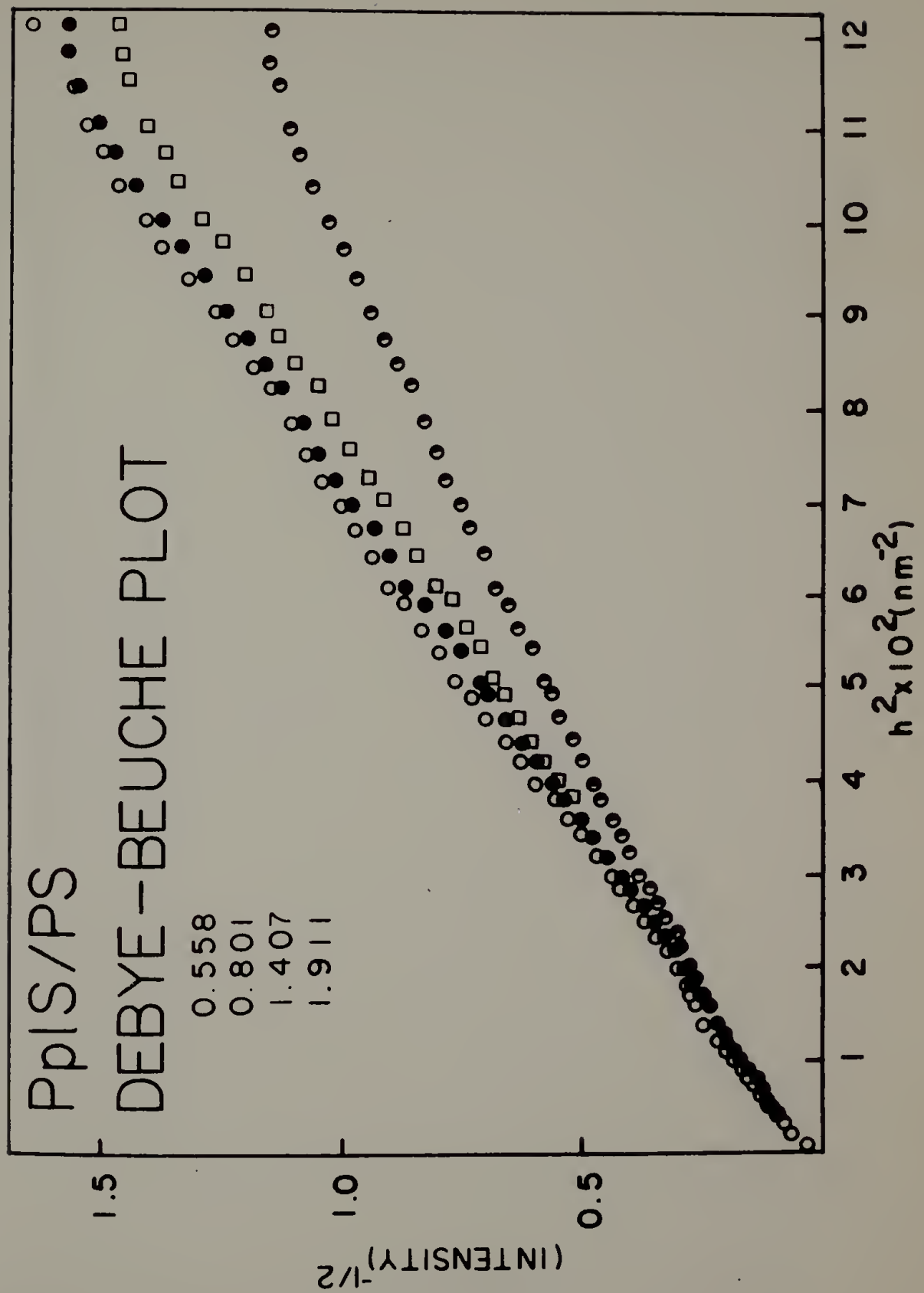
PpIS/PS
DEBYE-BEUCHE PLOT
0.558
0.801
1.407
1.911
(INTENSITY)^-1/2
h^2x10^2(nm^-2)
0.5
1.0
1.5
1
2
3
4
5
6
7
8
9
10
11
12

Figure 71. PpIS chord lengths in PS as a function of composition.

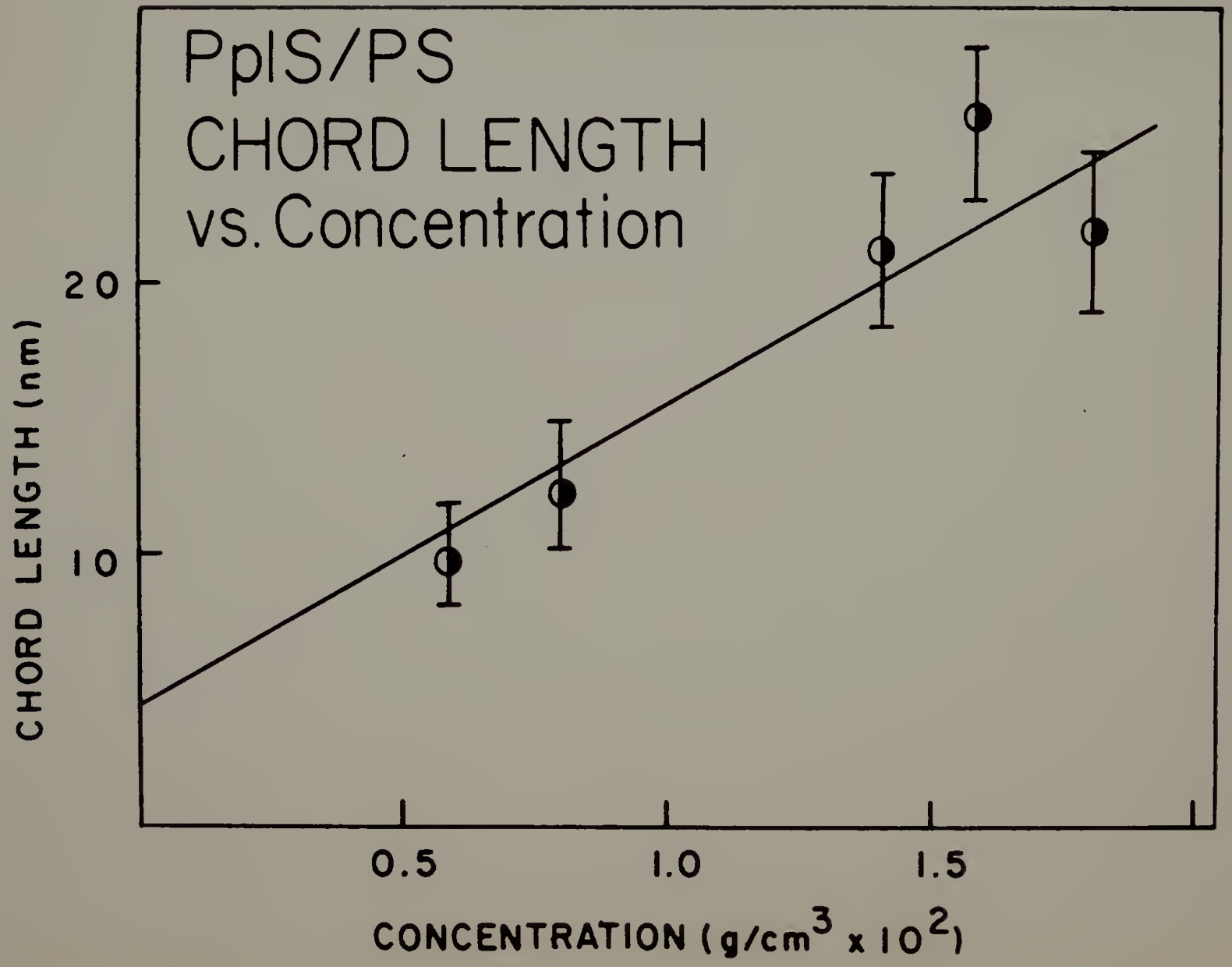
PpIS/PS
CHORD LENGTH
vs. Concentration
CHORD LENGTH (nm)
20
10
0.5
1.0
1.5
CONCENTRATION (g/cm3 x 10^2)

Figure 72. SAXS intensity profile for PPO.

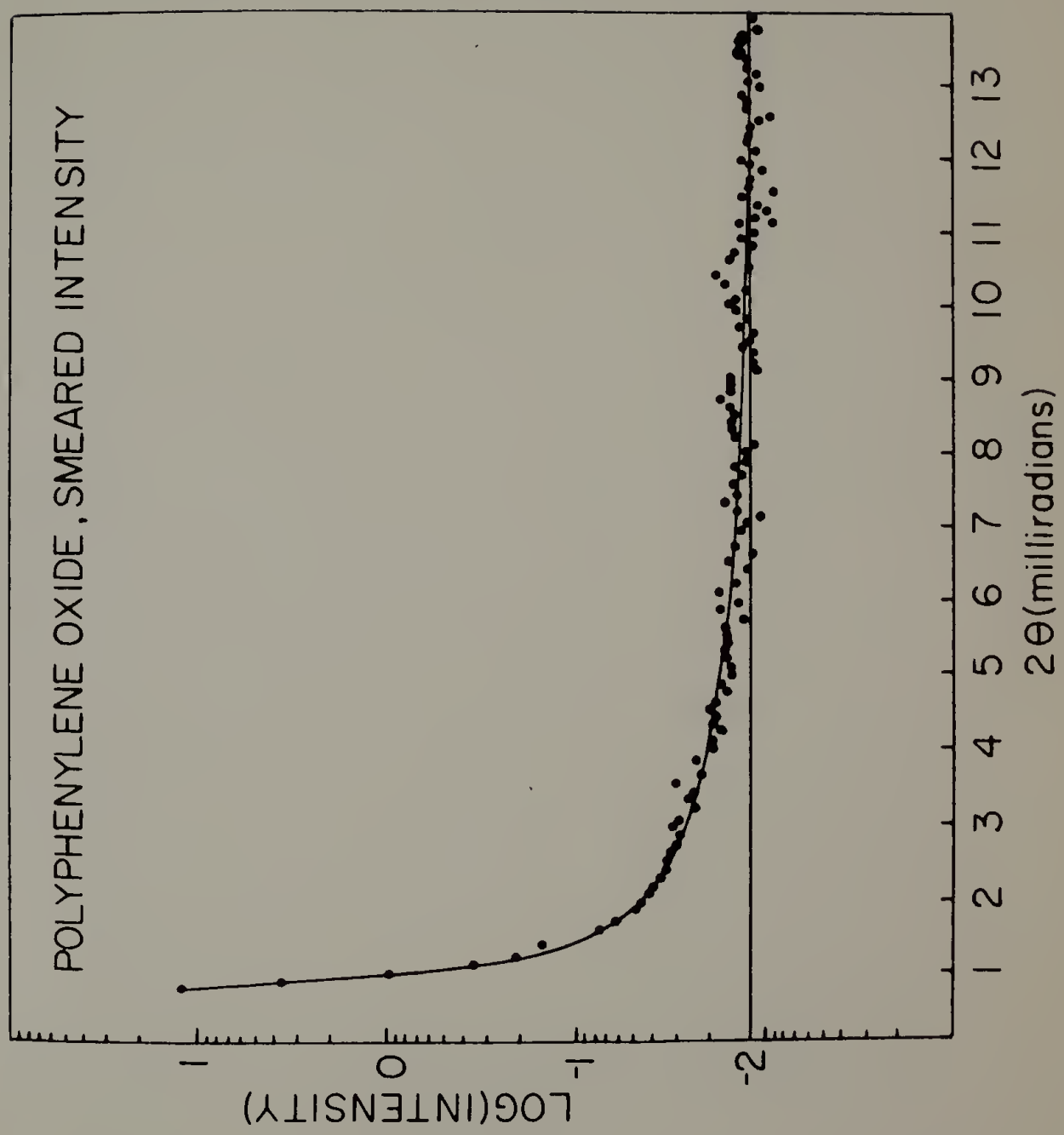
POLYPHENYLENE OXIDE, SMEARED INTENSITY
LOG(INTENSITY)
1
0
-1
-2
1 2 3 4 5 6 7 8 9 10 11 12 13
2θ(milliradians)

Figure 73. SAXS intensity for PoClS/PPO blends. Concentrations in grams of PoClS/cm^3 solution.

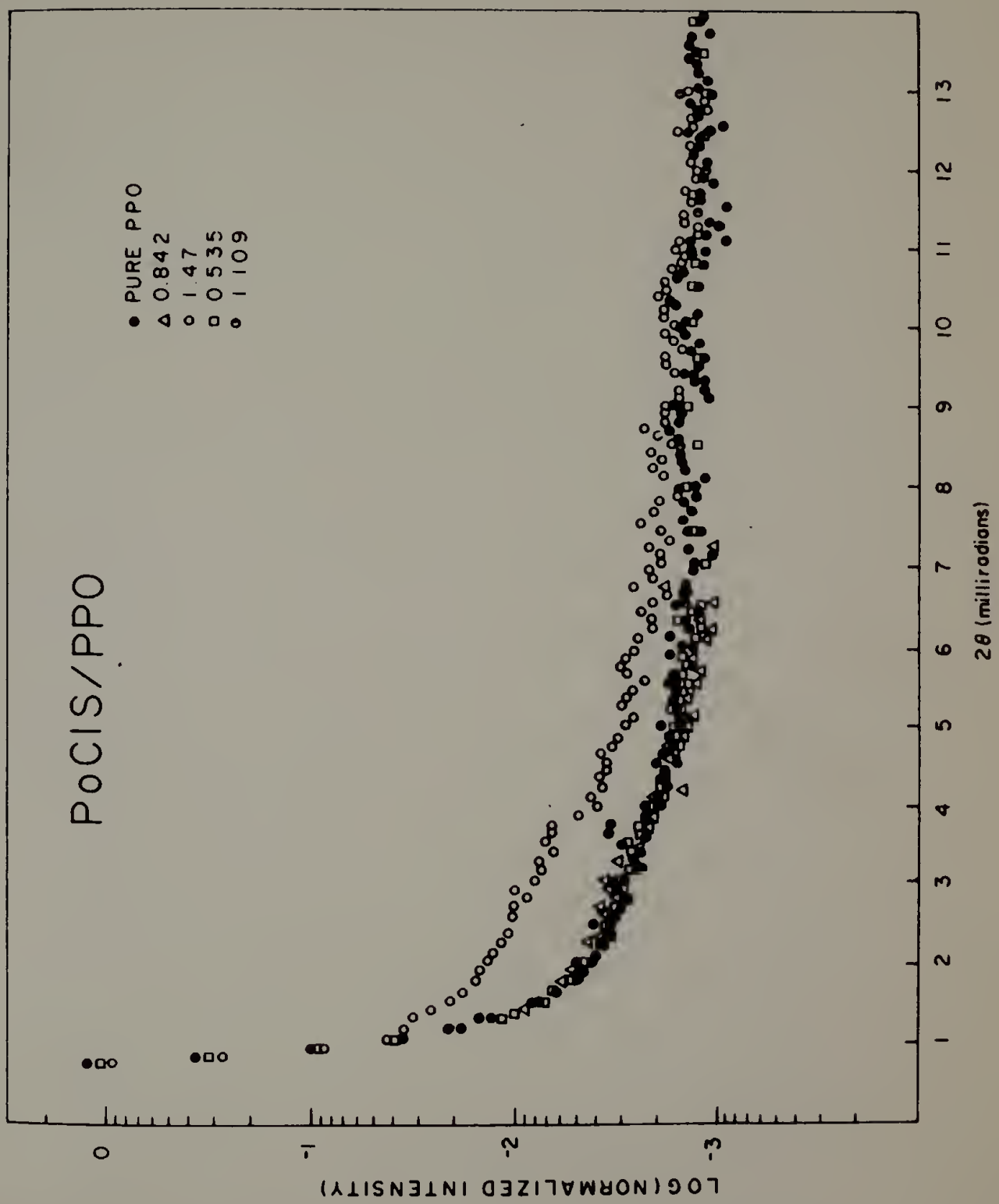
PoCIS/PPO
● PURE PPO
△ 0.842
○ 1.47
□ 0.535
● 1.109
LOG(NORMALIZED INTENSITY)
0
-1
-2
-3
1
2
3
4
5
6
7
8
9
10
11
12
13
2θ (milliradians)

Figure 74. SAXS intensity profiles for PpClS/PPO blends. Concentrations in grams of PpClS/cm^3 solution.

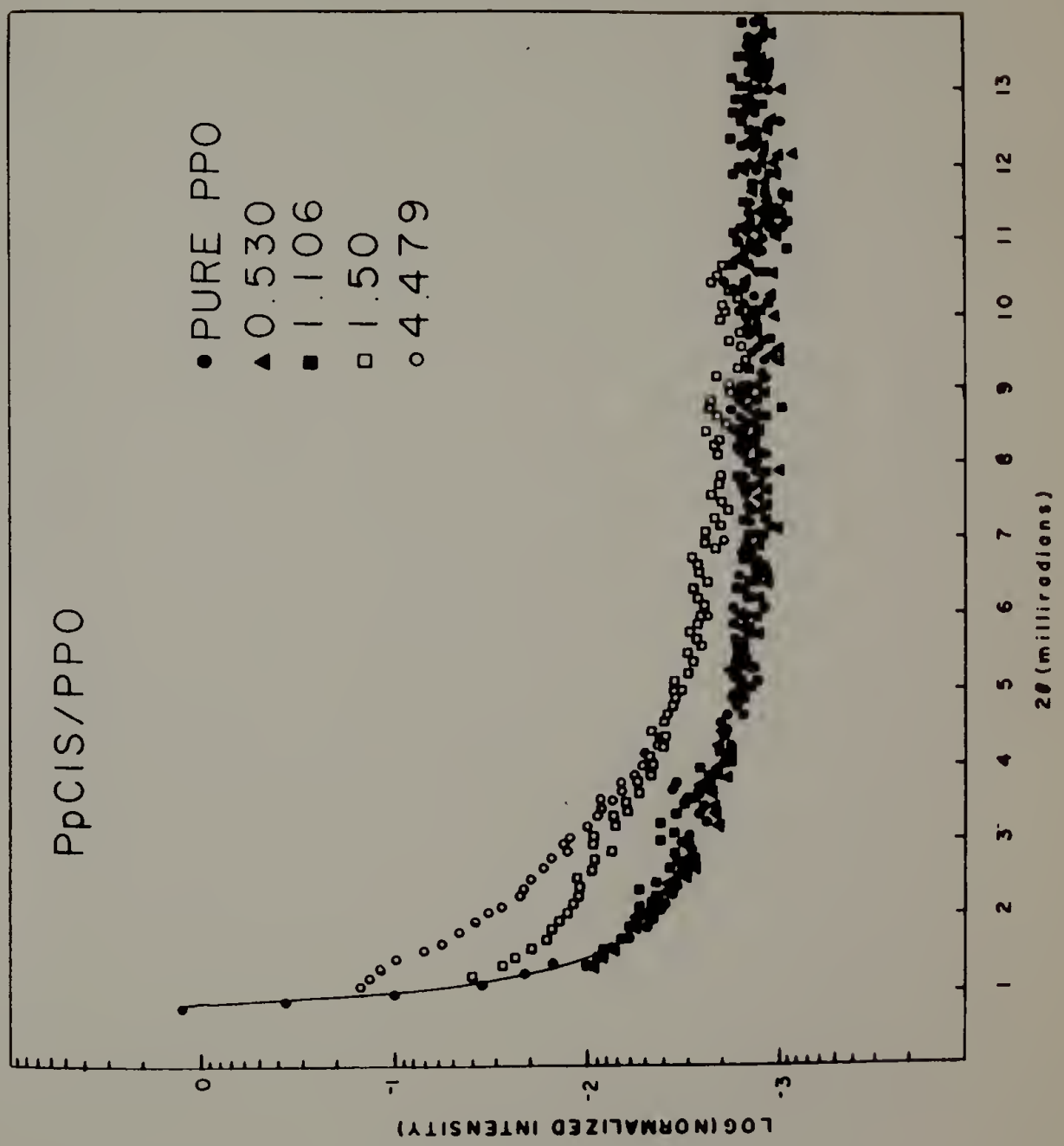
PpCIS/PPO
• PURE PPO
▲ 0.530
■ 1.106
□ 1.50
○ 4.479
LOG (NORMALIZED INTENSITY)
0
-1
-2
-3
1
2
3
4
5
6
7
8
9
10
11
12
13
2θ (millirodians)

Figure 75. SAXS intensity profiles for PoClS/PS blends. Concentrations in grams of PoClS/cm^3 solution.

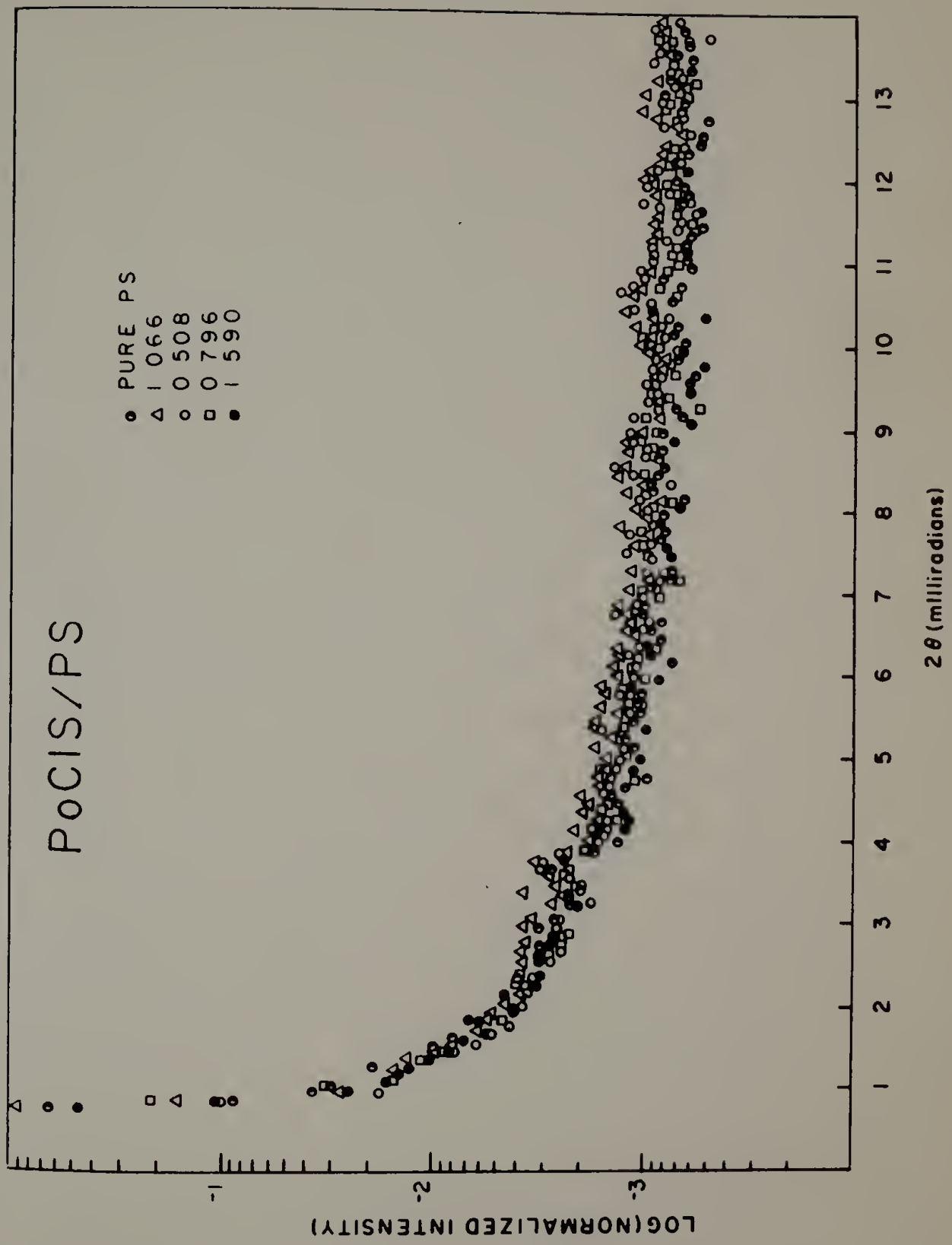
PoCIS/PS
PURE PS
1 066
0 508
0 796
1 590
LOG(NORMALIZED INTENSITY)
-1
-2
-3
1
2
3
4
5
6
7
8
9
10
11
12
13
2θ (milliradians)

Figure 76. SAXS intensity profiles for PpClS/PS blends. Concentrations in grams of PpClS/cm^3 solution.

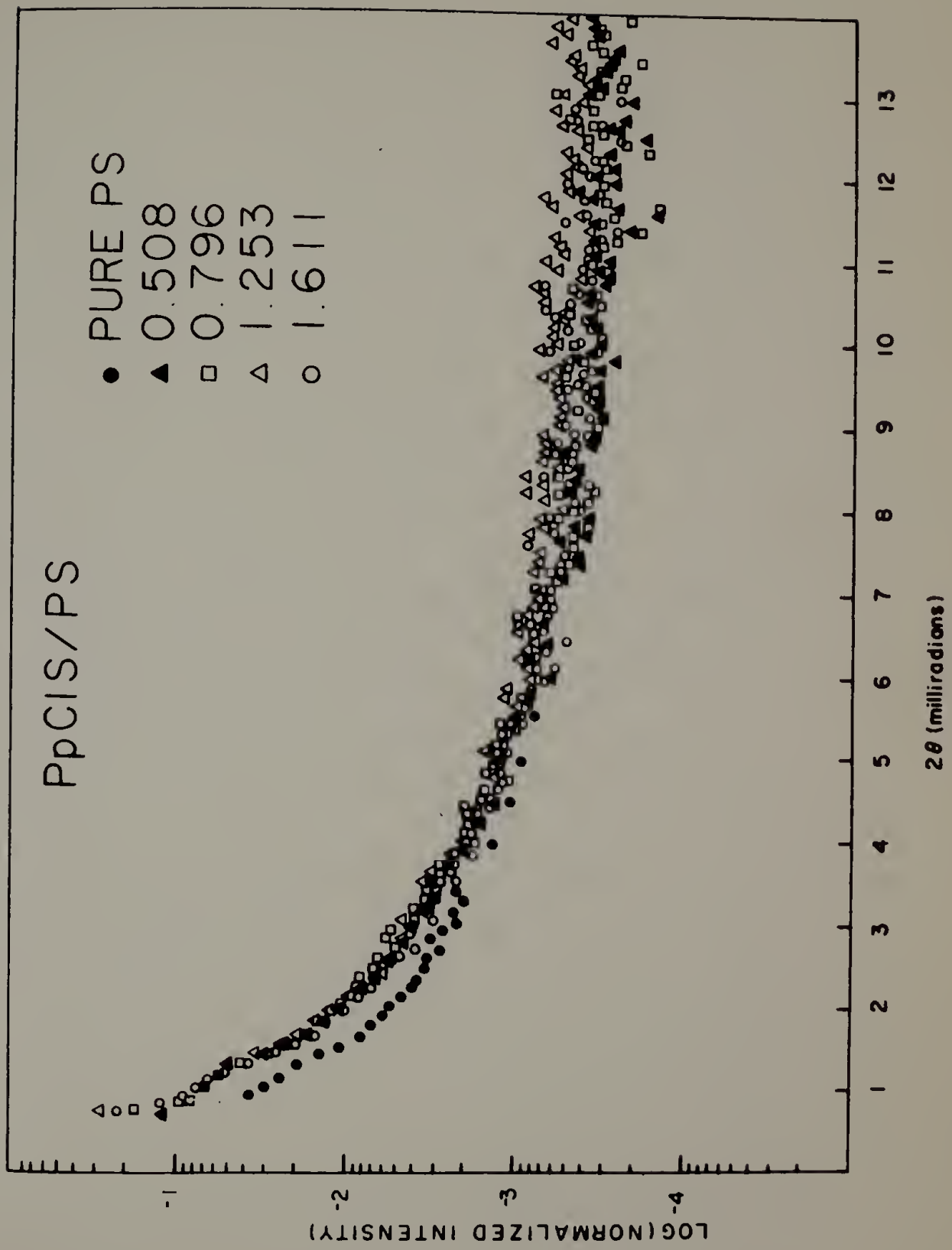
PpCIS/PS
PURE PS
0.508
0.796
1.253
1.611
LOG(NORMALIZED INTENSITY)
-1
-2
-3
-4
1
2
3
4
5
6
7
8
9
10
11
12
13
2θ (milliradians)

Figure 77. Guinier analysis of SAXS intensity for PpClS/PS blends. Concentrations in grams of PpClS/cm^3 solution.

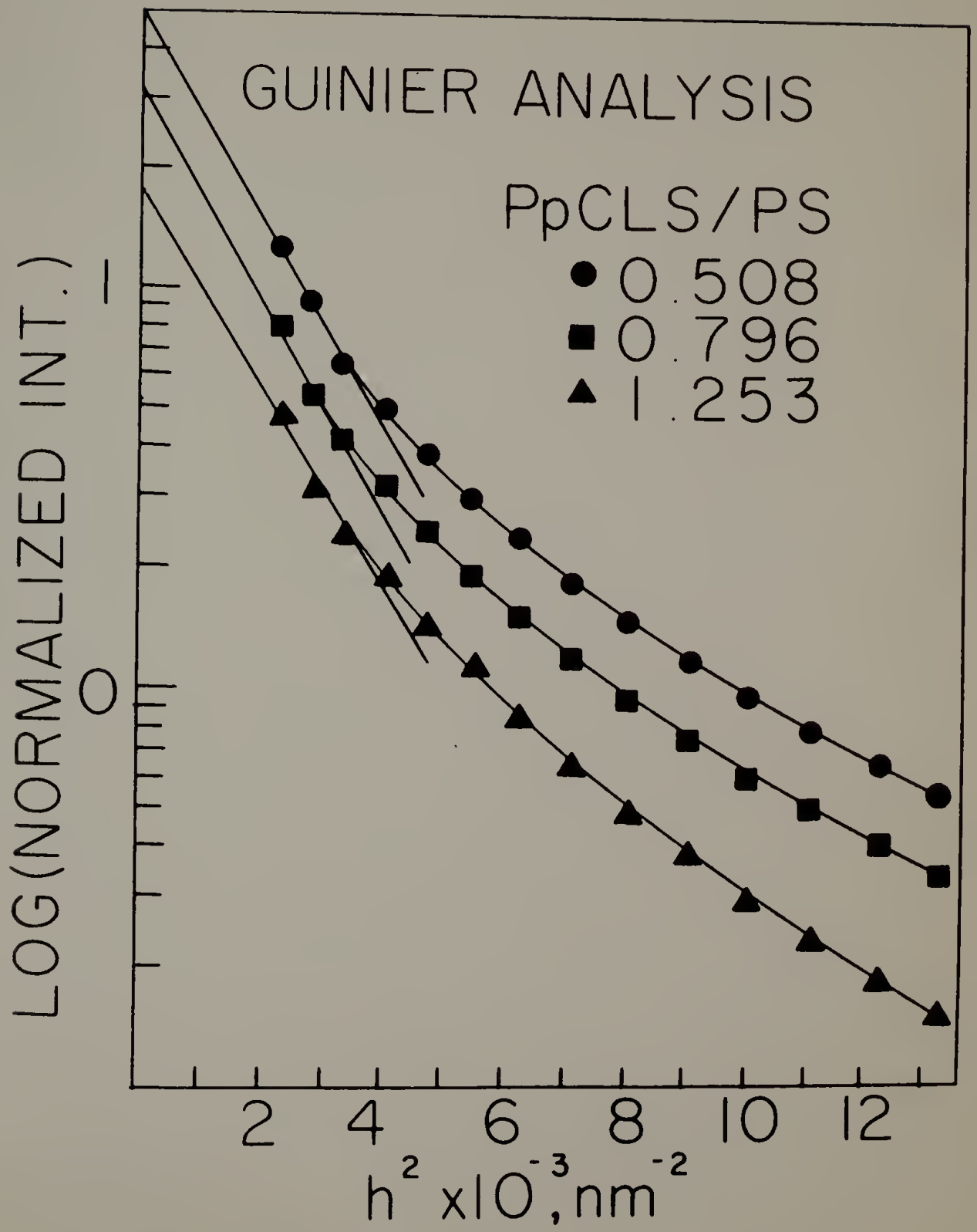
GUINIER ANALYSIS
PpCLS/PS
0.508
0.796
1.253
LOG(NORMALIZED INT.)
1
0
2
4
6
8
10
12
h² x10⁻³, nm⁻²

Figure 78. Radius of gyration vs. concentration for PpClS/PS blends.

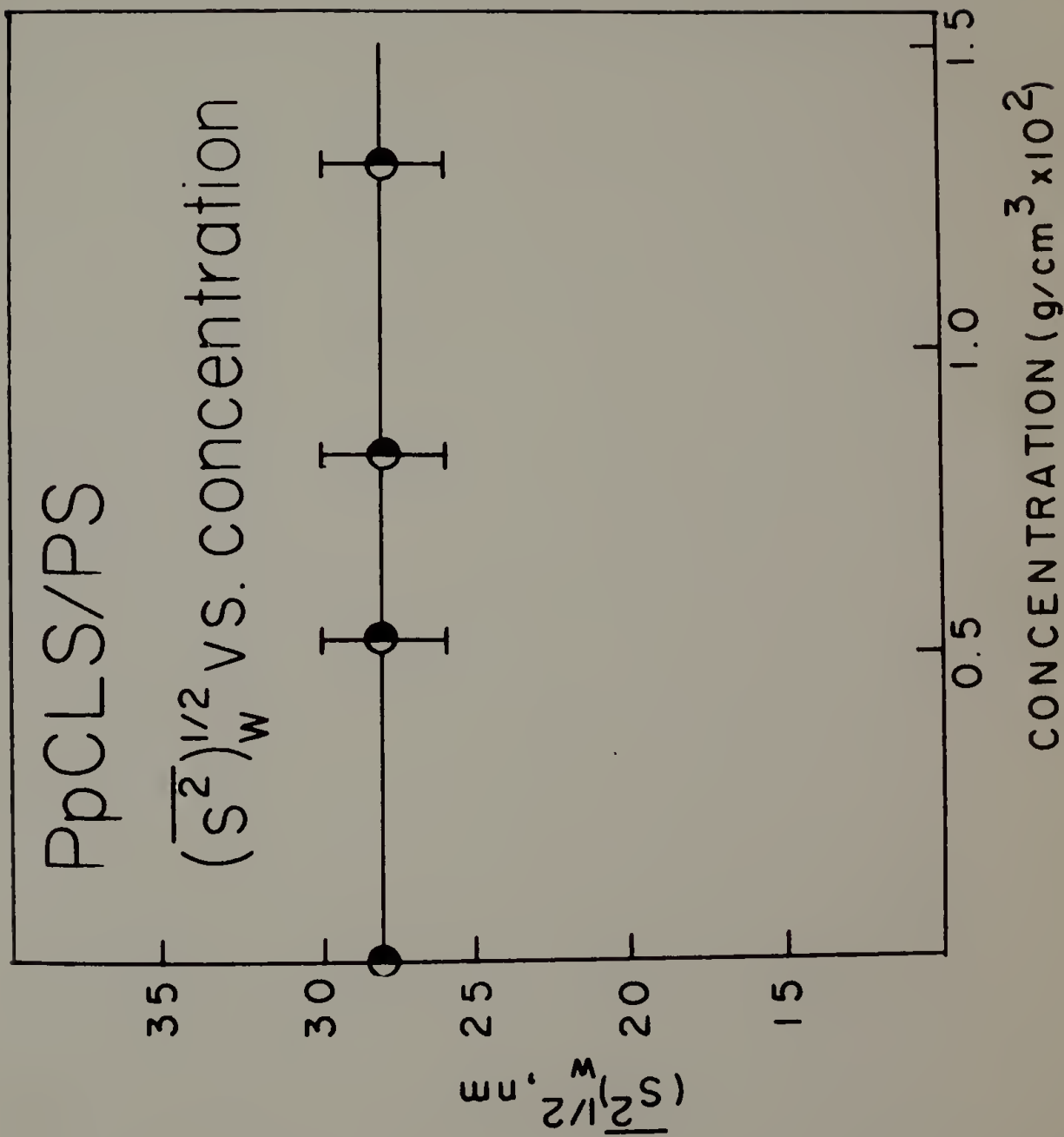
PpCLS/PS
$(\overline{s^2})^{1/2}_w$ vs. concentration
$(\overline{s^2})^{1/2}_w$, nm
35
30
25
20
15
0.5
1.0
1.5
CONCENTRATION ($g/cm^3 \times 10^2$)

Figure 79. KC/R(0) for PpClS/PS blends.

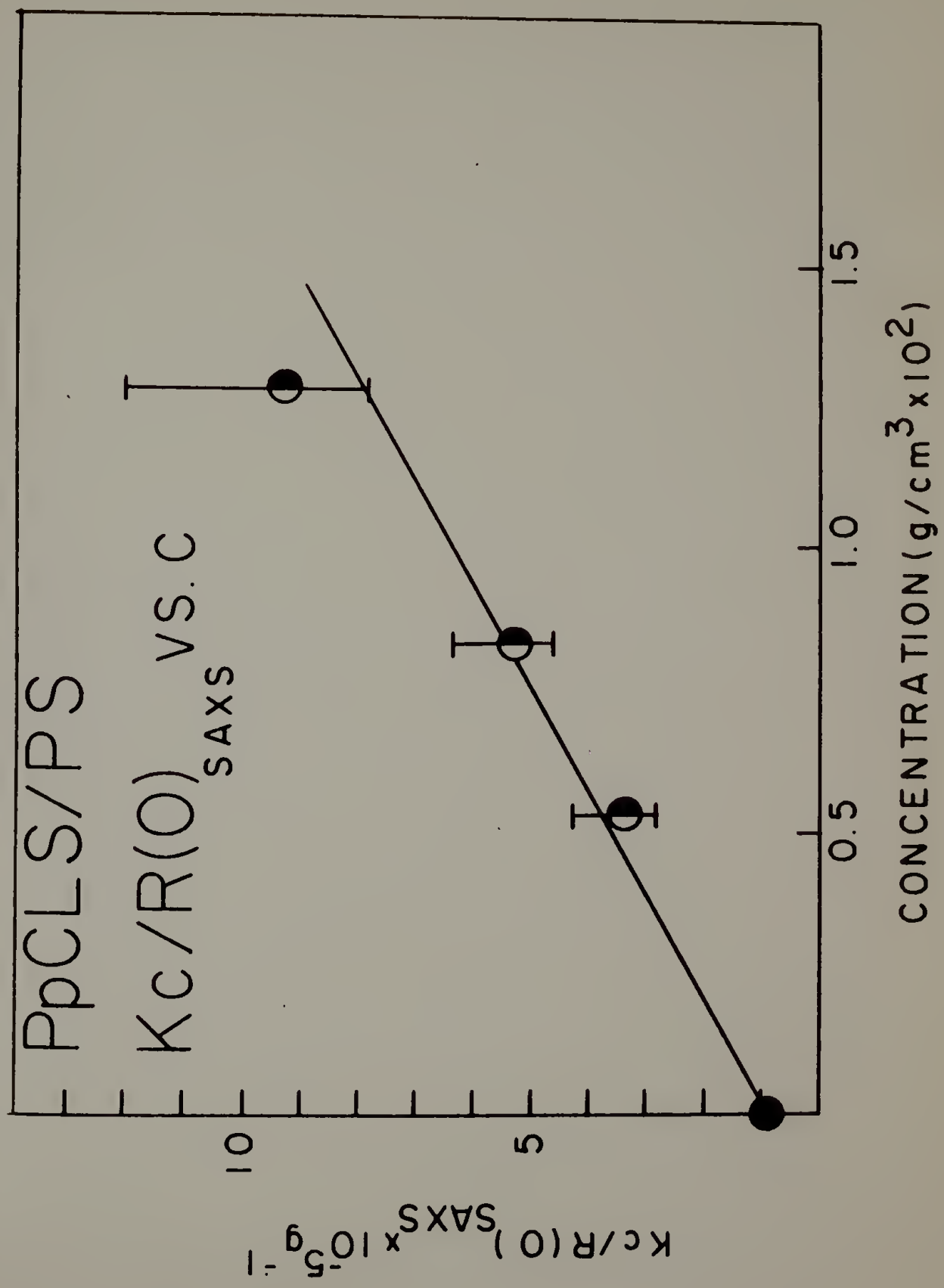
PpCLS/PS
Kc/R(0)SAXS VS. C
Kc/R(0)SAXS x 10^-5 g^-1
10
5
0.5
1.0
1.5
CONCENTRATION (g/cm^3 x 10^2)

Figure 80. Schematic diagram for the neutron scattering facility at the Oak Ridge Reactor.

SANS Geometry at ORR

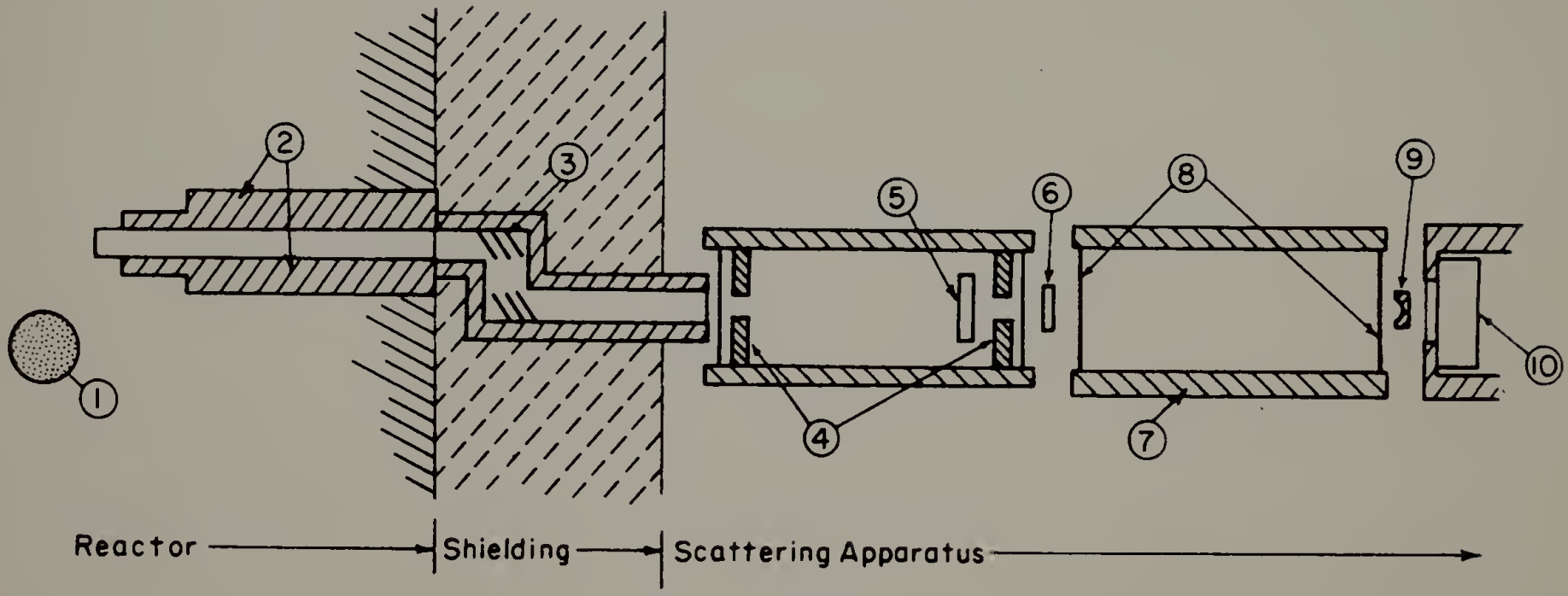

① Reactor Core
② Wave Guides
③ Graphite Monochromators
④ Boron Impregnated Cadmium Pinholes
⑤ Beam Monitor
⑥ Sample
⑦ Cadmium Coated Evacuated Flight Path
⑧ Aluminum Windows
⑨ Beam Stop
⑩ 2 D Area Detector

Figure 81. Small angle neutron scattering intensity profiles for d-PS in PoClS. Concentrations in grams of d-PS/cm^3 of solution.

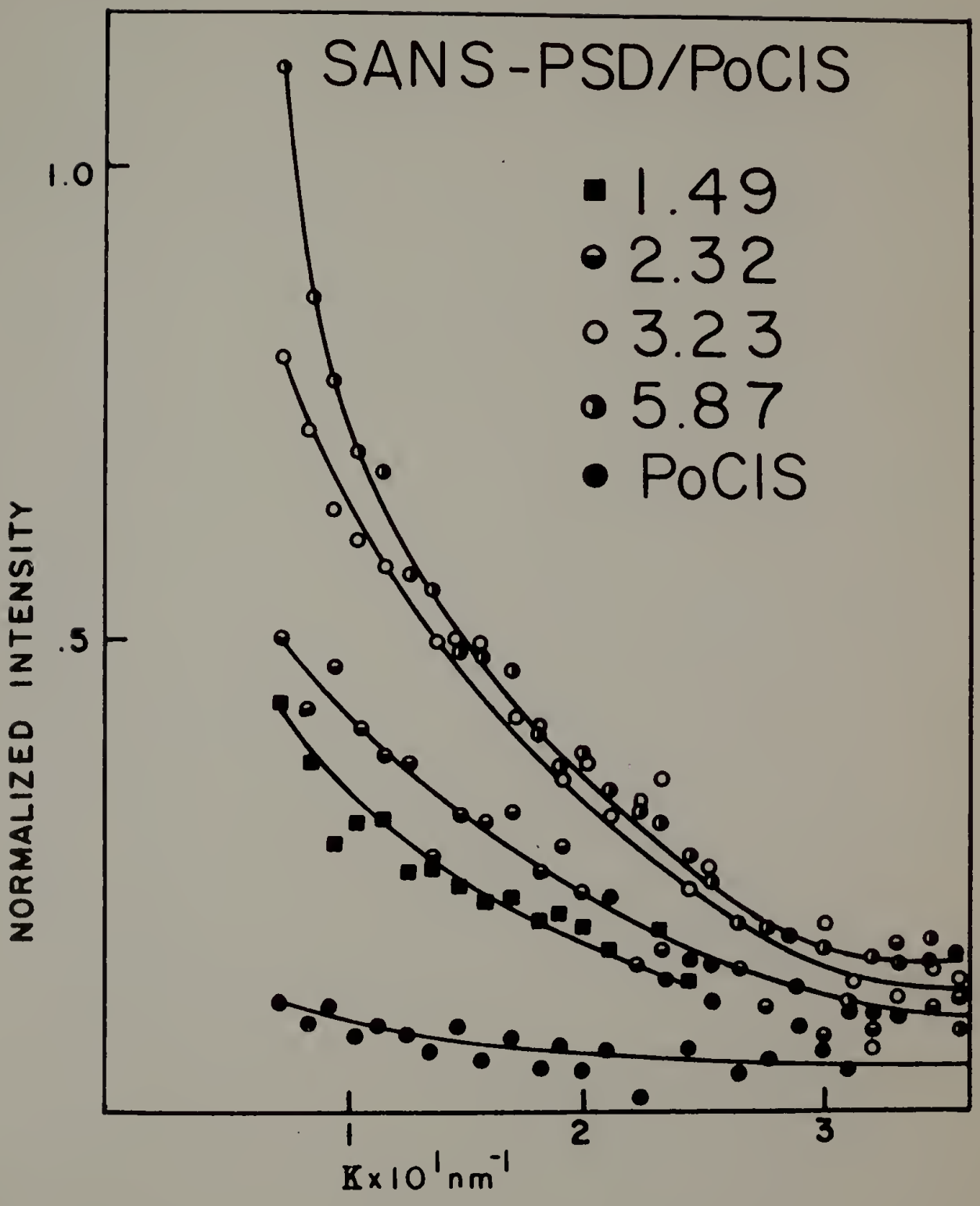
SANS-PSD/PoCIS
1.49
2.32
3.23
5.87
PoCIS
1.0
.5
NORMALIZED INTENSITY
1
2
3
K x 10 nm

Figure 82. Guinier analysis of SANS data (3.226 and 1.492 x 10^{-2} grams d-PS/cm^3).

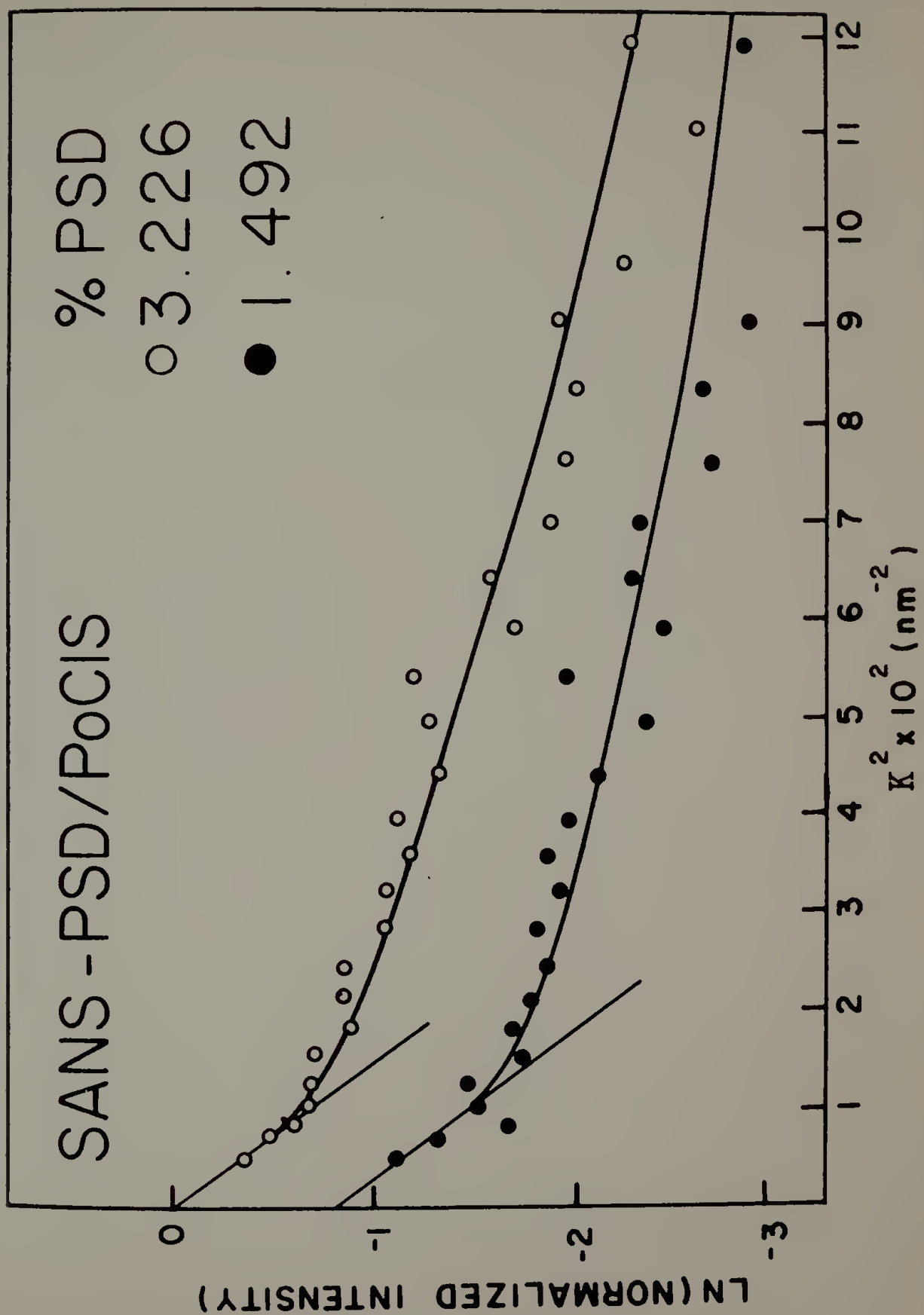
SANS-PSD/PoCIS
% PSD
○ 3.226
● 1.492
LN (NORMALIZED INTENSITY)
0
-1
-2
-3
1
2
3
4
5
6
7
8
9
10
11
12
K² x 10² (nm⁻²)

Figure 83. Guinier analysis of SANS data (0.03749 grams d-PS/cm^3 solution).

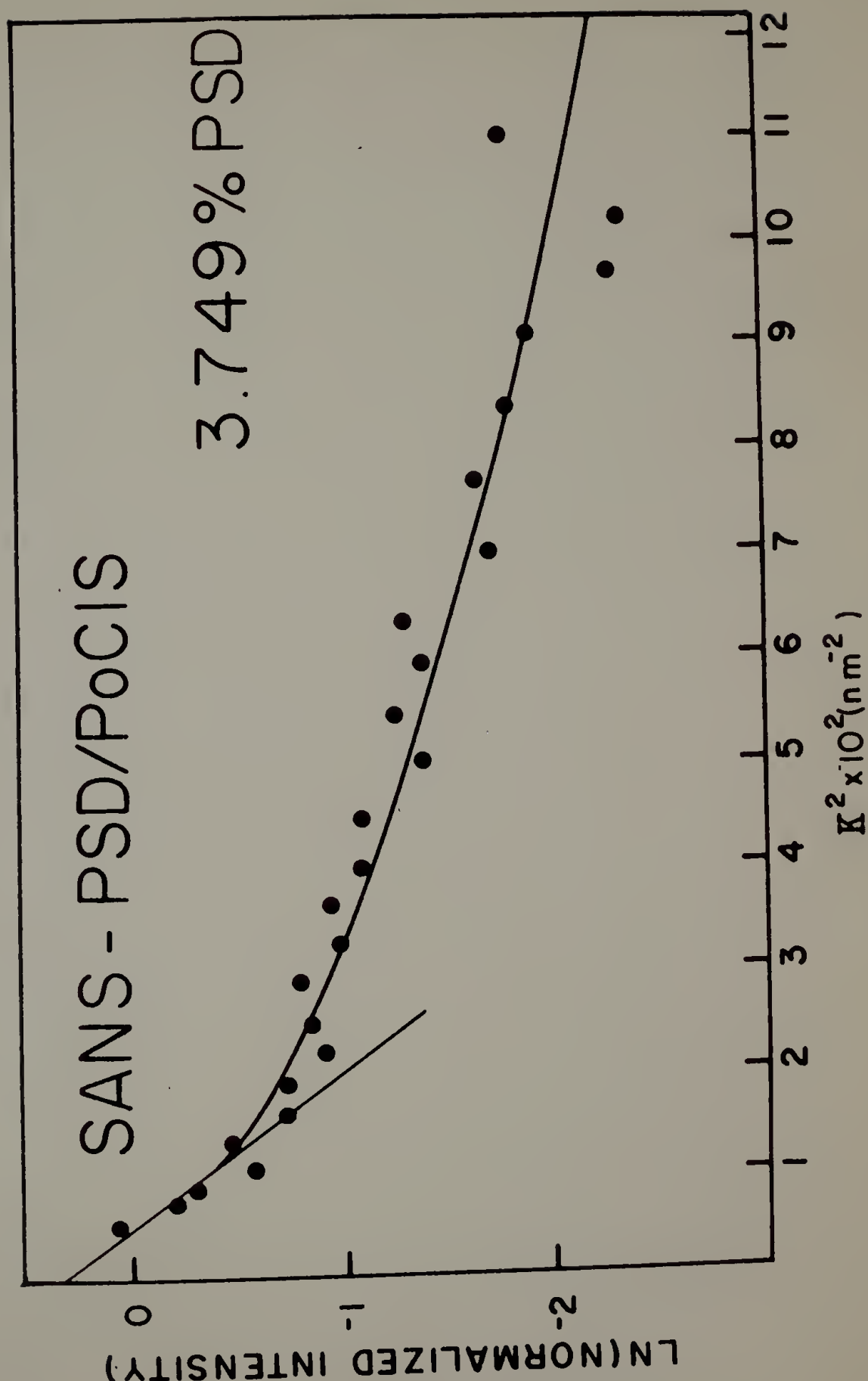
SANS - PSD/PoCIS
3.749% PSD
LN(NORMALIZED INTENSITY)
0
-1
-2
1
2
3
4
5
6
7
8
9
10
11
12
$K^2 \times 10^2 (nm^{-2})$

Figure 84. Guinier analysis of SANS data (0.02322 and 0.04399 grams of d-PS/cm^3 solution).

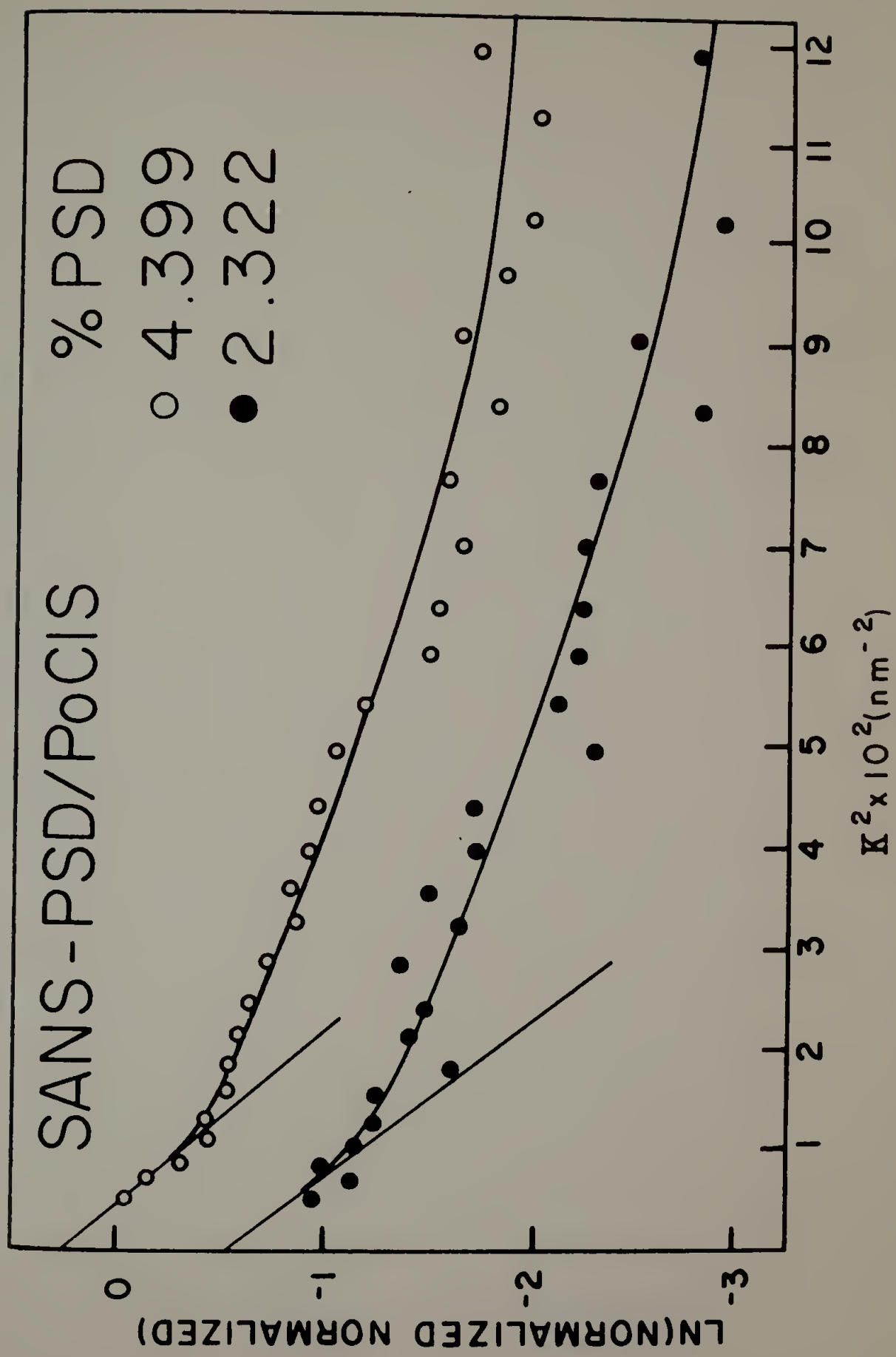
SANS-PSD/PoCIS
% PSD
○ 4.399
● 2.322
LN(NORMALIZED NORMALIZED)
0
-1
-2
-3
1
2
3
4
5
6
7
8
9
10
11
12
K² x 10² (nm⁻²)

Figure 85. Guinier analysis of SANS data (0.05872 grams d-PS/cm^3 solution).

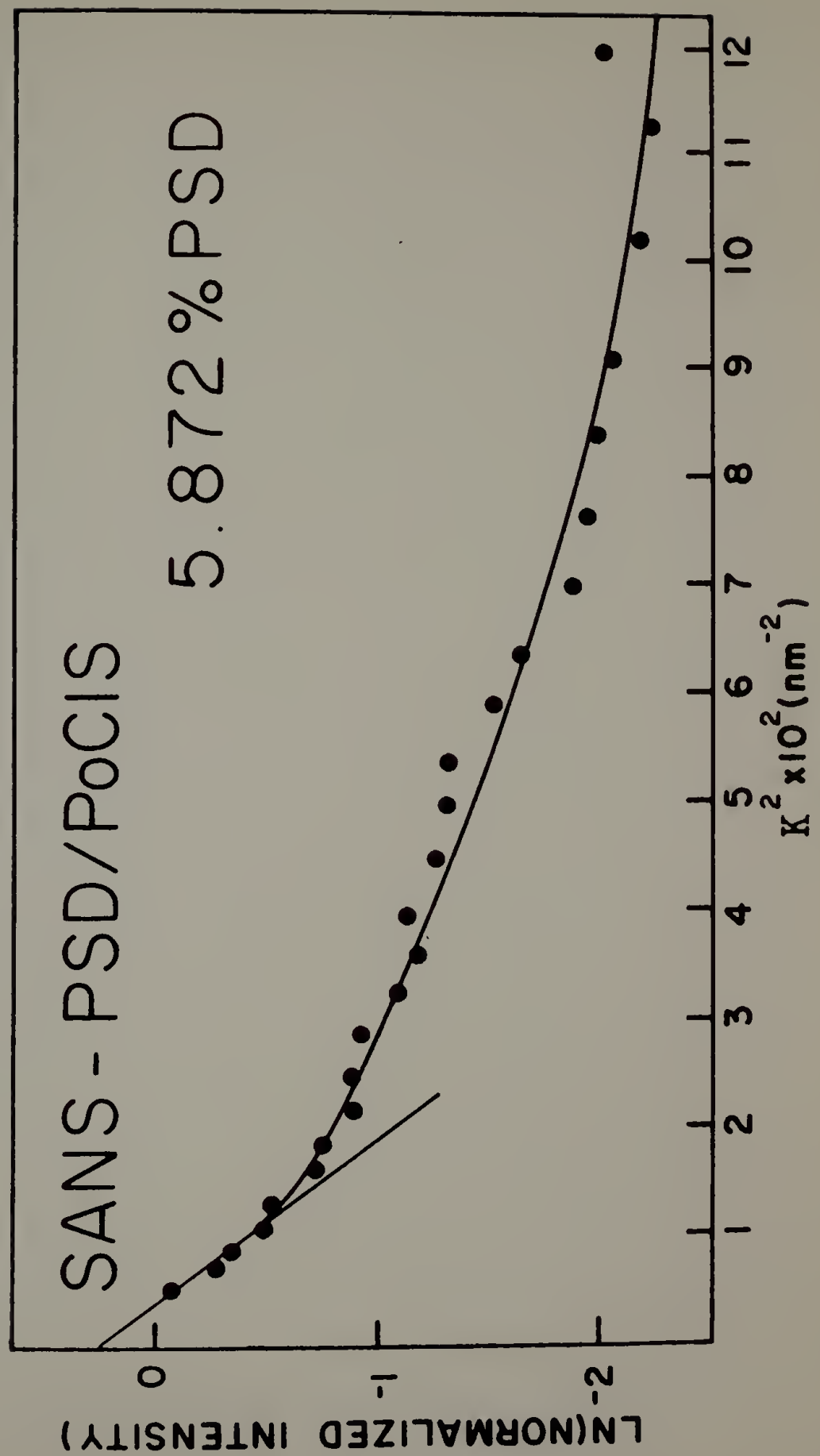
SANS - PSD/PoCIS
5.872% PSD
LN(NORMALIZED INTENSITY)
0
-1
-2
1
2
3
4
5
6
7
8
9
10
11
12
$K^2 \times 10^2 (nm^{-2})$

Figure 86. Radius of gyration as a function of composition for d-PS in PoClS matrix.

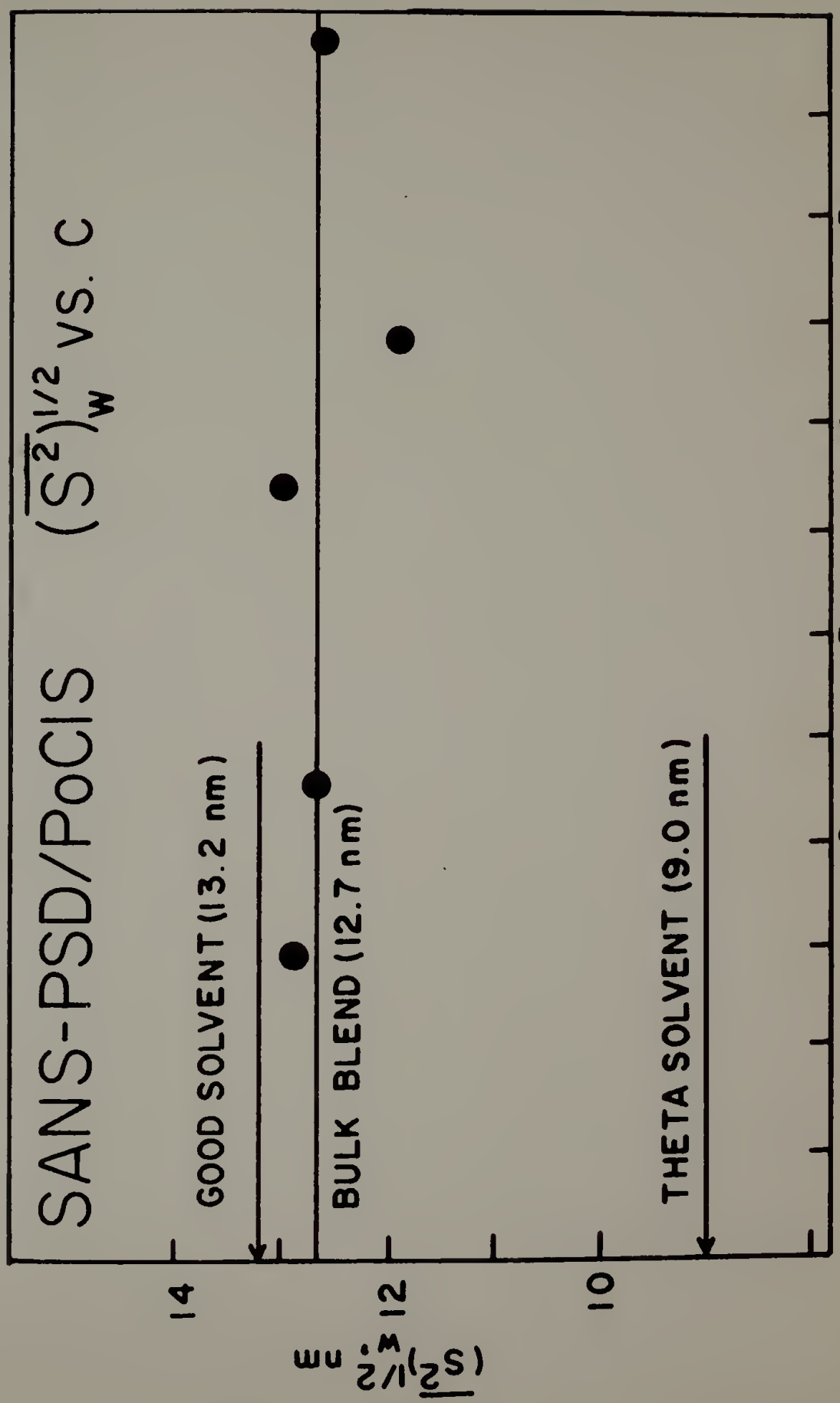
SANS-PSD/PoCIS
$(\overline{S^2})^{1/2}_w$ vs. C
GOOD SOLVENT (13.2 nm)
BULK BLEND (12.7 nm)
THETA SOLVENT (9.0 nm)
$(\overline{S^2})^{1/2}_w$, nm
14
12
10
1
2
3
4
5
CONCENTRATION (g/cm^3 x 10^2)

Figure 87. Guinier analysis on d-PS in PoClS (0.03749 grams of d-PS in PoClS). Data obtained on D-11 in Grenoble.

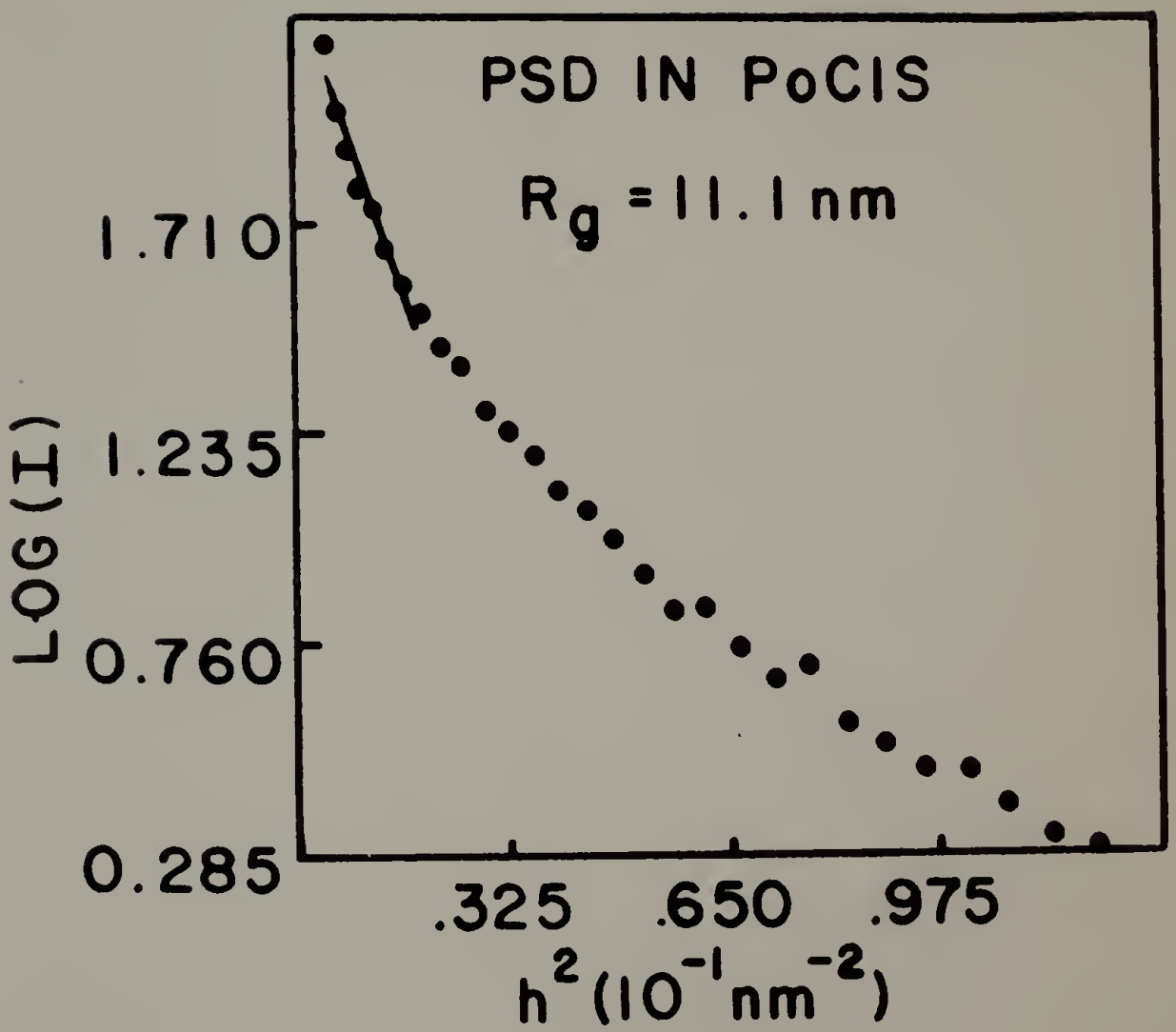
PSD IN PoCIS
R_g = 11.1 nm
1.710
1.235
0.760
0.285
LOG(I)
.325
.650
.975
$h^2(10^{-1}nm^{-2})$

Figure 88. KC/R(h) vs. h^2 of a 0.03749 gram d-PS in PoClS.
Data obtained on D-11 in Grenoble.

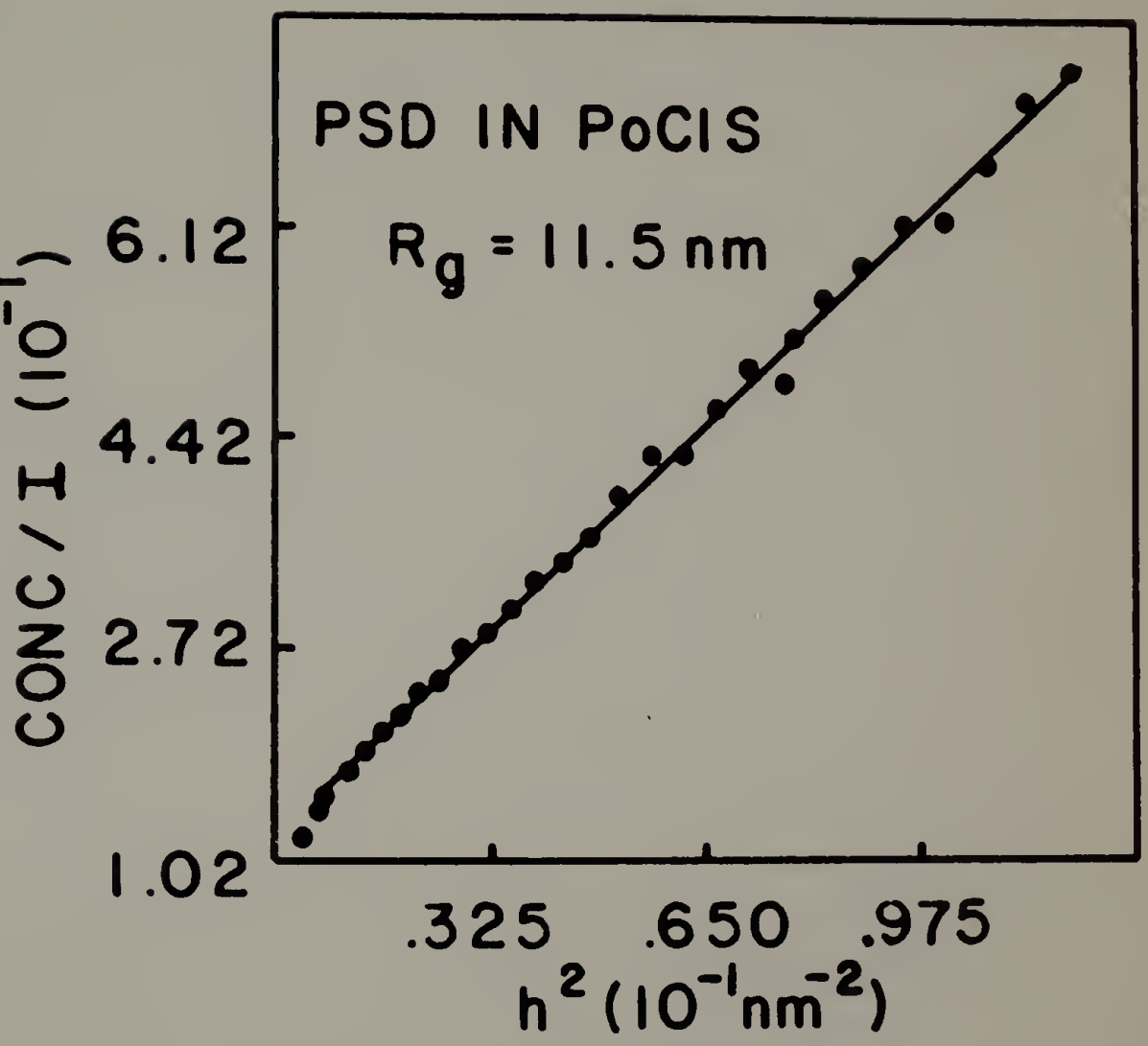
PSD IN PoCIS
R_g = 11.5 nm
CONC / I (10^{-1})
6.12
4.42
2.72
1.02
.325
.650
.975
h^2 (10^{-1} nm^{-2})

Figure 89. Calibration curve for a vanadium standard.

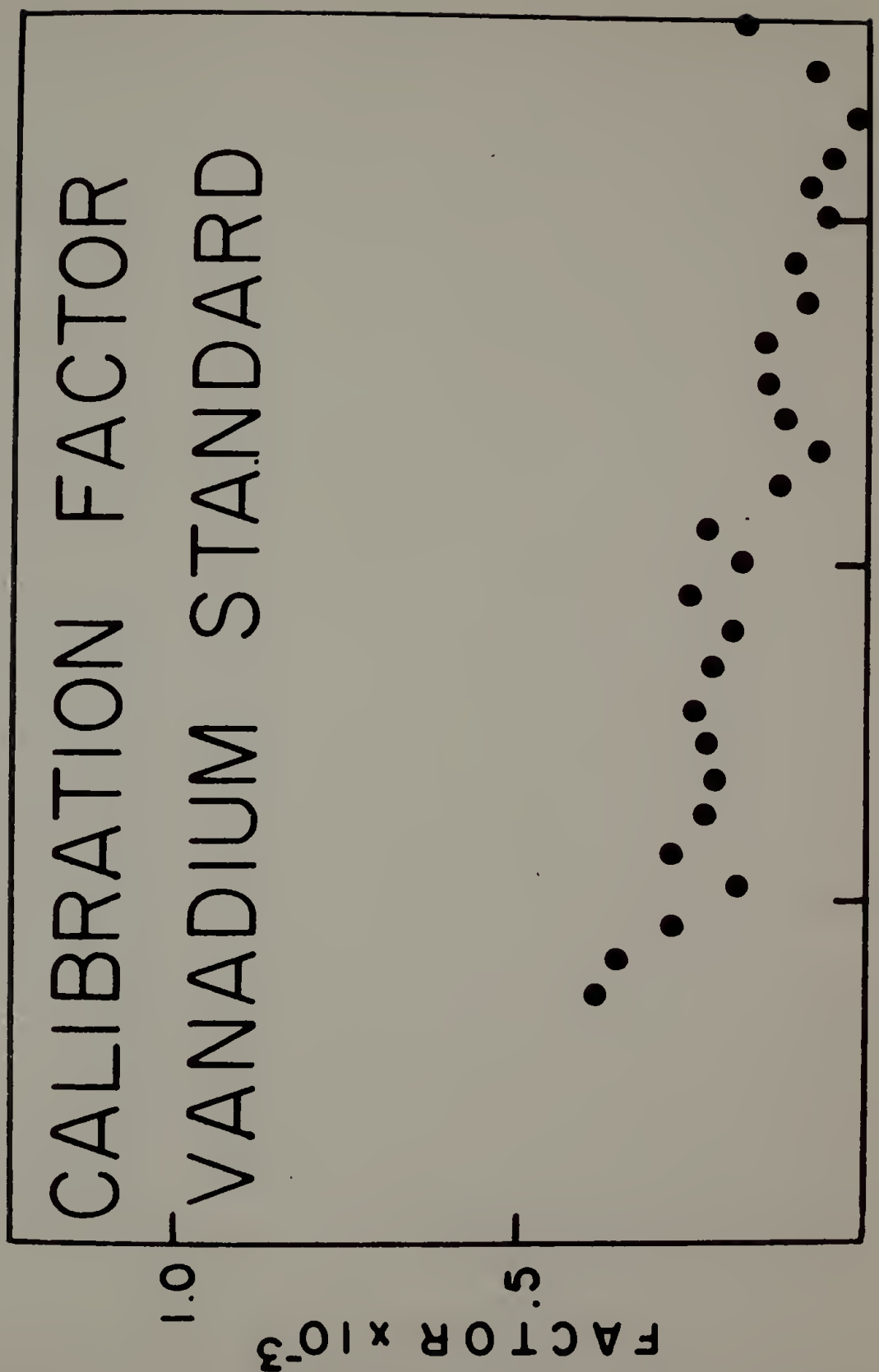
CALIBRATION FACTOR
VANADIUM STANDARD
FACTOR x 10^{-3}
1.0
.5
1
2
3
K x 10^{1} nm^{-1}

Figure 90. KC/R(0) vs. concentration of d-PS in PoClS.

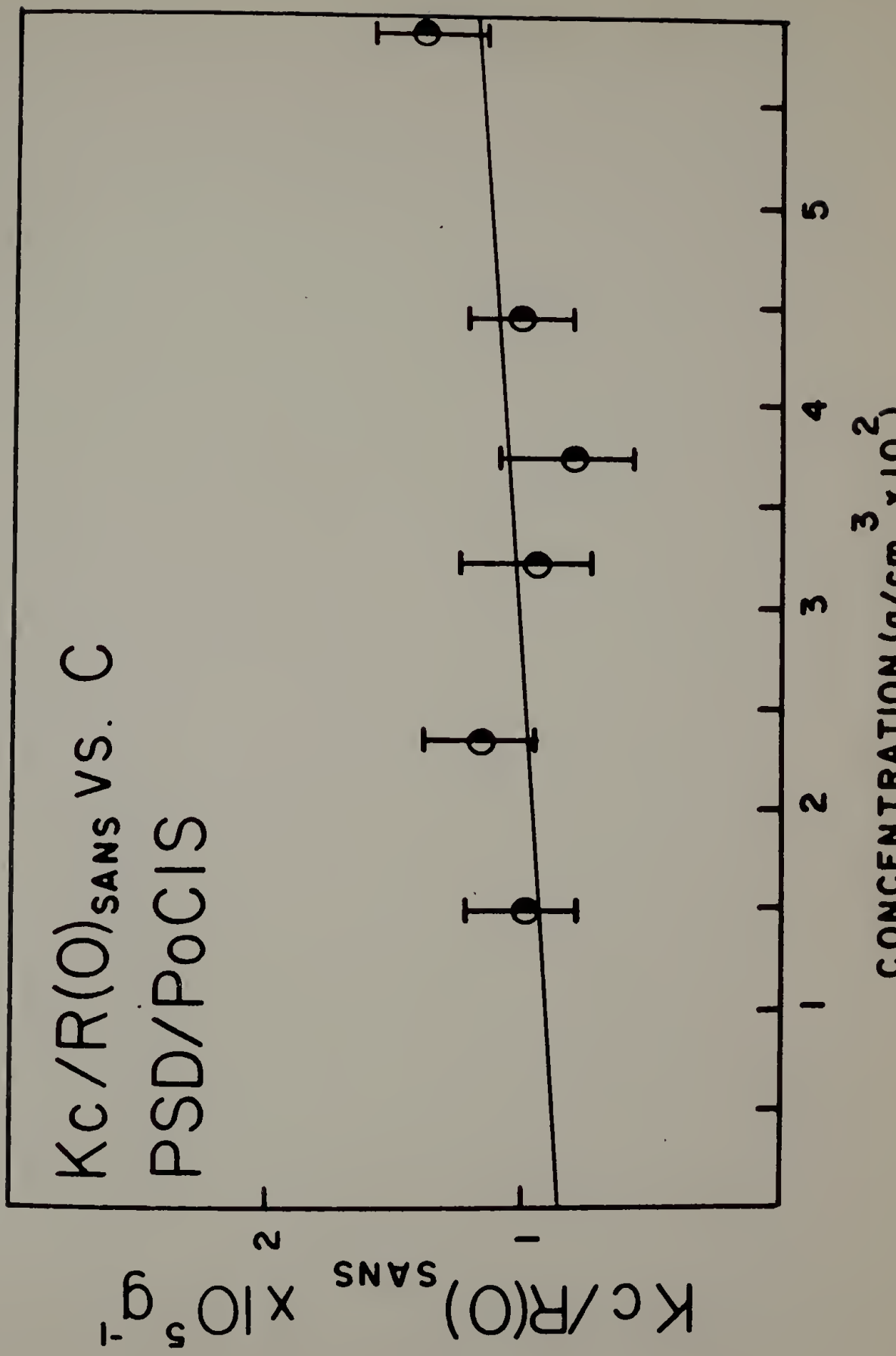
Kc/R(O)SANS VS. C
PSD/PoCIS
Kc/R(O)SANS x 10^5 g^-1
2
1
1
2
3
4
5
CONCENTRATION (g/cm^3 x 10^2)

Figure 91. Comparison of expected T_g and experimental values obtained for the PVC/PCL blends.

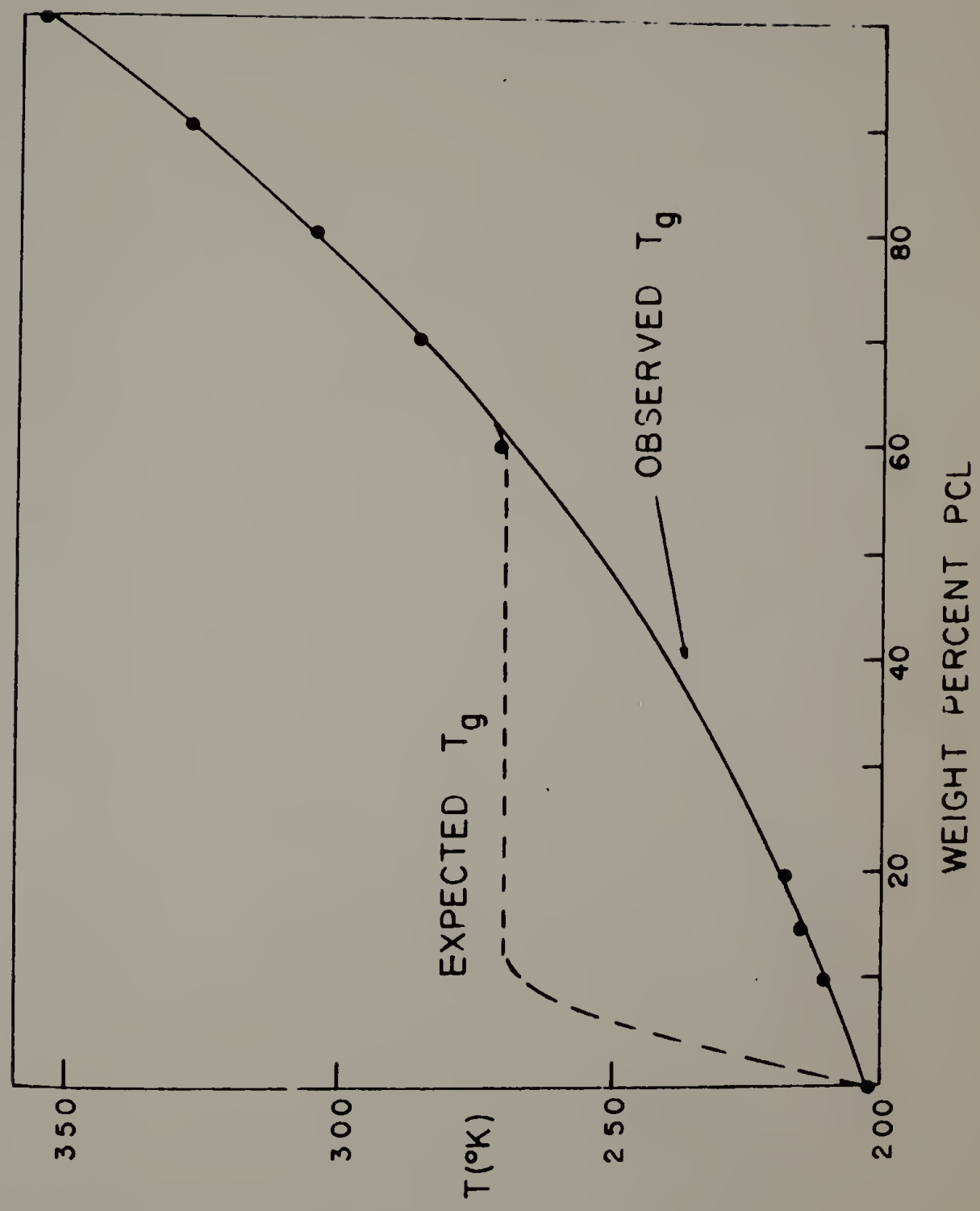
350
300
250
200
T(°K)
EXPECTED T_g
OBSERVED T_g
20
40
60
80
WEIGHT PERCENT PCL

Figure 92. Debye and Guinier scatterers plotted in Debye-Bueche fashion.

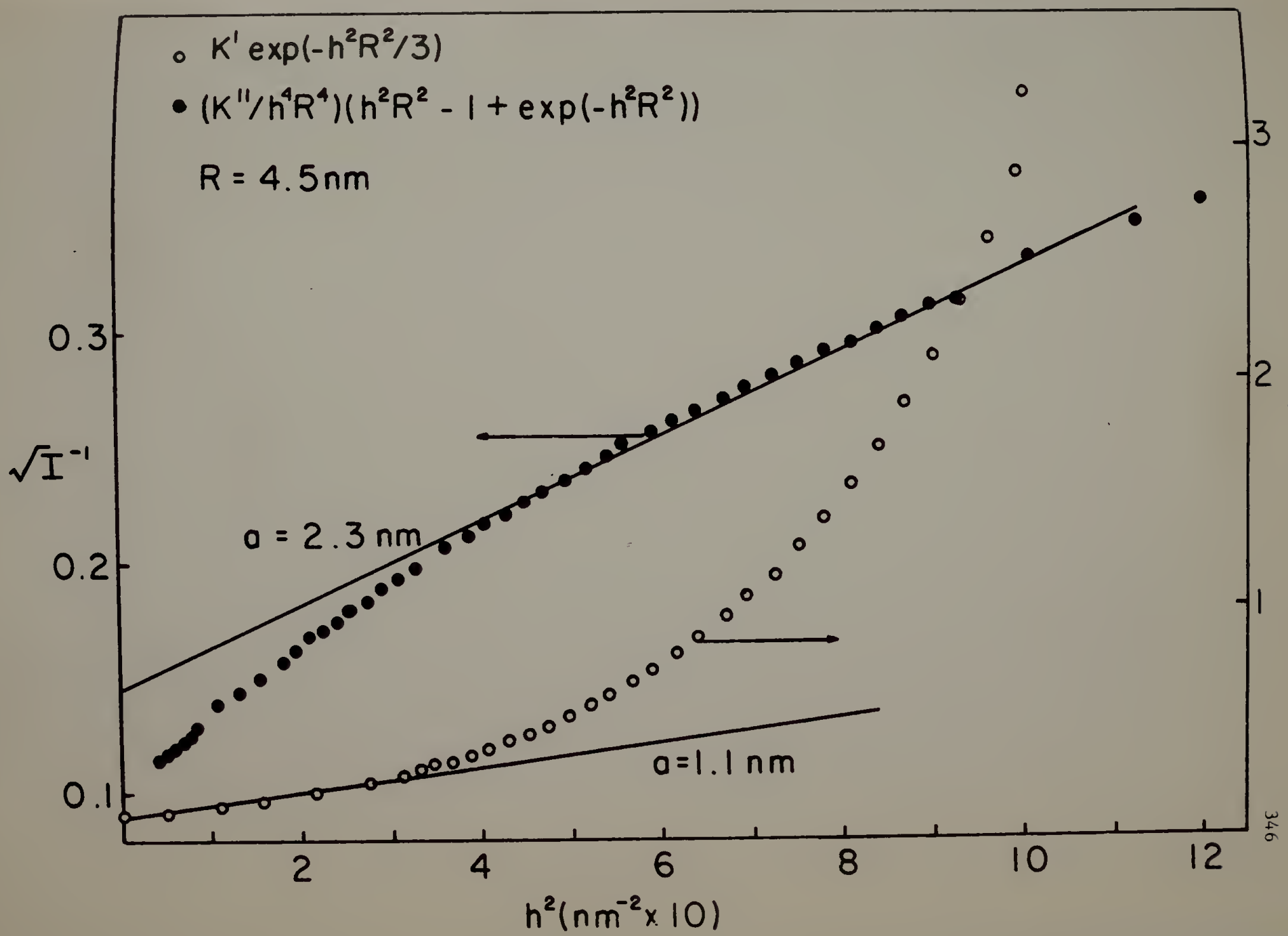
$\circ$ $K' \exp(-h^2R^2/3)$
$\bullet$ $(K''/h^4R^4)(h^2R^2 - 1 + \exp(-h^2R^2))$
R = 4.5nm
a = 2.3 nm
a=1.1 nm
$\sqrt{I^{-1}}$
0.3
0.2
0.1
3
2
1
2
4
6
8
10
12
$h^2(nm^{-2} \times 10)$

REFERENCES

1. S. Krause, J. Macromol. Sci., Rev. Macromol. Chem., C7, 251 (1972).

2. S. Krause and N. Roman, J. Polym. Sci., A3, 1631 (1965).

3. R.S. Stein, Optical Properties of Polymer Blends, in preparation.

4. J. Manson and L. Sperling, Polymer Blends and Composites, Plenum Press, New York, NY (1976).

5. P.F. Bruins, ed., Polyblends and Composites (J. Appl. Polym. Sci., Appl. Polym. Symp. No. 15), Interscience, New York, NY (1970).

6. N.A.J. Platzer, ed., Multicomponent Polymer Systems (Adv. Chem. Series No. 99), American Chem. Soc., Washington, DC (1971).

7. N.A.J. Platzer, ed., Copolymers, Polyblends and Composites (Adv. Chem. Series No. 142), American Chem. Soc., Washington, DC (1975).

8. S.L. Rosen, Polym. Eng. Sci., 7, 115 (1967).

9. T.G. Fox, Bull. Am. Chem. Soc., 2, 123 (1956).

10. M. Gordon and J. Taylor, J. Appl. Chem., 2, 493 (1952).

11. R. Buchdahl and L.E. Nielsen, J. Appl. Phys., 21, 482 (1950).

12. L.E. Nielsen and R. Buchdahl, J. Am. Chem. Soc., 75, 1435 (1953).

13. R. Buchdahl and L.E. Neilsen, J. Polym. Sci., 15, 1 (1955).

14. M. Takayanagi, Memoirs of the Faculty of Engineering, Kyushu University, 23, 1 (1963).

15. J. Stoelting, F.E. Karasz, and W.J. MacKnight, Polym. Eng. and Sci., 10(3), 133 (1970).

16. T.K. Kwei, T. Nishi, and R.F. Roberts, Macromol., 7, 667 (1974).

17. T. Nishi, T.K. Kwei, and T.J. Wang, J. Appl. Phys., 46, 4157 (1975).

18. E.J. Perry, J. Appl. Polym. Sci., 8, 2605 (1964).

19. L.J. Hughes and G.L. Brown, J. Appl. Polym. Sci., 5, 580 (1961).

20. E. Fischer, J. Macromol. Sci. Chem., A2, 1285 (1968).

21. G.L. Wilkes and R.S. Stein, J. Polym. Sci., A2, 7, 1525 (1969).

22. S.D. Hong, M. Shen, T.P. Russell, and R.S. Stein, in Polymer Alloys, ed. D. Klempner and K.C. Frisch, Plenum Press, New York, NY (1978).

23. D. McIntyre and E. Campos-Lopez, in Block Copolymers, ed. A. Aggarwal, Plenum Press, New York, NY (1970).

24. P. Gilmore, Ph.D. Dissertation, Polymer Science and Engineering, University of Massachusetts, Amherst, MA (1978).

25. J.J. Hickman and R.M. Ikeda, J. Polym. Sci., Phys. Ed., 11, 1713 (1973).

26. M.M. Coleman and P.C. Painter, J. Macromol. Sci.--Rev. Macromol. Chem., C16(2), 197 (1978).

27. M.M. Coleman and J. Zarian, in press (1978).

28. T. Nishi and T.T. Wang, Macromol., 8, 909 (1975).

29. J. Ong, Ph.D. Dissertation, Polymer Science and Engineering, University of Massachusetts, Amherst (1973).

30. R. Koningsveld, L.A. Kleintjins, and H.M. Schoffeleers, J. Pure Appl. Chem., 39, 1 (1974).

31. H. Tompa, Polymer Solutions, Butterworths Pub., London (1956).

32. P.J. Flory, Principles of Polymer Chemistry, Cornell University Press, Ithaca, NY (1953).

33. P.J. Flory, J. Chem. Phys., 9, 660 (1941); 10, 51 (1942).

34. M.L. Huggins, J. Chem. Phys., 9, 440 (1941); Ann. N.Y. Acad. Sci., 43, 1 (1942).

35. R.L. Scott and H. Magat, J. Chem. Phys., 13, 172 (1945).

36. R.L. Scott, J. Chem. Phys., 13, 178 (1945).

37. R.L. Scott, J. Chem. Phys., 17, 279 (1949).

38. O. Olabisi, Macromol., 8, 316 (1975).

39. J.E. Guillet, J. Macromol. Sci., Chem., 4, 1669 (1970).

40. J.E. Guillet, in Progress in Gas Chromatography, ed. J.H. Purnell, Wiley-Intersciences, New York, NY (1973).

41. J.H. Hildebrand and R.L. Scott, Regular Solutions, Prentice-Hall, Englewood Cliffs, NJ (1962).

42. G. Gee, Quarterly Review Chem. Soc., 1, 265 (1947).

43. M. Bank, J. Leffingwell, and C. Thies, J. Polym. Sci., A2, 10 (1972); Macromol., 4, 44 (1971).

44. T. Nishi and T.K. Kwei, Polymer, 16, 285 (1975).

45. R. Bernstein, C. Cruz, D. Paul, and J. Barlow, Macromol., 10, 681 (1972).

46. P. Alexandrovich, Ph.D. Dissertation, Polymer Science and Engineering, University of Massachusetts, Amherst, MA (1978).

47. L.P. McMaster, Macromol., 6, 760 (1973).

48. T. Orofino and P.J. Flory, J. Chem. Phys., 26, 1067 (1957); B.E. Eichinger and P.J. Flory, Trans. Faraday Soc., 64, 2035 (1968).

49. I. Prigogine, The Molecular Theory of Solutions, North-Holland Publishing Co., Amsterdam (1957).

50. A.A. Tager, L.V. Adamova, V.V. Serpinskii, and M.V. Tsilipotkina, Vysokomol. soyed., A16(1), 203 (1974); A14(2), 2090 (1972).

51. D. Patterson, Macromol., 2, 672 (1969); J. Polym. Sci., C-64, 3379 (1968).

52. D. Patterson and A. Robard, Macromol., 11, 690 (1978).

53. R.H. Lacombe and I.C. Sanchez, J. Phys. Chem., 80, 2568 (1968); J. Polym. Sci. Phys. Ed., in press.

54. N. Moore, Physical Chemistry, Prentice-Hall, Inc., Englewood Cliffs, NJ (1972).

55. C. Ryan, F.E. Karasz, and W.J. MacKnight, in preparation.

56. J. Fried, Ph.D. Dissertation, Polymer Science and Engineering, University of Massachusetts, Amherst, MA (1976).

57. J.W. Cahn, J. Chem. Phys., 42, 93 (1965).

58. J.W. Cahn and J.E. Hilliard, J. Chem. Phys., 31, 688 (1959).

59. J.W. Cahn, General Electric Report No. 63-RL-3256M (1963); Acta Metall., 10, 907 (1962); 14, 1685 (1966).

60. J.S. Langer, Ann. Phys., 65, 53 (1971).

61. J.S. Langer, in Fluctuations, Instabilities and Phase Transitions, ed. T. Riste, Plenum Press, New York, NY (1975).

62. H.E. Cook, Acta Metall., 18, 297 (1970).

63. K.B. Rundman and J.E. Hilliard, Acta Metall., 15, 1025 (1967).

64. N. Goldstein, private communication.

65. J. Gilmer, private communication.

66. I.C. Sanchez, private communication.

67. B.H. Zimm, J. Chem. Phys., 16, 1093, 1099 (1948).

68. H. Benoit, J. Polym. Sci., 11, 507 (1953).

69. A. Holtzer, H. Benoit, and P. Doty, J. Phys. Chem., 58, 624 (1954).

70. O. Kratky, G. Porod, and L. Kahovec, Z. Electrochem., 55, 53 (1951).

71. O. Kratky, Prog. Biophys., 13, 105 (1963).

72. O. Kratky, Z. Physikalische Chem., 9, 237 (1955).

73. W. Krigbaum and R. Godwin, J. Chem. Phys., 43, 4523 (1965).

74. H. Hayashi, F. Hamada, and A. Nakajima, Macromolecules, 7, 959 (1974); 9, 543 (1976); Polymer, 18, in press (1977).

75. H. Benoit, D. Decker, J. Higgins, C. Picot, J. Cotton, B. Farnoux, G. Jannink, and R. Ober, Nature Physical Science, 245, 15 (1973).

76. J. Cotton, D. Decker, H. Benoit, B. Farnoux, J. Higgins, G. Jannenk, R. Ober, C. Picot, and J. Des Cloizeaux, Macromol., 7, 863 (1974); Annales des Physique, 1, 112 (1976).

77. H. Benoit, J. Cotton, D. Decker, B. Farnoux, J. Higgins, G. Jannink, R. Ober, and C. Picot, J. Appl. Cryst., 7, 188 (1974).

78. J. Schelten, D. Ballard, G. Wignall, G. Longman, and W. Schmatz, Polymer, 17, 751 (1976).

79. G. Wignall, D. Ballard, and J. Schelten, Eur. Polym. J., 10, 861 (1974); 9, 965 (1973).

80. D. Ballard, M. Rayner, and J. Schelten, Polymer, 17, 640 (1976).

81. W. Schmatz, T. Springer, J. Schelten, and K. Ibel, J. Appl. Cryst., 7, 96 (1974).

82. D. Ballard, J. Schelten, and G. Longman, Polym. Preprints, 18(2), 167 (1977).

83. R. Kirste, W. Kruse, and J. Schelten, Die Makromol. Chemie, 162, 299 (1973).

84. R. Kirste, W. Kruse, and J. Schelten, J. Appl. Cryst., 7, 188 (1974).

85. R. Kirste, W. Kruse, and K. Ibel, Polymer, 15, 120 (1975).

86. R. Kirste and B. Lehnen, Makromol. Chemie, 177, 1137 (1976).

87. W. Kruse, R. Kirste, J. Haas, B. Schmitt, and D. Stein, Makromol. Chemie, 177, 1145 (1976).

88. D. Sadler and A. Keller, Polymer, 17, 37 (1976).

89. R. Kirste, unpublished results (1978).

90. J. Higgins, unpublished results (1978).

91. R.S. Straff and D.R. Uhlmann, JPS, Phys. Ed., 14, 353 (1976).

92. J.H. Wendorff and E.W. Fischer, Kolloid Z.Z. Polym., 251, 376 (1973).

93. A.L. Renninger, G.G. Wicks, and D.R. Uhlmann, J. Polym. Sci., Phys. Ed., 13, 1247 (1975).

94. A.L. Renninger and D.R. Uhlmann, JPS, Phys. Ed., 13, 1481 (1975).

95. A.L. Renninger and D.R. Uhlmann, JPS, Phys. Ed., 14.

96. E.W. Fischer, J.H. Wendorff, M. Dettenmaier, G. Lieser, and I. Voigt-Martin, J. Macromol. Sci.-Physics, B12(1), 41 (1976).

97. H. Benoit et al., Nature Phys. Sci., 245, 15 (1973).

98. P.J. Flory, J. Macromol. Sci.-Phys., B12(1), 1 (1976).

99. G. Patterson, J. Macromol. Sci., B12, 61 (1976).

100. D. Uhlmann et al., J. Macromol. Sci., B12, 153 (1976).

101. G.S.Y. Yeh, J. Macromol. Sci.-Phys., B6, 465 (1972).

102. G. Nielsen and S. Jabarin, J. Appl. Phys., 46, 1175 (1975).

103. P.M. Gezovich and P.H. Geil, Ind. J. Polym. Mat., 1, 3 (1971).

104. C. Singleton, J. Isner, D.M. Gezovich, P.K.C. Tson, P.H. Geil, and E.A. Collins, Polym. Eng. Sci., 14, 371 (1974).

105. P. Geil, J. Macromol. Sci.-Phys., B12, 173 (1976).

106. W. Pechold and S. Blasenbrey, Kolloid Z.Z. Polym., 241, 955 (1970).

107. V.A. Kargin, J. Polym. Sci., 30, 247 (1958).

108. P. Harget and S. Aharoni, J. Macromol. Sci., B12, 209 (1976).

109. D.G. Ballard, J. Schelten, and G.W. Longman, ACS Polym. Preprints, 18(2), 167 (1977).

110. A. Einstein, Ann. Physik., 33(4), 1275 (1910).

111. P. Debye, J. Applied Phys., 15, 338 (1944); J. Phys. and Colloid Chem., 51, 18 (1947).

112. A. Guinier and G. Fournet, Small Angle Scattering of X-rays, trans. C. Walker and K. Yudowitch, John Wiley and Sons, Inc., New York, NY (1955).

113. P. Debye, J. Phys. Chem., 51, 18 (1947).

114. B. Tabor, in Light Scattering from Polymer Solutions, ed. M.B. Huglin, Academic Press, New York, NY (1972).

115. Von K. Altgelt and G.V. Schulz, Makromol. Chemie, 36, 209 (1960).

116. J. Cotton, B. Farnoux, G. Jannink, and R. Ober, J. Appl. Cryst., 7, 189 (1974).

117. A.C. Albrecht, J. Chem. Phys., 27, 1014 (1957).

118. H. Benoit and C. Picot, Pure Appl. Chem., 12, 545 (1966).

119. A.J. Hyde and R.B. Taylor, Makromol. Chem., 62, 204 (1963).

120. A.J. Hyde and R.B. Taylor, in Solution Properties of Natural Polymers, The Chemical Society, London (1968).

121. A.J. Hyde, in Light Scattering from Polymer Solutions, ed. M.B. Huglin, Academic Press, New York, NY (1972).

122. P.J. Flory, J. Chem. Phys., 13, 453 (1945) .

123. J. Hildebrand, J. Am. Chem. Soc., 38, 1452 (1916); 41, 1067 (1919); 42, 2180 (1920).

124. G. Scotchard, Chem. Rev., 8, 321 (1931).

125. P. Debye and A.M. Bueche, J. Appl. Phys., 20, 518 (1940).

126. P. Debye, H.R. Anderson, and H. Brumberger, J. Appl. Phys., 28, 679 (1957).

127. O. Kratky, J. Pure and Appl. Chem., 12, 483 (1966).

128. G. Porod, Kolloid Z., 124, 83 (1951); 125, 51, 109 (1952).

129. G. Porod, Acta Phys. Aust., 2, 255 (1948).

130. D. Buchanan, J. Polym. Sci., A2(9), 645 (1971).

131. K. Vonk and G. Korleve, Kolloid Z.Z. Polym., 220, 19 (1967); 224, 225 (1968).

132. R. Hosemann and S.N. Bagchi, Direct Analysis of Diffraction by Matter, North Holland Publishing Co., Amsterdam (1951).

133. W. Ruland, Colloid and Polym. Sci. 25, 29 (1977).

134. S.K. Baczek, Ph.D. Dissertation, Polymer Science, University of Massachusetts, Amherst, MA (1977).

135. F.P. Warner, R.S. Stein, and W.J. MacKnight, J. Polym. Sci., Phys. Ed., 15, 12 (1977).

136. B. Crist, J. Polym. Sci., Phys. Ed., 11, 635 (1973).

137. B. Crist and N. Morosoff, J. Polym. Sci., Phys. Ed., 11, 1023 (1973).

138. D. Ya Tsvankin, Polym. Sci. USSR, 6, 2304, 2310 (1964).

139. D. Ya Tsvankin, U.A. Zubov, and J. Kitaigordskii, J. Polym. Sci., C16, 4081 (1968).

140. T. Russell, unpublished results.

141. R.W. Hendricks and J.S. Lin, The Lorentz Correction Factor in Small Angle Scattering, to be published.

142. L.E. Alexander, X-ray Diffraction Methods in Polymer Science, Wiley-Interscience, New York, NY (1969).

143. F.P. Warner, Ph.D. Dissertation, Loughborough University (1975).

144. F. Khambatta, F.P. Warner, T.P. Russell, and R.S. Stein, J. Polym. Sci., Phys. Ed., 14, 1391 (1976).

145. R. Brämer, Ph.D. Dissertation, University of Ulm (1973).

146. R. Brämer, Colloid and Polym. Sci., 252, 504 (1973).

147. W. Wenig, Ph.D. Dissertation, University of Ulm (1973).

148. W. Wenig, F.E. Karasz, and W.J. MacKnight, J. Appl. Phys., 46, 4194 (1975).

149. C. Vonk, J. Appl. Cryst., 6, 8 (1973).

150. W. Ruland, J. Appl. Cryst., 4, 70 (1971).

151. T. Hashimoto, K. Nagatoshi, A. Todo, H. Hasegawa, and H. Kawai, Macromol., 7, 364 (1974).

152. T. Hashimoto, A. Todo, H. Itoi, and H. Kawai, Macromol., 70, 377 (1977).

153. J. Koberstein, B. Morra, and R.S. Stein, A Critical Evaluation of Deviations from Porod's Law, to be published (1978).

154. R. Bonart and E.G. Miller, J. Macromol. Sci.-Phys., B10(1), 177 (1974); B10(2), 345 (1974).

155. R.W. Hendricks, J. Appl. Cryst., 11, 15 (1978).

156. T.P. Russell, R.S. Stein, R.D. Zedler, R.W. Hendricks, and J.S. Lin, Use of a One Dimensional Position Sensitive Detector on a Kratky SAXS Apparatus, in preparation (1978).

157. O. Kratky and H. Leopold, Makromol. Chem., 133, 181 (1970).

158. O. Kratky and Z. Skala, Z. Electrochem., 62, 73 (1958).

159. A. Guinier and G. Fournet, J. Phys. Rad., 8, 345 (1947).

160. A. Guinier and G. Fournet, Nature, 160, 501 (1947).

161. R.W. Hendricks, ORNL-TM-1950 (1972).

162. M. Buchanan and R.W. Hendricks, J. Appl. Cryst., 4, 176 (1971).

163. R.W. Hendricks and P.W. Schmidt, Acta Phys. Austr., 26, 97 (1967); 37, 20 (1973).

164. J.A. Lake, Acta Cryst., 23, 191 (1967).

165. J. Schelten and F. Hossfeld, J. Appl. Cryst., 4, 210 (1971).

166. O. Glatter, J. Appl. Cryst., 7, 147 (1974).

167. O. Glatter and P. Zipper, Acta Phys. Austr., 43, 307 (1975).

168. M. Deutsch and M. Luban, J. Appl. Cryst., 11, 87, 98 (1978).

169. P.W. Schmidt, J. Appl. Cryst., 3, 137 (1970).

170. P.W. Schmidt, Acta Cryst., 19, 938 (1965); 8, 772 (1955).

171. P.W. Schmidt and R. Hight, Acta Cryst., 13, 480 (1960).

172. L.B. Shaffer and R.W. Hendricks, USAEC Report-TM-4278 (1973).

173. R.B. Leighton, Principles of Modern Physics, McGraw-Hill Publishing Co., New York, NY (1959), p. 577.

174. R.W. Hendricks, J. Appl. Cryst., 5, 315 (1972).

175. C.J. Sparks, R.W. Hendricks, and L.B. Schaffer, submitted to J. Appl. Cryst. (1972).

176. O. Kratky, Makromol. Chem., 35A, 12 (1960).

177. O. Kratky, Z. Anal. Chem., 201, 161 (1964).

178. O. Kratky, I. Pilz, and P.J. Schmitz, J. Colloid Interface Sci., 21, 24 (1966).

179. O. Kratky and H. Wawra, Monatsch. Chem., 94, 981 (1963).

180. I. Pilz, J. Colloid Interface Sci., 30, 140 (1969).

181. J. Higgins and R.S. Stein, Recent Developments of Small Angle Neutron, X-ray and Light Scattering (1978).

182. R.S. Stein and R.L. Rowell, eds., Electromagnetic Scattering, Gordon and Breach Pub. Co., New York, NY (1967).

183. G. Herzberg, Molecular Spectra and Molecular Structure. II. Infrared and Raman Spectra of Polyatomic Molecules, Van Nostrand Co., Inc., New York, NY (1945).

184. L. Bellamy, Infrared Spectra of Complex Molecules, Methuen, London, and Wiley, New York, NY (1958).

185. R. Zbinden, Infrared Spectroscopy of High Polymers, Academic Press, New York, NY (1964).

186. M.J. Low, J. Chem. Ed., 47, 3 (1970).

187. Y. Shindo, Ph.D. Dissertation, Chemistry, University of Massachusetts, Amherst, MA (1968).

188. A. Zozulya and Z. Novikova, Zh. Analst. Khim., 18, 1105 (1963).

189. Fischer Chemical Company, Waltham, MA.

190. J. Riddick and W. Bunger, Organic Solvents. II. Techniques of Chemistry, ed. A. Weissberger, Wiley-Interscience, New York, NY (1970).

191. Union Carbide Corporation, New Product Information, Bulletin F-42501, Chemicals and Plastics, New York, NY.

192. D. Hubbell and S.L. Cooper, J. Appl. Polym. Sci., in press.

193. J.V. Koleske and R.D. Lundberg, J. Polym. Sci., A2(7), 795 (1969).

194. F.B. Khambatta, Ph.D. Dissertation, Polymer Science and Engineering, University of Massachusetts, Amherst, MA (1976).

195. P. Kratochvil, Czech. Chem. Comm., 29, 2767 (1964); 30, 1119 (1965).

196. M.A. Harrison, P.H. Morgan, and G.S. Park, Eur. Polym. J., 8, 1361 (1972).

197. M. Asahina and K. Okuda, Chem. High Polym. Japan, 17, 607, 612 (1960).

198. P.J. Lemstra, A. Keller, and M. Cudby, J. Polym. Sci., Phys. Ed., 16, 1507 (1978).

199. K.H. Illers, Makromol. Chem., 127, 1 (1969).

200. K. Kockott, Kolloid Z.Z. Polym., 198, 17 (1964).

201. R.J. D'Amato and S. Strella, Appl. Polym. Symp., 8, 275 (1969).

202. W. Jasching, Kunststoffe, 52, 8 (1962).

203. W. Chi-hsiung Robert and W. Der-ming Peter, Heat Stability of Polyvinyl Chloride (1971).

204. W. Hawkins, Polymer Stabilization, Wiley-Interscience, New York, NY (1972).

205. D. Braun, Makromol. Chemie, 30, 85 (1959).

206. W. Bray and A. Caulkins, J. Am. Chem. Soc., 53, 44 (1931).

207. C. Picot, unpublished results.

208. I. Tung and T. Taylor, J. Polym. Sci., 21, 144 (1956).

209. W. Ruland, Acta Cryst., 14, 1180 (1961); Polymer, 5, 89 (1964).

210. R.S. Stein, in Newer Methods of Polymer Characterization, ed. B. Ke, Interscience, New York, NY (1964).

211. A. Wasiak, D. Peiffer, and R.S. Stein, J. Polym. Sci., Polym. Lett. Ed., 14, 381 (1976).

212. R.S. Stein and M.B. Rhodes, ASTM Special Technical Pub., 348, 59 (1963).

213. R.S. Stein and M.B. Rhodes, J. Appl. Phys., 31, 873 (1960).

214. R.S. Stein and J.J. Keane, J. Polym. Sci., 17, 21 (1955); 20, 327 (1956).

215. A. Kejzers, J.J. van Aartsen, and W. Prins, J. Appl. Phys., 36, 2874 (1960).

216. R.S. Stein, in Structure and Properties of Polymer Films, ed. R.W. Lenz and R.S. Stein, Plenum Pub. Co., New York, NY (1973).

217. L.M. Robeson, J. Appl. Polym. Sci., 17, 3607 (1973).

218. G.E. Bacon, Neutron Diffraction, Oxford University Press, London (1962).

219. H.R. Child and S. Spooner, in press.

220. W. Wenig, J. Polym. Sci., Phys. Ed., 16, 1635 (1978).

221. J. Aklonis, W. MacKnight, and M. Shen, Polymer Viscoelasticity, John Wiley & Sons, New York, NY (1972).

222. M.M. Coleman, P.C. Painter, D.L. Tabb, and J.L. Koenig, J. Polym. Sci.-Polym. Lett., 12, 577 (1974).

223. D.L. Tabb, J.L. Koenig, and M.M. Coleman, J. Polym. Sci., Polym. Phys., 13, 1145 (1975).

224. S. Krimm, V.L. Folt, J.J. Shipman, and A.R. Berens, J. Polym. Sci., A1, 2621 (1963); Polym. Lett., 2, 1009 (1964).

225. K. Holland-Moritz and D.O. Hummel, J. Mol. Struct., 19, 289 (1973).

226. K. Holland-Moritz and H.W. Siesler, Appl. Spect. Revs., 11, 1 (1976).

227. A.E. Hallam, in Infrared Spectroscopy and Molecular Structure, ed. M. Davies, Elsevier Publishing Co., New York, NY (1963).

228. J. Koleske and R. Lundberg, J. Polym. Sci., A2(7), 897 (1967).

229. V. Luzzati, Acta Cryst., 13, 939 (1960).

230. E.L. Thomas, unpublished results presented at the March, 1978, APS Meeting in Washington, DC.

231. N. Kuwahara, K. Obins, S. Uens, and M. Kaneko, J. Polym. Sci., A3, 985 (1965).

232. B. Mohite, S. Gundiah, and S. Kapur, Die. Makromol. Chem., 116, 280 (1968).

233. Y. Noguchi, A. Aoki, G. Tanaka, and H. Yamakawa, J. Chem. Phys., 52(3) (1970).

A P P E N D I X I

ONE DIMENSIONAL POSITION SENSITIVE DETECTOR

ORNL/TM-6678

Contract No. W-7405-eng-26

Metals and Ceramics Division

THE APPLICATION OF A ONE-DIMENSIONAL POSITION-SENSITIVE DETECTOR TO A KRATKY SMALL-ANGLE X-RAY CAMERA*,†

T. P. Russell and R. S. Stein
Polymer Research Institute
University of Massachusetts
Amherst, MA 01003

M. K. Kopp and R. E. Zedler
Instrumentation and Controls Division

and

R. W. Hendricks and J. S. Lin
Metals and Ceramics Division

*Research performed by TPR in partial fulfillment of the requirements for the degree of Doctor of Philosophy from the University of Massachusetts.

†Research sponsored in part by the National Science Foundation under Grant No. DMR 7805925 to the University of Massachusetts and by the Division of Basic Energy Sciences, U.S. Department of Energy, under contract No. W-7405-eng-26 with Union Carbide Corporation.

CONTENTS

THE APPLICATION OF A ONE-DIMENSIONAL POSITION-SENSITIVE DETECTOR TO A KRATKY SMALL-ANGLE X-RAY CAMERA

T. P. Russell,* R. S. Stein,* M. K. Kopp†
R. E. Zedler,† R. W. Hendricks,† J. S. Lin‡

ABSTRACT

A conventional Kratky small-angle collimation system has been modified to allow the use of a one-dimensional position-sensitive x-ray detector. The detector was designed specifically for use with a long-slit camera and has uniform sensitivity over the entire beam in the slit-length direction. Procedures for alignment of the collimation system are given, and a variety of tests of the performance of the system are presented. Among the latter are measurements of electronic noise and parasitic scattering as well as comparisons against samples which were also measured on other cameras. The good agreement of these comparisons demonstrates the success of the use of a position-sensitive detector with the Kratky collimation system.

I. INTRODUCTION

An investigation was undertaken to study the small-angle x-ray scattering (SAXS) from amorphous polymers. Such systems are inherently weak, isotropic scatterers. Preliminary experiments on the ORNL 10-m small-angle x-ray scattering camera[1] indicated that the parasitic slit-edge background scattering precluded the use of this instrument. However, the advantages of position-sensitive detectors (PSDs)[2-4] are such that an alternative collimation system which has the necessary low parasitic scattering but which is also amenable to PSDs was sought. The Kratky

*Polymer Research Institute, University of Massachusetts, Amherst, MA 01003.

†Instrumentation and Controls Division.

‡Metals and Ceramics Division.

collimation geometry is one of several SAXS geometries noted for both high angular resolution and very low parasitic scattering.[5,6] This report describes our modifications of a commercial Kratky camera for use with an RC-line encoded one-dimensional position-sensitive detector (1DPSD) and illustrates its performance with scattering patterns from several well-established scattering systems. Recommendations for further modifications are made.

II. THE DETECTOR

A. Construction

With the use of a Kratky geometry, the recorded data must often be desmeared before proper interpretation can be made on an absolute level. As shown by Hendricks[7] the sensitivity of the detector along the slit-length direction is a function that enters into the desmearing calculations. Therefore, it is desirable to have a position-sensitive detector which has a uniform sensitivity along the slit length,* consequently simplifying the calculations. This was accomplished with an RC-line encoded 1DPSD specifically designed for use with a slit geometry. A diagram of the detector is shown in Fig. 1. The design of this detector differs from some of our previous detectors in that the width of the detector window is less than the detector diameter. Uniform x-ray absorption was obtained by using a flat beryllium window and a flat

*It is to be noted that a one-dimensional position-sensitive detector mounted with the wire along the 2θ direction has the slit-length direction normal to the wire.

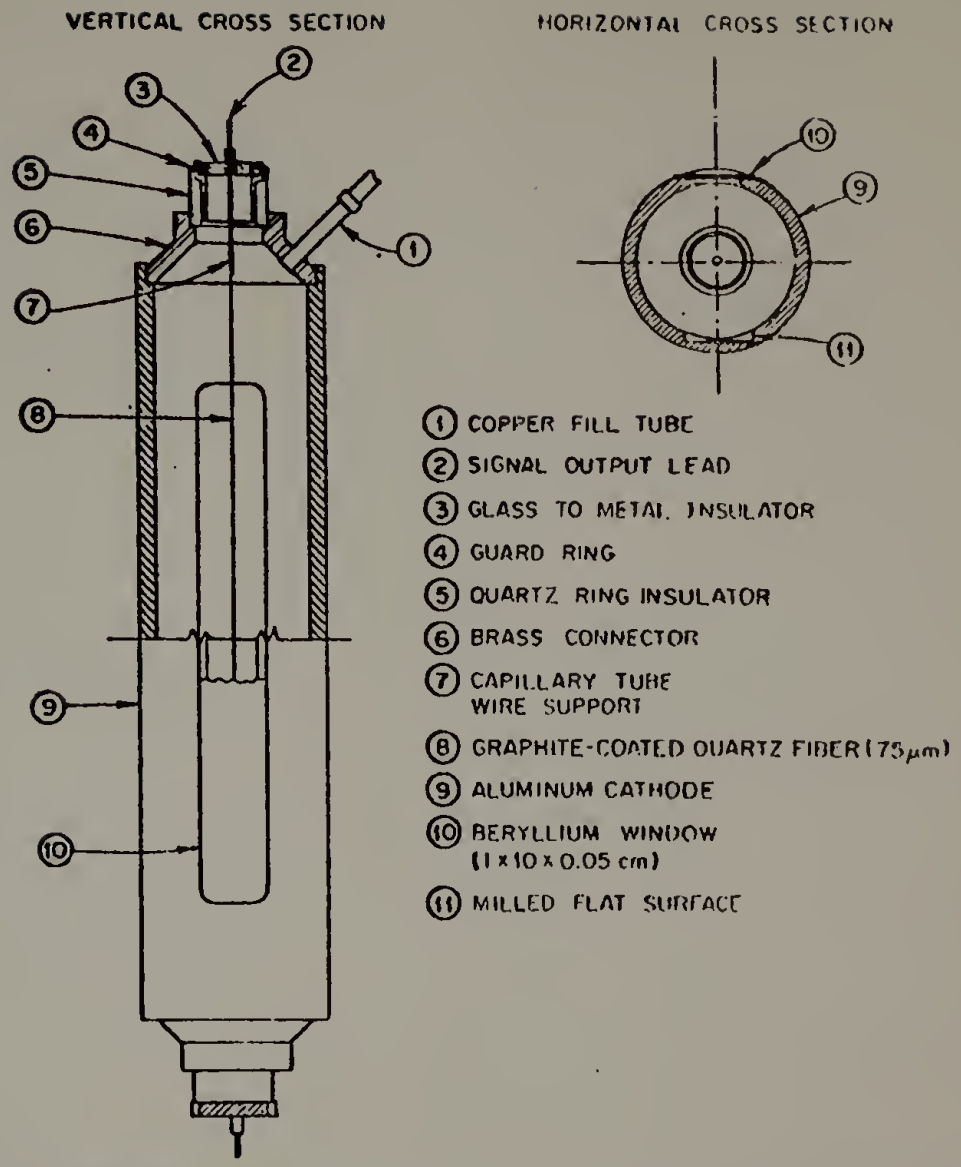

Fig. 1. One-dimensional position-sensitive detector designed for use with slit geometries.

surface machined opposite the window in the interior surface of the 3.2-cm-ID cylindrical aluminum cathode. These modifications ensured that radiation entering anywhere along the detector window would be absorbed with equal efficiency. Consequently, a uniform sensitivity along the slit length was obtained.*

* An alternate method of achieving the desired uniformity is to use elevated pressures of the fill gas. This is not desirable since additional precautions would have to be taken to contain the gas, higher operating voltages would be needed, and gas purity becomes more critical.

The components of the detector are shown in Fig. 1. Apart from the modifications described above, they follow standard practice for the construction of proportional counters as described previously.[2] As can be seen in Fig. 1, the detector is a sealed device. In addition to a 75 μm pyrolytic carbon-coated quartz anode, very low capacity guard ring structures were made to help achieve less than 0.5 mm spatial resolution. Specially shaped truncated conical counter ends were used, and anode capillary tubes were inserted to an experimentally determined length through the guard ring structures to minimize detector end effects and optimize field uniformity for the slit area. Before sealing, the detector components were thoroughly cleaned and the assembly degassed under high vacuum and then filled to 1 atm pressure with a purified mixture of 97% Xe–3% cyclopropane. Absorption efficiencies of about 50% for 17 keV x-rays and 100% for 8 keV were obtained. The fill tube was crimped closed and sealed with a low-melting solder.

B. Electronics

RC-line position encoding and decoding by pulse-shape analysis and crossover timing was used.[2–4] The electronics used for the data acquisition were the same as those used by Schelten and Hendricks,[8] a diagram of which is shown in Fig. 2. In addition to the position decoding electronics, a beam monitor[9] was also used. The output signal from its charge integrator was summed with that from the detector and stored in the highest few channels of the multichannel analyzer.

An important feature in the overall design of the detector system is the location of the preamplifiers. To minimize electronic noise these were placed as close as physically possible to the detector so

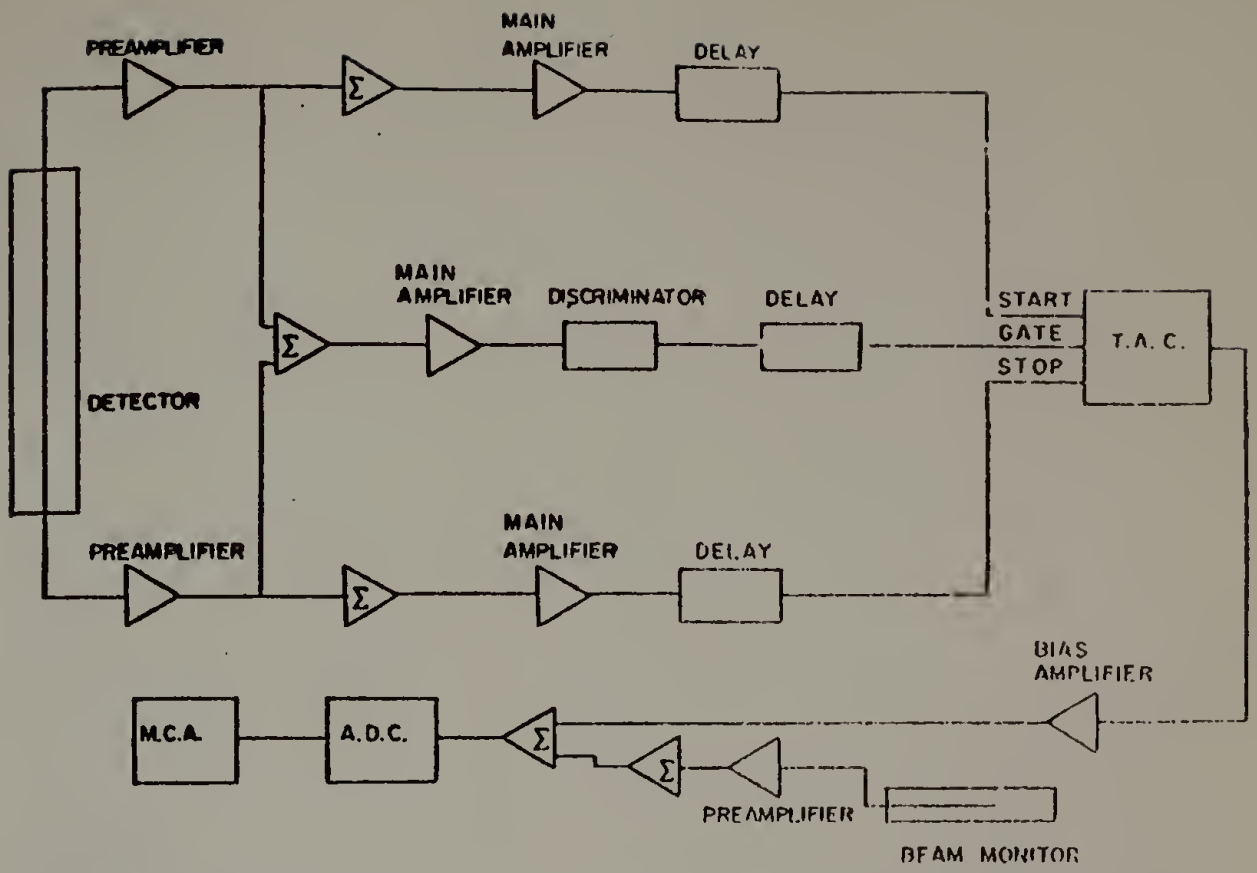

Fig. 2. Analog signal processing electronics for the detector. ADC = analog to digital converter; MCA = multichannel analyzer; TAC = time to amplitude converter; Σ = summing amplifier.

that the lengths of the output leads from the detector were minimized (Fig. 3). We used hybrid, voltage sensitive preamplifiers with pole-zero cancellation in the feedback circuit[10] which were designed specifically for position-sensitive detectors. In addition, the preamplifiers are dc-coupled to the detector anode. Thus, our detector anode was operated at ground potential and a high negative potential was applied to the shell. The Teflon standoffs for the detector and the safety shield are shown in Fig. 3.

C. Performance Tests

The performance of the detector was determined with a 1 mCi ^{55}Fe source (1 cm dia) enclosed in a brass container with a beryllium window,

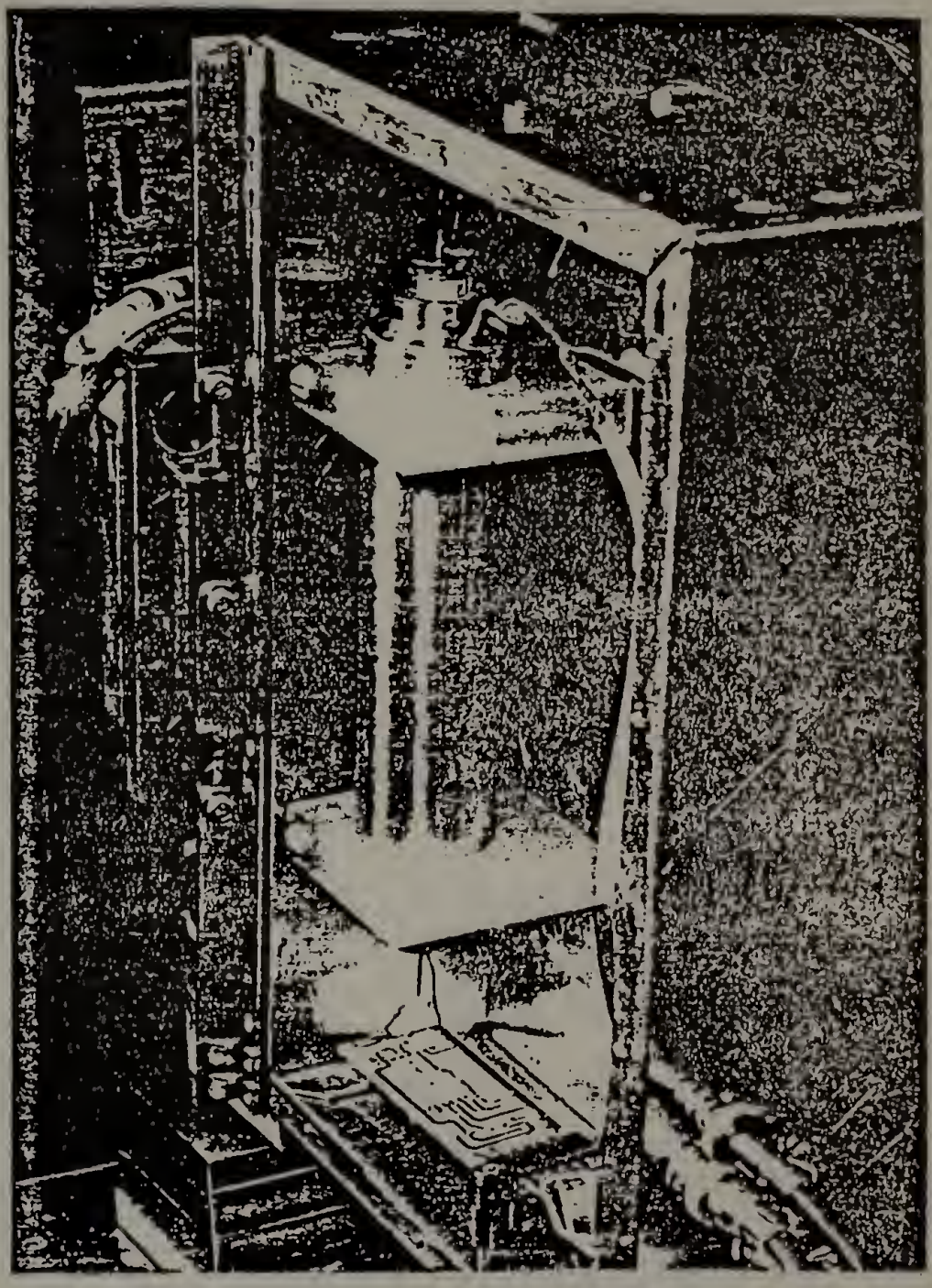

Fig. 3. Position-sensitive detector mounted on Teflon standoffs. One preamplifier is shown at bottom.

which was capable of operating in vacuum. Unless specified, the detector was operated at −2600 V.

(a) Energy Resolution

An energy spectrum was obtained with the ^{55}Fe source illuminating the detector and with the output of the summing amplifiers (Fig. 2) connected directly to the multichannel analyzer. The energy resolution for MnK_α (from ^{55}Fe source) and nickel-filtered copper radiation are shown in Fig. 4. The resolutions are 19 and 23%, respectively. The resolution was found to be sensitive to the detector bias voltage from −2400 to −2600 V. A decrease to 29% resolution was found at −2600 V.

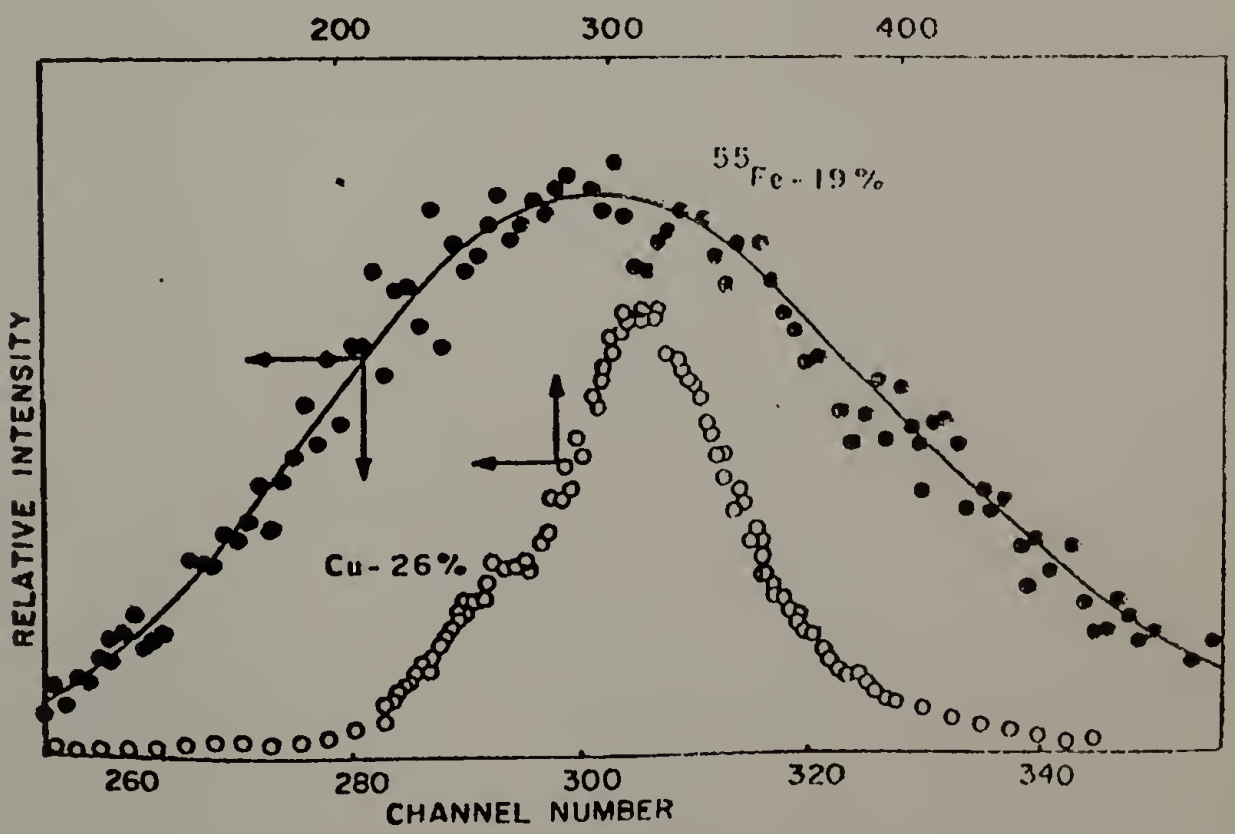

Fig. 4. Detector energy resolution for ^{55}Fe (bottom scale) and nickel-filtered CuK_α (top scale) radiation.

It is normally expected that the resolution of the higher energy radiation (CuK_α, 8.0 keV) would be better than that of the lower energy radiation (MnK_α, 5.9 keV). That such is not the case in the results of Fig. 4 can be accounted for because of the considerably broader energy spectrum of the filtered copper radiation, as opposed to the high monochromaticity of the MnK_α-MnK_β radiation emitted by ^{55}Fe.

(b) Spatial Resolution

The spatial resolution is the minimum length of the detector wire capable of being distinguished as a unique position. With a ^{55}Fe source (MnK_α radiation) in front of a Kratky collimation system, the detector was placed at various distances from the collimator. The width of the beam at the detector was determined geometrically from the width of the entrance slit and the detector to collimator distance. The FWHM of the peak on the MCA was determined as a function of the physical width of the beam.* When decreasing the beam width did not decrease the FWHM of the displayed resolution on the MCA, the resolution limit of the detector was reached. The spatial resolution is 390 μm (Fig. 5), in agreement with the electronically determined resolution. (A description of the electronic resolution measurement is given in Appendix I.)

(c) Uniformity of Detector Response

The ^{55}Fe source was placed approximately 1.5 m from the detector in an evacuated chamber ($\sim 5 \times 10^{-6}$ torr) in order to fully illuminate the detector with a uniform intensity. The resulting profile of the

*An alternate approach to evaluate the spatial resolution is to keep the distance between the detector and collimator fixed and vary the width of the beam by adjusting the entrance slit width.

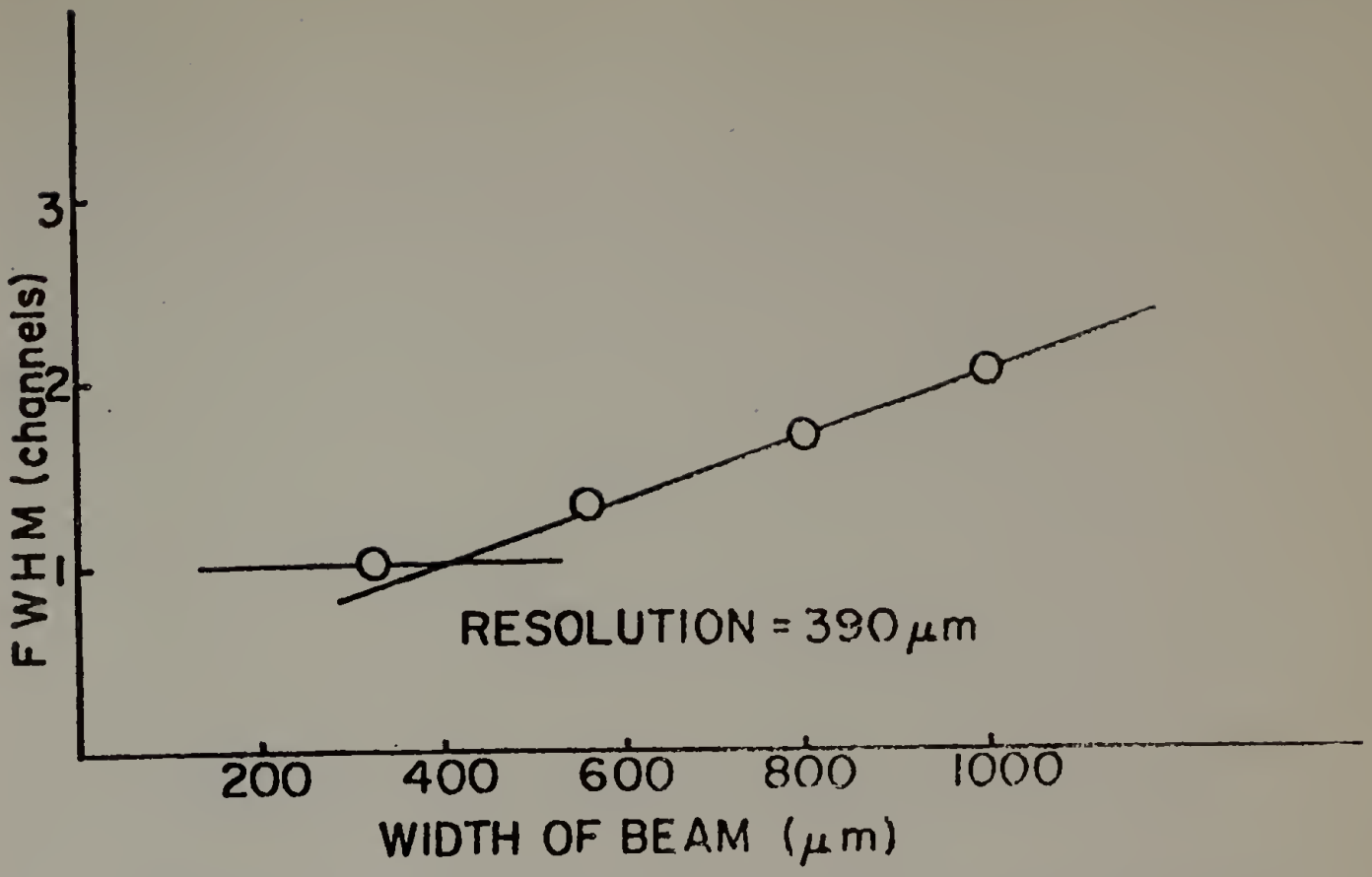

Fig. 5. Spatial resolution of the detector as determined by varying the width of a well-collimated incident beam. A FWHM of 1.0 channel (horizontal line) defines the observable resolution with a given MCA setting. For the data shown here, 512 channels were used.

uniformity or homogeneity of the detector is shown in Fig. 6. All subsequent scattering experiments must be corrected for nonuniform response using these data. We have chosen to scale the data of Fig. 6 to a mean value of unity and then to divide each scattering curve by the resultant normalized sensitivity run channel by channel. The maximum correction factor amounted to 10%.

(d) Homogeneity Across the Detector Face

The detector was designed to yield a uniform collection efficiency across the detector window normal to the wire direction. This was verified by moving a thick narrow slit (0.5 × 64 × 5 mm thick) oriented parallel to the detector wire across the face of the detector. Care was taken

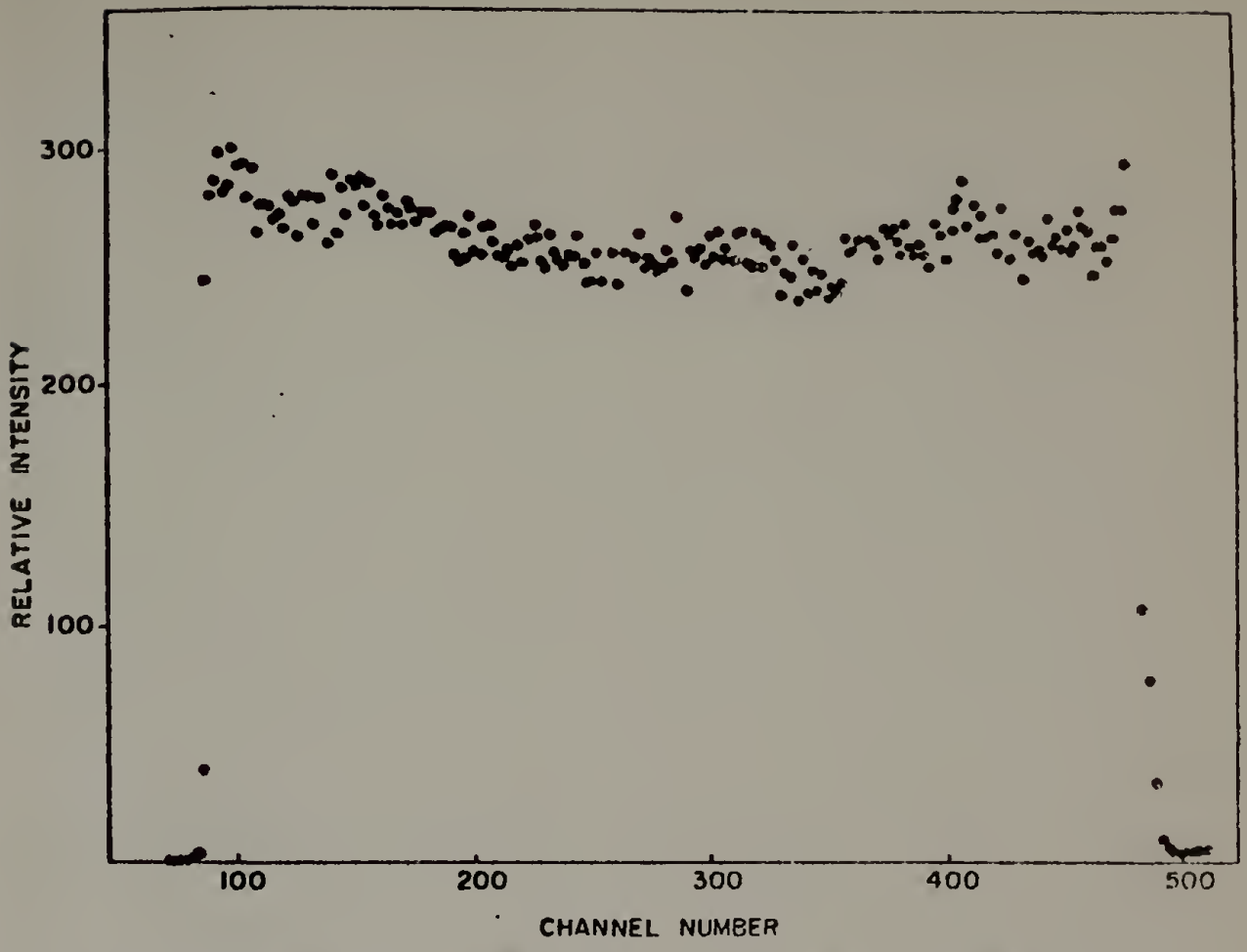

Fig. 6. Detector homogeneity as determined by measuring a ^{55}Fe source at 1.5 m.

to minimize the divergence of the beam. Figure 7 displays a superposition of several runs at various points across the window of the detector. As can be seen, the runs are indistinguishable. Therefore, the desired uniform collection efficiency was achieved.

The reason that Figs. 6 and 7 are not of identical shape is a result of the position of the ^{55}Fe source in each test. For the latter test the source-to-detector distance was much smaller in order to increase the intensity. However, the divergence in the direction normal to the wire was minimized by using a thick slit (5 mm).

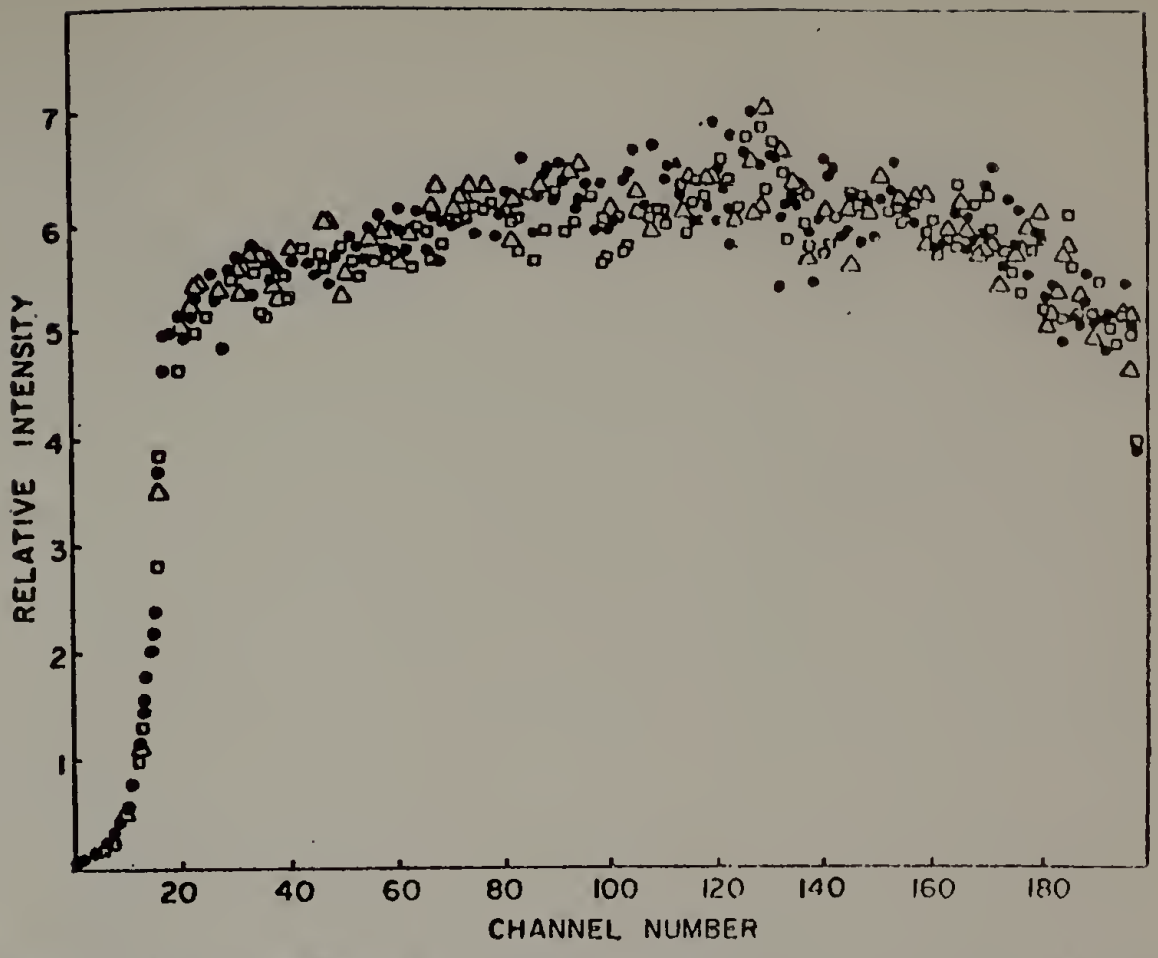

Fig. 7. Homogeneity across detector window as determined by moving a long, narrow (64 × 0.5 mm) slit across the detector face with the long dimension parallel to the detector wire.

(e) Linearity

The linearity of the detector was determined in a manner identical to that of Schelten and Hendricks.[8] With the source approximately 1.5 m from the detector, a lead mask containing sixteen 1-mm slots, separated by 6.1 mm from slot center to slot center, was placed immediately before the detector. The profile resulting from this is shown in Fig. 8. The centroids of the maxima were determined as a function of channel number and are plotted versus their real-space separation in Fig. 9. These data were fitted with various polynomials to calibrate

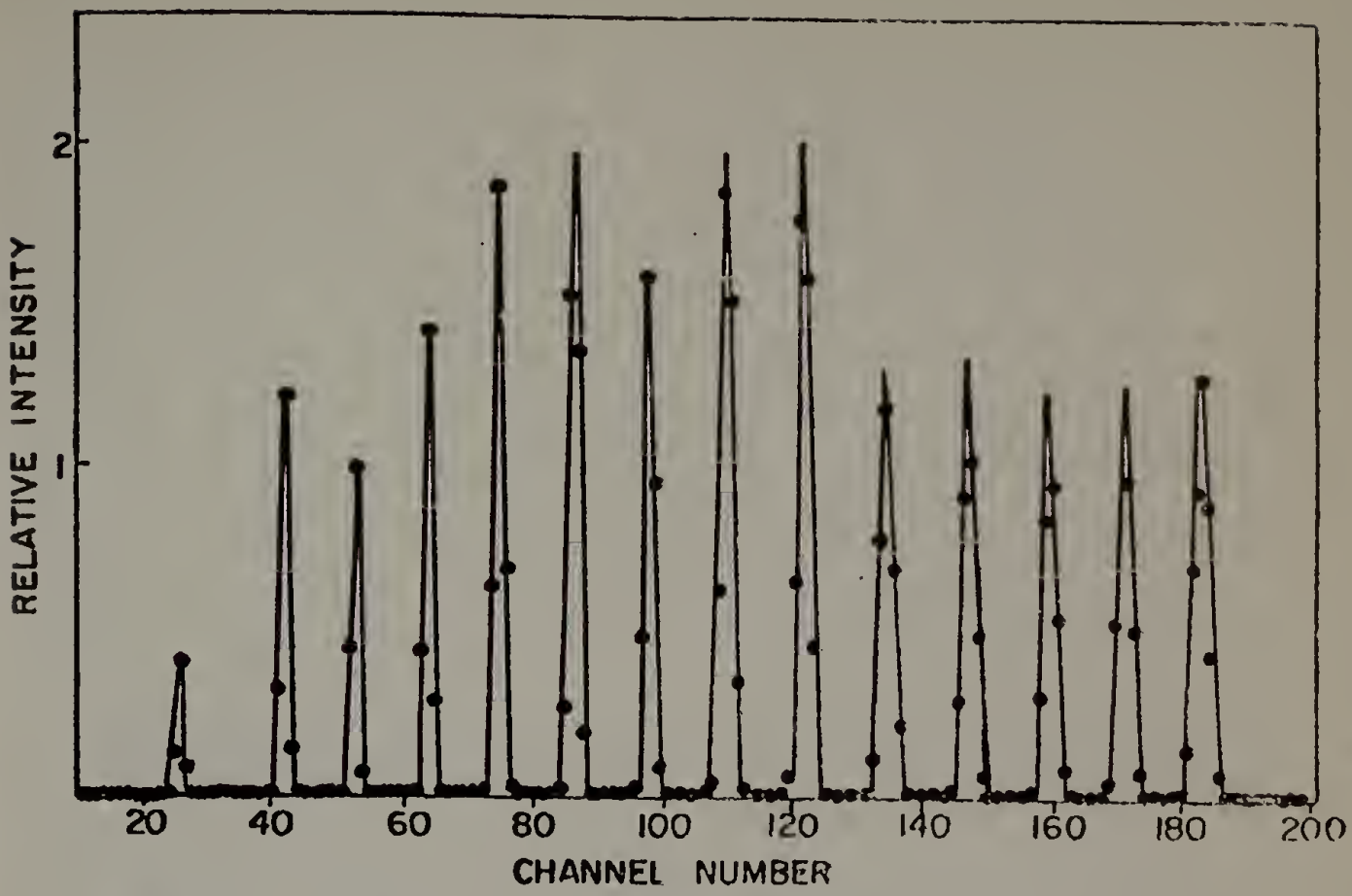

Fig. 8. Linearity test as determined by recording a ^{55}Fe spectrum with a mask consisting of 15 narrow (1 mm) slits normal to the detector length in front of the detector.

the MCA with real space.* The best fit was found to be a quadratic polynomial of the form

$$Y = -12.91 + 0.45\,X + 6.80 \times 10^{-4}\,X^2 - 2.36 \times 10^{-6}\,X^3 \qquad (1)$$

where Y represents the distance in real space from the origin corresponding to a channel X. These results demonstrate quite dramatically that the detector was reasonably linear over its useful length.

---

*The position of the origin on the MCA is arbitrary. During this experiment zero was selected as the position of the first maximum, occurring at channel number 26.

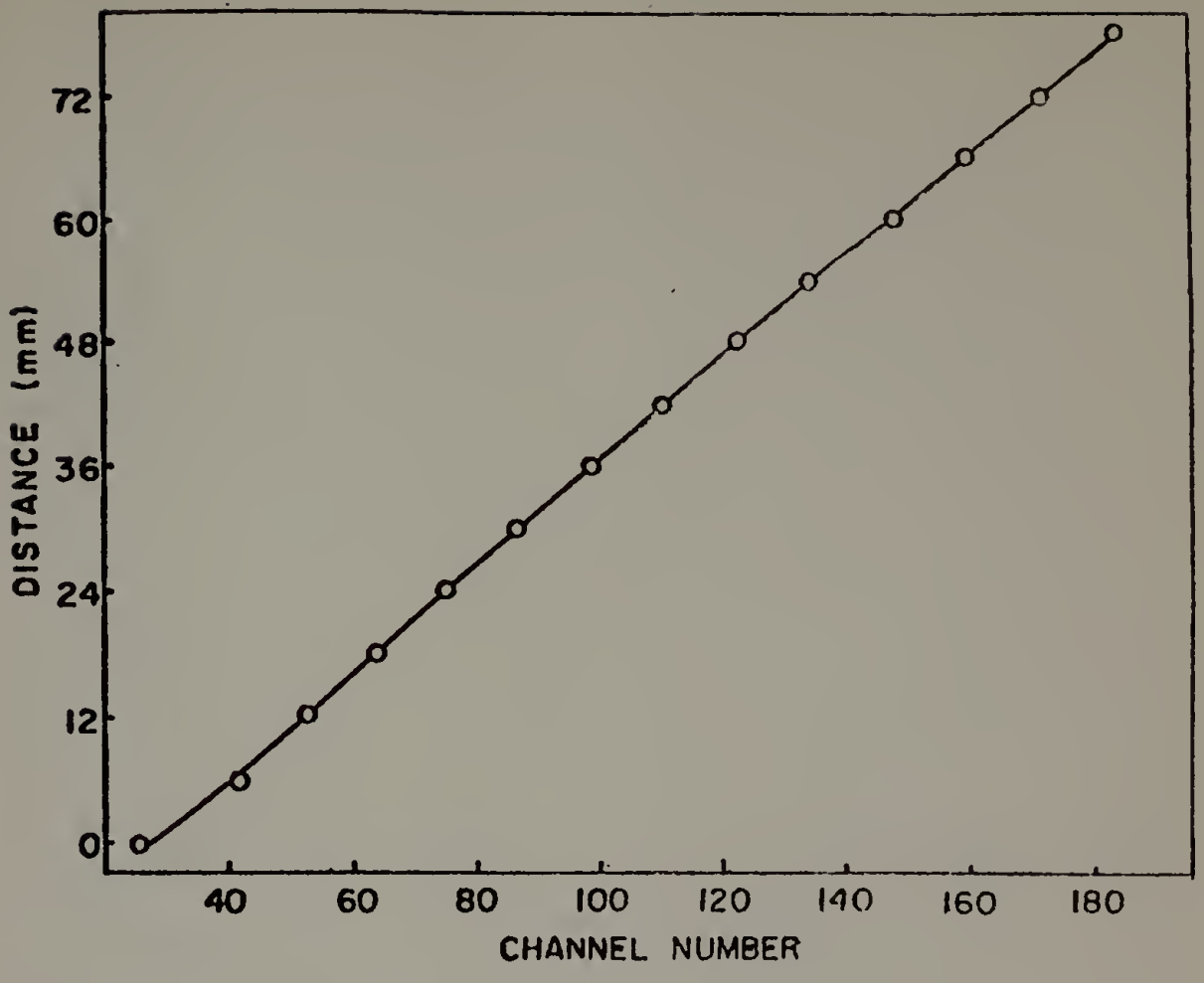

Fig. 9. Detector linearity.

III. MODIFICATIONS OF THE KRATKY COLLIMATION SYSTEM

The essential feature of the Kratky collimation system is the use of a U-block and bridge.[5,6] These components ultimately define the main beam profile, the amount of parasitic scattering, and the angular resolution. Although not so common these days as the camera with a moveable tank which is equipped with an adjustable narrow slit for step-scanning with electronic detectors, Kratky cameras have also been equipped with receiving slits some 10 × 50 mm for use with film cassettes. Since, like film, the 1DPSD acquires the entire scattering profile simultaneously, the vacuum tank for a system utilizing the PSD must be geometrically similar to the film camera. Therefore, the

commercially available camera (schematically shown in Fig. 10) had to be modified. The extent of modification depends upon the spatial resolution of the detector and the desired angular resolution. In this present case, a system was desired which had an angular resolution of 0.2 mradian/channel. With the 400 μm spatial resolution of the detector, this required a flight path (sample-to-detector distance) of 1.6 m. The collimation system parameters for the new camera are given in Table 1. In the modified camera (Fig. 11), the normal flight path (approximately 200–215 mm) was replaced by a length of aluminum tubing in which the diameter was doubled partway along its length. The first section was 36.5 cm long (8.9-cm inner diameter) and the second section was 93.4 cm long (19.1-cm inner diameter). The large diameter section was required to avoid intercepting the main beam by the inner walls of the tubing.* Both sections were lined with 0.04-cm-thick lead shielding to eliminate any small reflections or diffraction effects from the aluminum walls. The front section of the flight path was mounted onto a flange that was compatible with the initial section of the flight path of the commercially available camera. Therefore, the tilting mechanism of the original camera could be retained for alignment purposes. An aluminum flange, in which a 1 × 18 cm vertical slot was cut, was mounted with an O-ring on the rear of the new flight path. The slot was sealed with a sheet of 0.05-cm-thick beryllium on the outside surface of the flange as shown in Fig. 12(a). This was epoxied in place so that it was below the surface level of the external face. For alignment purposes the rear flange

*An earlier design, in which only 8.9-cm-dia tubing was used, had a parasitic scattering some 1000 times above that of the present design. This was determined to be scattering and fluorescence caused when the outer edges of the diverging main beam touched the tube walls.

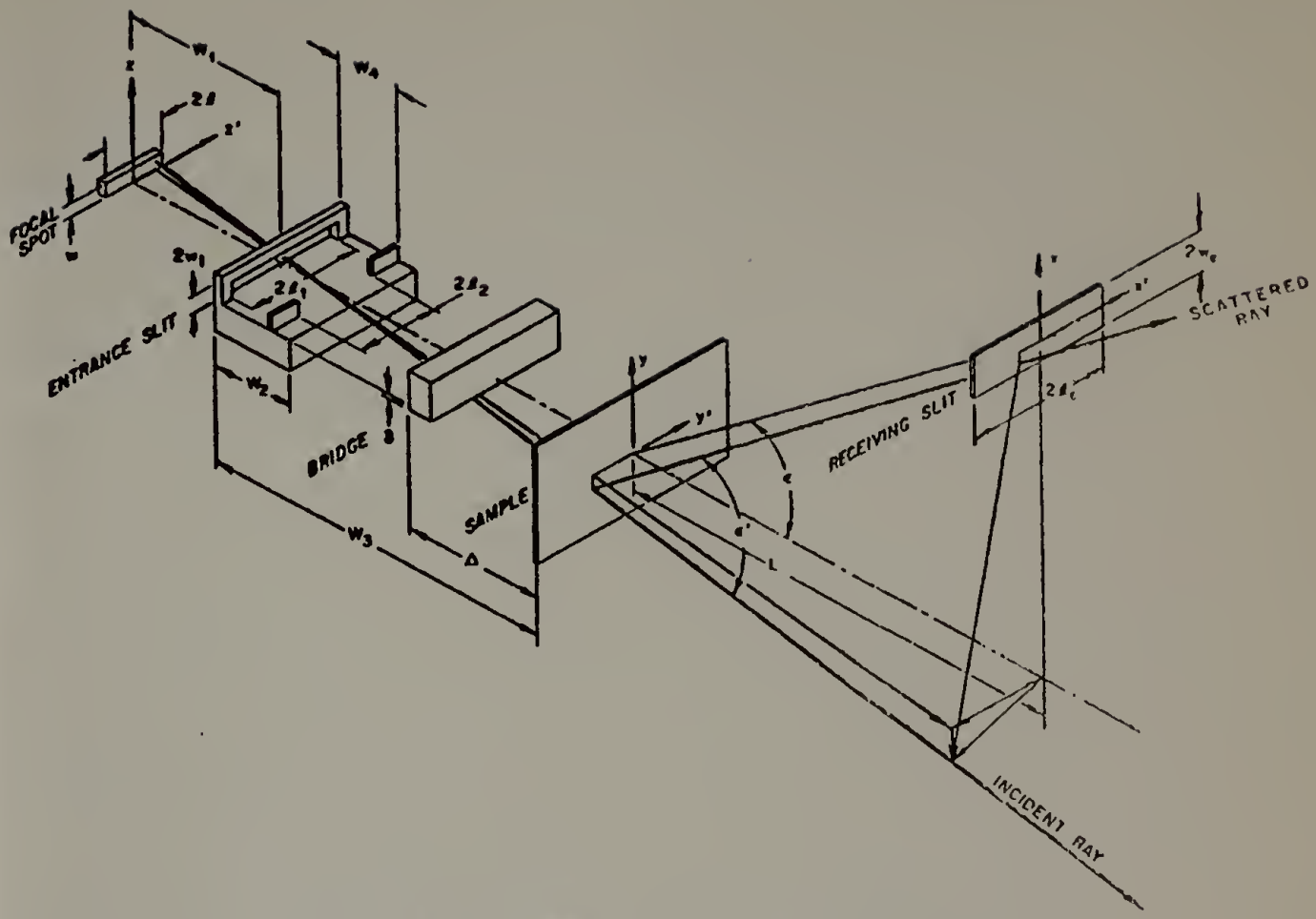

Fig. 10. Schematic of normal Kratky camera.

Table 1. Kratky Camera Collimation System Parameters*

Slit Width		Slit Length	
Parameter	Value (mm)	Parameter	Value (mm)
$2w_1$	0.065	2ℓ	7.0
δ	0.0	$2\ell_1$	∞
$2w_c$	0.450	$2\ell_2$	14.0
L_0	298.0	$2\ell_c$	10.0
W_1	103.0	W_4	125.0
W_2	60.0	L	1543.6†
W_3	195.0		
Δ	70.0		
L	1551.0†		

*See Fig. 10 for definition of variables.

†The value of L in the slit-width direction is from the sample to the wire, while in the slit-length direction it is from the sample to the machined edge of the detector window.

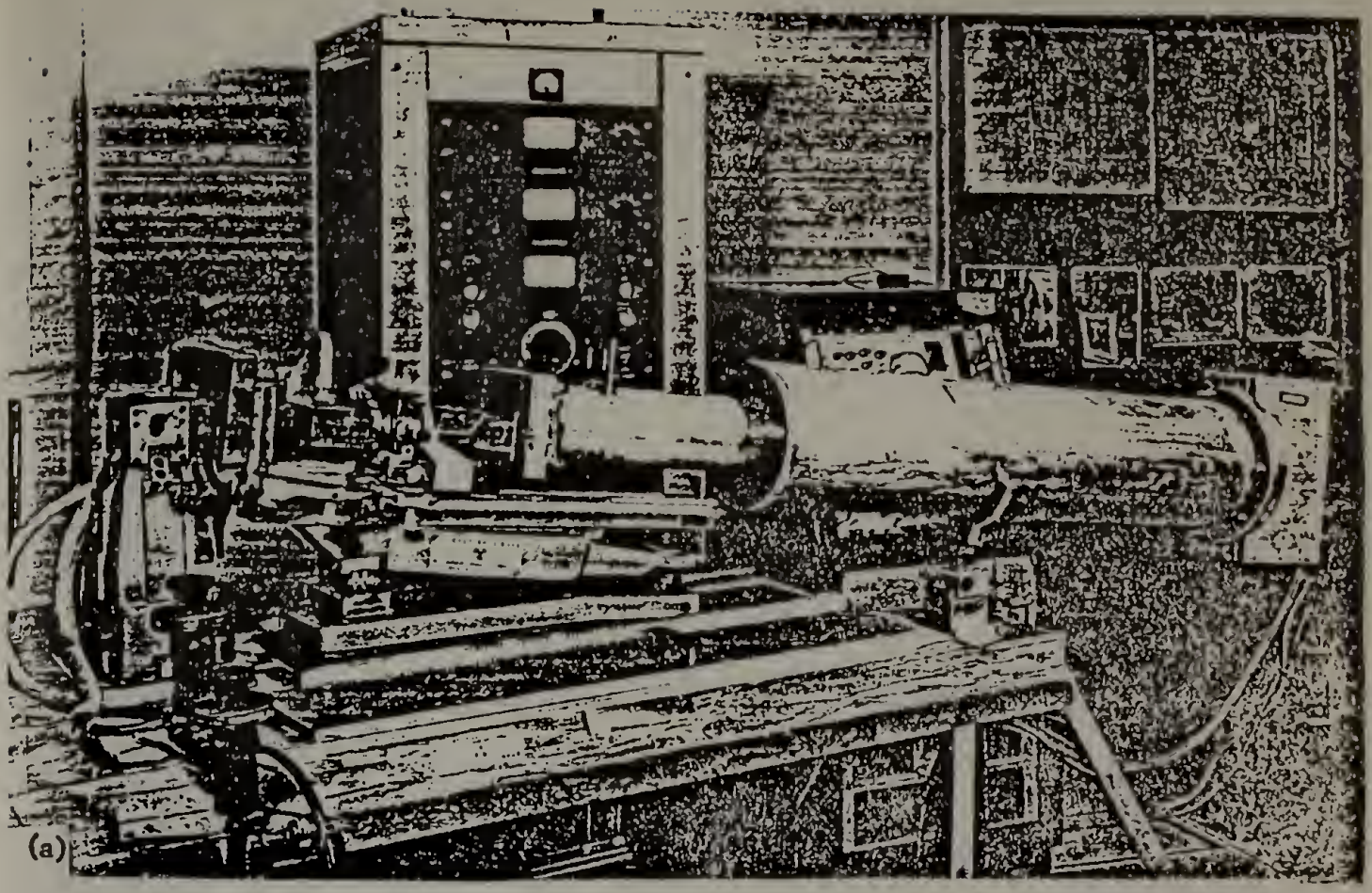

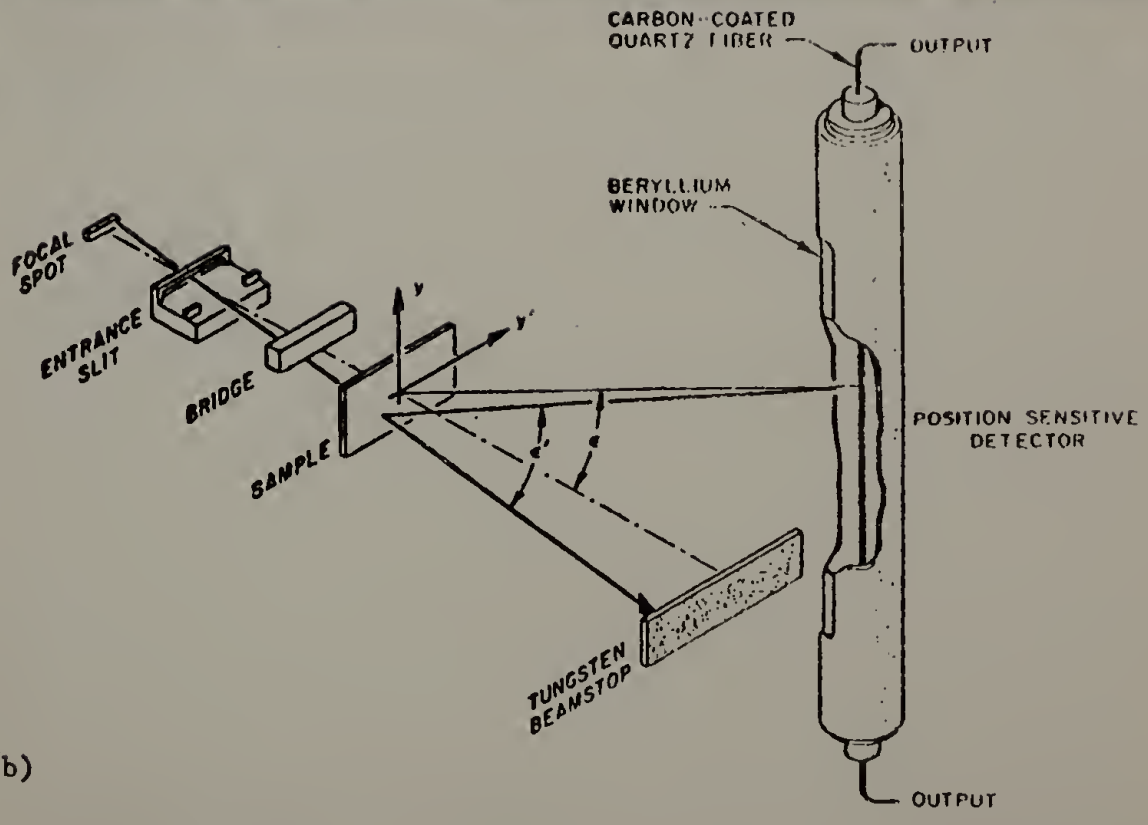

Fig. 11(a) Photograph of apparatus; (b) schematic of system with 1DPSD.

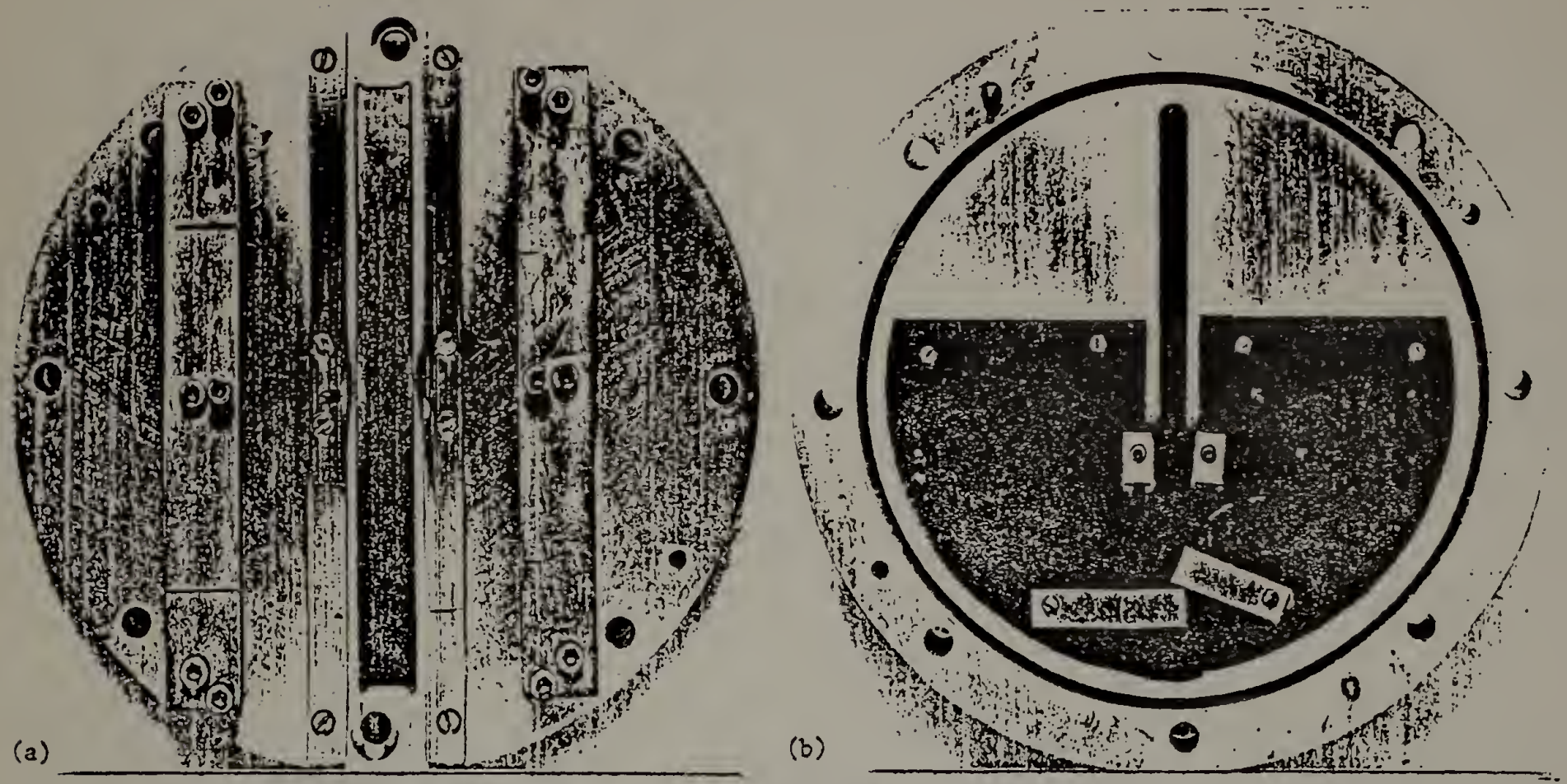

Fig. 12. Views of the rear flange. (a) Exterior, showing beryllium window and ways for mounting detector, and (b) interior, showing spring clamps for holding polished tungsten edge and alignment pins to allow precise 90° rotation of the detector.

contained two pairs of pins perpendicular to each other so that the slot could be oriented either parallel or penpendicular to the incident beam. A tungsten beam stop (polished to within 4×10^{-5} cm tolerance limits) was held across this slot by an adjustable mounting on the internal* face of the flange as shown in Fig. 12(b). Careful machining ensured that the beam stop was mounted perpendicular to the slot. The internal face was covered with 0.04 cm lead shielding to prevent any back reflections of the incident beam. Two slides for adjusting the position of the detector along the slot and for mounting various test equipment were placed on the external face of the flange parallel to the slot.

In addition to these modifications the camera was equipped with vacuum bellows from the bridge collimator to the sample chamber to the beam flight path, an automated balanced filter assembly and an incident beam monitor. All of these have been described elsewhere.[9,11,12]

Combining these modifications with the 1DPSD permitted the measurement of scattering patterns down to 0.7 mradian of angle with a minimum amount of parasitic and air scattering. One point that should be emphasized is that there is a significant loss in recorded intensity because of the extended flight path. Since the active area of the detector in the slit length direction was limited to 1 cm, due to the divergence of the beam in this direction the intensity loss at any scattering angle 2θ is 1550/220 = X7.

---

*It is essential to mount the tungsten beam stop on the internal face of the flange so that the indicent x-ray beam does not impinge upon the beryllium window. Strong diffraction maxima can be seen if the beam stop is placed after the beryllium window.[8]

IV. ALIGNMENT OF THE KRATKY CAMERA WITH A 1DPSD

The alignment procedure described in this report is that which was developed for the present camera geometry. The nomenclature used follows that of Anderegg et al.[13] The extended flight path placed severe limitations on using the normal procedures of alignment since it had to remain attached to the camera during the fine adjustments. It was found that if the camera was finely adjusted without the flight path using the normal alignment procedures then when the flight path was mounted the alignment was disturbed simply due to its size and mass. If a detector of higher spatial resolution were used, then the flight path could be shortened considerably, making normal alignment methods more feasible.

A. Tube Power

During the course of alignment the special Siemens Kratky tube (2.7 × 7 mm focal spot) was operated at 30 kV and 1 mA. The reasons for such low power settings are twofold. First of all, the low power avoids the use of thick nickel attenuators to reduce the power of the beam, thus avoiding the increasing amount of hard radiation in the energy spectrum. Secondly, the lower power reduces the chance of destroying the carbon coating on the quartz wire either by evaporation of the coating or by decomposition of the quenching gas with subsequent deposition on the wire. Both will seriously affect the response of the detector.

One problem that can arise from the use of lower power settings during the alignment stage is that ultimately the power must be increased for experimental use. This can easily cause a heating of the focal spot

and, consequently, the rocking curve can be disturbed. This can lead to either a reduction or an increase in the resolution by changing the first moment of the incident beam profile. Neither of these can be tolerated for precise work. Therefore, an independent investigation was conducted using a normal step-scanning Kratky apparatus where the rocking curve was determined as a function of power setting. Provided sufficient time was allowed for the focal spot to equilibrate, the rocking curve remained constant with the center of gravity (i.e., the first moment) changing by at most 2.0×10^{-2} mradian.

B. Initial Rail Alignment

A bridge system with the desired entrance slit width was placed at the front of the rail and a calibrated fluorescent screen (supplied with the camera) was mounted approximately 10 cm behind the bridge. Using V_1 the vertical position of the rail was roughly set so that the beam was visible on the fluorescent screen. If the beam was not perpendicular to the marks on the screen, then the bridge tilting micrometer, T_1, was adjusted to compensate for this. With the beam perpendicular to the markings and roughly maximized, the symmetry of the beam about the center of the rail was determined. If the symmetry was poor H_1 and H_2 were adjusted until satisfactory symmetry was obtained.

The fluorescent screen was moved further back on the rail (approximately 40 cm from the bridge) and the symmetry was checked. Again, if it was not satisfactory, H_1 and H_2 were adjusted accordingly. The screen was then returned to the initial position and symmetry was rechecked. Measurements of both settings were repeated until symmetry was obtained at both positions without moving the rail.

More quantitative adjustments can be made at this point with a non-position-sensitive detector mounted in the horizontal scanning device (supplied with the camera). With the detector equipped with a pinhole, the vertical position of the detector was adjusted to optimize the count rate. Horizontal scans were then made at 10 and 40 cm from the bridge system. These scans provided quantitative information regarding the symmetry, homogeneity and width of the beam. One of these scans is shown in Fig. 13. Adjustments were then made on T_1, H_1 and H_2 so that the resulting profile had the required trapezoidal shape.

The width of the beam can be quantitatively determined at various positions along the rail and can be compared to the geometrically calculated width. Similarly, once the beam width is known at various positions on the rail, the focal spot length can be calculated and compared

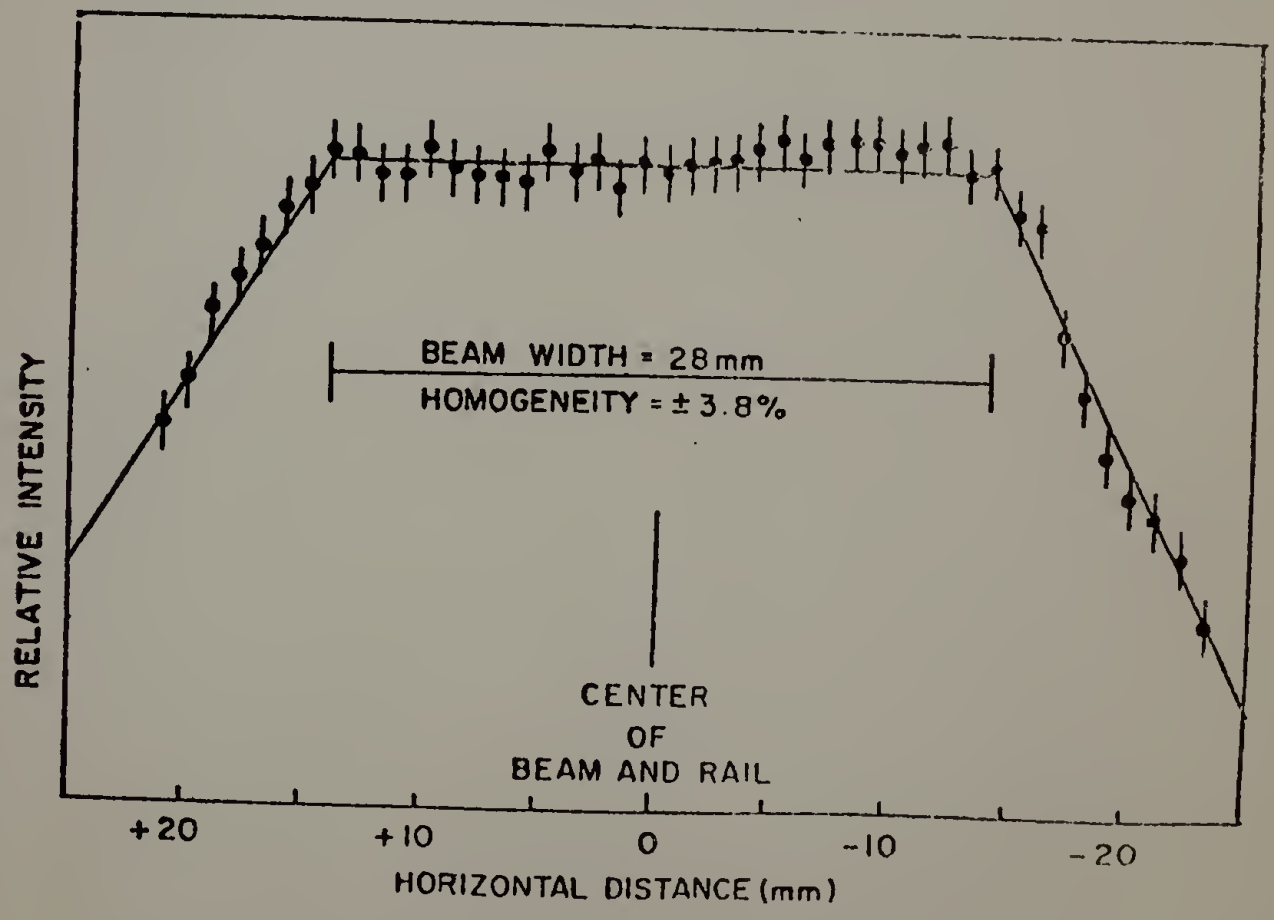

Fig. 13. Horizontal beam scans.

to the known (7 mm) length. If either method produces erroneous results, then the focal spot is not parallel to the collimation system. Once satisfactory agreement has been found by rotation of the x-ray tube and movements of H_1 and H_2, the sample chamber can be mounted on the rail so that it does not interfere with the main beam.

With the beam stop removed from the rear flange, the vacuum flight path was mounted and the system was evacuated to $\sim 5 \times 10^{-6}$ torr. The detector was attached to the rear flange perpendicular to the incident beam. By adjustment of the micrometer D_1, now mounted on an external stand with 1-cm-thick Al plates as adjustable shims for coarse adjustment, the beam, attenuated with copper foils, was brought to midrange on the MCA. The detector was now in a position to receive any radiation coming through the bridge system.

C. Tilt of the Bridge Collimator

The bridge collimation system was set parallel to the focal spot by determining the tilt at which a minimum traverse distance through the beam using V_1 was obtained.* For a given tilt setting the focal spot was scanned using V_1 noting the settings of V_1 corresponding to an arbitrary count rate on either side of the focal spot. The difference between these readings corresponds to an effective focal spot width. This difference was plotted as a function of the tilt of the collimator, and the minimum determined the tilt at which the bridge collimation system was parallel to the focal spot. These data, along with the tilt

*This procedure differs from that of Anderegg et al.[13] who used a narrow slit positioned at various distances along the focal spot. Because of inhomogeneities of the focal spot, it was concluded that the present procedure gives a better average alignment.

selected, are given in Fig. 14. (Note: The special locking bolt on the tilt mechanism described by Hendricks[11] must be tightened to a constant torque at each different tilt setting to ensure reproducibility.)

D. Vertical Positioning of the Bridge

The focal spot was scanned vertically using V_1 as shown in Fig. 15. An insensitive portion of the profile was selected for positioning V_1. A similar scan was performed using V_2 with V_1 locked in place. Again, an insensitive region was selected to position V_2. Scans of the focal spot were repeated until the readings of V_1 and V_2 did not change. A convenient check on the procedure verifying that the rail is at a 6° take-off angle is to calculate the effective width of the focal

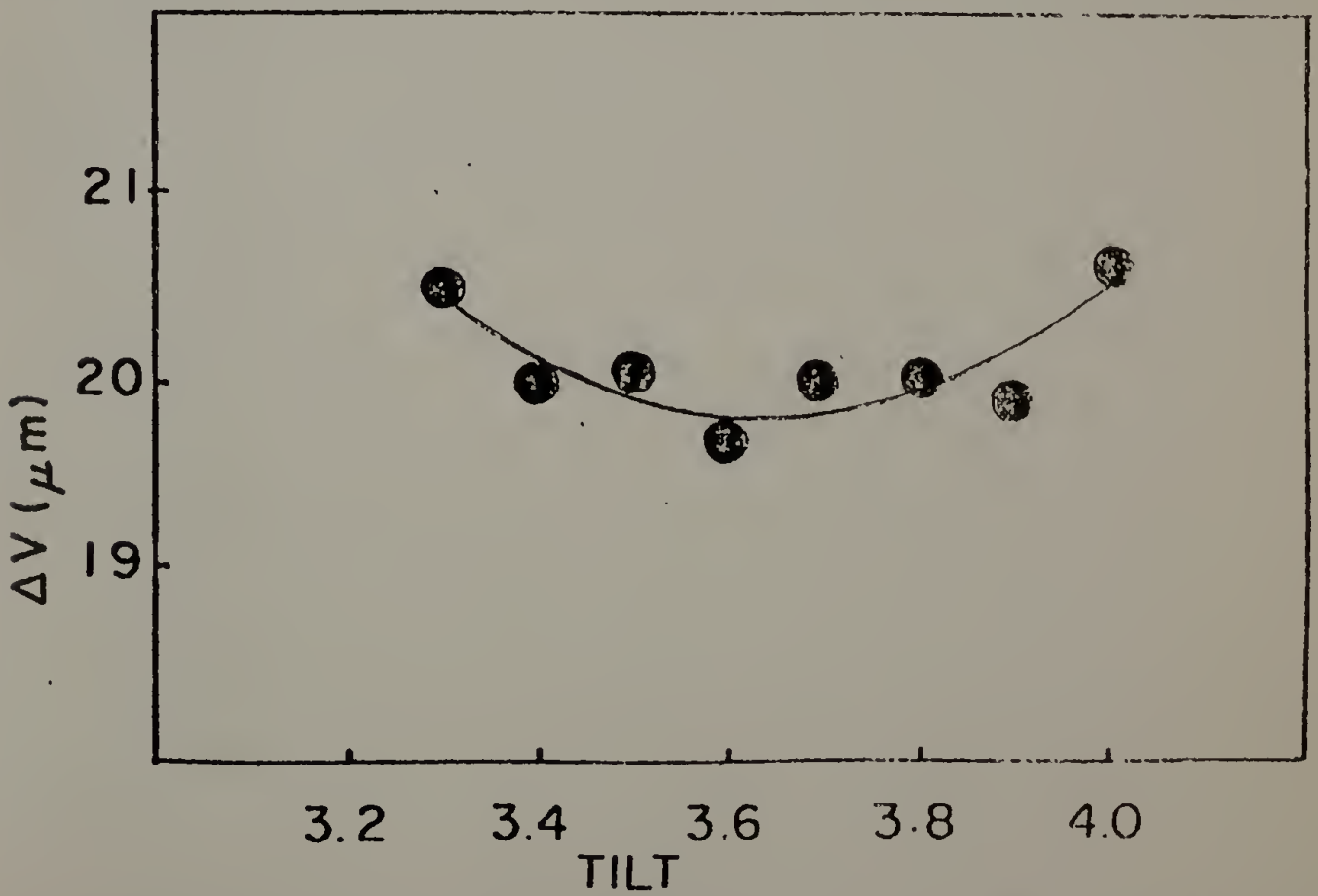

Fig. 14. Tilt of collimator experiment. The minumum is at a tilt of 3.65 units.

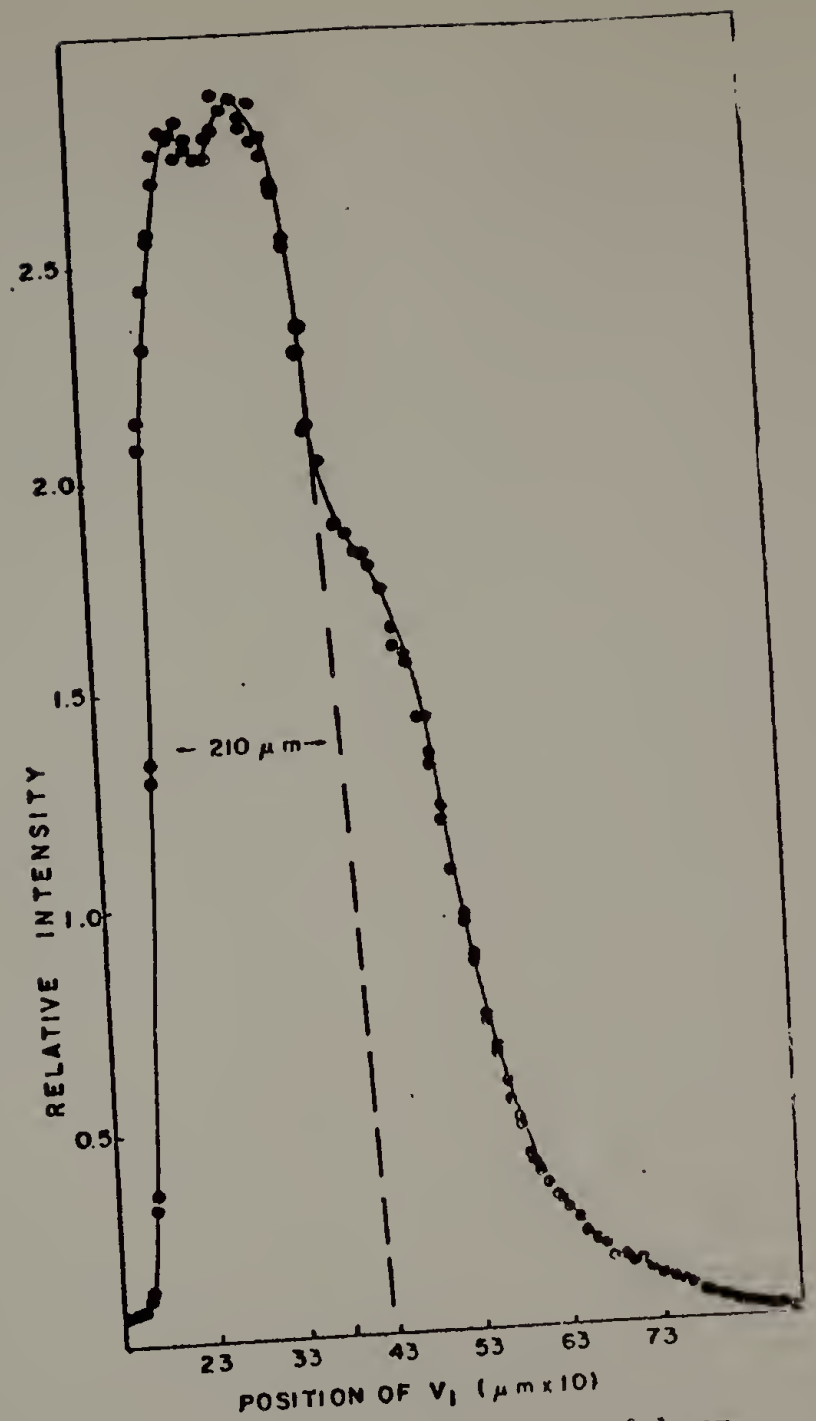

Fig. 15. Vertical profile of beam.

spot and compare this to the actual size of the focal spot. For this experiment the effective size of the focal spot was 0.0205 cm which corresponds to a 5.95° take-off angle.

E. Detector Tilt

The detector receiving slit and tungsten edge were set perpendicular to the incident beam by determining the total number of background counts versus the tilt of the vacuum chamber. When the edge is perpendicular to the beam, then the total counts will be minimized. Alternatively, the detector can be rotated 90° and the homogeneity of the beam can be determined and T_2 can be rotated until a homogeneous profile is found. Both methods were used with good agreement.

V. ALIGNMENT CHECKS

A. Horizontal Beam Profile

With an aligned Kratky camera the horizontal profile of the beam should have a trapezoidal shape. The length of both the homogeneous section and the penumbra can be geometrically determined and compared to that obtained experimentally. This was done as is shown in Fig. 16. Due to the physical size of the detector (10 cm in length), the two sides of the beam were obtained separately and superimposed. The experimental agreement with the theoretical shape is excellent.

B. Rocking Curves

A crucial test of the alignment is the comparison between the experimental and theoretical rocking curves. This cannot be done with a position-sensitive detector because for optimum resolution the full width of the incident beam is only six to eight channels. This relatively coarse measurement of the beam profile was insensitive to calculations of various predicted curves. At best, a geometric prediction

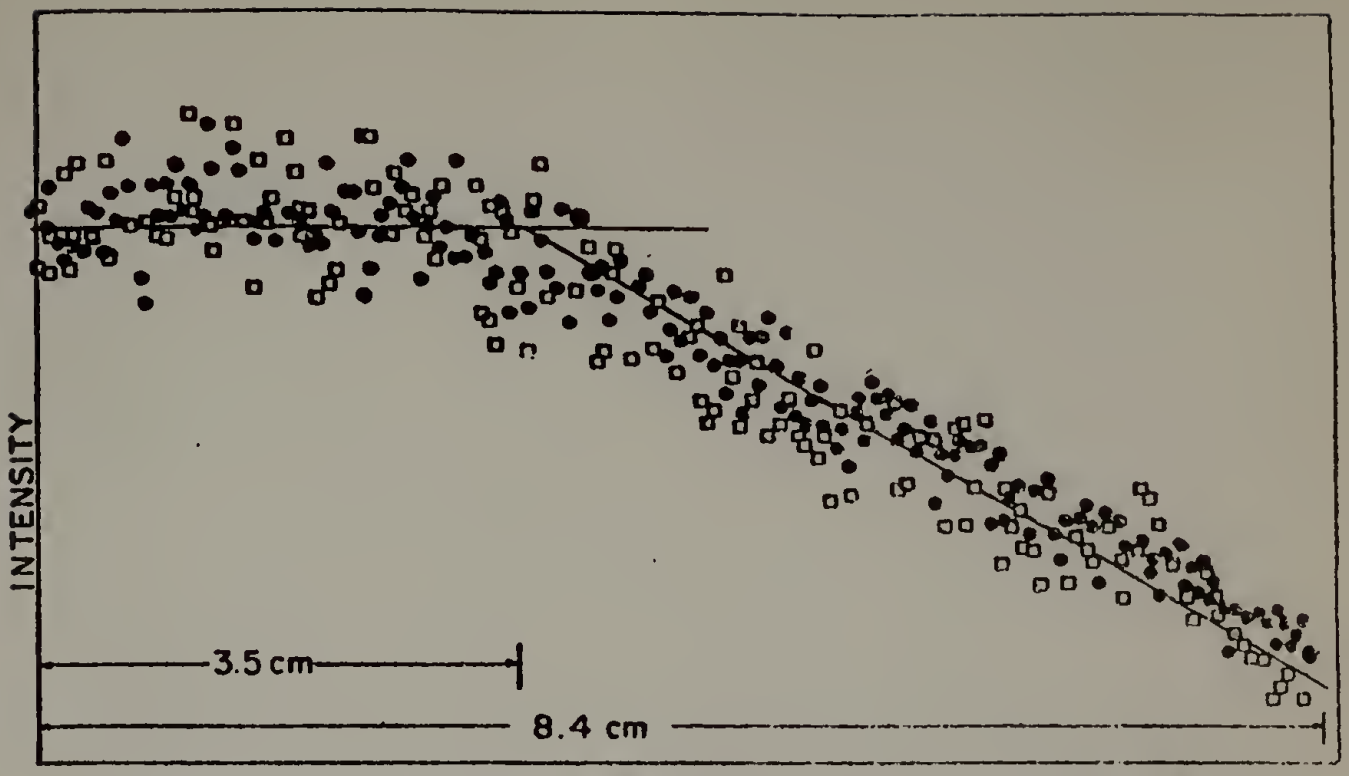

Fig. 16. Horizontal beam profile at the rear flange. ● left-hand side; □ right-hand side. The solid line is geometrically predicted.

of the beam size at the detector was compared to that obtained geometrically. The width of the beam predicted and observed was 1.5 mm. Despite this limitation, the data are sufficient to determine the centroid of the incident beam to a fraction of a channel as is described in the next section.

VI. DETERMINATION OF THE ZERO OF ANGLE

One characteristic of a Kratky collimation system is the asymmetric profile of the incident x-ray beam. Because of this the center of gravity of the beam (i.e., the zero of angle) must be determined experimentally. Using standard step-scanning equipment this can be done easily by scanning through the beam with subsequent integration and determination of the first moment of the profile. However, this could not be done with the 1DPSD used in this study for two reasons.

First of all, there was no easy method available for obtaining a beam profile without disturbing the system due to the positioning of the tungsten beam stop. Secondly, as mentioned previously, only six to eight channels are subtended by the beam which permit only a coarse integration of the profile. In addition to these, since the apparatus was aligned at low power settings, the profile of the beam could change during the power increase (28 kV, 30 mA) due to a focal spot heating. Consequently, an alternate method using a scattering sample was employed.

The sample selected for this purpose was a dry, uranyl-acetate stained duck-tendon specimen. Stinson et al.[14] have shown that up to seven orders of diffraction maxima were clearly visible in the low angle region. A scattering profile obtained on the same specimen with the apparatus used in this study is shown in Fig. 17. As can be seen up to the eleventh order was visible. This pattern was obtained with the vacuum chamber offset such that the tungsten beam stop was well below the incident beam. Instead, a piece of lead was used as an

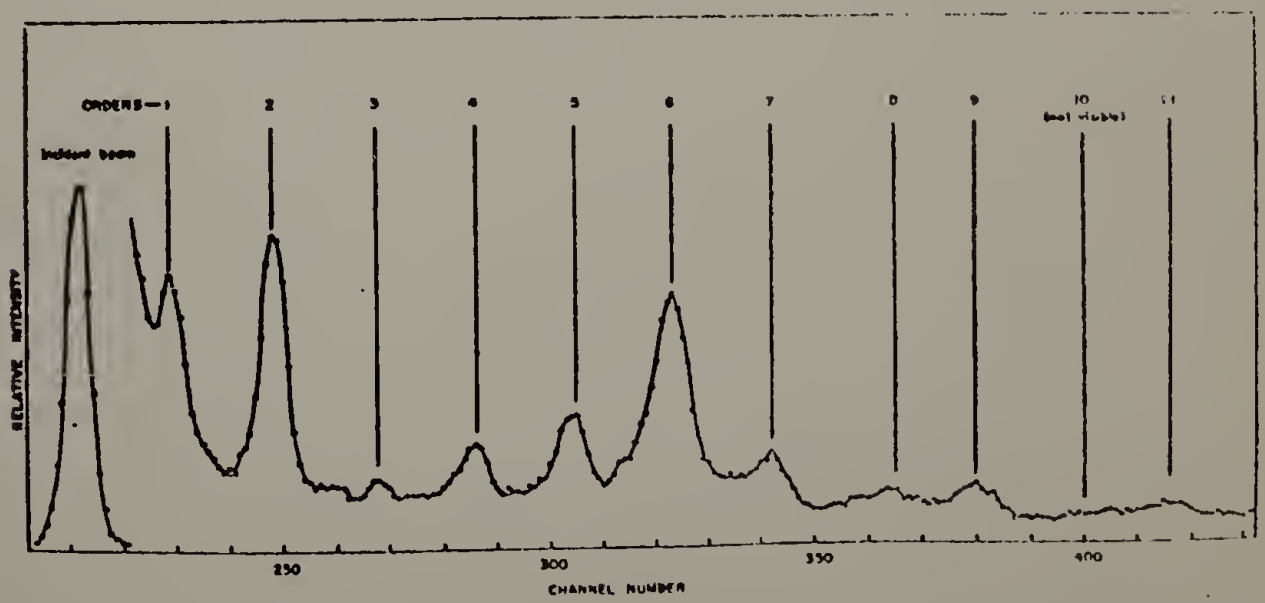

Fig. 17. Uranyl acetate stained duck tendon (with incident beam).

external beam stop. Subsequently, a main beam profile (nickel attenuated) was obtained with exactly the same geometry without the sample and lead beam stop. In this way the zero of angle could be calculated by integration of the main beam profile and by an extrapolation to the zeroth order diffraction peak. The two methods agreed to within 0.25 channel which corresponds to 0.05 mradian. This agreement is considered to be excellent and thus permits this specimen to serve as a standard for angular calibration. Experiments on this sample were also performed on a step-scanning Kratky apparatus where a much finer integration of the beam was permitted; agreement to < 0.006 mradian was found.

VII. NOISE LEVEL AND PARASITIC SCATTERING

The system's performance was characterized in three different ways. First of all, the apparatus should have a low noise level and minimal parasitic scattering, which are characteristic of the Kratky geometry. Secondly, the system's performance was compared to several other existing cameras using samples of moderate scattering intensity. Thirdly, the apparatus should be able to resolve weakly scattered intensities.

One distinct advantage of a 1DPSD over a conventional step-scanning apparatus equipped with a proportional counter is that, although the electronic noise per unit time is approximately the same in both cases, the 1DPSD distributes the noise over the entire angular range. Therefore, if 100 channels were being used on the MCA the electronic noise and background would be 100 times less per angular reading on the 1DPSD than with a conventional detector. This apparatus was found to

have a total background (including electronic noise) of 1 to 3 counts/s corresponding to a noise level of 0.01 to 0.03 count/s/channel.

With the camera aligned as described above, the scattering curve for the empty camera should exhibit an extremely rapid drop in intensity at very low angles, leveling off at the electronic noise. This characterizes the parasitic scattering and coupled with the slit width sets the experimental resolution. A typical blank run is shown in Fig. 18. These results should be compared with the parasitic scattering curve for

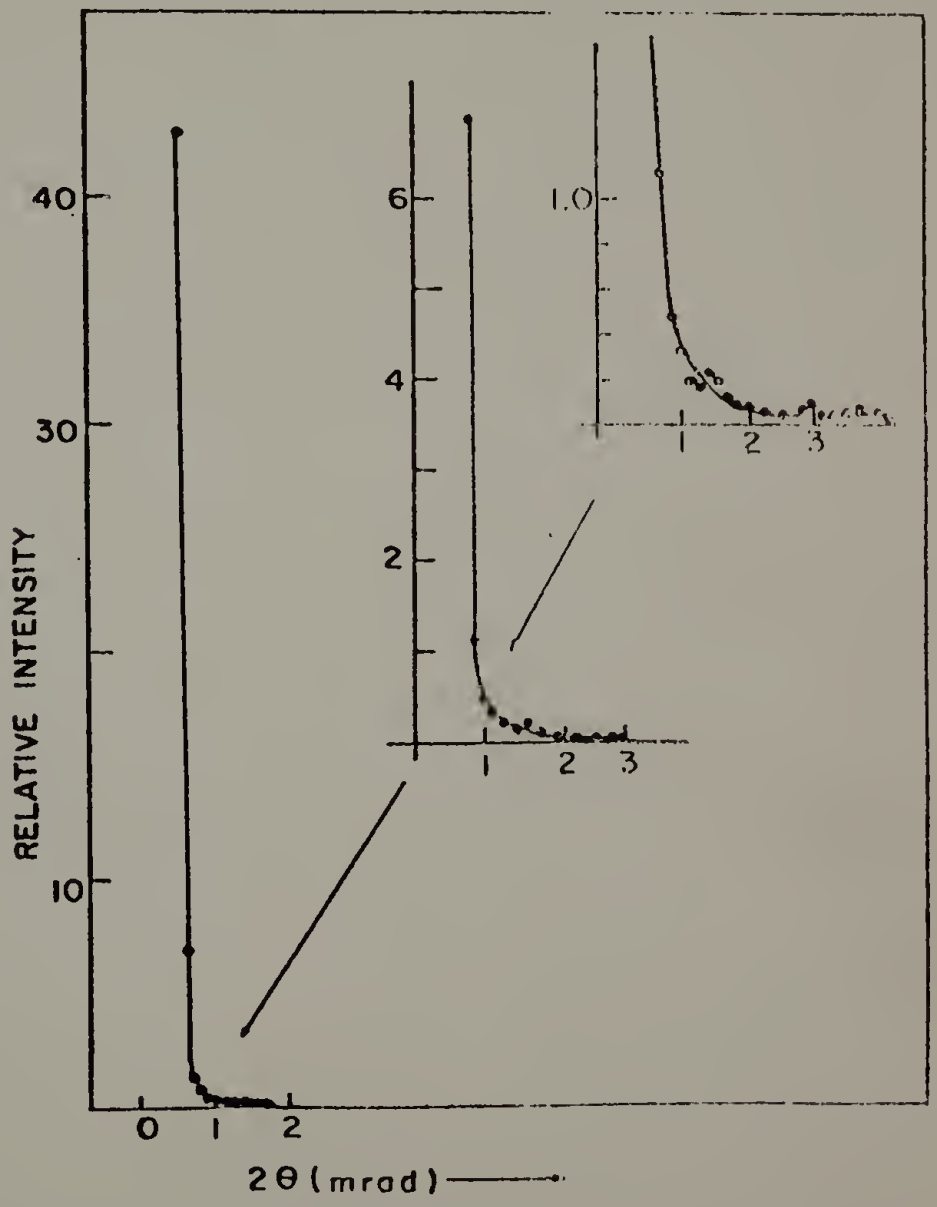

Fig. 18. Parasitic scattering of modified Kratky camera with 1DPSD.

a normal Kratky camera presented by Hendricks.[11] It is clearly seen that the predominant parasitic scattering occurs below 1 mradian. However, a low intensity tailing off was found to be present extending to 2–3 mradians. The exact origin of this could not be determined. It could not be attributed to a misalignment since the intensity is much too low. In fact, because the electronic noise of the present system is lower than any detector previously used on a Kratky camera, it is possible that this effect is present, but unresolvable, in all cameras. One possible explanation of the effect is that high energy radiation was impinging on the rear wall of the detector and fluorescing the aluminum or impurities in either the aluminum or the beryllium window. The fluorescent radiation could be of an energy that would be passed by the discriminator. As will be shown, this effect did not affect the analysis of the weak scatterers.

VIII. DEAD-TIME CORRECTIONS

Dead-time corrections were applied to all the 1DPSD data. This correction is associated with the counting capacity of the detector and associated electronics in which counts are lost due to the total number of events accumulated over the entire detector. This is the standard correction applied to any proportional counter. Following Chipman[15] the dead time, τ, was found from a plot of the ratio of an attenuated count rate (I_0) to a nonattenuated count rate (I_0^0) versus the total count rate as shown in Fig. 19. The dead time is given by

$$\tau = (\text{slope})/(R_t - 1) \tag{2}$$

where R_t is the intercept at zero count rate. For this system $\tau = 14$ μs.

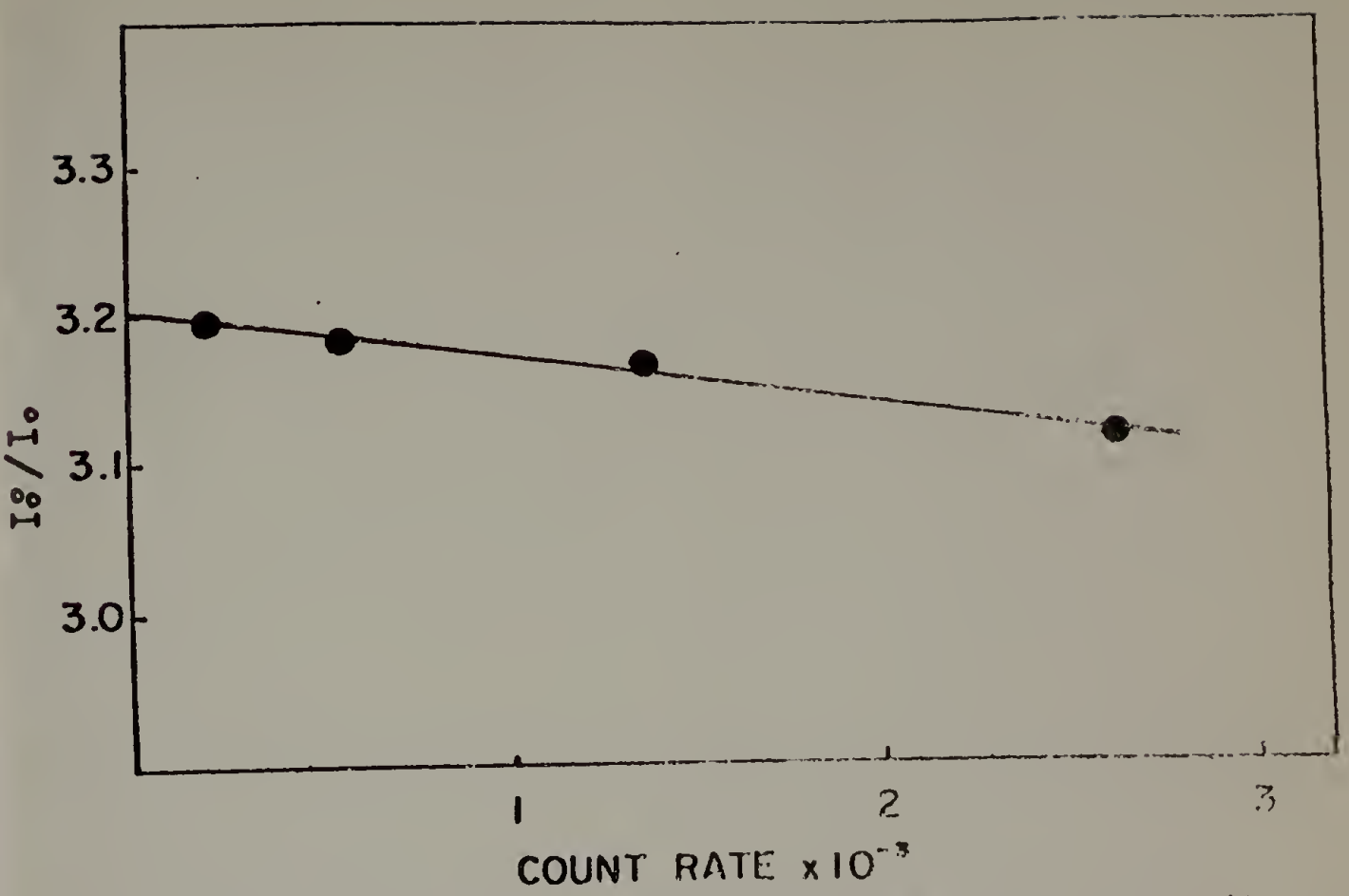

Fig. 19. Data for dead-time correction by method of Chipman.[15] The count rate is in thousands/s.

This correction, applied to the total number of counts, yields a factor by which each channel intensity is multiplied independent of channel number.

$$I_{i,corr} = \frac{I_{i,o}}{1 - \sum_i I_i \tau} \qquad (3)$$

where $I_{i,o}$ is the observed counts and $I_{i,corr}$ is the counts in channel i corrected for the overall dead time, τ, and $\sum_i I_i$ is the sum of all the counts in all the channels used. This method of dead-time measurement includes the effects of all components of the detector system including those of the multi-channel analyzer. For the samples of interest in the present investigations, the dead-time correction was not significant.

IX. COMPARISON WITH OTHER EQUIPMENT

The performance of the camera described in this report was compared to that of other small-angle x-ray scattering instruments. Scattering profiles from several specimens were compared to those obtained on: (1) the ORNL 10-m SAXS camera,[1] (2) a Bonse-Hart system,[16] and (3) in an international absolute intensity calibration project.[17] The specifications of the various samples are given in Table 2 along with the system used for comparison.

Table 2. Sample Specifications for Intercomparison Experiments

Sample Description	Sample Identification	Thickness (mm)	Transmission Coefficient	Comparison Level	Comparison to:
Polyethylene	Marlex, PE	1.26	0.367	Relative	Two-dimensional pattern in point collimation[1]
Polystyrene	PS-3	1.002	0.217	Absolute	IUCr project[17]
Glassy carbon	GC-3	1.831	0.315	Relative	IUCr project[17]
Polyvinyl-chloride	PVC	0.530	0.325	Absolute	Bonse-Hart[16]

Initially an attempt was made to place all the scattering profiles on an absolute basis by measuring the power of the incident beam via the multiple foil technique. However, in performing the comparison with the ORNL 10-m SAXS camera using a polyethylene specimen the absolute intensities were not in agreement. Therefore, the same polyethylene specimen was used as a secondary standard with subsequent calibration against a

Kratky Lupolen specimen[19] with satisfactory results. The discrepancy, although disturbing, could possibly be associated with space charging effects. This effect, as will be discussed later, arises when there is a localized region of high intensity. As mentioned previously, the incident beam is confined to six to eight channels on the MCA and even with attenuation this localized beam is very intense.

Before discussing the various scattering profiles, the overall power specifications of our device are compared to those of a normal step-scanning Kratky camera and the ORNL 10-m SAXS camera.[1] Table 3 shows this comparison. Column 4 contains the specifications of the current 1DPSD Kratky system, column 3 contains these same specifications when the entrance slit has been normalized to that of the step-scanning Kratky in column 2, and column 5 typifies the power of the 2DPSD facility.

A. Comparison with the ORNL 10-m SAXS Camera

A sample of Marlex (polyethylene) was used to compare the 1DPSD system with the 2DPSD system. Before the comparison could be performed the data from the 1DPSD system, as recorded in the MCA, had to be reduced to yield the intensity profile as a function of scattering angle. A FORTRAN IV program was developed to perform this task. Once the angular intensity was obtained, the data were desmeared to reduce the data to that which would have been obtained with a pinhole geometry. This was done using the desmearing procedure of Schmidt[20] assuming an infinite slit-length geometry.*

*This assumption is valid because, as is seen from Fig. 20, the scattering from Marlex decreases to essentially zero within 15 mradians, while from Fig. 16 it is seen that the incident beam is constant to 35/1545 = 22 mradians.

Table 3. Comparison of Equipment

Property	Kratky Camera			10-m Small Angle X-Ray Scattering Camera[1]
	Step Scanning	1DPSD Normalized to Step Scanning	1DPSD	
RADIATION CHARACTERISTICS	Siemens special Kratky tube			Rigaku Denki 6 kW rotating anode
X-Ray Source				
Focal spot size, mm^2	2.8 × 7	2.8 × 7	2.8 × 7	0.5 × 5
Power (kV, mA)	(40, 30)	(40, 30)	(38, 30)	(45, 100)
Monochromator	Graphite (diffracted beam)	Nickel filtered (incident)	Nickel filtered (incident)	Graphite (incident)
ϕ, apparent brilliance of focal spot (photons s^{-1} sr^{-1} mm^{-2})	0.32×10^{12}	0.36×10^{12}*	0.26×10^{12}	8×10^{12}
COLLIMATION CONDITIONS				
ε_{min}, minimum angle to which data are collected (mradian)	2.52		1.0	0.4
F_1, area of entrance slit (mm^2)	$0.098 \times 10 = 0.98$	$0.098 \times 10 = 0.98$*	$0.065 \times 10 = 0.65$	$\frac{\pi}{4}(1) = 0.79$
$\Delta\Omega_1$, solid angle of incident beam (sr)	$\frac{0.222 \times 18}{(288)^2} = 48 \times 10^{-6}$	$\frac{0.256 \times 19}{(298)^2} = 54 \times 10^{-6}$*	$\frac{0.17 \times 19}{(298)^2} = 36 \times 10^{-6}$	$\frac{0.79}{(5000)^2} = 32 \times 10^{-9}$
$\Delta\Omega_2$, solid angle of receiving slit (sr)	$\frac{0.633 \times 10}{(259)^2} = 94 \times 10^{-6}$	$\frac{0.4 \times 10}{(1543.6)^2} = 1.7 \times 10^{-6}$	$\frac{0.4 \times 10^4}{(1543.6)^2} = 1.7 \times 10^{-5}$†	$\frac{(200/64)^2}{(5000)^2} = 39 \times 10^{-8}$†
P_0, power of beam bathing specimen (photon s^{-1})	15×10^6	19×10^6*	6.1×10^6	1.0×10^6

*Normalized according to entrance slit width and power. †Sterad per detector element.

The comparison of the two scattering curves obtained on each instrument is shown in Fig. 20. As can be seen, the curves differ by up to 10%. Schelten and Hendricks[8] noted similar differences in a previous publication. These authors outlined four possible sources of the discrepancies between the scattering profiles -- (1) failure to correct the data for slit-width smearing, (2) systematic errors resulting from nonsimultaneous detection, (3) systematic errors in the slit-length desmearing procedure, and (4) nonuniformities of the sample. It is to be noted that the data obtained with the 2DPSD were not corrected for collimation errors, and because of the extent of the electronic resolution,

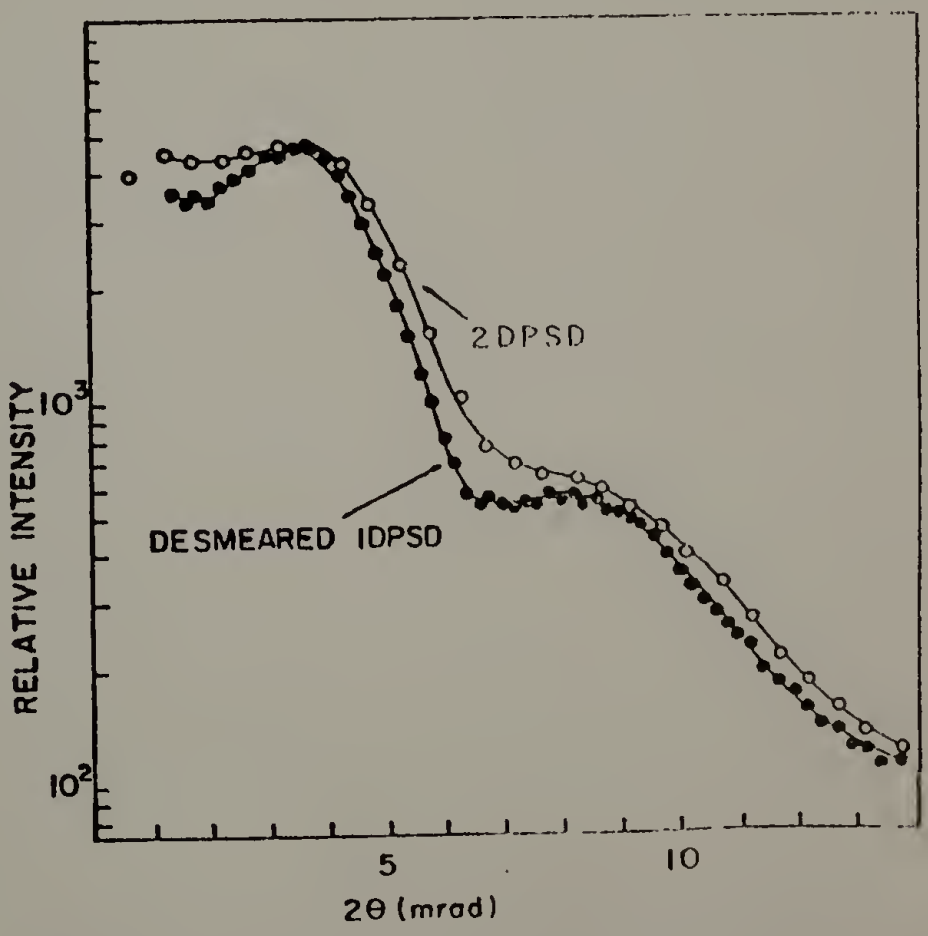

Fig. 20. Scattering curves for Marlex (polyethylene) as determined on the 10-m SAXS camera in point collimation (○) and on the present device, after collimation correction (●).

these effects are not entirely negligible. The use of position-sensitive detectors for both runs eliminated the second effect. The possibility of systematic errors in the desmearing procedure or nonuniformity in the specimen still remains. Despite the differences, the agreement should be considered as being very good.

B. Comparison with a Bonse-Hart System

A polyvinylchloride (PVC) sheet was used for this comparison. PVC is a very weak scatterer with a high attenuation factor due to the high concentration of chlorine. The scattering observed from PVC arises from two sources. The first, which is an angularly independent scattering, is due to thermal density fluctuations, as discussed by Straff and Uhlmann[16] and Wendorff and Fischer.[21] Superimposed on this is a very low-angle scattering arising from heterogeneities within the sample. The purpose of this report is to recognize the presence of this low-angle scattering and is not intended to determine the nature of these heterogeneities.

The smeared data obtained with the 1DPSD is shown in Fig. 21 along with the data of Straff and Uhlmann.[16] As can be seen, the 1DPSD data agree in the outer regions of the scattering profiles; however, in the very low-angle section the 1DPSD data lie slightly below the data of Straff and Uhlmann.[16] In light of their work this angular dependent scattering can be described by

$$I = c(1 - c)V(\Delta\rho)^2 \exp(-R_g^2 h^2/3) \qquad (4)$$

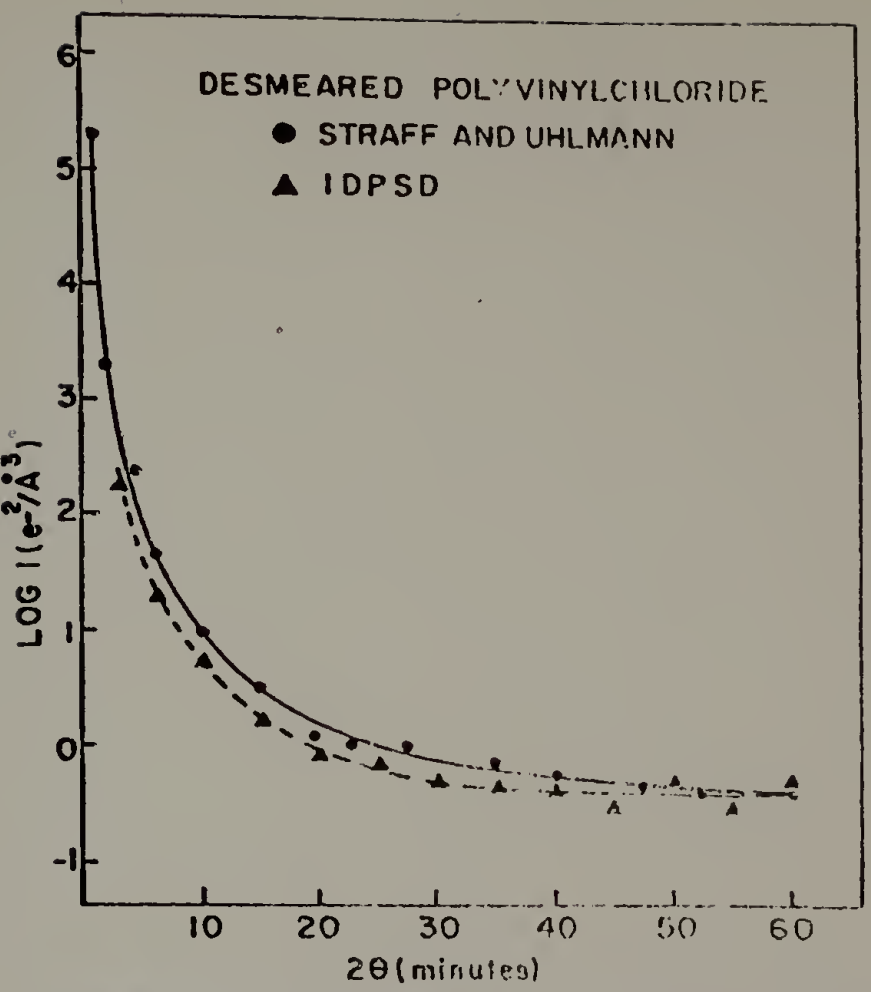

Fig. 21. Comparison of scattering from polyvinylchloride as determined by Straff and Uhlmann[16] (●) on a Bonse-Hart camera and in the present work (▲).

where c is the concentration of heterogeneities of radius R_g characterized by an electron density difference relative to the matrix of $\Delta\rho$. Since the PVC used in this study was purified and that of Straff and Uhlmann was not, it is reasonable to expect that the two curves should not be identical. However, simply by varying c and R_g, Eq. (4) can be used to describe both curves.

It will also be noted that the data of Straff and Uhlmann extend to smaller scattering angles than the data obtained here. This is a result of the difference between the Kratky and Bonse-Hart apparatus.[22]

However, the resolution lost by use of the Kratky camera is minimized and is compensated by a higher intensity. It is concluded that the 1DPSD system developed here displays a very good agreement with the Bonse-Hart apparatus.

C. Comparison with Other Kratky Geometries

Probably the most critical comparison to be performed is that between the 1DPSD and other Kratky geometries. Provided identical specimens and resolutions are used, there should be no discrepancies. Such a comparison was easily conducted using the polystyrene and a glassy carbon sample prepared for the International Union of Crystallography's *Commission on Crystallographic Apparatus International Project for the Calibration of Absolute Intensities in Small-Angle X-Ray Scattering* as described by Hendricks et al.[17] Comparisons with both samples were performed on the smeared scattering intensities to eliminate the possibility of desmearing errors.

(a) Polystyrene Comparison

The polystyrene specimen (PS-3) scattering profiles obtained from the 1DPSD and as published in the IUCr report are shown in Fig. 22. As can be seen the two profiles superimpose. This result is reassuring and indicates that any differences encountered with prior comparisons are not due to the apparatus and must be attributed to other genuine sample differences or to subsequent data treatment.

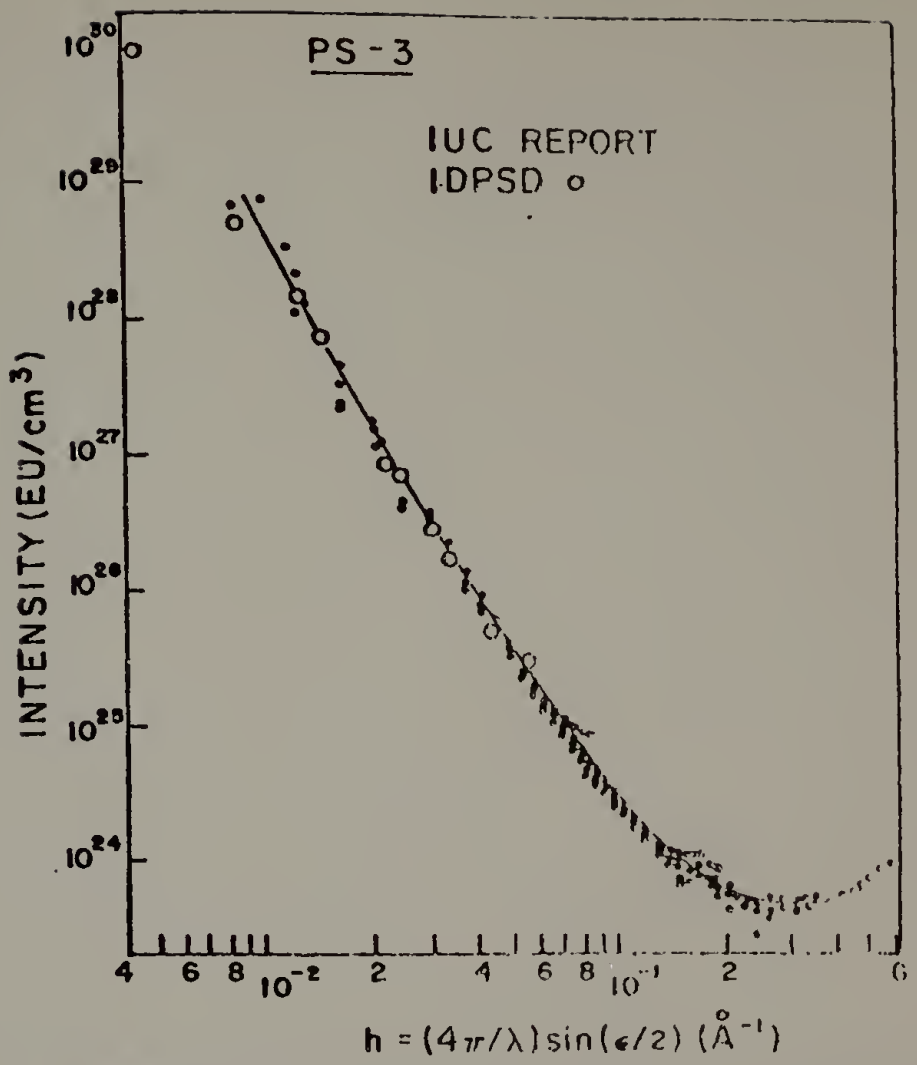

Fig. 22. Comparison of scattering curves for polystyrene (PS-3) determined by numerous investigators participating in an IUCr absolute intensity project on a variety of instruments[17] (●) and that obtained in the present work (O).

(b) Glassy Carbon Comparison

Up to this point the various specimens investigated scattered in the very weak (PVC) to moderate (Marlex) range. A glassy carbon specimen was chosen to study the effect of very strong scatterers. The scattering from glassy carbon originates from a high concentration of voids, and is among the most intense observed at very low angles.

Quite surprisingly, the spectrum obtained from the IDPSD system contained a scattering peak at approximately 3 mradians. This result

is in error because the well-established scattering curve from this glassy carbon specimen (GC-3) is monotonically decreasing.[17] Repeated experiments on the 1DPSD produced identical results. As will be discussed shortly, this peculiar spectrum of the GC-3 specimen can be attributed to space charge effects in the detector. Upon attenuating the beam and counting for longer times, a glassy carbon spectrum was obtained that had the same angular dependence of intensity as that of the IUCr report[17] (not shown here).

D. Comments on the Comparisons

Despite the various problems encountered during the performance tests of the modified Kratky collimation system with the 1DPSD described here, it has been shown that, provided sufficient care is taken, the results are essentially the same as those obtained on any other scattering facility. Agreement was found with a very wide range of scattering specimens on a wide and varied range of equipment. However, as will be discussed, extreme caution must be exercised when intense scatterers are being investigated.

X. SPACE CHARGE EFFECTS

The phenomenon of space charge effects in non-position-sensitive proportional counters has been understood for some time.[23-26] Basically, when count rates are high in a localized region, the slowly moving positive charges created by a preceding event shield the anode wire from the electrons created in a succeeding event, thus lowering the effective potential on the anode. This causes a decrease in the gas amplification

factor and a broadening of the energy resolution. A quantitative theory of this effect has been developed by Hendricks.[26] Although the effect of space charges has not been worked out quantitatively for position-sensitive detectors, qualitatively several effects on the spatial resolution are to be expected. First, a localized region of high count rate (as would be expected at a Bragg reflection, for instance) will cause a distortion of the normally radial electric field lines which will cause a focusing of the in-coming electrons toward the positive ion cloud (Fig. 23). Such a focusing would be expected to distort the shape of a scattering curve. Secondly, the localized reduction in apparent potential

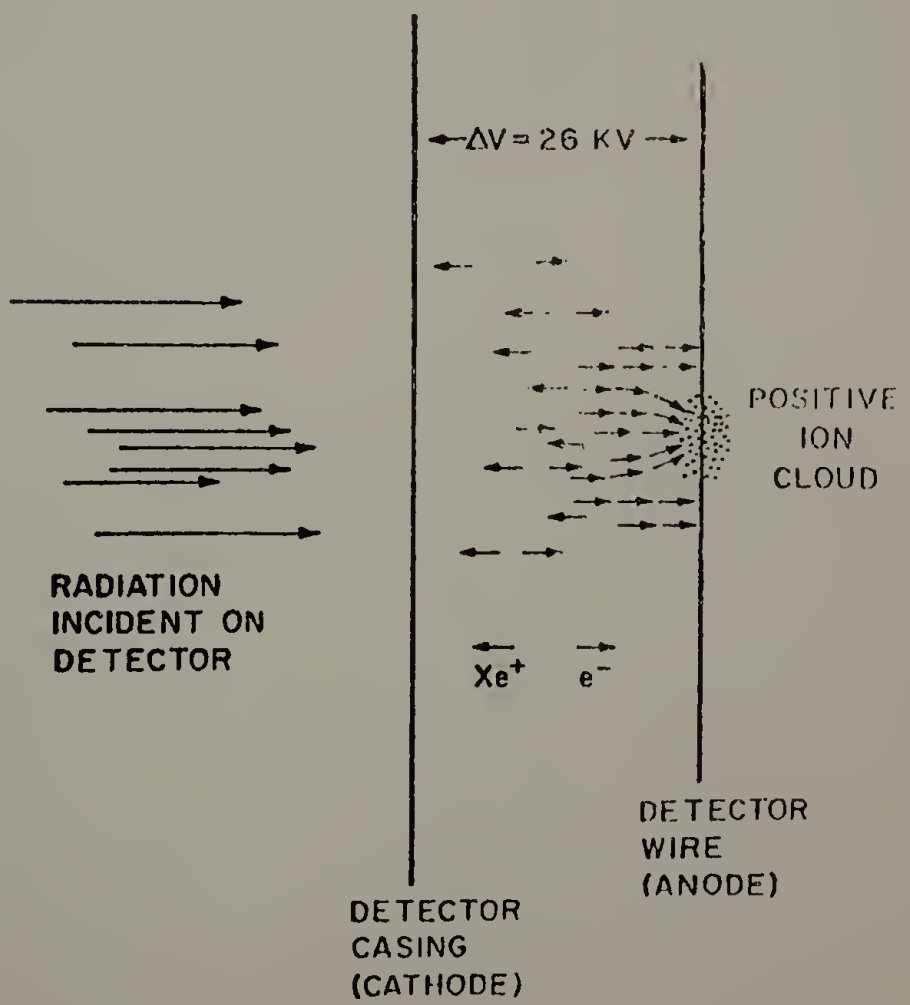

Fig. 23. Space charge effect: deflection of electrons.

between the anode and cathode is expected to cause a position-dependent decrease in the gas amplification factor, thus causing an apparent loss of photons due to energy discrimination.

We present below our first experimental results demonstrating the effect of space charge in 1DPSDs. The sample used for this investigation was a glassy carbon specimen (GC-3, as described in ref. 17) which at a source power setting of 28 kV and 30 mA had an integrated scattering of 200-250 k counts/s. The intensity profile is characterized by an exponential increase in intensity at very low angles.

The scattering curves shown in Fig. 24 were obtained under two different conditions. Spectrum A (full circles) was obtained with the full power of the main beam impinging on the specimen, whereas with spectrum B (open circles) the main beam was attenuated (× 1/80) with nickel foils. The recording times were 5 and 400 s, respectively. The profiles were obtained so as to normalize the tail region of the curves.

As can be seen, the two profiles are virtually identical except in the 0 to 5 mradians region where the count rate is quite high. At the smallest angles spectrum A has a lower count rate than spectrum B but at slightly higher angles then it exceeds B, and develops a maximum. As discussed above and in detail by Hendricks[26] the initial, very significant reduction in the recorded intensity is the result of a change in the local electric field resulting in a count rate loss due to energy discrimination. At somewhat higher angles (3-4 mradians), the intensity of the distorted spectrum actually rises above that of the undistorted, low count rate spectrum. This can be accounted for by the focusing effect of the space charge cloud (described above) attracting electrons

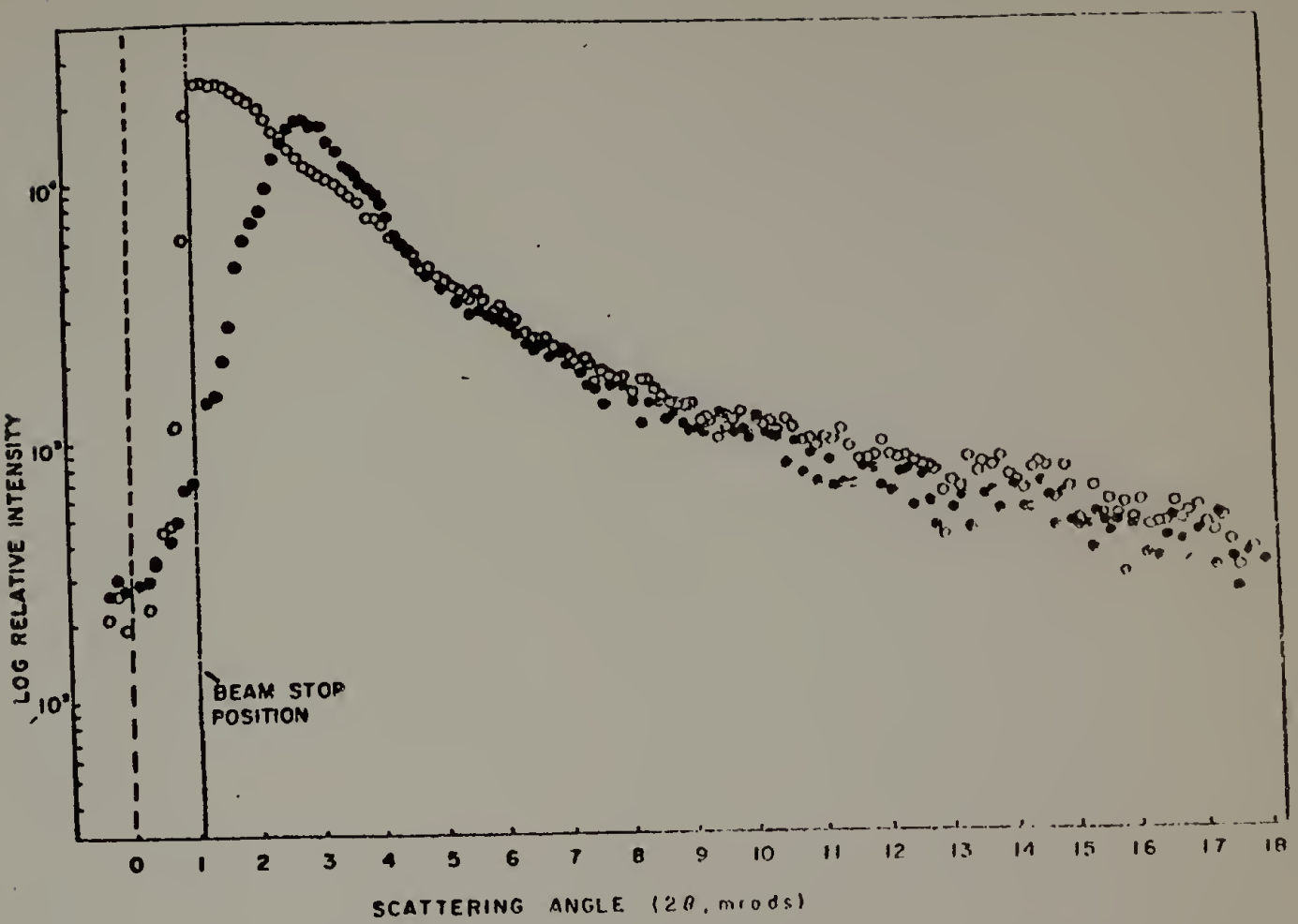

Fig. 24. Scattering curves for glassy carbon as determined with the present apparatus at two different integrated count rates. ● 5-s count time; O 400-s count time. The differences are due to space charge effects.

from events which occurred at somewhat higher angles into the low-angle region.

An important point to be made here is that the excess intensity observed at about 5 mradians with the 1DPSD would not be observed with a normal step-scanning apparatus and a non-position-sensitive detector. With the latter device the deflected electrons would still be included in the accumulated counts at that angle, whereas with the 1DPSD these deflected electrons are included in the total events occurring at another position on the wire corresponding to another angle. Therefore, a conventional apparatus would only experience a loss in intensity due solely

to the apparent loss of photons caused by a change in the electric field at the wire and their resultant rejection by the energy discriminator.

Aside from the effects described above, space charges can also affect the determination of system dead times. In the method of Chipman[15] the parameters of interest are the total count rate (I_0^0) and an attenuated count rate (I_0). If a scatterer such as GC-3 is used to obtain these parameters, then there can be losses in the count rates due to the space charges. The ratio (I_0^0/I_0) determined at high count rates can be decreased considerably causing an erroneously high τ. Figure 25 clearly illustrates such effects. Using only points at the

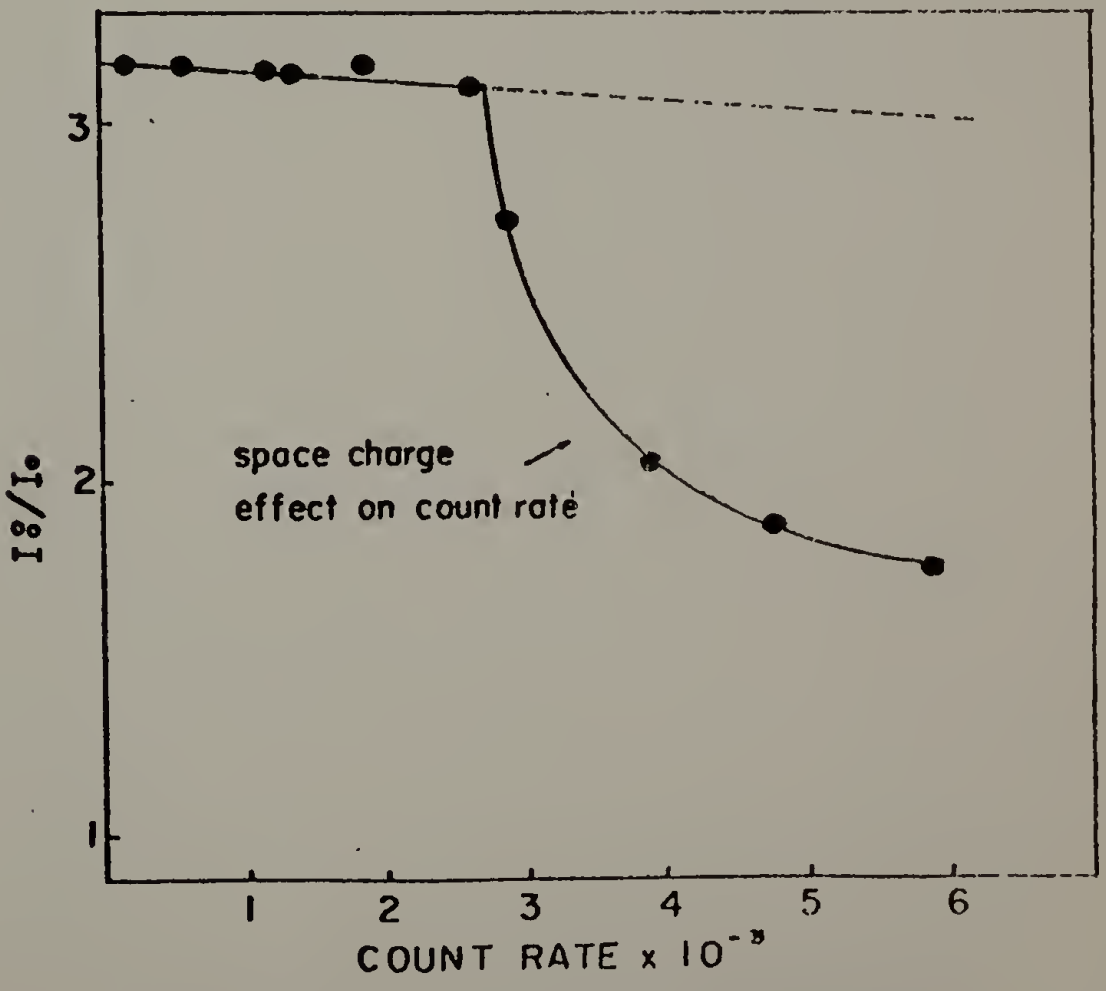

Fig. 25. Effect of space charge on dead time experiment. Count rate in counts per second.

extreme ends of the curve leads to a dead time of 140 μs rather than the correct value of 14 μs. This problem can be circumvented by using a scatterer with a fairly uniform profile so that there are no areas with extremely intense scattering.

XI. FILL-GAS EFFECT

The detector used in this study was filled with a mixture of 97% Xe–3% C_3H_6. The reason C_3H_6 (cyclopropane) was used as a quenching gas rather than CO_2 was because C_3H_6 is a much faster quenching gas which leads to higher spatial and energy resolution. However, organic gases have a serious drawback in comparison to gases like CO_2 because they are decomposed and polymerized, especially at high gas amplification. When decomposition occurs, the detector wire is coated (usually not uniformly) with a dielectric carbonaceous material and/or carbon thus altering the resistivity and diameter and reducing the electric field (locally) and consequently causing a drop in gas amplification of the incident electrons in that region. When a discriminator is used, then this causes a reduction in the count rate in the regions that are coated with the decomposition products of the quench gas. This was seen in the scattering profiles of a series of blends of poly(p-iodostyrene) with polystyrene diluted in poly(p-iodostyrene). In Fig. 26 profiles are shown with and without this effect. This problem can be avoided by two different routes. If it is desirable to use fairly tight energy discriminators then the detector must be shifted physically such that the coated area of the wire is below the beam stop. If the discriminator setting is not critical, then the lower energy level can be decreased

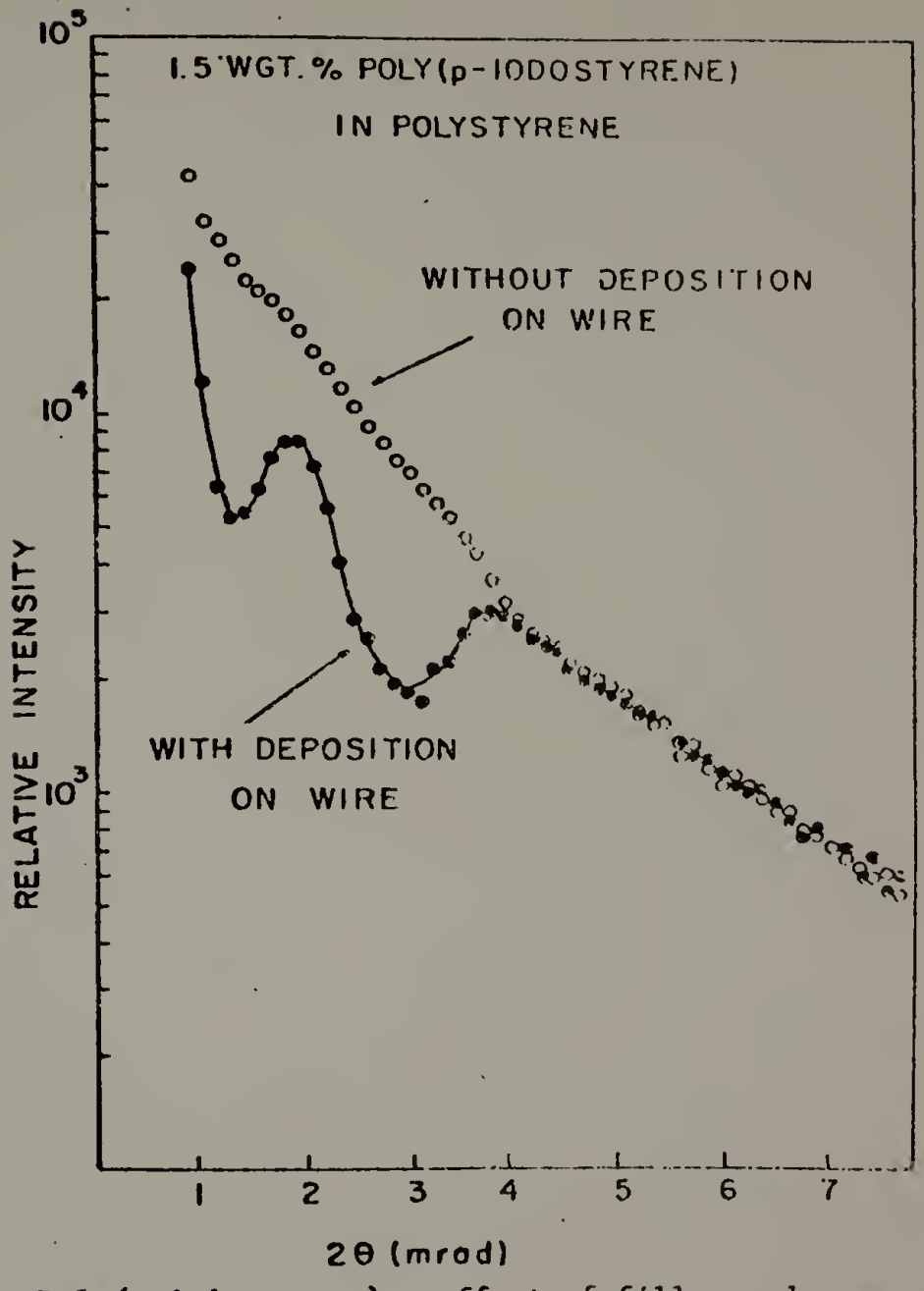

Fig. 26. Poly(p-iodostyrene): effect of fill-gas decomposition.

and the window can be opened to allow all the counts of interest to be acquired. In this way the effect can still be eliminated to some extent. However, a possibly more desirable method is to use CO_2 as a quench gas and apply a higher voltage to the detector to increase the resolution.

XII. COMMENTS AND RECOMMENDATIONS

The one-dimensional position-sensitive detector used in conjunction with a Kratky camera resulted in a small-angle x-ray scattering facility with both high resolution and low parasitic scattering. The facility was capable of resolving the scattering profiles of weak scatterers, such as PVC, as well as very intense scatterers, such as glassy carbon. During the course of this investigation several areas where precautions must be taken, not only with this facility but with position-sensitive detectors in general, were discerned.

As with most facilities and equipment, retrospective views give rise to areas of improvement. The apparatus described here is no different, and we make several recommendations below.

A. Fill Gas

As discussed in the previous section, the cyclopropane gas could be replaced with CO_2 to reduce the problems associated with deposition of decomposition products on the wire. It is to be noted that CO_2 also decomposes at high gas amplification but at a much slower rate.

B. Detector Wire

Although not emphasized in this report, the wire used in the detector described in Sect. II was a carbon-coated quartz fiber. A serious drawback to this design is that the wire can easily be destroyed by direct exposure to the incident beam. This will cause a local evaporation of the carbon coating and consequently affect the uniformity of the wire by changing the resistance at that point. If

the wire is burned severely enough, this can cause a total failure of the detector. This problem is magnified with the use of a Kratky-type collimation system since the full power of the x-ray beam must be placed close to the edge of the tungsten beam stop in order to achieve resolution.

During the course of this study the detector was burned to only a minor degree in one position. This inhomogeneous position on the wire was avoided by physically lowering this section below the beam stop. However, ideally a detector wire that can withstand exposure to the incident beam is desirable. At present a detector equipped with a metal wire which meets these requirements is in the final stages of development and testing.

C. Detector Resolution

The resolution of the detector used in this study was 400 μm and necessitated the use of the extended flight path. A detector with higher spatial resolution would have been much easier to work with since the flight path would have been shorter. This would make the system much less sensitive to vibrations and other minor disturbances. Alignment would be significantly easier. With the current geometry, alignment was difficult due to the size and mass of the flight path. Small changes in the positioning of the flight path caused significant changes in the bridge alignment. With a shorter geometry, these problems would be alleviated.

XIII. ACKNOWLEDGMENTS

The authors are indebted to D. Shapira for his encouragement and suggestions throughout the course of this work; to R. H. Ward, R. Barnes, A. J. Millet, M. Ball and R. P. Cumby of Oak Ridge National Laboratory and C. Napikoski and J. Zolty of the University of Massachusetts for providing technical assistance during the construction of the system and F. A. Scarboro for preparing the manuscript. We express our appreciation to J. R. Weir, Jr., C. J. McHargue, H. L. Yakel, and A. Wohlpart for their administrative assistance in arranging the joint project between the University of Massachusetts and Oak Ridge National Laboratory. Finally, one of us (TPR) is particularly grateful to the Oak Ridge Associated Universities, Oak Ridge National Laboratory, and the Polymer Research Institute of the University of Massachusetts for their financial assistance.

APPENDIX I

Electronic Determination of Spatial Resolution

The spatial resolution of the detector can be adjusted as follows. With a radioactive source illuminating the detector, obtain a trace of the bipolar output pulse from the main amplifier at either end of the anode wire, as illustrated in Fig. 27. Measure the noise level (N) in rms volts with an RMS voltmeter with OV bias. Apply the bias voltage and determine the slope of the pulse at crossover (S_c) in volts/time. Also determine the sensitivity of the detector (S_D) in time/length as the product of the multichannel analyzer conversion factor (channels/length) as in Fig. 9 (p. 13, this report) multiplied by the delay time per channel (time/channel). (The latter may be determined by changing the delay on the single channel analyzer and observing how many channels a given peak in the scattering pattern is moved.) The spatial resolution, R, is then

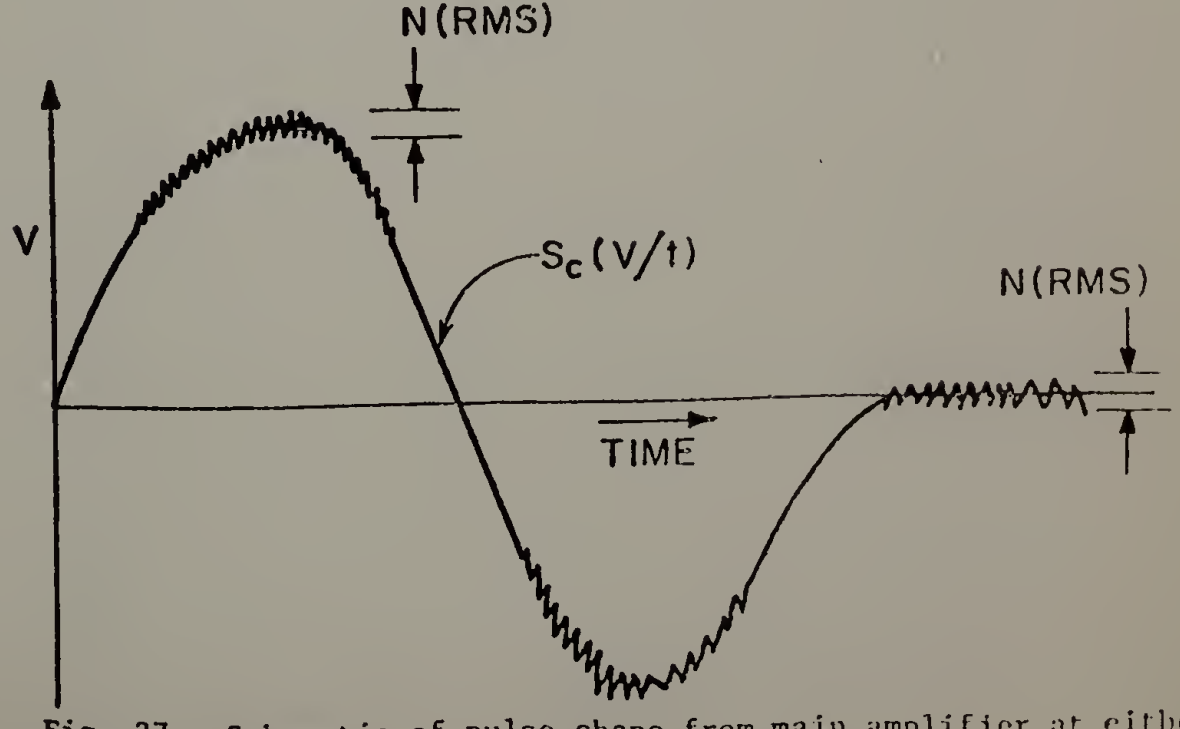

Fig. 27. Schematic of pulse shape from main amplifier at either end of detector wire.

$$R(RMS) = \frac{1}{S_c} \cdot N \cdot \frac{1}{S_D} .$$

For the detector described in this report (at bias = −2600 V)

$N \cong 1$ mV,

$S_D \approx 12$ ns/mm,

$S_c \approx 0.4$ V/μs, and

$R \cong 0.2$ mm (RMS) or 0.5 mm FWHM*.

Increase the bias voltage until the slope has increased sufficiently to achieve the desired value of R.

---

*FWHM = 2.35 σ.

REFERENCES

1. R. W. Hendricks, *J. Appl. Cryst.* 11, 15 (1978).

2. C. J. Borkowski and M. K. Kopp, *Rev. Sci. Instrum.* 39, 1515 (1968).

3. C. J. Borkowski and M. K. Kopp, *IEEE Trans. Nucl. Sci.* NS17, 340 (1970).

4. C. J. Borkowski and M. K. Kopp, *IEEE Trans. Nucl. Sci.* NS19, 161 (1972).

5. O. Kratky, Z. *Electrochem., Ber. Bunsenges. Physik Chem.* 58, 49 (1954); 62, 66 (1958).

6. O. Kratky, in *Small-Angle X-Ray Scattering* (H. Brumberger, ed.), Proceedings of Conference held at Syracuse University, June 1965, Gordon and Breach, New York (1966).

7. R. W. Hendricks, *J. Appl. Cryst.* 5, 315 (1972).

8. J. Schelten and R. W. Hendricks, *J. Appl. Cryst.* 8, 421 (1975).

9. R. W. Hendricks, J. T. DeLorenzo, E. M. Glass, and R. E. Zedler, *J. Appl. Cryst.* 6, 129 (1972).

10. M. K. Kopp and J. A. Williams, *Rev. Sci. Instrum.* 48, 383 (1977).

11. R. W. Hendricks, *J. Appl. Cryst.* 3, 348 (1970).

12. R. W. Hendricks, J. S. Arrington, and W. J. Mason, *J. Appl. Cryst.* 1, 128 (1968).

13. J. W. Anderegg, P. G. Mardon, and R. W. Hendricks, *An Alignment Procedure for the Kratky Small-Angle X-Ray Camera*, Oak Ridge National Laboratory Report ORNL-4476 (1970).

14. R. H. Stinson, M. W. Bartlett, T. Kurg, P. R. Sweeney, and R. W. Hendricks, *Biophysical J.* (submitted 1978).

15. D. R. Chipman, *Acta Cryst.* A25, 209 (1969).

16. R. S. Straff and D. R. Uhlmann, *J. Polymer Sci.: Poly. Phys. Ed.* 14, 353 (1976).

17. R. W. Hendricks and L. B. Shaffer, *J. Appl. Cryst.* 11, 196 (1978).

18. J. M. Schultz, J. S. Lin, and R. W. Hendricks, *J. Appl. Cryst.* 11, 551 (1978)

19. O. Kratky, I. Pilz, and P. J. Schmitz, *J. Colloid. Interface Sci.* 21, 24 (1966).

20. P. W. Schmidt, *J. Appl. Cryst.* 3, 137 (1970).

21. J. H. Wendorff and E. W. Fischer, *Kolloid Z.Z. Polymere* 251, 876 (1973).

22. O. Kratky and H. Leopold, *Makromol. Chem.* 133, 181 (1970).

23. D. K. Wilkinson, *Ionization Chambers and Counters*, Cambridge University Press, London (1950).

24. S. L. Binder and E. J. Rapperport, *The Electron Microprobe* (T. D. McKinley et al., eds.), John Wiley and Sons, Inc., New York (1966).

25. R. S. Vogel and L. A. Ferguson, *Rev. Sci. Instrum.* 37, 934 (1966); L. A. Ferguson, *Rev. Sci. Instrum.* 37, 964 (1966).

26. R. W. Hendricks, *Rev. Sci. Instrum.* 40, 1216 (1969).

ORNL/TM-6678

INTERNAL DISTRIBUTION

1–2. Central Research Library
3. Document Reference Section
4–5. Laboratory Records Department
6. Laboratory Records, ORNL RC
7. ORNL Patent Office
8. R. K. Abele
9. B. S. Borie
10–59. R. W. Hendricks
60. H. N. Hill
61. M. R. Hill
62. W. C. Koehler
63. M. K. Kopp
64–65. J. S. Lin
66. C. J. McHargue
67. C. H. Nowlin
68. H. Postma
69. D. B. Trauger
70. J. R. Weir, Jr.
71. M. K. Wilkinson
72. H. L. Yakel
73. R. E. Zedler
74. A. Zucker

EXTERNAL DISTRIBUTION

75. Geoffrey Allen, Imperial College, London
76. B. W. Batterman, Cornell University, Ithaca, NY
77. R. F. Bonart, Universität Regensburg, Regensburg, Germany
78. S. Bram, University of California, Berkeley, CA
79. H. Brumberger, Syracuse University, Syracuse, NY
80. S. L. Cooper, University of Wisconsin, Madison, WI
81. B. Crist, Northwestern University, Evanston, IL
82. C. R. Desper, Army Materials & Mechanics Research Center, Watertown, MA
83. E. W. Fischer, Universität Mainz, Mainz, Germany
84. P. J. Flory, Stanford University, Stanford, CA
85. R. W. Gould, University of Florida, Gainesville, FL
86. I. R. Harrison, Pennsylvania State University, University Park, PA
87. T. Hashimoto, Kyoto University, Kyoto, Japan
88. J. S. Higgins, Imperial College, London, England
89. L. C. Ianniello, Department of Energy, Washington, DC
90. F. Kelley, University of Akron, Akron, OH
91. F. A. Khoury, National Bureau of Standards, Washington, DC
92. J. Koberstein, University of Massachusetts, Amherst, MA
93. O. Kratky, University of Graz, Graz, Austria
94. P. Krautwasser, Kernforschungsanlage, Jülich, Germany
95–96. C. Macosky, University of Minnesota, Minneapolis, MN
97. D. L. Mitchell, National Science Foundation, Washington, DC
98. L. H. Nosanow, National Science Foundation, Washington, DC
99. Z. Ophir, Virginia Polytechnic Institute, Blacksburg, VA
100. J. F. Reardon, Boston State College, Boston, MA
101. E. J. Roche, CENG, Grenoble, France
102. R. J. Roe, University of Cincinnati, Cincinnati, OH
103. W. Ruland, Universität Marburg, Marburg, Germany
104–113. T. P. Russell, University of Massachusetts, Amherst, MA
114. D. W. Schaeffer, Sandia Laboratories, Albuquerque, NM
115. J. Schelten, Kernforschungsanlage, Jülich, Germany
116. P. W. Schmidt, University of Missouri, Columbia, MO

117. B. P. Schoenborn, Brookhaven National Laboratory, Upton, NY
118. J. M. Schultz, University of Delaware, Newark, DE
119. Y. Shindo, Fukui University, Fukui, Japan
120. C. G. Shull, Massachusetts Institute of Technology, Cambridge, MA
121–125. R. S. Stein, Unive sity of Massachusetts, Amherst, MA
126. D. K. Stevens, Department of Energy, Washington, DC
127. C. G. Vonk, Centraal Laboratorium Staatsmijnen, Geleen, Netherlands
128. M. Wai, University of Massachusetts, Amherst, MA
129. F. Warner, Polymer Laboratories, Ltd., Shrewsbury, England
130–131. A. Wasiak, Polish Academy of Sciences, Warsaw, Poland
132. R. Wetton, Loughborough University, Loughborough, UK
133. C. A. Wert, University of Illinois, Urbana, IL
134. G. L. Wilkes, Virginia Polytechnic Institute, Blacksburg, VA
135–161. Technical Information Center

A P P E N D I X I I

A PROCEDURE FOR USING THE KRATKY SMALL ANGLE X-RAY APPARATUS

INTRODUCTION

During the course of assembling Kratky small angle x-ray goniometer an attempt at alignment was made using the manual supplied. This produced very unsatisfactory results and consequently the procedures outlined here were developed. The alignment procedure consists of a series of steps beginning with the initial alignment of the optical bench rail. It should be noted that any alignment should begin here since small maladjustments or movements of the rail can cause rather complicated and, perhaps, unsolvable problems at a step further on. Unless an experimenter can rule out misalignment of the rail then it is strongly advised that the rail be stripped of its various components and the alignment begun from step one.

Throughout the course of the alignment one crucial assumption must be made. That is, that the track of the horizontal scanning device (HSD) is in a plane parallel to the plane containing the surface of the optical bench rail. The reason this assumption is crucial is not really associated with the alignment itself since one can produce a collimated system oriented in whatever fashion one desires. However, if the track of the HSD, and consequently the line of x-rays, is not parallel to the rail then one can not use the scanning equipment supplied with the system. A scattering profile must be collected in a direction strictly perpendicular to the beam in order to correctly apply the various dismearing routines. If the condition mentioned above is not fulfilled then scattering profile can not legitimately be obtained.

As is evident the procedure consists of a series of steps labeled with an appropriate number. This does not necessitate that the order

and raising it so that the bridge system is approximately the same height as the aperture on the x-ray tower. Bringing the entrance slit to the midpoint of the x-ray port will accomplish this. Now, looking down the optical bench from the end furthest from the tower (referred to as rear of the optical bench) the bridge system is squared visually with the x-ray tower mount. It was found that the low resolution bridge system is best suited for this purpose.

Step II A. Vertical Beam Scan with V_1

With the appropriate bridge system on the optical bench a vertical scan of the beam is made. This is done by observing the intensity as a function of dial setting on the fron leg, V_1. These data are plotted and the vertical position that is least sensitive to slight fluctuations is chosen. By selecting this position the stability of the beam intensity is maximized so that drastic fluctuations in the incident beam intensity are not observed.

The data for a 19 micron slit is given below.

Vertical Position, V_1	Intensity
32	2262
33	13438
34	35879
35	66221
36	72159
37	59396
38	47239
39	41714
40	38314
41	36971
42	36557
43	37370

Vertical Position, V_1	Intensity
44	38933
45	42360
46	49450
47	62863
48	83783
49	81884
50	52404
51	23429
52	6419
53	2809

The plot for these data are shown in Figure 1. Indicated also is the position selected for the best vertical positioning.

The irregularity of the focal spot profile is due to the shape of the filament and/or current variations along the filament in the x-ray tube used to produce the electrons. Since the filament is a coil the beam of electrons impinging on the copper target will not be homogeneous and will contain irregularities. Consequently, the x-ray intensity across the target will not be homogeneous.

Step II B. Vertical Scan With V_2

After the optimum position, i.e. the least sensitive position, of V_1 has been determined the frong leg is raised or lowered to this position and locked in. Using V_2 a similar scan was performed by adjusted the rear of the optical bench. Again an insensitive position in the profile (not shown) is determined and V_2 is slit and locked in place.

Step II A is repeated and the previous setting is compared to the newly obtained setting. If there is a wide discrepancy V_1 is set and locked at the new setting and Step II B is repeated. A comparison to the old setting is made. These steps are repeated until reproducible

settings with V_1 and V_2 are found. When satisfactory reproducibility is obtained the rail should be at a 6° take-off angle and in a position that is not sensitive to small vibrations or fluctuations in the focal spot.

A convenient check on the take-off angle can be made from the profile of the focal spot with V_1. The width of the vertical beam profile is directly related to the size of the focal spot, the width of the entrance slit, and the distance between the focal spot and the entrance slit. The geometry is shown in Figure 2 and the calculations are straightforward.

Step III: Tilt Adjustment of the Bridge System

Using the horizontal scanning device (referred to as HSD) and the detector equipped with a pinhole mounted flush to its face, the beam intensity is observed in the zero position of the HSD. This ensures the experimenter that contributions from both sides of the slit will be collected with equal weighting. In order to perform the remaining part of the tilt experiment it is mandatory that there be two workers present or that there be a rate meter visible to the worker while adjustments are made. The procedure is as follows: By vertical variation of the front leg the entrance slit is brought out of the main beam until the count rate is virtually nil. By reversing the direction, the slit is brought into the main beam to an arbitrarily selected count rate. This is strictly an arbitrary selection and 1 x (10^3) counts per second proved to be adequate. The slit is then moved through the main beam until the same count rate is found on the opposite side of the beam. The two readings of the vertical position are recorded along

be unchanged. For example the order of steps 1, 2, 3 can be rearranged to 2, 3, 1 if desired. The sequencing listed here was the preference of the authors but can be modified if one desires.

With the use of a one dimensional position sensitive detectors (1DPSD) the basic camera alignment remains unchanged. Modifications to use a one dimensional position sensitive detector can be found in an ORNL-TM by Russell et al. (1).

The nomenclature used in this report was modified to be consistent with that used by Anderegg et al. (2)

Alignment Procedure

Before entering into a detailed alignment procedure an overview of the strategy used in alignment may assist the reader in understanding why various steps were taken in the order as presented.

In brief, the overall task of alignment requires that the focal spot be parallel to both the entrance slit and receiving slit and that all three are symmetric about a center line in the camera. Consequently, the camera was divided into three sections: the rail, entrance slit collimation and the receiving slit geometry. Sections involving the rail alignment address the problem of symmetry whereas the entrance and receiving slit sections are concerned predominantly with the homogeneity of the beam. Via this approach a systematic and rigorous alignment of the apparatus can be achieved.

Step 1: Initial Alignment of Optical Bench

Before any sort of quantitative aligning can be done the optical bench must be roughly aligned by eye. This can easily be accomplished by placing the low resolution bridge system at the front of the bench

with the difference and the tilt angle. The tilt angle is then changed and the procedure is repeated with the distance traversed through the beam being determined as a function of tilt angle. These data are then plotted (path length vs. tilt angle) as shown in Figure 3.

Lower Height	Upper Height	Path Difference	Tilt Angle
30.7	55.3	24.6	3.6
30.9	55.55	24.65	3.7
31.0	55.25	24.25	3.8
31.05	55.15	24.12	3.9
31.15	55.2	24.05	4.0
31.2	55.3	24.10	4.1
31.1	55.3	24.20	4.2
31.0	55.35	24.32	4.3

The minimum in the curve is selected as the best tilt angle since when the slit is parallel to the main beam the distance traversed through the beam is at the minimum.

Since the scale on V_1 is not calibrated to the tenths position one can question the accuracy of these results. However, the results were found to be reproducible and the subsequent homogeneity run bore this out.

Alternatively, Anderegg et al (2) describe an alternate technique which may be substituted for the above procedure. The slit which those experimenters employed was not supplied with the camera and a suitable replacement was constructed in this laboratory in order to conduct the tilt experiment as they prescribe.

Step IV A: Beam Homogeneity

The height and tilt determined in sections II and III are set by tightening of the adjustment screws. The beam is then scanned horizontally

to determine the width of the beam and it's homogeneity. If the intensity of the beam is not constant across the width of the beam then the tilt was not done properly and Step II should be repeated.

Step IV B: Beam Symmetry

Once homogeneity is obtained the symmetry of the beam about the zero point on the HSD is determined. If the beam is not symmetric then the frong leg needs adjustment or the back leg needs adjustment in the horizontal plane. This is accomplished by adjusting H_1 and H_2. It is rather difficult to determine whether H_1 or H_2 require adjustment due to their peculiar pivot paints. Trial and error, although tedious was the choice of attack. It will be found that accurate eyeing of the rail (Step I) will yield fairly good results.

Once satisfactory symmetry is obtained in this position (± 5%) the detector is placed ∿ 30 cm down the rail and the symmetry is again determined (± 5%). Adjustment of legs with the detector in this position until symmetry is obtained should be minimal. Once symmetry of the beam along the rail is found, then the set screws for the horizontal positions are tightened. The results of this section are shown in Figure 4.

Step V: Placement of the Bridge Beam Limiters

The beam limiters positioned just before the final bridge collimator serve two important functions. First of all they restrict the size of the beam to eliminate parasitic scattering arising from the walls of the vacuum flight path. Secondly, coupled with the actual size of the focal spot the limiters define the beam in the length (horizontal) direction. The size of the limiters used in the apparatus will determine whether or not an "infinite height" beam assumption can

be used for dismearing purposes (this also depends upon the receiving slit width and vacuum chamber length (3)). This will be discussed at a later point.

In any event, the geometry of the camera should be schematically drawn to facilitate the selection of the maximum allowable limiter size. Once the desired size is selected care must be exercised in placing them symmetrically about the center of the rail. Step IV B should then be repeated to check for beam symmetry and homogeneity. Figure 4 illustrates the symmetry that can be achieved with correctly positioned limiters.

An example of a schematic drawing is shown in Figure 5 as demonstrated by Schaffer and Hendricks (4). Other examples can be found in the Kratky literature (5).

Step VI: Sample Holder Placement

If a sample holder has been made for the system it is now placed on the rail as close to the bridge system as possible yet in a reproducible position. Care should be taken to make sure that the sample holder does not interfere with the incident beam path as well.

Step VII: Vacuum Chamber Placement

The vacuum chamber along with the micrometer dial is placed on the rail directly after the sample holder. The placement of the vacuum tube must be such that the axis of rotation of the chamber is centered on the sample. This is easily accomplished by placing a wire through the holes in the pivot point, or by placing a rod through the hole and positioning either at the position of the sample center.

Step VIII: Optimization Calculations

Hendricks and Shaffer (4) presented procedures for the calculations of the optimum parameters for use in the Kratky camera. A detailed discussion of the optimization calculations will not be given here and the reader should consult the report if interested. A sample of the calculations are given below for the desired 200 nm resolution. If the entrance slit on the camera at this point can not yield the desired resolution then it should be changed with the homogeneity of the beam being checked.

Δ = 52 mm

W_2 = 60 mm

W_3 = 152 mm

L_i = 200 mm

Desired Resolution - 200 nm

$\varepsilon_{min} = (2\theta)_{min} = \lambda/d = 0.0007$

$$W_1^* = \text{optimum entrance} = \frac{W_2(W_3 - \Delta)\, L_i\, \varepsilon_{min}}{(W_3 - \Delta)\,(L_i + W_3 - W_2) + W_2(L_i + \Delta)}$$

$$= 22.6\ \mu$$

[19 μ slit used]

$$W_c^* = \text{optimum receiving slit width} = \frac{L_i\, \varepsilon_{min}}{3} = 51.4\ \mu$$

$$2\, W_c^* = 102.8\ \mu$$

[85 μ slit used]

For the specific designations of the variables and for further elucidation, the report by Shaffer and Hendricks (4) should be consulted.

Step IX: Tilt of Lower Portion of the Receiving Slit

With the Kratky apparatus in our laboratory, the lower section of the receiving slit is permanently mounted onto the vacuum tube. Therefore, the tilt of the vacuum tube must be adjusted to obtain a parallel slit.

In order to proceed correctly the detector must be so positioned in the HSD so that the entire portion of the beam is visible. With the detector (again with lead pinhole) fixed the vacuum tube is raised and lowered to locate the beam. The vacuum chanber is then lowered until the count rate is maximized and insensitive to further motion (downward) of the vacuum chamber.

[Note: The upper slit must be completely raised so that it does not interfere.]

Setting the vacuum chamber in this position, the detector is raised and lowered until a maximum in count rate as a function of the vertical position of the detector is attained. The detector is then moved to this maximum position, and is thus aligned with the main beam. With the detector in its optimum position the tilting procedure can be continued. The HSD is placed at +5 mm and -5 mm and the vacuum chamber is first raised, to completely block the beam, then lowered to a position where an arbitrarily selected count rate is obtained. When the position at +5 mm and -5 mm are equal then the slit is horizontally aligned with the beam. If desired, then a plot of tilt angle versus the differences between the +5 and -5 readings could be made with the difference intercept corresponding to the proper tilt being determined.

The procedure used previously was to proceed by an observation of the +5 and -5 readings and tilting to compensate until even readings were obtained.

Step X: Alignment of the Upper Portion of the Receiving Slit

The detector, equipped with the make-shift pinhole, is placed at the +5 mm or -5 mm position. The vacuum tube is placed vertically in

a position where sufficient counts are obtained. It is advisable to recheck the horizontal homogeneity of the beam before proceeding. This is absolutely necessary for this final alignment.

With the detector and vacuum tube so placed the upper receiving slit is brought down until the count rate is at background. The slit is then reopened until a moderate, though not excessive, count rate is obtained. This reading is then compared to the reading on the opposite side, i.e. at -5 or +5. If the count rates are the same then the upper slit is aligned. If not, then the upper slit must be tilted so as to compensate for this difference. Since this tilt is not calibrated, then the measurements are more or less a one shot deal. As will be seen, there are two rather irritating aspects of the tilting procedure and they are:

1. The tilting screw used is extremely sensitive.
2. The screw has quite a bit of lag. The counting rates are affected drastically by the slightest touch of the tilting screw but return to their previous level with relaxation.

Once the tilt has been adjusted to the desired level there is no way of locking the tilt into position and the alignment is essentially finished. The detector is then placed into its attachment on the vacuum chamber.

Step XI: Micrometer Dial Setting for Receiving Slit Width

Carefully the micrometer dial's ruby surface is brought down onto the upper slit. This can be detected by movement of the needle on the scale. When the needle reaches the upper range (near +40 - +50) the slit is closed. If necessary the micrometer dial range is changed

simply by relieving or adding pressure on the ruby, by raising or lowering the entire assemblage. With the slit fully closed (background count rate), the micrometer dial is brought to its lower range (-40 - -50). The slit is opened to -30 μ, i.e. a small amount, and a vertical profile of the beam is found by plotting intensity as a function of vertical position of the micrometer dial. A region in the profile will be found where the intensity increases linearly with vacuum tube displacement. For this experiment it is essential to work in this region. The vacuum tube is placed at the lower region of this linear portion as shown in Figure 6.

The principle behind the following experiment rests on the fact that within this linear range, as the slit width is varied uniformly (in a stepwise position), the increase in counts is simply additive. If the intensity is plotted as a function of slit width a curved line will result. However, if the preceeding intensity is subtracted from total new intensity then the increase in intensity achieved will be the same as the intensity of that range covered by a slit (fixed). Since the intensity increases linearly with vertical displacement then this difference should also increase linearly.

Now, the slit is closed and the micrometer dial should be at the lower end of the linear range. The intensity is then found as a function of micrometer dial reading and these data as well as the increase in counts are plotted as a function of micrometer reading.

An example of this is given below.

Micrometer Dial Reading	I	ΔI
-55	0	----
-50	16	16
-45	40	24
-40	139	99
-35	691	552
-30	1767	1076
-25	3301	1534
-20	5426	2125
-15	8304	2878
-10	11737	3433
-5	15582	3845
0	20123	4541
5	25302	3179
10	30585	5283

The intensity difference curve is shown in Figure 7 along with the extrapolation to zero count rate.

As can be seen, the difference plot yields a straight line with a slight region of curvature at the lower end. This curvature is attributable to parasitic scattering. The linear section is extrapolated to zero counts and the intercept is taken as the zero of the slit width.

The slit is then opened to the value of $2W_c^*$ calculated from the optimization equations.

Step XII: Receiving Slit Limiters

From the sketch of the optics, the receiving slit limiters located just before the receiving slit must be optimized. This is done by including all rays from the sample but eliminating any rays due to parasitic scattering from the edge of the vacuum tube entrance. Once the optimum width of the limiters is found they are screwed into position.

Note: In order to accurately place these limiters in the front plate must be removed. It is advisable to set the limiters in before any alignment of the vacuum chamber is started. The screws to the limiters are then rotated a known number of rotations until they are out of the way for the alignment. Once the alignment has been accomplished the screws to the limiters are rotated back the known number of rotations.

It is unfortunate that this must be done in this fashion but if the plate is removed then the receiving slit alignment will be disrupted.

Step XIII: Stability Check

Due to the fact that vibrations will be experienced by the apparatus during normal operations it would be advisable to subject the setup to several mild vibrations and to check the alignment subsequent to these shocks. Simply scanning across the length of the beam for homogeneity will detect any changes in the alignment.

If it is found that these vibrations do cause changes in the alignment then the various locking bolts have not been adequately tightened or there is some stress in the system that is being relieved. In any case the camera should be re-aligned. During the course of any experiments, vibrations and any other sort of disturbances should be minimized. This point is alluded to later on in this report when the speed of the stepping motor is being selected.

The intensity of the incident beam was monitored as a function of time with the detector near zero degree in angle. This is shown in Figure 8. The purpose of this was to determine the stability of the intensity as a function of the normal vibrations experienced during a run. The intensity was found to be constant to within ±0.7%.

Desmearing Procedures

With the use of a Kratky camera the question arises concerning the desmearing routines applicable. Is the infinite beam geometry or the finite beam geometry applicable? What desmearing routines are more preferable? etc. This section is designed to briefly outline the concept of an infinite height geometry and to briefly discuss the various desmearing routines.

In itself the term "infinite height" geometry is contradictory since it is impossible for the x-ray beam to be infinitely wide. In addition to this the term overlooks the extreme importance of the receiving slit dimensions. Both the beam width and the dimensions of the receiving slit must be considered.

In order to understand the phrase "infinite height" consider the diagrams in Figure 9. Let l_B one half the length homogeneous portion of the beam at the receiving slit, l_C is one half the length of the receiving slit, w_c is the receiving slit width and l_S is the distance in the detector plane corresponding to the angle where the scattering from the sample is negligible.

An x-ray beam is considered to be infinitely high when the contributions to the sample scattering from the penumbra, i.e. the non-homogeneous part of the beam, is not detectable. This basically means that the beam could be infinitely wide and it would yield the exact same scattering profile. Therefore, as in Case I of Figure 8, $l_S + l_C < l_B$ and the infinite height assumption is in vogue. However in Case II, $l_S + l_C > l_B$ and the assumption no longer applied.

As can be seen, there are three parameters that can effect this assumption. If l_C or l_S is very large then one would expect the infinite height assumption not to apply. Similarly for l_B being very small by using narrow beam limiters in the bridge. One can go even a step further and consider angular ranges where the infinite height assumptions holds as discussed by Hendricks and Schmidt (3). Indeed, if one wishes to use the infinite height assumption these ranges must be calculated to ensure oneself of the legitimacy. Various programs exist, e.g. Vonk (6) and Schmidt (7) where the infinite height assumption is used for desmearing.

If for a given geometry the infinite height assumption does not hold then the weighting function of the camera geometry must be calculated in order to perform the desmearing correctly. This can easily be done by the procedure outlined by Buchanan and Hendricks (8) with subsequent numerical treatment of the smeared data. This weighting function can be used exactly as determined in the procedure of Lake (9), for example, or can be approximated by a Gaussian function and used in the procedure outlined by Schmidt (7). Whichever course is taken, care must be exercised in the use of the numerous desmearing routines available in order to apply them in the correct situation.

Operations of Electronics

A. System Description

The Kratky goniometer at the University of Massachusetts is interfaced with a series of modules (Canberra Industries) for controlling the scanning rate and counting characteristics for each scattering

profile. Figure 10 depicts a very rough outline of the system now being used.

The operator communicates with the system at the teletype by sending a series of commands to the computer interface. Either the driving motor or the counting system is activated to perform the desired function. Once performed the interface then responds to the operator by digitally displaying the result on the appropriate modular displays and by simultaneously printing the result at the teletype. In essence this is what occurs during a sample run. The remaining parts in this section will describe the various addresses that are used with the system as well as the proper method for performing a sample scattering run.

B. System Commands and Addresses

In the course of collecting the scattering profile of the sample the operator must address various components in the system in order to make the detector move to a desired angle and to collect an intensity at that angle for either a preset count or time. The means of addressing the system along with a sample command for each component is given below.

i. Axis Positoner

This device controls the motion of the stepping motor and consequently the angular displacement of the detector. The address is P11. Following the address the operator must specify the desired speed at which the motor should operate. These speeds range from a slow (very slow) speed designated by a zero (0) to a very fast speed coded as an eight (8). A speed of 5 or 6 was found to be the best suited speed. This allows the time required to step to a desired angle

to be reasonable while maintaining vibrations from the movements of the motor at a tolerable level. The direction in which the motor should move must be specified now. A zero (0) denotes the forward while a one (1) denotes reverse motion. With the Kratky apparatus in this laboratory the stepping motor occupies a position behind the camera driving the angular displacement gear by a pulley. Because of this positioning if one desires to collect scattering information at increasing angles from zero then the zero is used. To return the axis positioner to zero from a high angle the one (reverse) direction is used.

Originally the axis positioner was designed to drive a stepping motor in a 1:1 gear ratio with a goniometer. Consequently, the axis positioner display runs from 00000 to 36000 corresponding to the degrees on a circle. However, this is not the case with the UMass Kratky and the axis positioner only serves to specify an accurate displacement of the detector.

Note: The degrees displayed on the axis positioner do not equal degrees in real space and must be correctly converted.

The method of converting the degrees displayed to the actual number of degrees in real space is very straightforward. Let x be the step size of the desired angular displacement, for example 00100 is one modular degree and 30525 is 305.25 modular degrees. The gear on the Kratky was designed to elevate the vacuum chamber by 25 μ for each full rotation. The gear ratio from the stepping motor to the Kratky gear is 7:5. The distance on the camera from the sample position to the detector will be approximately 214 mm (the distance is

specified on the vacuum chamber). Using this information, the angle in real space is found by:

$$2\theta = \tan^{-1} ((x)(7/5)(25)/214000)$$

$$= \tan^{-1} ((x)(35)/2.14 \times 10^5)$$

So that one modular degree corresponds to 0.1636 milliradians or 0.00937 degrees.

There is no set rule to follow when collecting a scattering profile. However, for various smoothing routines an even angular increment is required. Generally one can collect data at increments of one or two modular degrees until the scattered intensity is low. Then the angular increment can be increased to every 10 or 20 modular degrees. The main concern is to document the curves accurately so profiles with a maximum require more documentation than monotonically decreasing curves. Therefore, the angular increment finally selected will depend strictly on the sample profile.

Combining all the information mentioned in this section a command to advance the vacuum chamber by 25 μ in the positive angular direction at a speed of six would be: P116000100*. The asterisk is required at the end of every command to any of the components.

One very confusing aspect of the axis positioner is that a positive angular displacement is recorded as a decrease in angular position. This results from the fact that the 0 and 1 directions were juxtaposed due to the positioning of the stepping motor. So zero of angle would correspond to 36000. A positive displacement of 10.15 modular degrees would be recorded as 34985.

Finally, what occurs when the axis positioner has stepped 360

modular degrees, i.e. a display of 00000. This has absolutely no effect on the motor and it will continue to make as many further displacements in the forward direction as one desires. All that really happens is that the display begins anew where 00000 corresponds to 36000. So if one is at 00000 and commands the motor to drive 5 modular degrees forward at a speed of six (P116000500*) the display will record 35500 at the completion of the movement.

ii. Counter/Timer Address

The system is designed to allow the operator to collect information up to a preset time or a preset count. Both the counter and times are addressed with a "D" followed by a four digit number where the first two digits specify the address. D41XY* and D42XY* are address to the counter and timer, respectively. More specifically, D41XY* commands the system to count to a preset count of $(x)\cdot 10^{y}$ and D42XY* commands the system to count to a preset time of $(x)\cdot 10^{y-2}$. For example, a command of D4115* will activate the counting system until 1×10^{5} counts have been collected.

In either case when the counter or timer has reached its preset level the display on the counter timer will record the preset count or time and the corresponding time or count level accumulated.

iii. Printing Command

In order to obtain a record of the event that has just been executed a command of R* is sent to the interface. In turn the interface prints out the position, total counts and total time that are displayed on the modules. This would appear as:

```
R*
05450     682024     05000
```

This means that the axis positioner has displaced the vacuum chamber by 305.5 modular degrees and has collected 682,024 counts in 50 seconds.

This response will automatically be printed on the teletype and can be recorded on paper tape if desired.

iv. Writing Command

If by any coincidence the operator wishes to change the display of the axis positioner without driving the stepping motor, then the writing command can be used. The command essentially reads W11??35450*. This addresses the axis positioner and states that whatever six digit number follows the question marks should be on the display. The question marks are used to eliminate the speed and direction in the normal commands to the axis positioner. This command will then erase whatever is on the display and replace it with 35450.

Performing a Scattering Experiment

A. Determination of Zero Angle

One characteristic of a Kratky small angle x-ray camera is the asymmetric shape of the incident beam. This originates in the type of collimation employed and necessitates the determination of zero angle prior to each run. If the camera had a symmetric beam profile then zero of angle would be equal to zero on the goniometer. However, it is the center of gravity, i.e. the first moment, of the intensity profile that determines where the zero of angle will occur. This will change its position if there are any disturbances in the collimation system or in the focal spot.

The procedure is quite simple but requires approximately 1.5 hours to execute (predominantly in counting time). The detector is brought through the attenuated incident beam to approximately 2 modular degrees on the minus side. The position is then moved 1.5 modular degrees forward so that now the detector is just about to enter the beam. The previous maneuvers ensures the operator that all the machine and gear lags have been taken up. Using the receiving slit that is used during the actual scattering experiment the incident beam is scanned at 0.25-0.50 modular degree intervals with a preset time of 100 seconds. Depending on the width of the entrance slit this will take 0.75-1.5 hours to complete. The beam is scanned until the detector is just out of the incident beam and the scanning is stopped.

The beam profile is then numerically integrated by summing the intensities, $\Sigma_T I_i$. This sum is divided by 2 and the beam is then integrated step by step up to modular degree N until the sum is just below half the total integral. This sum is called $\Sigma_N I_i$. The next step integrated should place the sum above half the total integral. The difference between $\Sigma_T I_i$ and $\Sigma_N I_i$ is found and this difference is divided by the intensity value of the next point and multiplied by the increment in modular degrees. This is then subtracted from modular degree N (due to the decreasing angular reading) to determine the zero of angle. This process can be written as

$$\text{Zero} = N - \frac{(\Sigma_T I_i/2 - \Sigma_N I_i)}{I_{N+1}} \times \Delta.$$

With the zero of angle known the true angular position of the axis positioner is known and is given by

$$T = P - Z$$

Where T is the true number of modular degrees from the zero position, Z,

P is the reading of the axis positioner as it reads on the module.

The axis positioner is now stepped forward so that in reality the detector will be on an even number or on an even fraction of modular degrees from zero. Using the write command the true position is then written on the axis positioner.

This is illustrated in Figure 11. The incident beam was scanned from 360 modular degrees to 349.5 modular degrees in steps of 0.5 modular degrees. The beam was integrated yielding a total intensity of 9,927,425. So $\Sigma_T I_i$ = 9,927,425 and $(\Sigma_T I_i)/2$ = 4,963,712.5. A stepwise integration up to 354.4 was performed yielding $\Sigma_N I_i$ = 4,436,156 where N = 354.5 modular degrees. The count at position 354.00 or I_{N+1} = 945,321. So zero is given by

$$354.5 = \left(\frac{4,963,712.5 - 4,436,156}{945,321}\right) \times (0.5) = 354.22.$$

Since the detector is now at 349.5 then it is 349.5 - 354.22 or 5.72 modular degrees from zero. The axis positioner was then moved 0.28 modular degrees forward (P116000028*) and this placed the detector precisely 6 modular degrees from zero. This was then written on the positioner module as W11??35400*.

Now the detector's position has been set and calibrated with respect to zero and a run can be started after the attenuators are removed.

B. Running A Specimen

After the procedures outlined in Section A have been performed the attenuators are removed and the sample is placed on the sample

holder (double-stick adhesive tape can serve as an adequate support). The specimen holder can then be screwed into place. At this point the only tasks left to be done are to get the attention of the system (typing a $!), loading the tape containing a series of commands and begin reading the tape. The teletype should in the line mode and not the local mode. There should be no preset time on the modules and the preset count should read 96. The run will continue until the tape is removed at which time a new tape with a different series of commands can be loaded or the run can be stopped.

Mention was made of loading a tape containing a series of commands. The use of a tape allows the operator to let the apparatus run by itself without the constant need of attention. In order to avoid having reams of tape to perform one single run, a loop can be made that contains the desired commands. This is easily made by splicing together a tape using scotch tape to join the ends.

C. Parasitic Scattering Run

A parasitic scattering profile is basically an attenuated background run. Provided the counting times are the same this can be directly subtracted from the sample scattering run and will remove all contributions to the sample scattering curve from slit edge scattering and electronic noise.

The run is performed in exactly the same fashion as a sample scattering run only the sample is now placed just before the detector, i.e. an absorbing position, rather than in the scattering position.

D. Liquid Scattering Run

In the course of examining the scattering from semi-crystalline materials one is only interested in the scattering arising from the

amorphous-crystalline electron density difference and the resulting crystal-crystal interferences. Therefore, it is necessary to subtract contributions due to thermal density fluctuations and dust scattering. This can be done by melting the material and observing the scattering arising from the melt. After subtraction of the parasitic scattering the scattering profile from the molten material remains being composed of dirt scattering and thermal density fluctuations. The latter scattering is nearly angularly independent and can easily be subtracted from the total remaining profile leaving only the contributions due to dirt scattering. This should be directly subtracted from the sample scattering profile assuming that the concentration of extraneous matter does not change upon melting and that the sample expansion is small. The latter assumption may not be strictly correct but can easily be accounted for.

A composite scattering profile indicating all the various contributions is given in Figure 12. The shaded section is the section of interest when applying the various model calculations and in the calculation of the invariant.

Pulse Height Analysis

An assumption that has been implicitly made throughout this report is that the radiation originating in the x-ray tube and subsequently scattering is pure CuKα radiation. This is not the case however. The spectrum of copper radiation coming from the tube is predominantly CuKα and CuKβ but this is superposed on a continuous "white" spectrum. Within the collimation system there is a N_i filter which removes most of the white radiation and the CuKβ as well. However, there is still

some high energy radiation as well as a distribution of energies around the CuKα peak. So really the radiation being scattered is not mono-energetic (monochromatic) radiation.

In order to circumvent this problem one can discriminate the radiation being collected in the detector. Since elastic scattering is of interest the scattered radiation being analyzed should lie between certain energy levels. Characterization of CuKα the energy levels of incoming radiation can electronically be separated and discriminated. The discrimination is easily done by observing the spectrum of energy of the incoming radiation and placing the discrimination's energy level and window width (in the differential mode) around the CuKα peak. However, before this is done the gain on the detector as well as the high voltage on the detector must be set so that the incoming pulses can be seen. This is accomplished via a pulse height analysis as described by Miller (11). For the geometry of interest the detector was placed at the peak in the scattering profile of a styrene-butadiene-styrene block copolymer. This afforded enough radiation to perform the analysis. The energy spectrum was observed as a function of detector voltage (900, 1000, 1100 v) as well as gain. These spectra are shown in Figures 12 a, b, c. An operating voltage of 1000 v with amplifier gains of 4 (coarse) and 1.5 (fine) were selected. This allowed an energy level of 3.5 with a window of 3.5 to be used on the discriminator in the differential mode.

References

1. T. Russel, R.S. Stein, R. Zedler, R.W. Hendricks and J.S. Lin, Use of a One dimensional Position Sensitive Detector on a Kratky Camera, ORNL-TM, In preparation (1978).

2. J.W. Anderegg, P. J. Mardon and R.W. Hendricks, An Alignment Procedure for the Kratky Small Angle X-Ray Camera, ORNL-TM-4476 (1970).

3. R.W. Hendricks and P.W. Schmidt, Acta. Phys. Austr., 26 7 (1967).

4. L.B. Shaffer and R.W. Hendricks, Optimization of the Kratky Small Angle X-Ray Scattering Collimation System Parameters, ORNL-TM-4278 (1973).

5. Specification Sheets for the Kratky Camera, Anton-Parr, Austria.

6. C.G. Vonk, J. Appl. Cryst., 4, 340 (1971).

7. P.W. Schmidt, Acta Cryst., 8, 772 (1955); 19, 938 (1965); J. Appl. Cryst., 3, 137 (1970).

8. M.G. Buchanan and R.W. Hendricks, J. Appl. Cryst., 4, 176 (1971).

9. J.A. Lake, Acta Cryst., 23, 191 (1967).

10. D.C. Miller, Norelco Reporter, 4, 37 (1957).

List of Figures

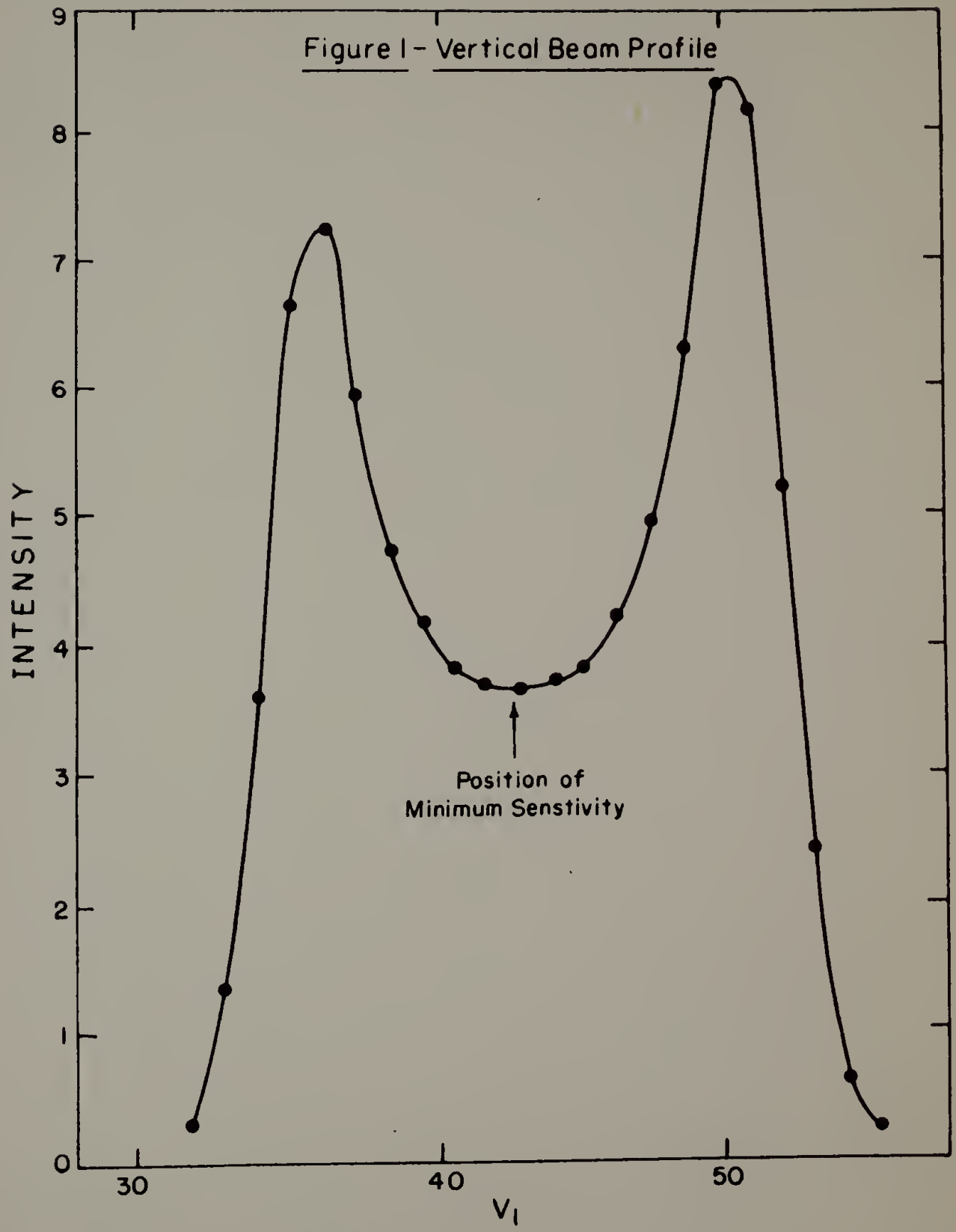
Figure I - Vertical Beam Profile
INTENSITY
0
1
2
3
4
5
6
7
8
9
30
40
50
V_1
Position of
Minimum Senstivity

Figure 2- Apparent Focal Spot Size

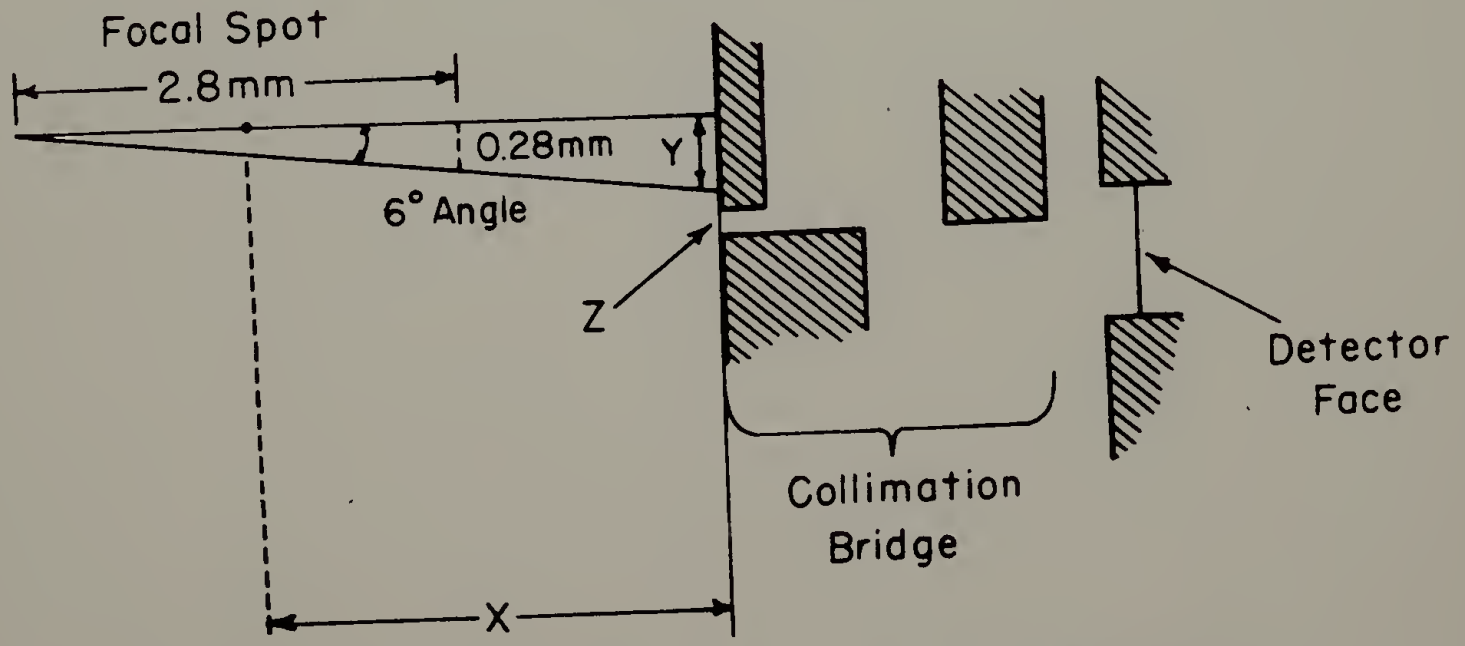

X = Distance from tower center to entrance slit (mm)

Y = Apparent focal spot size at entrance slit
= (0.1)(X + 1.4)

Z = Entrance slit width

Width of focal spot measured = 2Z + Y

Figure 3 - Tilt Experiment

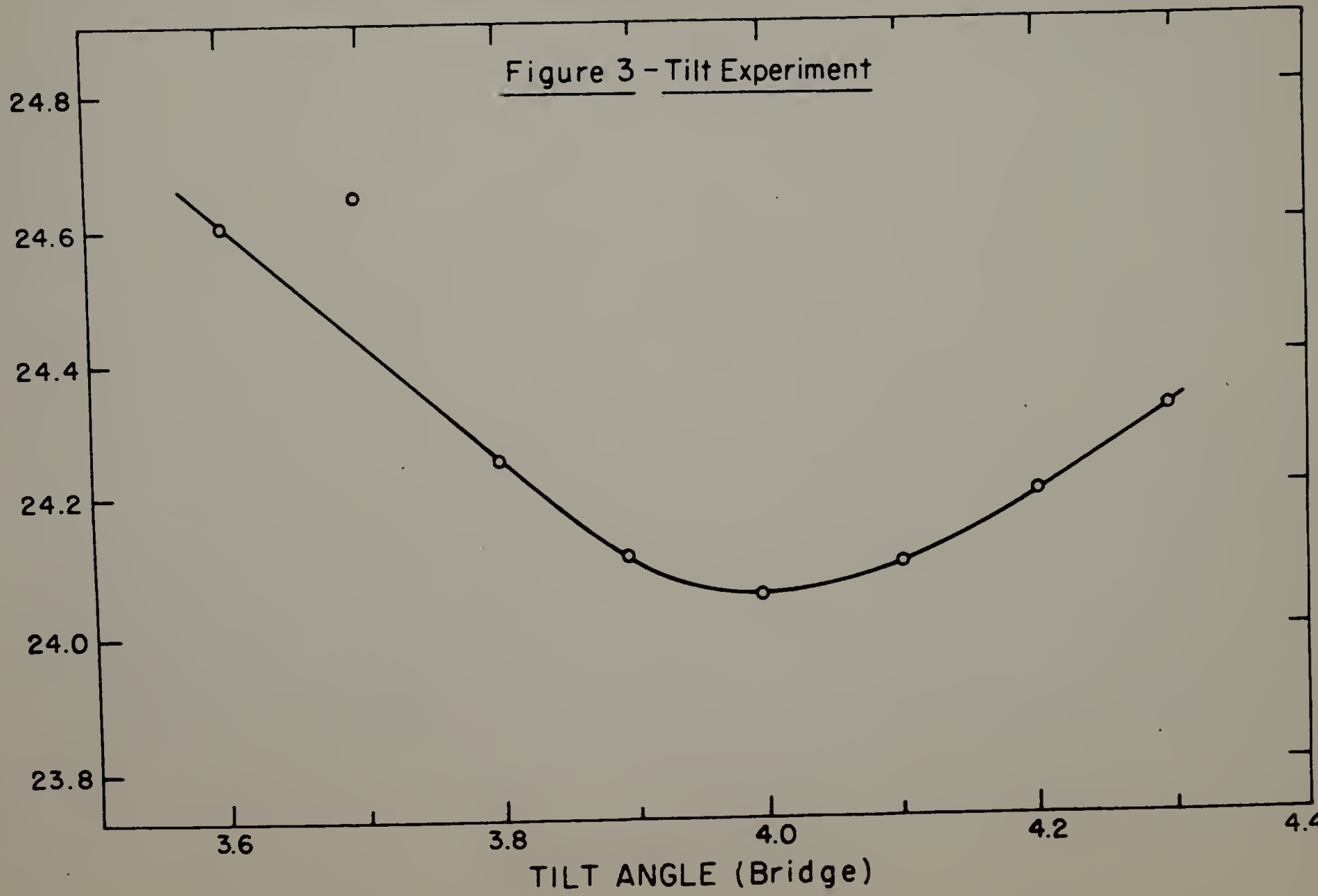

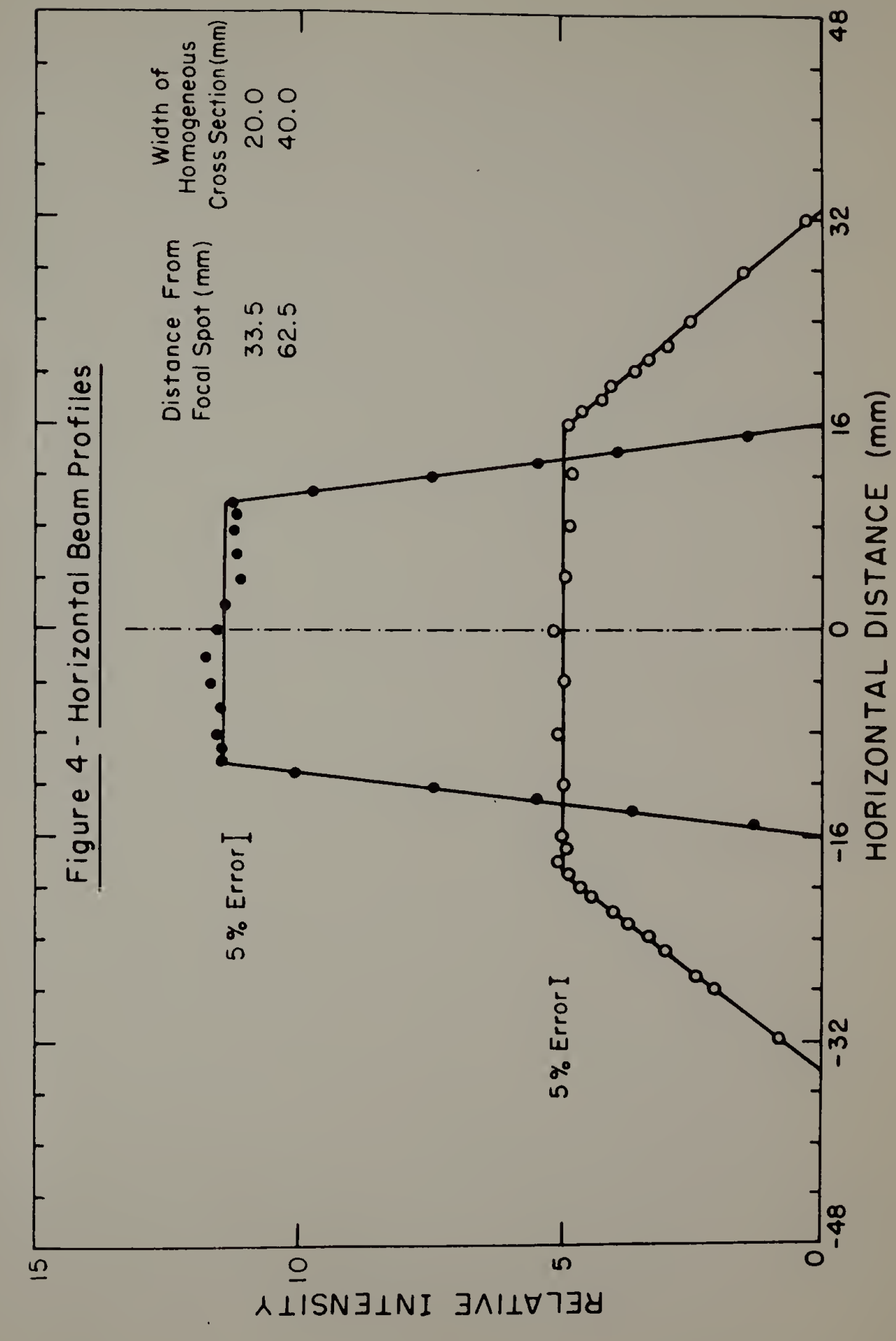
Figure 4 - Horizontal Beam Profiles
Distance From Focal Spot (mm)
33.5
62.5
Width of Homogeneous Cross Section (mm)
20.0
40.0
5% Error
5% Error
RELATIVE INTENSITY
HORIZONTAL DISTANCE (mm)
15
10
5
0
48
32
16
0
-16
-32
-48

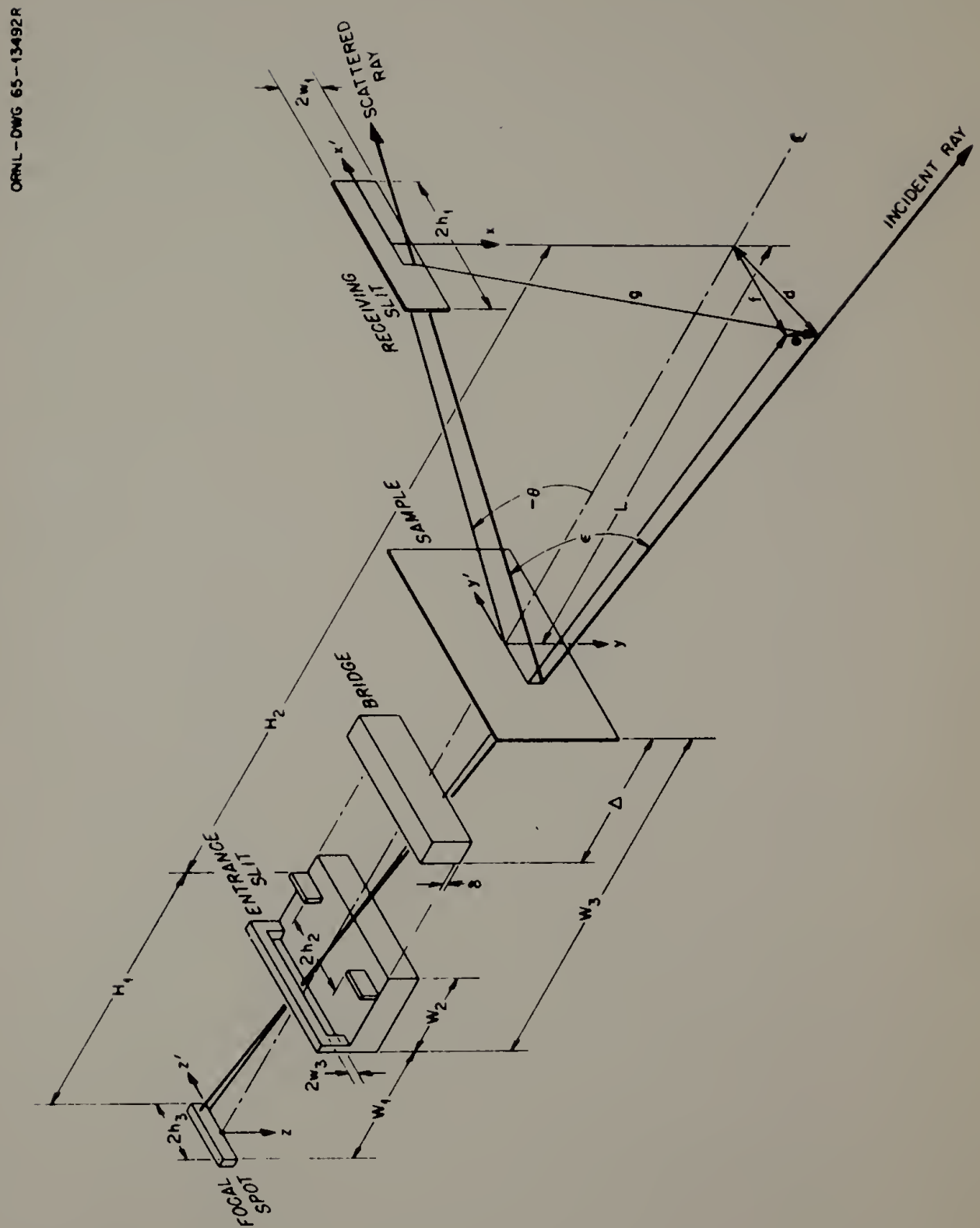
ORNL-DWG 65-13492R
SCATTERED RAY
INCIDENT RAY
RECEIVING SLIT
SAMPLE
BRIDGE
ENTRANCE SLIT
FOCAL SPOT
$2w_1$
$2h_1$
$2h_2$
$2w_3$
$2h_3$
H_1
H_2
W_1
W_2
W_3
Δ
δ
θ
$-\theta$
ϵ
L
f
d
x
x'
y
y'
z
z'

Figure 6 – Location of Linear Region of the Beam Profile

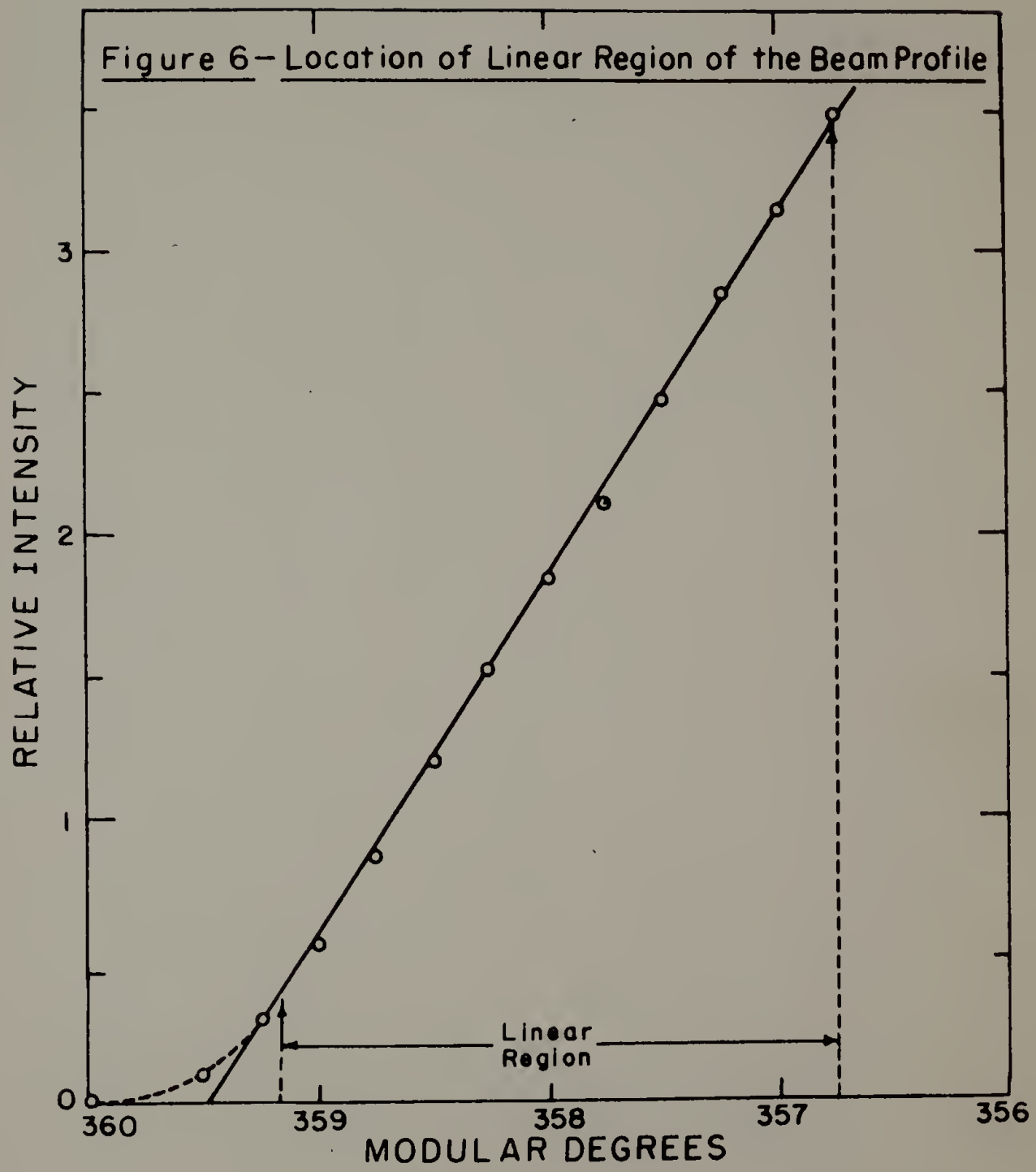

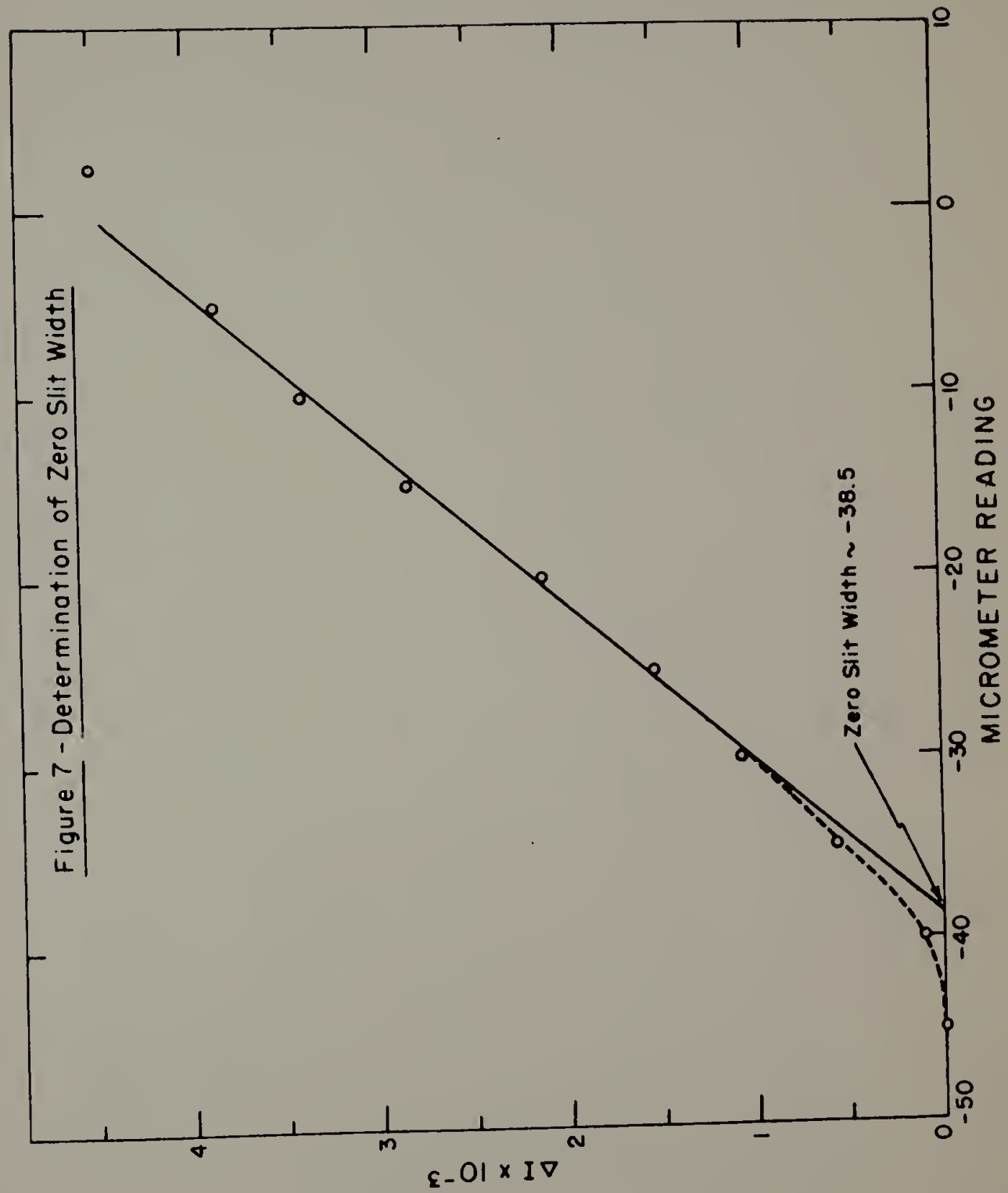

Figure 7 - Determination of Zero Slit Width

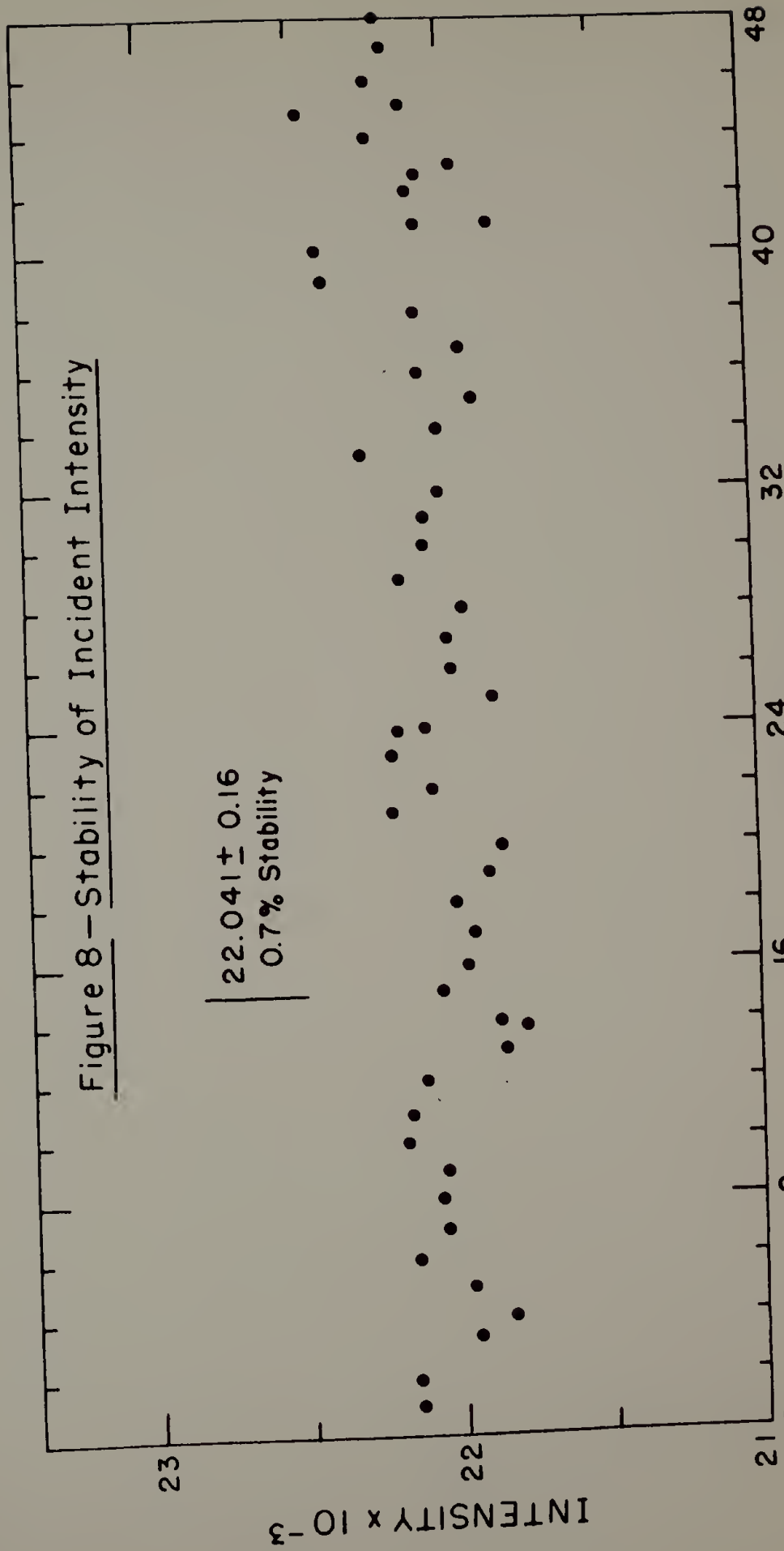

Figure 8—Stability of Incident Intensity

Figure 9 - Infinite Height Assumption

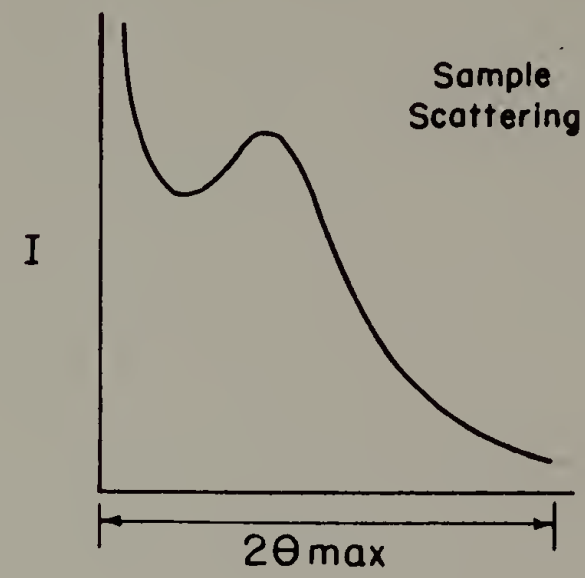

$\ell_s = (\tan(2\theta)) \times p$

p = Sample to detector distance

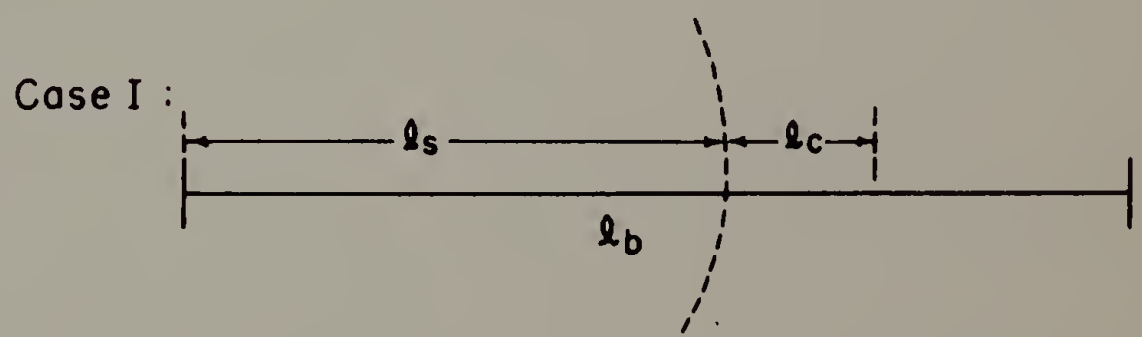

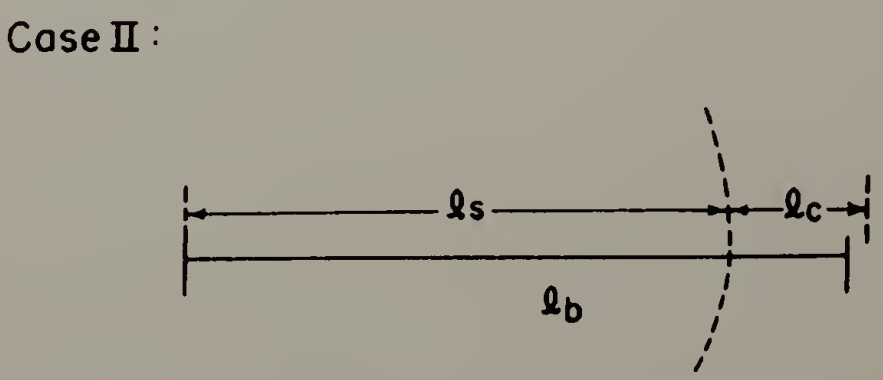

Figure 10 - System Schematic

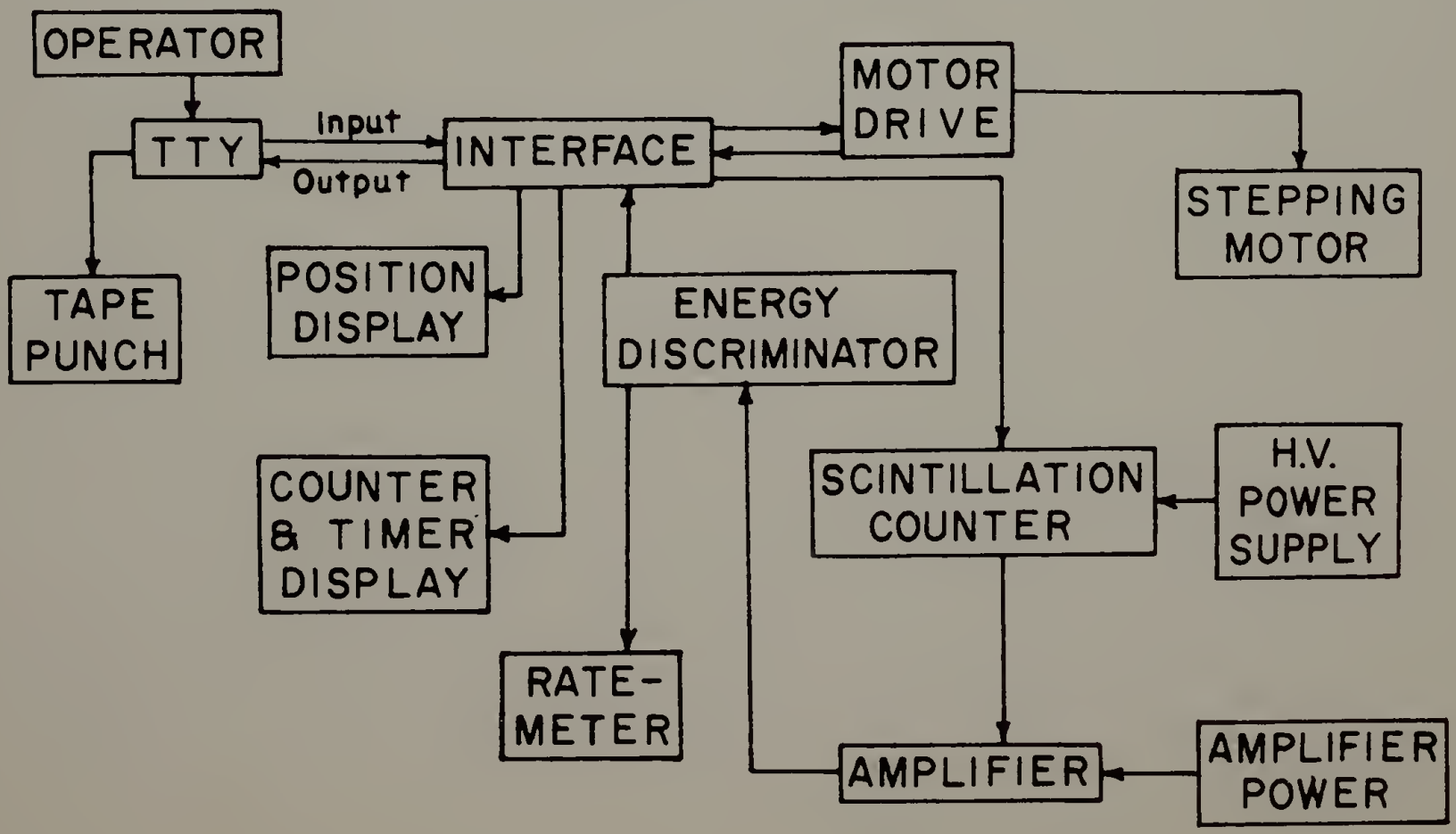

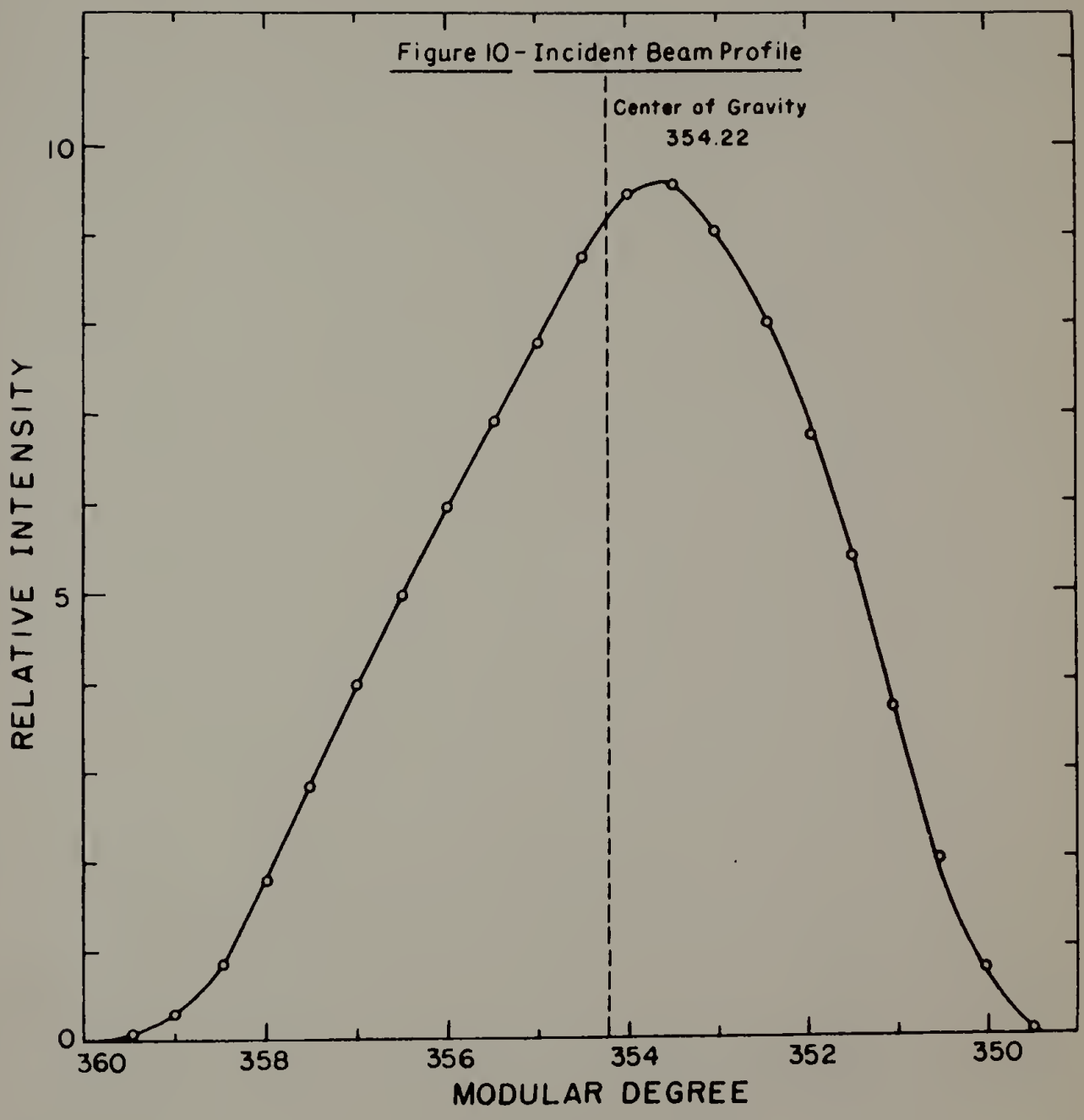
Figure 10 - Incident Beam Profile
Center of Gravity
354.22
RELATIVE INTENSITY
10
5
0
360
358
356
354
352
350
MODULAR DEGREE

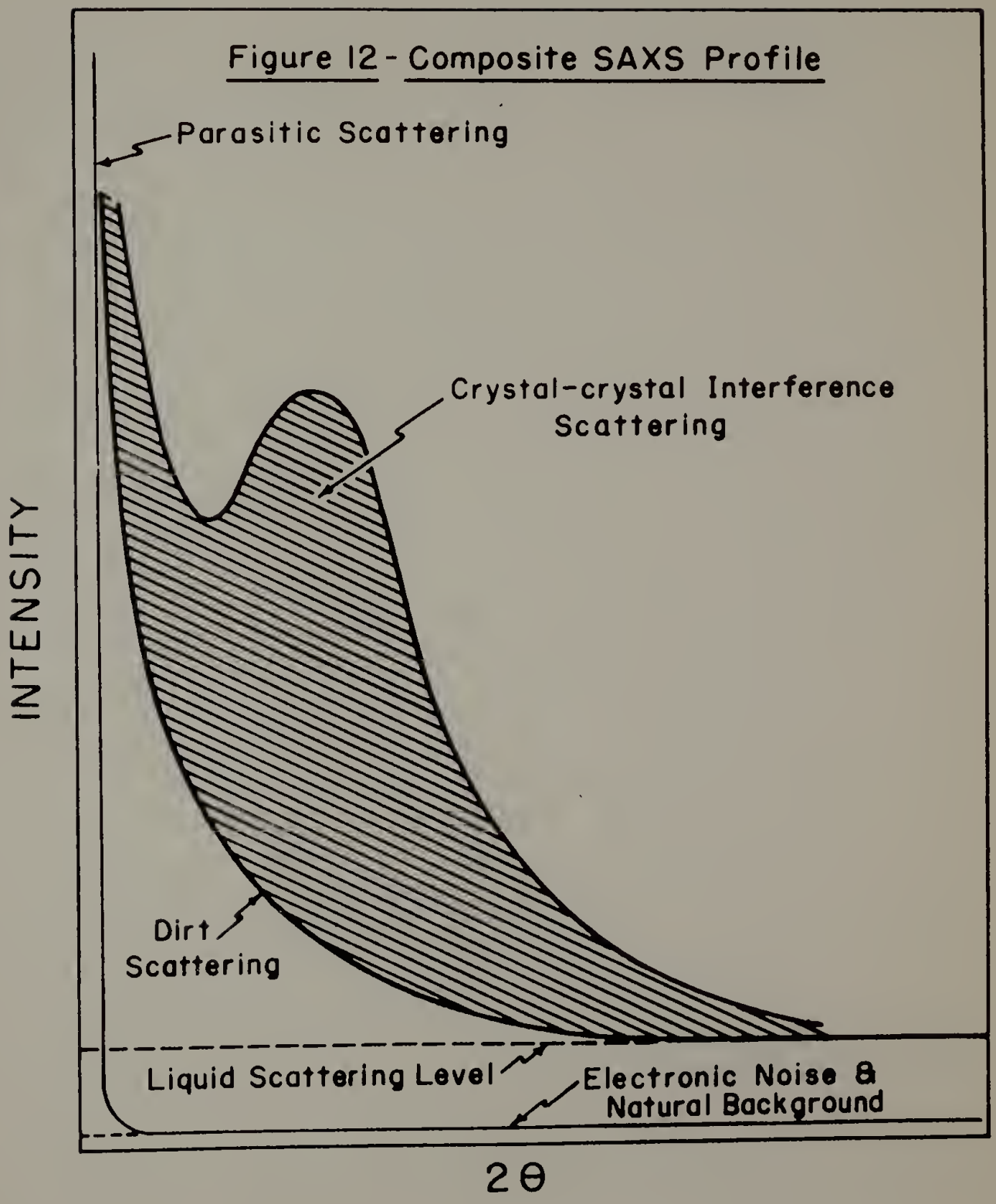

Figure 12 - Composite SAXS Profile

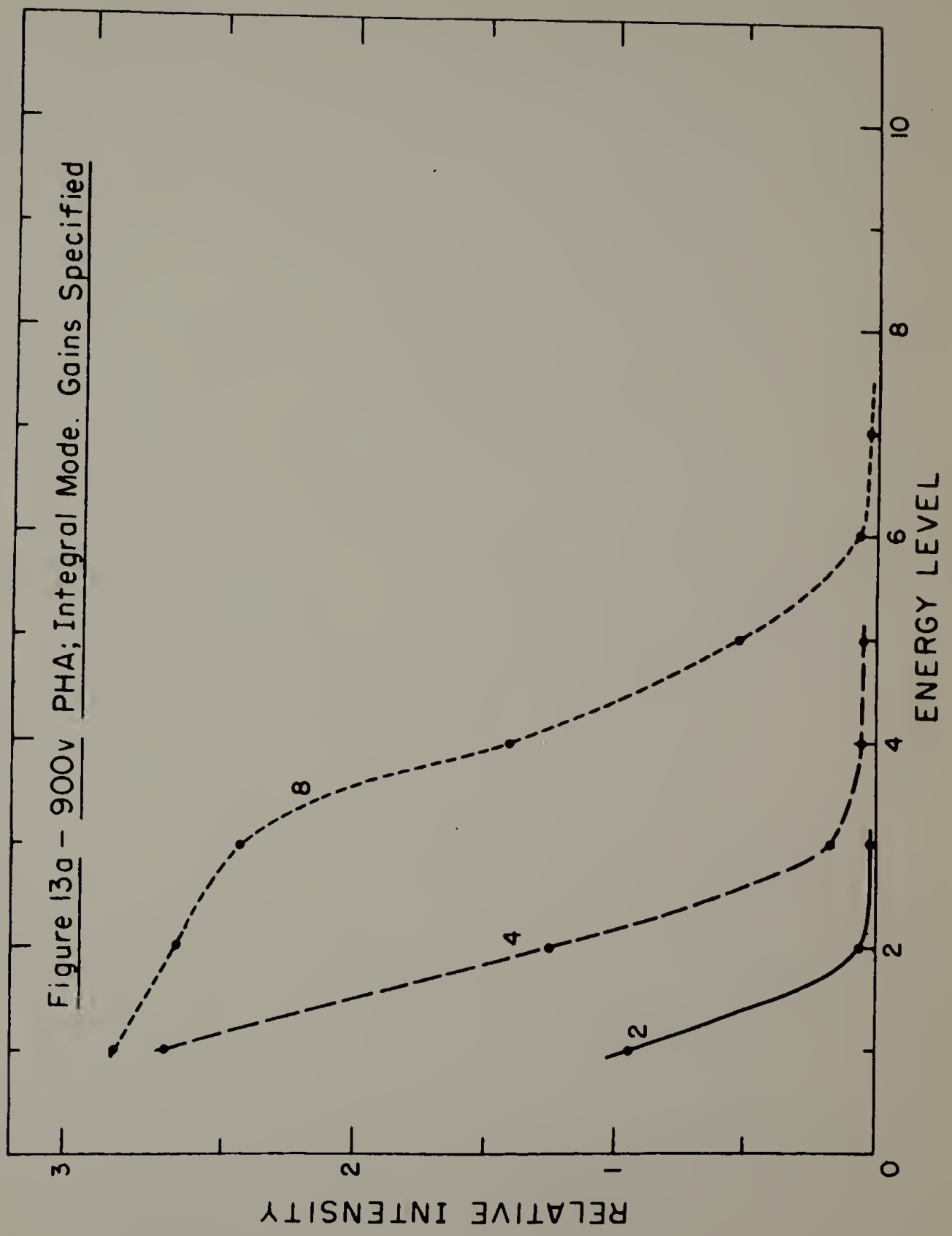

Figure 13a – 900v PHA; Integral Mode. Gains Specified

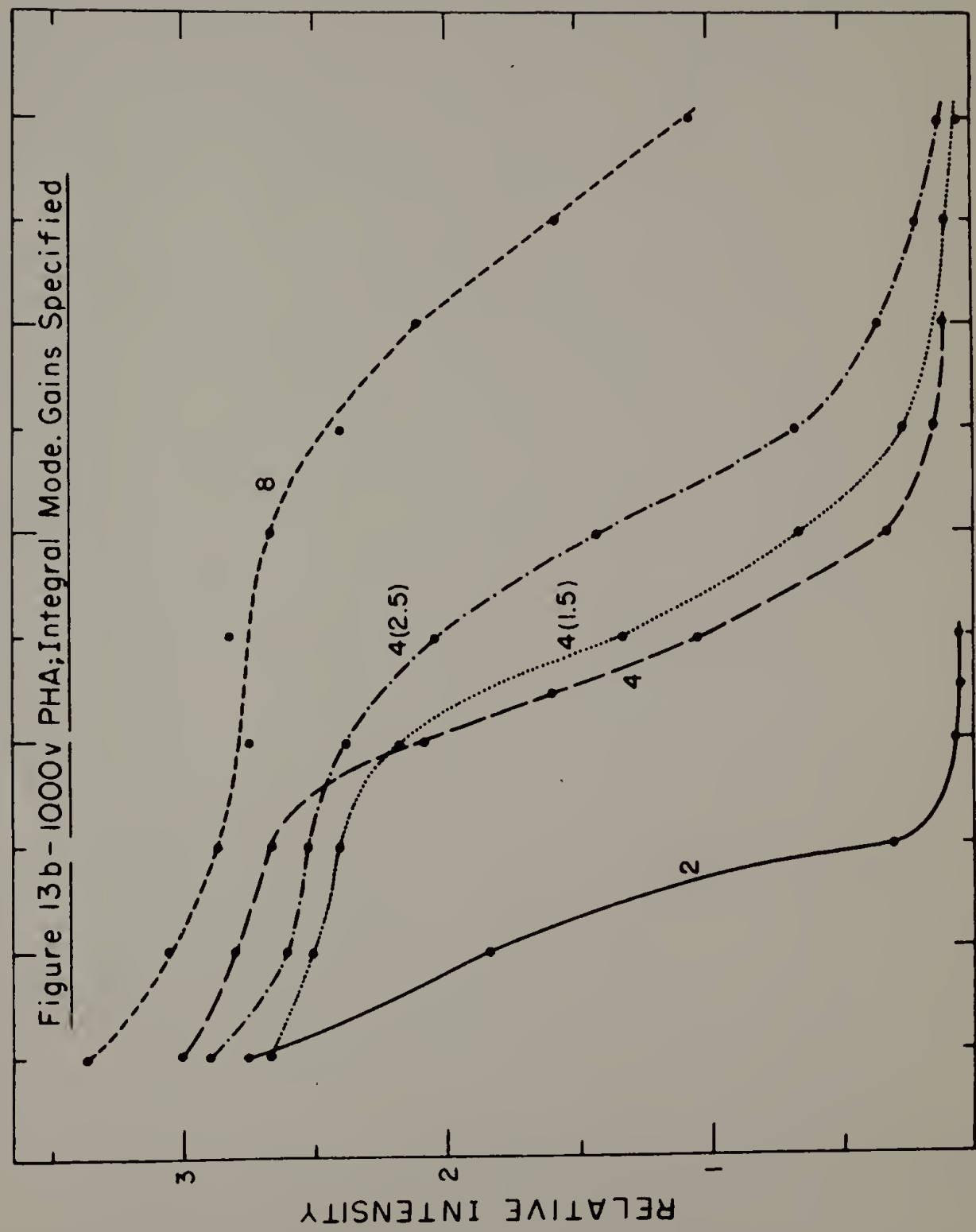
Figure 13b - 1000v PHA; Integral Mode. Gains Specified
RELATIVE INTENSITY
ENERGY LEVEL
0
1
2
3
2
4
6
8
10
2
4
4(1.5)
4(2.5)
8

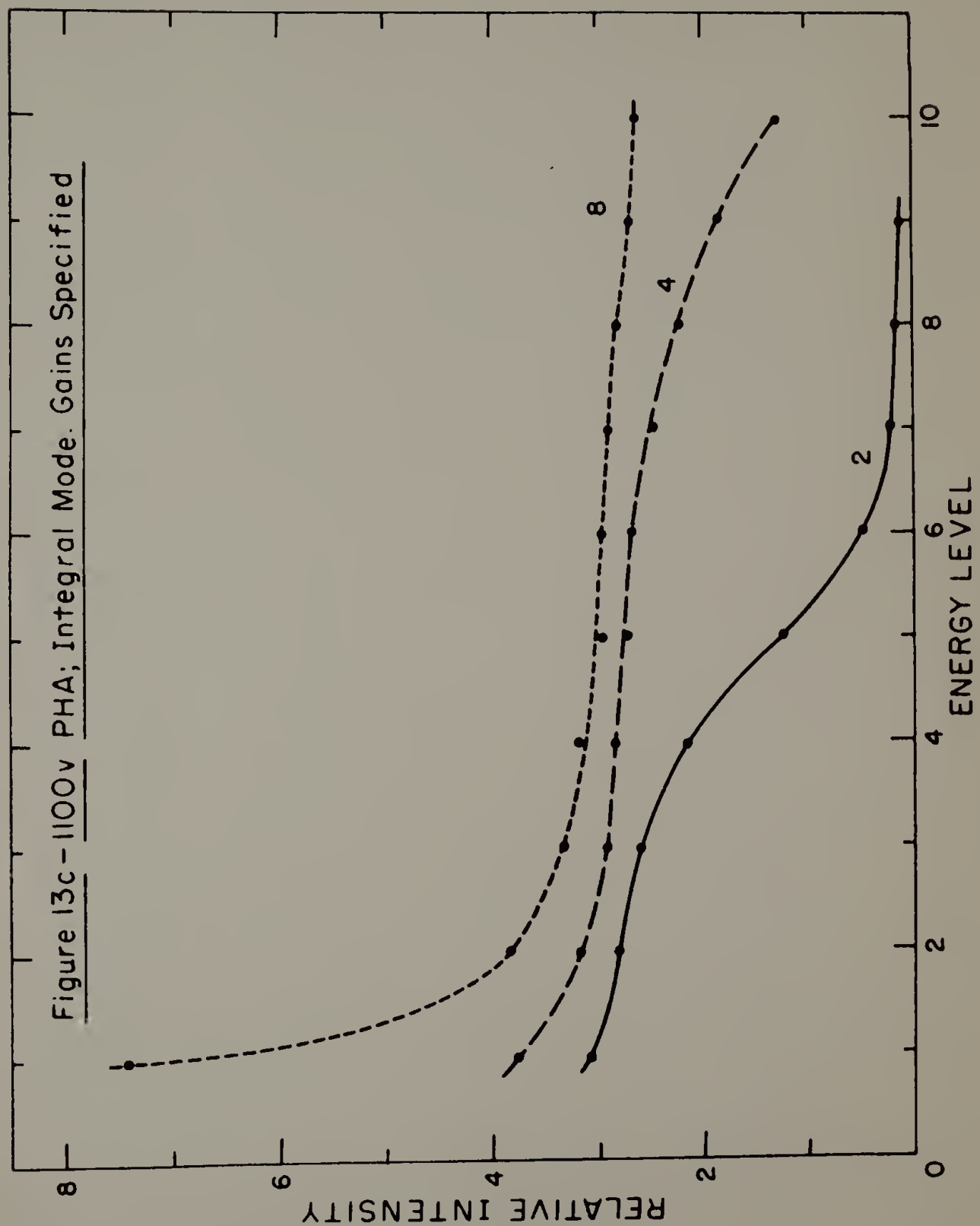

Figure 13c - 1100v PHA; Integral Mode. Gains Specified